PHYSICS AT HIGH AND LOW p_T AT THE LHC

By

ROSHAN MAMMEN ABRAHAM

Bachelor of Technology in Electronics and Communication Engineering
National Institue of Technology, Calicut
Calicut, India
2013

Master of Science in Physics
Case Western Reserve University
Cleveland, Ohio
2018

Submitted to the Faculty of the
Graduate College of the
Oklahoma State University
in partial fulfillment of
the requirements for
the Degree of
DOCTOR OF PHILOSOPHY
August, 2023

PHYSICS AT HIGH AND LOW p_T AT THE LHC

Dissertation Approved:

Assistant Prof. Dorival Gonçalves

Dissertation Advisor

Regents Prof. Kaladi S. Babu

Prof. Flera Rizatdinova

Associate Prof. Kaan Kalkan

ACKNOWLEDGMENTS

I want to first express my gratitude to my advisor, Dr. Dorival Gonçalves for his infinite patience, wisdom, and constant encouragement. His deep insight into physics, philosophy of research, and constructive criticism heavily influenced my academic career.

I am thankful to all my wonderful collaborators, Dr. Ahmed Ismail, Dr. Felix Kling, Dr. Tao Han, Sze Ching Iris Leung, Dr. Han Qin, Dr. Brian Batell, Dr. Jonathan Feng, Dr. Sebastian Trojanowski, Max Fieg, Dr. Sudip Jana, Dr. Yu-Dai Tsai, Saeid Foroughi-Abari, Vishnu P.K, Ajay Kaladharan, Dr. Rahool Barman, and Samiur Mir. In particular, I want to thank Dr. Ahmed Ismail, and Dr. Felix Kling from whom I learned a lot about physics and research. I want to thank all the HEP group members and the Physics department at OSU for being wonderful friends, and colleagues during my time here.

I would like to thank my doctoral committee members, Assistant Prof. Dorival Gonçalves, Regents Prof. Kaladi S. Babu, Prof. Flera Rizatdinova, and Associate Prof. Kaan Kalkan for all their support and feedback that went into this dissertation.

I finally thank my friends, and family without whom none of this would have happened.

The work done in this dissertation is supported in part by the DOE under Grant No. DE- SC0016013.

Acknowledgments reflect the views of the author and are not endorsed by committee members or Oklahoma State University.

Name: ROSHAN MAMMEN ABRAHAM

Date of Degree: AUGUST, 2023

Title of Study: **PHYSICS AT HIGH AND LOW p_T AT THE LHC**

Major Field: PHYSICS

Abstract: The Standard Model (SM) of particle physics does a very good job of explaining the interactions of fundamental particles. The discovery of the Higgs boson over a decade ago was the final piece. But even before this discovery, there was mounting evidence that it is an incomplete theory, to be subsumed by a more accurate description of nature at higher energies. Neutrino masses, dark matter (DM), and various theoretical considerations like the strong CP problem, hierarchy problem, etc. all motivate us to keep searching for this more complete theory.

The Large Hadron Collider (LHC) is one of the biggest scientific machines ever built. Colliding protons at high energies, it has two principal detectors around the beam line. We perform a phenomenological study of the Higgs boson and top quark at the LHC, in search of new physics and to constrain possible beyond the standard model theories. The heavy mass of these particles ensures they scatter in a transverse direction, where their decay products can be detected by the LHC detectors. But light and weakly interacting particles are also produced in these proton collisions and escape these detectors, as they are produced with very low transverse momentum. The Forward Physics Facility (FPF) is a new proposal that aims to detect this forward flux of particles by placing detectors downstream of the interaction point. A large number of neutrinos are expected to interact with these detectors, enabling precision measurements. We study various properties of neutrinos like their electromagnetic properties, neutral current scattering cross section, and coupling to heavy neutral leptons using this forward flux of neutrinos. If DM is sufficiently light, it can also be produced in the forward direction. The FPF detectors can also be used to constrain various light DM models that aren't otherwise well constrained by direct detection techniques.

TABLE OF CONTENTS

LIST OF TABLES

LIST OF FIGURES

Figure Page

CHAPTER I

INTRODUCTION

It is an incredible testament to the human mind that most of the physical phenomena around us can be explained by one equation (albeit a rather large one) and a handful of particles[1]. Theoretical and experimental progress over the last century has resulted in this wonderful framework that is now called the Standard Model (SM) of particle physics, the last piece of which, the Higgs boson, was only discovered eleven years ago [29, 30]. But this success of the Standard Model is tempered by large unknown questions plaguing us. Dark matter [31–33], neutrino masses [34, 35], matter antimatter asymmetry [36, 37], etc. are some of these unanswered questions. Many experimental observations indicate that there are missing pieces in our understanding of nature, and the Standard Model needs to be extended. The search for Beyond Standard Model (BSM) physics is one of the goals of the physics community at present.

The word physics comes from ancient Greek, and it means *knowledge of nature* and much like anything ancient, how physics is pursued has changed drastically. The initial days of *modern physics* were dominated by individual brilliant minds like Galileo and Newton. Even in more recent times like the beginning of the 20th century, much of the progress in physics was made by singular minds. Then came the age of big machines, and bigger collaborations, resulting in one of the greatest scientific machines ever built, the Large Hadron Collider (LHC) [38]. Exploration of BSM physics proceeds via experimental and theoretical avenues, and even within it, there are many approaches. In this dissertation, we take a data-driven phenomenological approach to search for physics beyond the SM. In particular, we look at

[1]Except gravitational interactions.

new ways to study the data coming from LHC to search for any signatures of well-motivated BSM theories. We also look at a new proposal to expand the physics potential at LHC in the forward direction [39, 40]. This new suite of experiments can significantly aid in the search for BSM physics in a complementary manner to the conventional detectors currently present at the LHC. Pilot experiments like FASER [41–43] and FASERν [44, 45] are already installed and taking data. The first collider neutrinos were reported recently by the FASER collaboration [46]. We now introduce the SM and some of its main features. We then briefly mention some shortcomings of this model and why we need to look beyond it, motivating the work done in this dissertation.

1.1 The Standard Model of Particle Physics

1.1.1 Particle Content of the SM

The particle content of the SM is shown in Fig. 1. All matter we see around us is made of these quarks and leptons. They are grouped into three generations, where the only difference is their mass. Together, they are called fermions, as they are spin-$\frac{1}{2}$ particles. But their more familiar property is their electric charge. The up-type quarks (up, charm, top) have an electric charge of $+\frac{2}{3}$, the down-type quarks (down, strange, bottom) have $-\frac{1}{3}$, and charged leptons (electron, muon, tau) have -1. The neutrinos are electrically neutral. The proton gets its $+1$ charge from its up-up-down quark composition, and the neutron is electrically neutral, as it is made up of two down quarks and one up quark. One of the ways fermions interact with one another is by exchanging gauge bosons. In the SM they are the photon, Z boson, W boson, and gluon, and they have spin-1. The photon, Z boson and gluons are electrically neutral, whereas the W boson comes with $\pm$ 1 charge. There is also a third type of particle, the Higgs boson, with spin-0 and zero electric charge. Spin 0 and 1 particles are called bosons, as they have integer values for spin. Together, fermions and bosons make up the particle content of the SM.

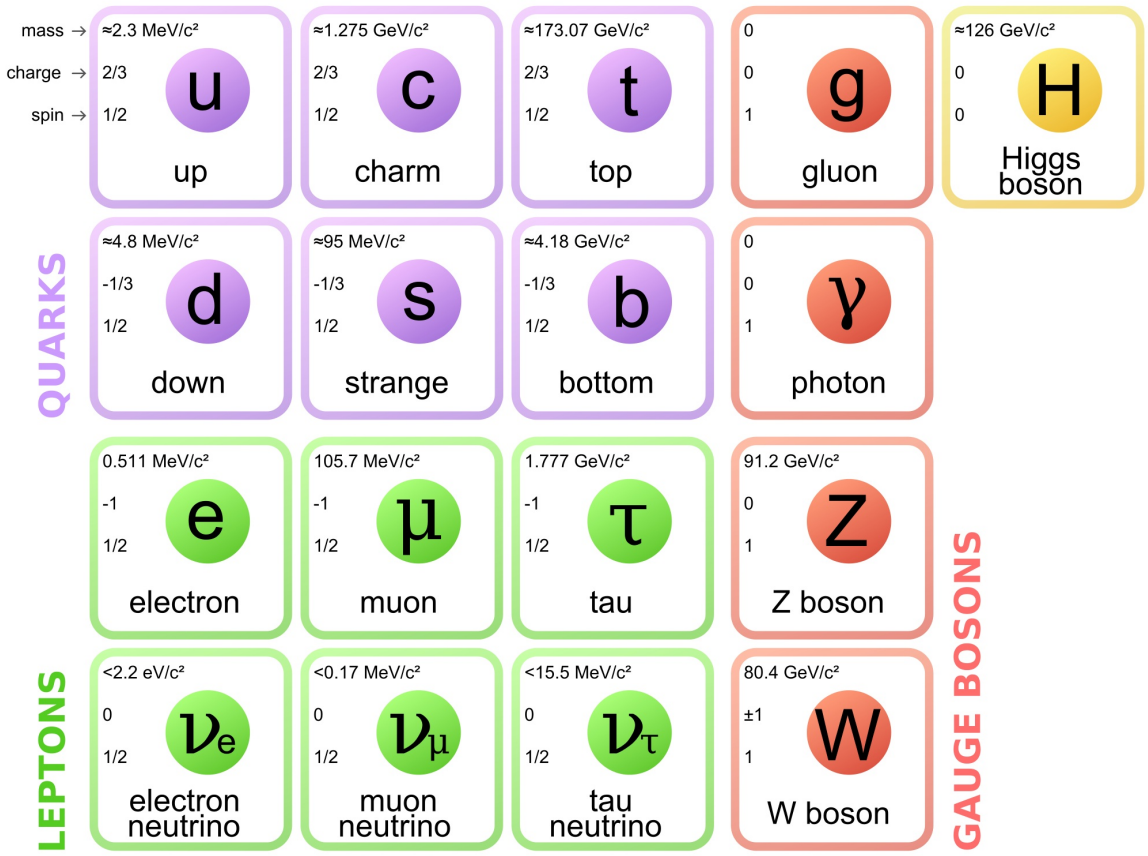

Figure 1: Particle content of the SM. The first three columns on the left are the three generations of fermions. The fourth column is the gauge bosons, and the right-most column is the Higgs boson.

1.1.2 Gauge Symmetry of the SM

These fermions and bosons of the SM interact with each other in a multitude of ways. Each interaction, which manifests as a term in the Lagrangian, must be symmetric under certain gauge transformations. The gauge group of the SM is

$$G_{SM} = SU(3)_C \times SU(2)_L \times U(1)_Y. \tag{1.1.1}$$

Here the subscripts $C, L,$ and Y stand for color, weak isospin, and hypercharge respectively. $SU(3)_C$ is the gauge theory that describes the strong interactions or Quantum Chromodynamics (QCD). The theory of electroweak interactions is described by the gauge group $SU(2)_L \times U(1)_Y$. All possible terms that respect these symmetries can and must be written

down in the Lagrangian. For SM, this is

$$\mathcal{L}_{\mathcal{SM}} = \mathcal{L}_{gauge} + \mathcal{L}_{fermions} + \mathcal{L}_{Higgs} + \mathcal{L}_{Yukawa} \tag{1.1.2}$$

where each term is explained below.

1.1.3 Gauge Fields

Each gauge group of the SM comes with its own gauge boson fields. The number of gauge bosons associated with a group corresponds to the number of generators the group has. $SU(3)$ has eight generators, given in terms of the Gell-Mann matrices (Λ), $T^a = \Lambda^a/2$ where a runs from 1 to 8. So there are 8 gauge bosons called gluons in QCD. The theory of electroweak interactions has 4 gauge bosons. This comes from the three generators of $SU(2)$ which are given in terms of the Pauli matrices (σ), $T^a = \sigma^a/2$ for a from 1 to 3 and the one generator of the $U(1)_Y$ group. These gauge bosons are the photon, $W^{\pm}$ boson, and Z boson[2].

To write down gauge invariant terms, we must first define gauge transformations. Every gauge transformation can be represented by a unitary matrix U. This unitary matrix can be written in terms of the generators of the corresponding gauge group, T^a, as

$$U = \exp\left(i\theta_a T^a\right). \tag{1.1.3}$$

The gauge bosons of a group will transform under transformations belonging to that group as $A^\mu_a T^a \rightarrow U\left(A^\mu_a T^a - \frac{1}{ig}\partial^\mu\right)U^\dagger$ where g is the coupling constant of the group. We next define a field strength tensor from the gauge fields, $A^{\mu\nu}_a = \partial^\mu A^\nu_a - \partial^\nu A^\mu_a + g f^{abc} A^\mu_b A^\nu_c$, where f^{abc} are the structure constants of the gauge group defined by $\left[T^a, T^b\right] = i f^{abc} T^c$. The last term exists only for the non-Abelian gauge groups $SU(3)_C$, and $SU(2)_L$. A gauge invariant

[2]Technically they manifest as such only after electroweak symmetry breaking.

kinetic term for the gauge bosons can now be written down as $-\frac{1}{4}A_a^{\mu\nu}A_{\mu\nu,a}$. For the SM, we have three such terms for the three gauge groups and their corresponding gauge fields. So

$$\mathcal{L}_{gauge} = -\frac{1}{4}G_a^{\mu\nu}G_{\mu\nu,a} - \frac{1}{4}W_a^{\mu\nu}W_{\mu\nu,a} - \frac{1}{4}B^{\mu\nu}B_{\mu\nu}, \tag{1.1.4}$$

where G, W, B are the gauge fields of $SU(3)_C,\ SU(2)_L,$ and $U(1)_Y$ groups respectively. This is the first term in Eq. (1.1.2)

1.1.4 Fermion Fields

The fermion fields ψ transform as $\psi \to U\psi$. But not all transformation act on all fermion fields. This is determined by the quantum numbers of the fields, Table 1. The SM has two left-handed fermion fields, Q_L and L_L, and three right-handed fermion fields, $u_R,\ d_R$ and l_R. For instance, Q_L is a triplet (3) under $SU(3)_C$ and a doublet (2) under $SU(2)_L$. This means it transforms under $SU(3)_C$ and $SU(2)_L$ transformations as a triplet and a doublet representation, respectively. The doublet components of Q_L are the left-handed up and down type quarks, as shown in Table 1, whereas the triplet components are the three colors each of the quarks come in. Contrast this with u_R, the right-handed up quark. It is a singlet (1) under $SU(2)_L$ which means it is not effected by any $SU(2)_L$ transformations. This also demonstrates the chiral nature of SM. It does not treat left- and right-handed fermion fields equally, as they have different representations under the electroweak gauge groups.

To construct gauge invariant terms for the fermions, we define the covariant derivative $D^\mu = \partial^\mu - igA_a^\mu T^a$ from the gauge boson fields. With this definition, we now have the covariant derivative transforming as $D^\mu \to UD^\mu U^\dagger$. The covariant derivative when acting upon a fermion field transforms as $D^\mu\psi \to UD^\mu\psi$. We can now write down the gauge invariant kinetic term for a fermion as

$$\mathcal{L}_{fermions} = i\overline{\psi}\gamma_\mu D^\mu\psi + h.c, \tag{1.1.5}$$

Field	$SU(3)_C$	$SU(2)_L$	$U(1)_Y$
$Q_L = \begin{pmatrix} u \\ d \end{pmatrix}_L$	3	2	1/3
u_R	3	1	4/3
d_R	3	1	-2/3
$L_L = \begin{pmatrix} \nu \\ l \end{pmatrix}_L$	1	2	-1
l_R	1	1	-2
$\phi = \begin{pmatrix} \phi^+ \\ \phi^0 \end{pmatrix}$	1	2	1

Table 1: Quantum numbers of the SM fields.

where γ_μ are the Dirac matrices. In full generality, the form of the covariant derivative in the SM is $D^\mu = \partial^\mu - i\left(g_s G_a^\mu \Lambda^a/2 + g_L W_a^\mu \sigma^a/2 + g_Y B^\mu Y/2\right)$. For each SM fermion, only the relevant gauge boson terms will be present depending on their quantum numbers, and this is the second term in Eq. (1.1.2).

1.1.5 Electroweak Symmetry Breaking and Gauge Boson Masses

The last two terms of Eq. (1.1.2) contain the Higgs boson. So before writing the terms down, we need to introduce the idea of electroweak symmetry breaking (EWSB). The concept of symmetry breaking was introduced into the SM to solve the problem of gauge boson masses. The short-range nature of electroweak interactions required that some gauge bosons be massive. But a mass term for them, $m_A^2 A_\mu A^\mu$, would violate gauge invariance and is not allowed in the SM. The idea behind symmetry breaking was that every time a continuous symmetry was broken, massless particles corresponding to each broken generator would appear. These massless modes would then be absorbed as longitudinal modes of gauge bosons, giving them a mass. In the SM, this is the Higgs mechanism [47–52].

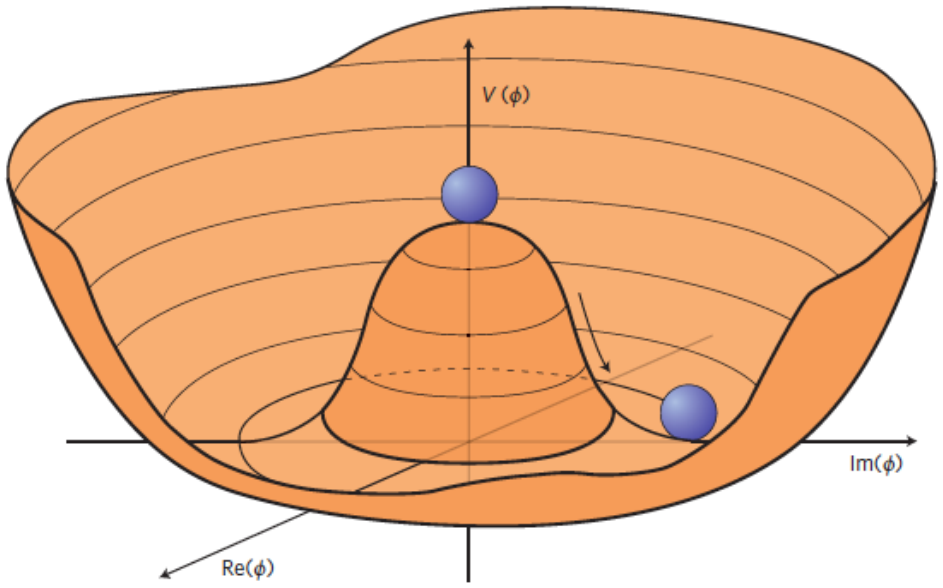

Figure 2: The Mexican hat potential of the Higgs boson within the SM.

The Higgs mechanism spontaneously breaks $SU(2)_L \times U(1)_Y$ to $U(1)_{EM}$, the theory of electromagnetism. This can be done if the spin-0 scalar Higgs field, ϕ, has a potential, whose ground state solution is not symmetric under $SU(2)_L \times U(1)_Y$. So when the field value relaxes to this vacuum expectation value (VEV), $SU(2)_L \times U(1)_Y$ is spontaneously broken. The Higgs field is a complex scalar field, being a $SU(2)_L$ doublet with hypercharge 1. So we can write down the gauge invariant kinetic term and potential for the Higgs field as

$$\mathcal{L}_{Higgs} = \left(D_\mu \phi^\dagger D^\mu \phi\right) - V(\phi). \tag{1.1.6}$$

The covariant derivative acting on it will be $D^\mu = \partial^\mu - i\left(g_L W_a^\mu \sigma^a/2 + g_Y B^\mu Y/2\right)$ and the Higgs potential $V(\phi)$ is given by

$$V(\phi) = -\mu^2 \phi^\dagger \phi + \lambda(\phi^\dagger \phi)^2. \tag{1.1.7}$$

For $\mu^2 > 0$ and $\lambda > 0$, the Higgs potential has the shape shown in Fig. 2. The minima of

the potential occurs when the Higgs doublet acquires the value

$$\langle\phi\rangle = \frac{1}{\sqrt{2}}\begin{pmatrix}0\\ v\end{pmatrix} \text{ with } v = \sqrt{\frac{\mu^2}{\lambda}}. \tag{1.1.8}$$

Once the ϕ field acquires a VEV, it spontaneously breaks $SU(2)_L \times U(1)_Y$ to $U(1)_{EM}$. This means three generators are broken. Corresponding to them, there are three massless modes called Goldstone bosons that get absorbed by the gauge bosons and give them mass. Hence, there are three massive gauge bosons in the SM.

In the unitary gauge, one can expand the Higgs field about this VEV as

$$\phi = \begin{pmatrix}0\\ \frac{1}{\sqrt{2}}(v+h)\end{pmatrix} \tag{1.1.9}$$

where h is the field corresponding to the Higgs boson particle. The kinetic term in Eq. (1.1.6) when expanded about the VEV as above contains terms such as

$$\mathcal{L}_{Higgs} \supset -m_W^2\left(1+\frac{h}{v}\right)^2 W_\mu^+ W^{-\mu} - \frac{1}{2}m_z^2\left(1+\frac{h}{v}\right)^2 Z_\mu Z^\mu. \tag{1.1.10}$$

These terms give rise to gauge boson masses as well as their coupling to the Higgs boson. The physical electroweak gauge fields can be written as

$$W_\mu^\pm = \frac{W_\mu^1 \mp i W_\mu^2}{\sqrt{2}} \tag{1.1.11}$$

$$Z_\mu = \frac{g_L W_\mu^3 - g_Y B_\mu}{\sqrt{g_L^2+g_Y^2}} \tag{1.1.12}$$

$$A_\mu = \frac{g_Y W_\mu^3 + g_L B_\mu}{\sqrt{g_L^2+g_Y^2}}, \tag{1.1.13}$$

and their masses are given by

$$m_W^\pm = \frac{g_L v}{2}\ ,\ m_Z = \frac{\sqrt{g_L^2+g_Y^2}\,v}{2}. \tag{1.1.14}$$

The photon filed A_μ has no such mass term and is massless in the SM.

1.1.6 Yukawa term and Fermion Masses

There is one more gauge invariant term involving the Higgs field that can be written down,

$$\mathcal{L}_{Yukawa} = -\left(\overline{Q}_L Y_d \phi d_R + \overline{Q}_L Y_u \tilde{\phi} u_R + \overline{L}_L Y_l \phi l_R\right) + \text{ h.c.} \tag{1.1.15}$$

where $\tilde{\phi} = i\sigma_2\phi^*$. $Y_{d,u,l}$ are 3×3 matrices that contain the Yukawa couplings of Higgs boson to the three generations of down-type quarks, up-type quarks, and charged leptons respectively. After the Higgs field acquires a VEV, these matrices can be diagonalized to give the fermions their masses,

$$M_u = \frac{v}{\sqrt{2}} Y_u \ , \ M_d = \frac{v}{\sqrt{2}} Y_d \ , \ M_l = \frac{v}{\sqrt{2}} Y_l. \tag{1.1.16}$$

The lack of right-handed neutrinos in the SM means we cannot write down an analogous Yukawa term for neutrinos. Hence, the neutrinos are massless within the SM.

1.2 Going Beyond the Standard Model

The SM as expressed in Eq. (1.1.2) and Table 1 has had incredible success over the last half a century. It successfully explains three of the four fundamental forces of nature. Its predictions agree with experimental observation across a large range of energies to a very high degree of precision. But we know its not the final theory. There are very good experimental and theoretical reasons to consider the SM as a low energy effective theory, and that a more complete Beyond the SM theory must exist. My dissertation has focussed on Higgs, top quark, dark matter and neutrino physics. We briefly introduce these topics below and how they motivate searches for new physics beyond the SM.

1.2.1 Higgs and top quark Physics

Expanding the Higgs potential about the VEV we find

$$\mathcal{L}_{Higgs} \supset -\mu^2 h^2 - \lambda v h^3 - \frac{1}{4}\lambda h^4. \tag{1.2.1}$$

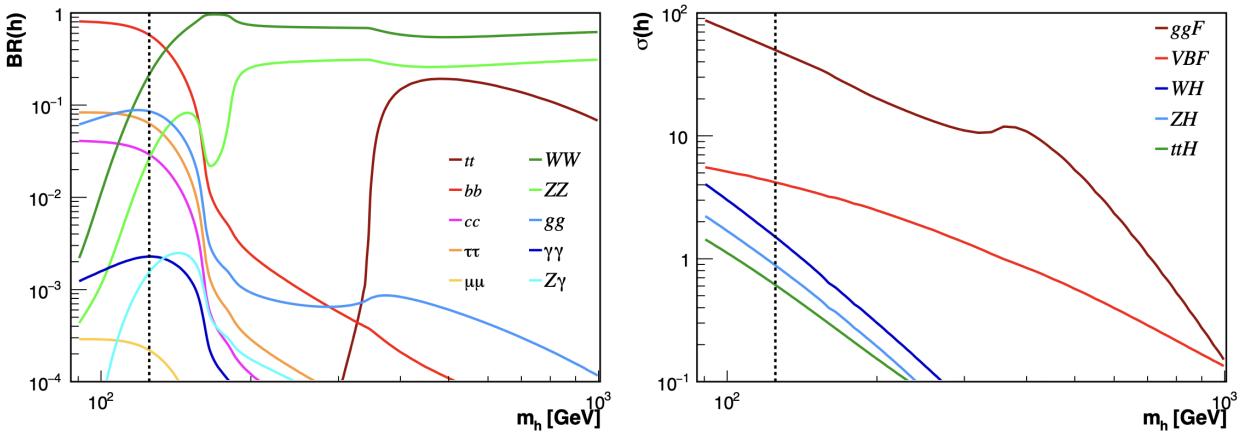

Figure 3: **Left:** The branching ratio for the dominant decay modes of the Higgs boson as a function of its mass. At higher masses, decay channels to heavier particles open up. **Right:** The production cross section for the Higgs boson as a function of its mass. The gluon-fusion (ggF) is the most dominant channel [1, 2].

The mass of the Higgs boson can be read off as $m_h = \sqrt{2}\mu$. The cubic and quartic self couplings are given by $g_{hhh} = -6i\lambda v$, and $g_{hhhh} = -6i\lambda$. The couplings of Higgs boson to fermions are proportional to the fermion mass. Expanding Eq. (1.1.15) in the same way we have

$$\mathcal{L}_{Yukawa} \supset -\frac{\lambda_f v}{\sqrt{2}}\left(1+\frac{h}{v}\right)\overline{f}f = -m_f\left(1+\frac{h}{v}\right)\overline{f}f. \tag{1.2.2}$$

The Higgs couplings to fermions are given as,

$$g_{hff} = -i\frac{\lambda_f}{\sqrt{2}} = -i\frac{m_f}{v}. \tag{1.2.3}$$

The heavier the fermion, the stronger it's coupling to Higgs. This has huge phenomenological implications [3, 53]. The decay of Higgs will be more often into heavier particles as long as it is kinematically allowed. For a 125 GeV Higgs, Fig. 3 left panel, the dominant decay is to $b\bar{b}$. Decays to gauge bosons are suppressed as $m_h < 2m_{Z,W}$, and only off-shell decays to ZZ^*, WW^* are allowed. Decays to leptons are suppressed by their low masses and also by the absence of a color factor. The Higgs can couple to massless gauge bosons via a loop.

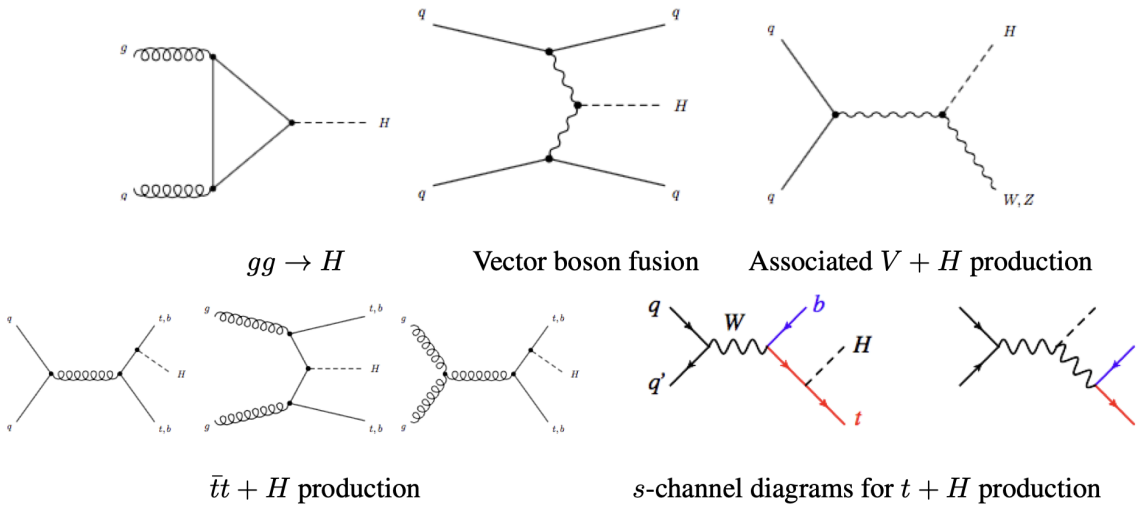

Figure 4: Some of the dominant production channels for the Higgs boson. Figure taken from Ref. [3].

The $h \to gg$ decay is difficult to observe due to the QCD background, but is manifest in the enhanced production cross section of the gluon fusion channel (ggF), Fig. 3 right panel. The electroweak decay of $h \to \gamma\gamma$ is suppressed, but has backgrounds that can be controlled and was one of the channels via which the Higgs was discovered.

There are many ways to produce the Higgs at the LHC. Some dominant diagrams are shown in Fig. 4. Apart from gluon fusion, diagrams containing the tth vertex are interesting. This vertex is proportional to the top quark mass, which is the heaviest particle in the SM. This enhanced coupling strength of the top quark to the Higgs boson makes it particularly sensitive to the Higgs sector and an attractive place to look for new physics effects from BSM theories, such as a shift in the Higgs-top Yukawa coupling (Chapter II). The top quark has a mass of 173.5 ± 1.4 GeV [54]. This high mass means it has a very short lifetime of $\approx 10^{-25}$ seconds [54]. So it will decay before it can hadronize and gives us a unique opportunity to probe the unbounded quark's properties. This can help constrain how the top quark couples to gauge bosons (Chapter III). Taken together, it is apparent the importance top quark and the Higgs boson have to the search for BSM physics.

Standard Model Effective Field Theory (SMEFT) Framework

It is important to discuss the Standard Model Effective Field Theory (SMEFT) Framework, which plays a prominent role in our analysis. It is a model-independent way to analyze data for new physics effects. In this framework, one considers the SM to be an effective theory that is only valid till a certain energy scale Λ. The more complete theory that is valid above Λ is unknown to us, but its effects may be deduced from low energy measurements. To remain completely agnostic to the higher energy theory, we parameterize its effects with higher dimensional operators (dimension > 4) that are only made from SM fields respecting the SM gauge symmetries. These higher dimensional operators are suppressed by powers of Λ as

$$\mathcal{L}_{\text{SMEFT}} = \mathcal{L}_{\text{SM}} + \sum_i \frac{c_i^{dim=5}}{\Lambda} \mathcal{O}_i^{dim=5} + \sum_i \frac{c_i^{dim=6}}{\Lambda^2} \mathcal{O}_i^{dim=6} + \dots . \tag{1.2.4}$$

In SMEFT there is only one dimension 5 operator, the Weinberg operator [55], which plays a prominent role in neutrino mass model building [56]. At dimension 6 there are over 2000 operators [57, 58]. The coefficients, c_i, are called Wilson coefficients. If SM were the true theory at all energies, then all the c_is for dimension > 4 would be 0. But in the SMEFT framework, SM is considered as the leading term in the approximation, and we generically expect contributions from some of these higher dimensional operators. These may manifest as a modification of the process cross section, or a distortion of the kinematic distributions. Though they are suppressed by powers of Λ, they can be constrained by precision measurements from the LHC [59–63]. The ATLAS collaboration, for e.g., looked at the 4 lepton final state [4]. They focused on a subset of dimension 6 operators that could contribute to this final state at the LHC. By comparing the SM prediction to the measured distribution of events, they were able to place constraints on the relevant Wilson coefficients, Fig. 5.

In chapters II and III, we explore a complementary direction to this above analysis. The effects of higher dimensional operators can show up in any observable, and it may not be

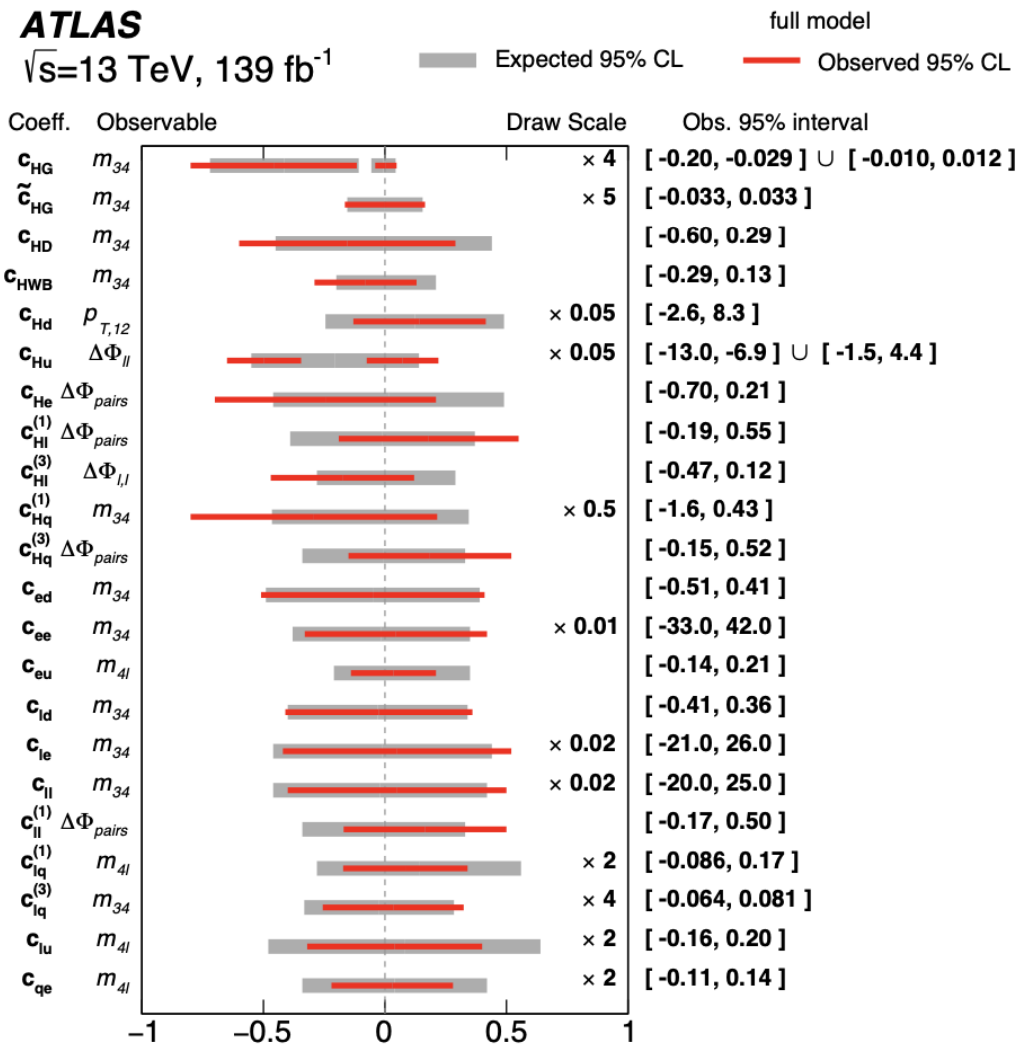

Figure 5: Constraints placed by the ATLAS collaboration on the 22 Wilson coefficients contributing to the 4 lepton final state they analyzed in Ref. [4].

obvious a priori where to look for them. In chapter II, we show how new physics effects can be enhanced in the boosted Higgs regime. Focusing on this part of the phase space enhances the sensitivity of the analysis, allowing for better constraints on the Wilson coefficients. In chapter III, we introduced new angular observables that increased the sensitivity to new physics, especially CP violating higher dimensional operators. Such studies enable one to take full advantage of the SMEFT framework.

1.2.2 Neutrino Physics

As we saw earlier, it is impossible to write down a mass term for neutrinos within the SM. Yet we know neutrinos have a non-zero mass. This comes from observing neutrinos oscillate between three flavors as it propagates [34, 35]. Neutrino oscillations can be explained if we introduce a mass difference between the three neutrino flavors and a slight misalignment between the neutrino flavor basis (in which they interact), and the mass basis (in which they propagate). This misalignment is parameterized by the Pontecorvo-Maki-Nakagawa-Sakata (PMNS) matrix [64–66]. The neutrino flavor basis can be written as ($\nu_e,\ \nu_\mu,\ \nu_\tau$) and the mass basis as ($\nu_1,\ \nu_2,\ \nu_3$). Then we can write

$$\nu_l(x) = \Sigma_j U_{lj}\nu_j(x); \qquad l = e,\ \mu,\ \tau; \quad j = 1,\ 2,\ 3 \tag{1.2.5}$$

where U is the PMNS matrix. This is parameterized in terms of three mixing angles and a phase, and two extra phases for Majorana neutrinos

$$U = \begin{pmatrix} c_{12}c_{13} & s_{12}c_{13} & s_{13}e^{-i\delta} \\ -s_{12}c_{23} - c_{12}s_{23}s_{13}e^{i\delta} & c_{12}c_{23} - s_{12}s_{23}s_{13}e^{i\delta} & s_{23}c_{13} \\ s_{12}s_{23} - c_{12}c_{23}s_{13}e^{i\delta} & -c_{12}s_{23} - s_{12}c_{23}s_{13}e^{i\delta} & c_{23}c_{13} \end{pmatrix} \begin{pmatrix} 1 & 0 & 0 \\ 0 & e^{i\frac{\alpha_{21}}{2}} & 0 \\ 0 & 0 & e^{i\frac{\alpha_{31}}{2}} \end{pmatrix} \tag{1.2.6}$$

with c_{ij} and s_{ij} are $\cos\theta_{ij}$ and $\sin\theta_{ij}$, δ is the Dirac phase, and α_{ij} the two Majorana phases. So along with the three neutrino masses m_i with i from 1 to 3, there are 7 parameters for Dirac neutrinos and 9 for Majorana neutrinos. Precision measurement of neutrino oscillations constrains the three mixing angles and the mass squared differences, Δm^2_{31} and Δm^2_{21}. This is shown in Fig. 6 [5]

Other than oscillations, another avenue to study neutrinos is through their electromagnetic properties [67]. In the SM, the neutrino is electrically neutral and hence won't couple to photons. However, if one were to write a fully general effective electromagnetic form factor (Λ^μ) for the neutrino, then it will have terms that couple to a photon [68, 69]

$$\left\langle \nu_f(p_f)|j^\mu_{\nu,\mathrm{EM}}|\nu_i(p_i)\right\rangle = \overline{u}_f(p_f)\Lambda^\mu_{fi}(q)u_i(p_i), \tag{1.2.7}$$

	Normal Ordering (best fit)		Inverted Ordering ($\Delta\chi^2 = 2.7$)	
	bfp $\pm 1\sigma$	3σ range	bfp $\pm 1\sigma$	3σ range
$\sin^2\theta_{12}$	$0.304^{+0.013}_{-0.012}$	$0.269 \to 0.343$	$0.304^{+0.013}_{-0.012}$	$0.269 \to 0.343$
$\theta_{12}/^\circ$	$33.44^{+0.78}_{-0.75}$	$31.27 \to 35.86$	$33.45^{+0.78}_{-0.75}$	$31.27 \to 35.87$
$\sin^2\theta_{23}$	$0.570^{+0.018}_{-0.024}$	$0.407 \to 0.618$	$0.575^{+0.017}_{-0.021}$	$0.411 \to 0.621$
$\theta_{23}/^\circ$	$49.0^{+1.1}_{-1.4}$	$39.6 \to 51.8$	$49.3^{+1.0}_{-1.2}$	$39.9 \to 52.0$
$\sin^2\theta_{13}$	$0.02221^{+0.00068}_{-0.00062}$	$0.02034 \to 0.02430$	$0.02240^{+0.00062}_{-0.00062}$	$0.02053 \to 0.02436$
$\theta_{13}/^\circ$	$8.57^{+0.13}_{-0.12}$	$8.20 \to 8.97$	$8.61^{+0.12}_{-0.12}$	$8.24 \to 8.98$
$\delta_{\rm CP}/^\circ$	195^{+51}_{-25}	$107 \to 403$	286^{+27}_{-32}	$192 \to 360$
$\frac{\Delta m^2_{21}}{10^{-5}\ \text{eV}^2}$	$7.42^{+0.21}_{-0.20}$	$6.82 \to 8.04$	$7.42^{+0.21}_{-0.20}$	$6.82 \to 8.04$
$\frac{\Delta m^2_{3\ell}}{10^{-3}\ \text{eV}^2}$	$+2.514^{+0.028}_{-0.027}$	$+2.431 \to +2.598$	$-2.497^{+0.028}_{-0.028}$	$-2.583 \to -2.412$

Figure 6: Three flavor oscillation parameter fit from global data taken from Ref. [5]

with

$$\Lambda^\mu_{fi}(q) = \gamma^\mu(Q_{fi} - \frac{q^2}{6}\left\langle r^2\right\rangle_{fi}) - i\sigma^{\mu\nu}q_\nu\mu_{fi}. \tag{1.2.8}$$

Here Q (millicharge), μ (neutrino magnetic moment), and $\langle r^2\rangle$ (neutrino charge radius) are the electromagnetic (EM) properties of the neutrino. These EM properties are good probes of new physics (Chapter V) as in the SM only the neutrino charge radius should exist. Any other EM property would be a sign of new physics. Also, they can help distinguish between Dirac and Majorana neutrinos as Majorana neutrinos can have only off-diagonal neutrino magnetic moments whereas Dirac neutrinos can have both diagonal and off-diagonal ones. So along with neutrino oscillations, neutrino EM properties also provide a path to new physics searches.

1.2.3 Dark Matter

Several astronomical observations indicate that SM particles only constitute around 4.9% of the total energy budget of the universe. The remaining fraction is made up of dark matter (DM), around 26.8%, and dark energy (DE), 68.3% [31]. Evidence for DM is overwhelming and comes from observation of flat galaxy rotation curves [32], matter distribution in the

Bullet cluster [33], measurements from CMB [31, 70], etc. and is one of the most important questions in particle physics.

One of the earliest pieces of evidence for DM came from Fritz Zwicky, who in 1933 applied the virial theorem to obtain the mass of the Coma cluster [71, 72]. He began by calculating the visible mass of the cluster from an estimate of the number of galaxies in the cluster, and the average mass of each galaxy. Using an approximation for the physical size of the cluster, he used the virial theorem to calculate the gravitational potential, and average kinetic energy of each galaxy. The velocity estimate coming from this was far lower than that obtained from the redshifts of these galaxies. This led him to conclude that some form of *dark matter* resided in these galaxy clusters. This way of estimating the velocity of galaxies in a galaxy cluster relied on various assumptions and as yet failed to convince the community of the existence of dark mater[3]. The subsequent decades provided more conclusive evidence, pushed forward by advances in observational techniques. Most of the mass in a galaxy is concentrated in its center. As stars revolve around the galactic center, their speed of rotation depends on the mass contained within their orbit. For stars sufficiently far from the galactic center, we expect their speed to fall off due to increasingly less dense visible matter. But observations of rotation curves from various galaxies [32,73] showed the rotational velocity of stars peak (as expected) and then maintain that constant value even far outside the galactic center. This could be explained if there was missing mass or dark matter in the galaxy that extends far out from the center. Furthermore, one can compare the hydrogen surface density (HI) profile, and the rotation curve from 21 cm line [6]. While the former drops off at large radii, the rotation curves flatten out as seen in Fig. 7. This was another very important piece of evidence in favor of dark matter.

More recently, gravitational lensing observations have also lent credence to dark matter. The most striking example is the Bullet cluster [8] which is a pair of merging galactic clusters. In the absence of dark matter, one would expect the distribution of baryonic matter inferred

[3]For a good historical account see Ref. [7]

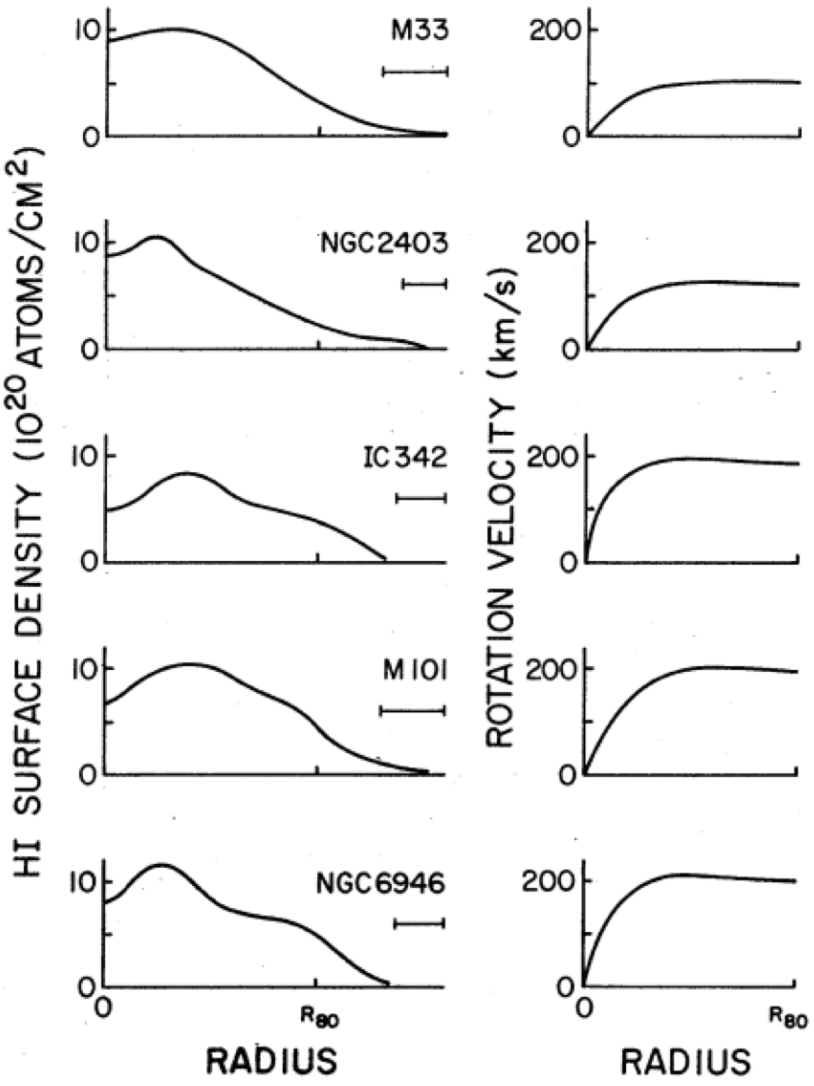

Figure 7: **left:** Hydrogen surface density profile for 5 galaxies studied in [6]. **Right:** The rotation velocity curves for the same 5 galaxies, which show they flatten out at large radii instead of falling off. Figure taken from Ref. [7]

from X-ray observations and gravitational lensing to overlap. But this is not the case. The X-ray map coming from hot baryoinc matter, and lensing map coming from the total matter potential have a spatial separation that can only be explained by some missing mass as seen in Fig. 8.

We now know not only about the presence of dark matter, but also have some tantalizing

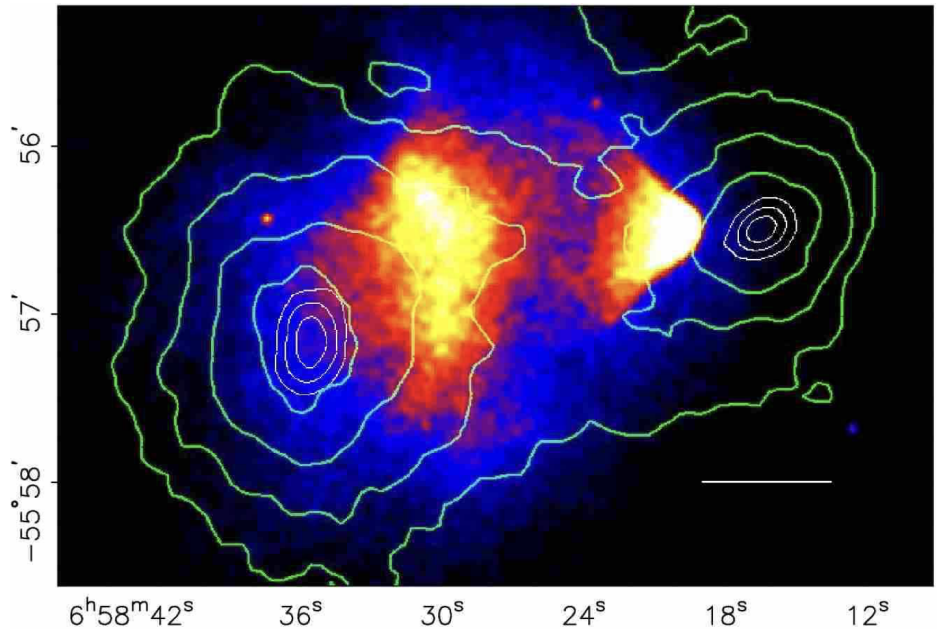

Figure 8: The color map shows the distribution of matter coming from X-ray observation, and the green contours come from the gravitational lensing observations. The two do not overlap, indicating the presence of some hidden matter in the Bullet cluster. Figure taken from Ref. [8]

hints as to its nature. Extensive simulations of structure formation in the early universe seem to imply that most of the DM in the universe must be non-relativistic [74, 75] or cold. Relativistic or hot dark matter would result in structure formation in a *top-down* manner, large structures are formed first from the collapse of hot dark matter and then only the smaller galaxy-sized structures. On the other hand, non-relativistic or cold dark matter follows a *bottom-up* approach, forming small structures which then gravitationally bind to form larger ones. Cosmological surveys [76] indicate a *bottom-up* approach to structure formation, ruling out hot dark matter and in particular SM neutrinos as the primary component of DM. A particle candidate for DM can only be found beyond the SM.

1.3 Brief Overview of the Dissertation

There is a concerted effort to search for new physics from both the experimental and theoretical side. In the following chapters, we present various theoretical studies done in the context of the LHC to study some unresolved questions in particle physics. Each chapter is based on a research paper that was done during my PhD. The chapters are written to be self-contained; it introduces the model, the question it aims to answer, and the analysis techniques used. They draw their own conclusion at the end of each chapter.

In Chapters II and III, we study Higgs and top quark physics using the conventional detectors at the LHC. Making use of novel analysis techniques, and by introducing new experimental observables, we place limits on new physics models. In the second half of the dissertation, we make use of the newly proposed Forward Physics Facility (FPF). Hosting five new detectors, we explore its potential to study neutrino properties in chapters IV to VI. Since DM in certain models can also be produced in the far forward direction, the FPF can be used to study DM, which we pursue in chapters VII and VIII. We finally conclude in chapter IX.

CHAPTER II

DIRECTLY PROBING THE HIGGS-TOP COUPLING AT HIGH SCALES

2.1 Introduction

The top-quark Yukawa coupling (y_t) is the strongest interaction of the Higgs boson in the Standard Model (SM) with $y_t \sim 1$. Owing to its magnitude, it plays a central role in Higgs phenomenology in the SM and could be most sensitive to physics beyond the Standard Model (BSM) associated with the electroweak symmetry breaking [77]. It is crucial for the stability of the SM vacuum during the electroweak phase transition in the early universe [78, 79]. It yields the largest quantum correction to the Higgs boson mass and can trigger the electroweak symmetry breaking in many well-motivated new physics scenarios [80–85]. Thus, the precise measurement of y_t can be fundamental to pin down possible new physics effects.

The top-quark Yukawa coupling has been determined indirectly at the LHC from the Higgs discovery channel $gg \to h$ via the top-quark loop [86]. It can also be directly measured via top pair production in association with a Higgs boson, $t\bar{t}h$. The observation of this channel was reported in 2018 by both ATLAS and CMS collaborations, with respective significances of 6.3 and 5.2 standard deviations [87, 88]. These measurements confirm the SM expectation that the Higgs boson interacts with the top-quark with an order one Yukawa coupling. The high-luminosity LHC (HL-LHC) projections indicate that the top Yukawa will be probed to a remarkable precision at the end of the LHC run, reaching an accuracy of $\delta y_t \lesssim \mathcal{O}(4)\%$ [89].

The current measurements are performed near the electroweak scale $Q \sim v$. If the new physics scale Λ is significantly larger than the energy probed at the LHC, the BSM

effects generally scale as $(Q/\Lambda)^n$ with $n \geq 0$ [57, 58, 90], before reaching a new resonance. Therefore, it is desirable to enhance the new physics effects by exploring the high energy regime associated with the Higgs physics. Proposals have been made recently to study the off-shell Higgs signals $gg \to h^* \to VV$ [62, 91–96]. This process could be sensitive to potential new physics of the tth^* and VVh^* interactions or a h^* propagation at high energy scales $Q > v$.

In the present study, we *directly* explore the Higgs-top coupling at high energy scales using the $t\bar{t}h$ production channel. For an on-shell Higgs production with high transverse momentum, this process effectively probes the top-quark Yukawa interaction at a high scale in both the space-like and time-like regimes. In contrast, the off-shell Higgs physics probes the complementary physics only in the time-like domain [94–96]. As a concrete formulation, we study the BSM effects to the Higgs-top Yukawa in the Effective Field Theory (EFT) framework, focusing on two relevant higher dimensional contributions. Then, we move on to a BSM hypothesis that features a non-local momentum-dependent form factor of the Higgs-top interaction [95,96]. This form factor generally captures the top Yukawa composite substructure. To combine the large event yield with a high energy physics probe, we focus on the channel with the largest Higgs decay branching fraction, $\mathcal{BR}(h \to b\bar{b}) \sim 58\%$, in association with jet substructure techniques at the boosted Higgs regime.

The rest of the presentation is organized as follows. In Section 2.2, we present the theoretical parameterization associated with the potential new physics for the Higgs-top couplings in the EFT framework and an interaction form factor. We then derive the new physics sensitivity to those interactions in Section 2.3, featuring the effects that benefit with the energy enhancement at the boosted Higgs regime. Finally, we present a summary in Section 2.4.

2.2 New Physics parametrization

In this section, we describe two qualitatively different new physics parametrizations for beyond-the-Standard Model effects to the Higgs-top coupling at high energy scales. The first one considered is in the effective field theory framework by adding in a few relvant dimension-6 operators that are results from integrating out some heavy degrees of freedom mediating the Higgs and top interactions. The second formulation is a non-local Higgs-top form factor, motivated from a strongly interacting composite theory for the Higgs and top quarks. These two forms of new physics parameterizations are quite representative in capturing the general features of the BSM couplings for the Higgs and the top quark.

2.2.1 Effective Field Theory

The Standard Model Effective Field Theory (SMEFT) provides a consistent bottom-up framework to search for new physics [57–63]. In this scenario, the beyond the SM particles are too heavy to be produced on-shell. The new states can be integrated out and parametrized in terms of higher dimension operators as contact interactions [90]. In general, the EFT Lagrangian can be written as

$$\mathcal{L}_{\rm EFT} = \mathcal{L}_{\rm SM} + \sum_i \frac{c_i}{\Lambda^2}\mathcal{O}_i + \mathcal{O}\left(\frac{1}{\Lambda^4}\right) , \tag{2.2.1}$$

where Λ is the scale of new physics, $\mathcal{O}_i$ are effective operators of dimension-six compatible with the SM symmetries, and c_i are corresponding Wilson coefficients. Higher dimensional operators can modify the existing SM interactions, as well as generate new Lorentz structures, both of which can give rise to phenomenologically relevant energy enhancements in the scattering amplitudes.

We follow the SMEFT framework to study the new physics effects to the Higgs-top coupling at high scales. We adopt the Warsaw basis of operators [58] and focus on two-fermion operators, leading to contributions to $t\bar{t}h$ production at the LHC which are relatively

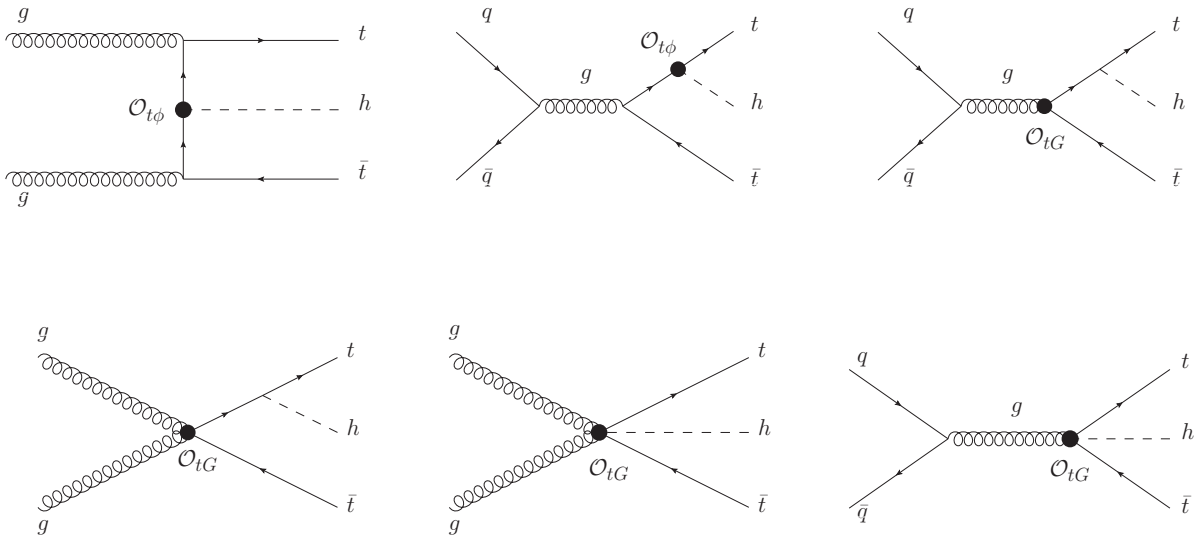

Figure 9: Representative Feynman diagrams contributing to $t\bar{t}h$ production. The black dots represent the BSM vertices arising from the EFT operators.

unconstrained

$$\mathcal{O}_{t\phi} = (H^\dagger H)(\bar{Q}t)\tilde{H} + \text{h.c.}\,, \tag{2.2.2}$$

$$\mathcal{O}_{tG} = g_s(\bar{Q}\sigma^{\mu\nu}T_A t)\tilde{H}G^A_{\mu\nu} + \text{h.c.}\,. \tag{2.2.3}$$

The first new physics operator, $\mathcal{O}_{t\phi}$, rescales the SM top Yukawa coupling. The second one, $\mathcal{O}_{tG}$, corresponds to the chromomagnetic dipole moment of the top-quark. Besides modifying the gtt vertex in the SM, $\mathcal{O}_{tG}$ also gives rise to new interaction vertices, namely $ggtt$, $gtth$ and $ggtth$. While $\mathcal{O}_{tG}$ results in phenomenological effects to the associated $t\bar{t}$ processes, it amounts to possibly significant new physics sensitivity in the $t\bar{t}h$ channel [97]. Hence, we incorporate it in our analysis exploring its high energy behavior. In Fig. 9, we present a representative set of Feynman diagrams for $t\bar{t}h$ production arising from the EFT interactions. The experimental LHC analyses constrain these Wilson coefficients at 95% Confidence Level (CL) to the ranges [98, 99]

$$c_{t\phi}/\Lambda^2 = [-2.3, 3.1]/\text{TeV}^2, \quad c_{tG}/\Lambda^2 = [-0.24, 0.07]/\text{TeV}^2.$$

Guided by these results, we choose illustrative values of the coefficients as

$$|c_{tG}/\Lambda^2| = 0.1 \text{ TeV}^{-2} \quad \text{and} \quad |c_{t\phi}/\Lambda^2| = 1 \text{ TeV}^{-2}, \tag{2.2.4}$$

for our following representative kinematic distributions. For recent phenomenological SMEFT global fit studies, see Refs. [59, 60].

2.2.2 Higgs-Top coupling form-factor

The top-quark Yukawa coupling has a special role in the naturalness problem, displaying the dominant quantum corrections to the Higgs mass. Thus, it is crucially important to probe the Higgs-top interaction at high scales into the ultra-violet regime. It is well-motivated to consider that the top-quark and Higgs boson may not be fundamental, but composite particles arising from strongly interacting new dynamics at a scale Λ [83, 85, 100, 101]. In such scenarios, the top Yukawa may exhibit a momentum-dependent form-factor near or above the new physics scale Λ, rather than a point-like interaction. It is challenging to write a form-factor, in a general form, without prior knowledge of the underlying strong dynamics of the specific composite scenario. Inspired by the nucleon form-factor [102], we adopt the following phenomenological ansatz

$$\Gamma(Q^2/\Lambda^2) = \frac{1}{(1 + Q^2/\Lambda^2)^n}\,, \tag{2.2.5}$$

where Q is the energy scale associated with the physical process. This educated guess results in a dipole form-factor for the $n = 2$ scenario with an exponential spatial distribution in a space-like probe. Higher values of n correspond to higher multi-poles, typically leading to a stronger suppression.

2.3 Analysis

To probe these new physics contributions, we explore the $pp \to t\bar{t}h$ channel at high energy scales. We combine the large signal event rate with controlled backgrounds, studying the

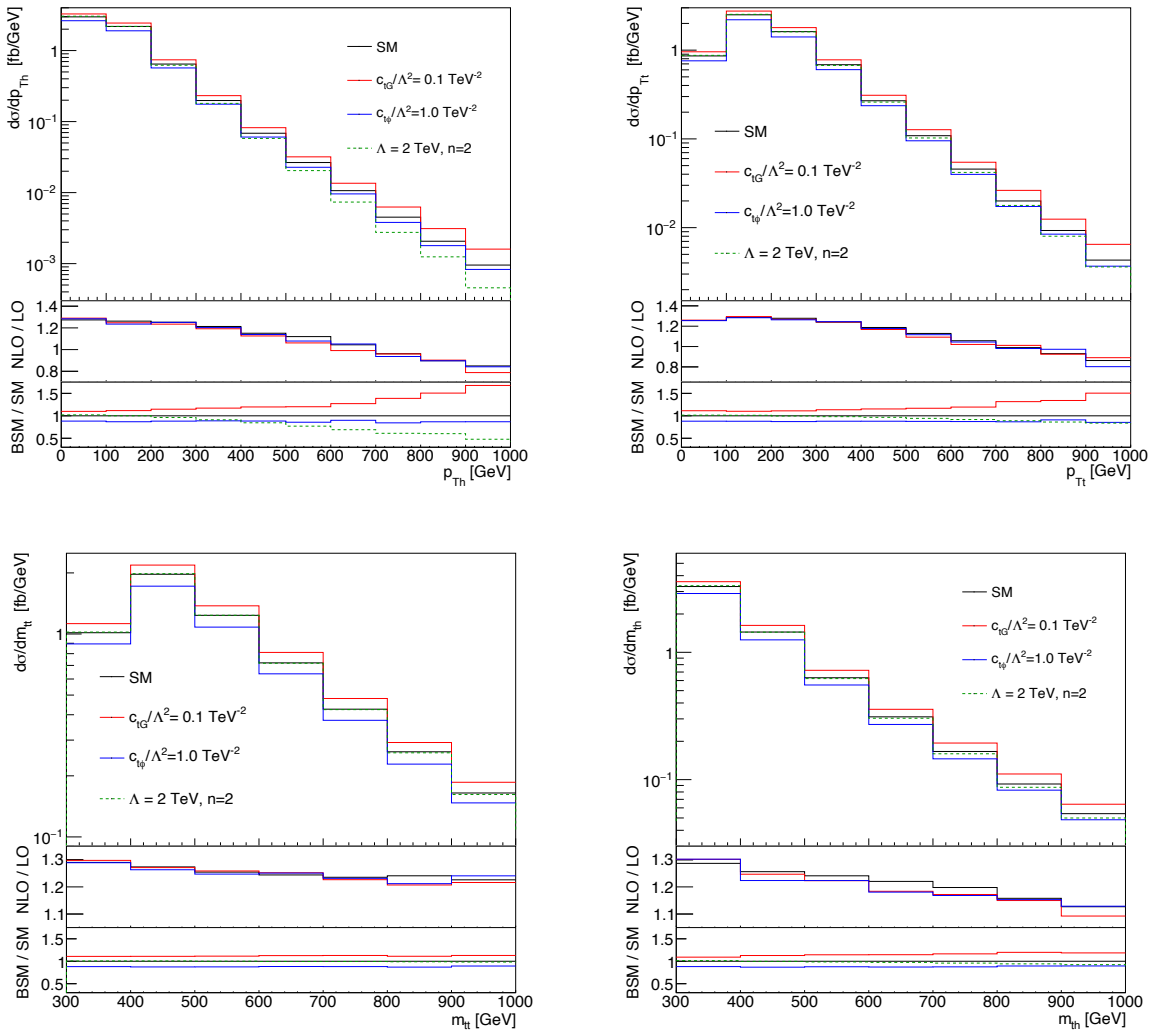

Figure 10: Top panels: Transverse momentum distributions for the Higgs boson p_{Th} (left) and the hardest top-quark p_{Tt} (right). Bottom panels: Invariant mass distributions for the top pair m_{tt} (left) and the Higgs and top-quark m_{th} (right). Each panel shows on the top the $t\bar{t}h$ sample in the SM and new physics scenarios. The results are presented at the NLO QCD fixed order. We also show the local NLO K-factor (middle panel in each figure as NLO/LO) and the ratio between new physics and SM scenarios (bottom panel in each figure as BSM/SM). We assume the LHC at 14 TeV.

boosted $h \to b\bar{b}$ final state in association with leptonic top-quark pair decays. The signal is defined in the four b-tag sample and displays two opposite sign leptons. The leading

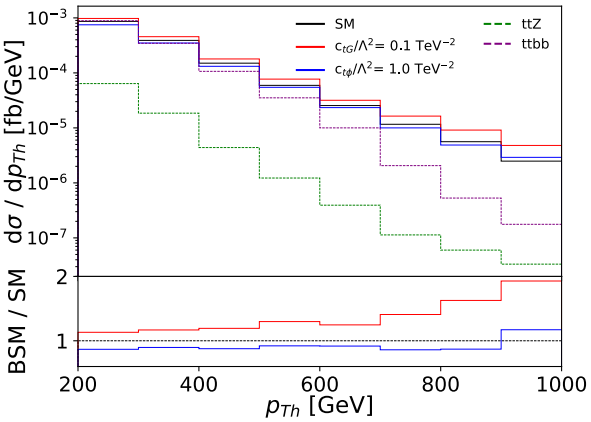

Figure 11: Transverse momentum distribution of the Higgs boson p_{Th} for the $t\bar{t}h$ sample in the SM (black) and new physics scenarios with $c_{tG}/\Lambda^2 = 0.1$ TeV^{-2} (red), $c_{t\phi}/\Lambda^2 = 1$ TeV^{-2} (blue). The leading backgrounds $t\bar{t}b\bar{b}$ (purple) and $t\bar{t}Z$ (green) are also presented. We assume the LHC at 14 TeV.

backgrounds, in order of relevance, are $t\bar{t}b\bar{b}$ and $t\bar{t}Z$.

We perform the signal and background event generation with `MadGraph5_aMC@NLO` [103]. The $t\bar{t}h$ and $t\bar{t}Z$ samples are generated at NLO QCD and the $t\bar{t}b\bar{b}$ sample at LO. The dimension-six EFT contributions are added through the FeynRules model `SMEFT@NLO` [104]. This implementation grants one-loop QCD computations, accounting for the EFT contributions. In particular, it incorporates relevant extra radiation effects at the matrix element level [105]. Shower, hadronization, and underlying event effects are simulated with `Pythia8` [106] using the `Monash` tune [107]. We use `MadSpin` to properly describe the top-quark decays, accounting for spin correlation effects [108]. We adopt the parton distribution functions from MMHT2014 NLO with $\alpha_S(m_Z) = 0.118$ [109] in the five flavor scheme. Additional relevant parameters are $m_t = 172$ GeV, $m_h = 125$ GeV, $m_Z = 91.1876$ GeV, $m_W = 79.82$ GeV, and $G_F = 1.16637 \times 10^{-5}$ GeV^{-2}. We set our scales to a constant value of $\mu_F = \mu_R = m_t + m_h/2$ to align better with previous studies [97]. We assume the LHC at $\sqrt{s} = 14$ TeV.

Robust new physics studies at the LHC usually come hand in hand with precise theoretical

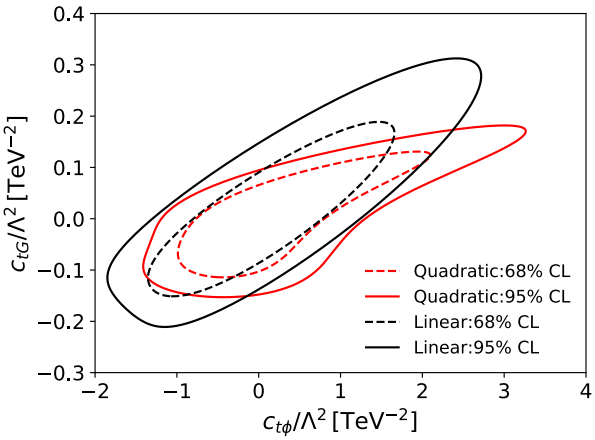

Figure 12: 95% (full line) and 68% (dashed line) CL limits on the Wilson coefficients $(c_{tG}/\Lambda^2, c_{t\phi}/\Lambda^2)$ at the 14 TeV HL-LHC with 3 ab^{-1} of data. The results are presented both at the linear (black) and quadratic (red) order in dimension-6 SMEFT operator coefficients.

calculations. The impact of the higher order QCD corrections, which can be conventionally estimated by a K-factor (*i.e.* the ratio between the NLO and LO predictions), usually result in significant contributions. To illustrate the higher order and new physics effects at high energies, we present in Fig. 10 the NLO fixed order parton level distribution for several relevant kinematic observables associated with the $t\bar{t}h$ signal sample: the transverse momentum distribution for the Higgs boson p_{Th} (upper left), for the hardest top-quark p_{Tt} (upper right), the invariant mass distribution for the top pair m_{tt} (lower left), and for the Higgs and top-quark m_{th} (lower right). We observe that the higher order QCD corrections are correlated with the kinematic observables, resulting in about $20\% - 30\%$ variation (as seen in the panels of NLO/LO) and cannot be captured by a global NLO K-factor. It is thus crucial to include the higher order predictions in the full differential analysis.

New physics contributions may sensitively depend on the kinematics as well, as demonstrated in the panels of BSM/SM in Fig. 10. High transverse momenta of an on-shell top quark or Higgs boson could probe the space-like regime for the top-Higgs interactions, while the high invariant mass of the tH system could be sensitive to the time-like regime from

heavy states in s-channels. First, we observe sizable energy enhancement arising from the $\mathcal{O}_{tG}$ operator, in particular, for the transverse Higgs momentum distribution (as seen in the panels of BSM/SM), starting with a 10% increase at the non-boosted regime $p_{Th} < 100$ GeV, adding up to 65% for $p_{Th} = 1$ TeV. In contrast, due to the generic dipole suppression, the form-factor scenario displays a depletion in cross-section at higher energies. The rate is reduced by 5% at $p_{Th} = 200$ GeV, reaching 55% suppression at $p_{Th} = 1$ TeV. For the form-factor scenario, we adopt a representative scale $Q = p_{Th}$. New physics effects associated with the operator $\mathcal{O}_{t\phi}$ do not result in a distinct energy profile with respect to the SM. In the $t\bar{t}h$ process, this operator only contributes with a shift to the top Yukawa, resulting in a flat rescale with respect to the SM cross-section, independent of the process energy scale. Despite the absence of a manifest energy enhancement, this new physics contribution can also benefit from our high energy scale analysis due to more controlled backgrounds at the boosted Higgs regime, as we will show in the following.

The boosted Higgs analysis, in combination with jet substructure techniques effectively suppress the initially overwhelming backgrounds for the $t\bar{t}h$ signal with the dileptonic top decays and $h \to b\bar{b}$, as first shown in Ref. [110]. Here we follow a similar strategy. We start our analysis requiring two isolated and opposite sign leptons with $p_{T\ell} > 10$ GeV and $|\eta_\ell| < 3$. For the hadronic component of the event, we first reconstruct jets with the Cambridge-Aachen algorithm with $R = 1.2$ [111], requiring at least one boosted fat-jet with $p_{TJ} > 200$ GeV and $|\eta_J| < 3$. We demand that one of the fat-jets be Higgs tagged with the Butterworth-Davison-Rubin-Salam (BDRS) algorithm [112, 113]. Higgs tagging of the fat-jet via the BDRS algorithm involves identifying three subjets within the fat-jet. This is done by shrinking the jet radius until the fat-jet splits into three filtered jets. The radius of separation among the filtered jets is defined as $R_{\rm filt} = \min(0.3, R_{bb}/2)$. Among the three filtered jets, the two hardest are required to be b-tagged, while the third filtered jet tracks the dominant $\mathcal{O}(\alpha_s)$ radiation from the Higgs decay.

As we only have one hadronic heavy particle decay, namely the Higgs boson, we proceed

with the event reconstruction using a smaller jet size to further reduce the underlying event contamination. Thus, we remove all the hadronic activity associated with the Higgs fat-jet and re-cluster the remaining particles with the jet radius $R = 0.4$, using the anti-k$_t$ jet algorithm. We demand two b-tagged jets with $p_{tb} > 30$ GeV and $|\eta_b| < 3$. As our final state displays in total four b-tagged jets, we exploit the improvements in the central tracking system, that will be in operation for the HL-LHC run, to enhance the event rate for our signal. Based on the ATLAS report [114], we assume 85% b-tagging efficiency and 1% mistag rate for light-jets. To further suppress the backgrounds, the filtered mass for the Higgs candidate is imposed to be around the Higgs boson mass $|m_h^{\rm BDRS} - 125 \text{ GeV}| < 10$ GeV. We show in Table 2 more details on the cut-flow analysis.

cuts	$t\bar{t}h$	$t\bar{t}b\bar{b}$	$t\bar{t}Z$
BDRS h-tag, $p_{T\ell} > 10$ GeV, $\|\eta_\ell\| < 3$, $n_\ell = 2$	3.32	6.35	1.02
$p_{Tj} > 30$ GeV, $\|\eta_j\| < 3$, $n_j \geq 2$, n_b=2	0.72	1.97	0.22
$\|m_h^{\rm BDRS} - 125\| < 10$ GeV	0.15	0.14	0.009

Table 2: Cut-flow for signal and backgrounds at LHC $\sqrt{s} = 14$ TeV. The selection follows the BDRS analysis described in the text. Rates are in units of fb and account for 85% (1%) b-tag (mistag) rate, hadronization, and underlying event effects.

2.3.1 Scale for the EFT operators

In Fig. 11, we go beyond the partonic level calculation and display the hadron level transverse momentum distribution (p_{Th}) for the Higgs boson candidate from the $pp \to t\bar{t}h$ channel in the SM and the EFT contributions, in addition to the leading backgrounds $t\bar{t}b\bar{b}$ and $t\bar{t}Z$. We observe that the boosted Higgs search dovetails nicely with our BSM physics study as presented in Fig. 10. At the higher energy scales, both the backgrounds get further depleted and the new physics effects become more prominent. In particular, we observe a large enhancement from the $\mathcal{O}_{tG}$ contributions at the high energy scales.

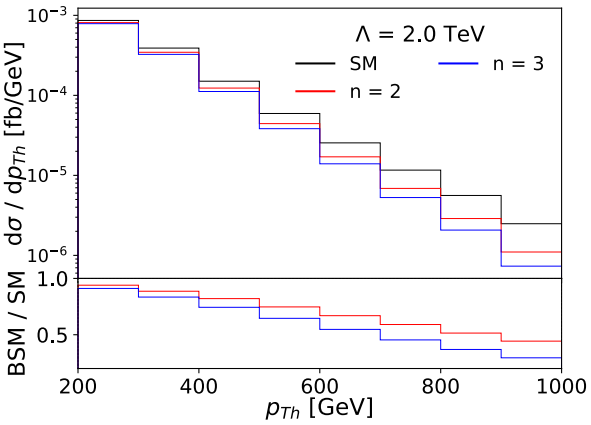

Figure 13: Transverse momentum distribution of the Higgs boson p_{Th} for the $t\bar{t}h$ sample in the SM (black) and new physics scenarios with $n = 2$ (red) and $n = 3$ (blue), assuming $\Lambda = 2$ TeV. We assume the LHC at 14 TeV.

To explore the sensitivity reach for these effects in the boosted regime, we perform a binned log-likelihood analysis on the p_{Th} distribution. In Fig. 12, we present the 68% and 95% CL limits on the Wilson coefficients $(c_{tG}/\Lambda^2, c_{t\phi}/\Lambda^2)$. We assume the HL-LHC at 14 TeV with 3 ab^{-1} of data. To infer the uncertainty on the EFT expansion, we present the results accounting for terms up to linear and quadratic order on the Wilson coefficient c_i/Λ^2. We observe only small differences between these two scenarios, which is a good indication of the robustness of our results.

CMS has recently reported an EFT interpretation using associated top quark production data with an integrated luminosity of $\mathcal{L} = 41.5$ fb^{-1} [115]. The signal samples include, in particular, the $t\bar{t}h$ and thq processes, being direct sensitive to the top-quark Yukawa coupling. The resulting constraint at the 95% CL for the chromomagnetic operator leads to two regions $c_{tG}/\Lambda^2 = [-1.26, -0.69]$ TeV^{-2} and $[0.08, 0.79]$ TeV^{-2}. The same holds for the $\mathcal{O}_{t\phi}$ operator where $c_{t\phi} = [-14.12, -1.46]$ TeV^{-2} and $[32.30, 44.48]$ TeV^{-2}. While CMS does not focus on the very high energy scales and uses the leptonic Higgs decays, we explore the largest Higgs branching ratio, $h \to b\bar{b}$, in the boosted Higgs regime, and thus obtaining significantly higher sensitivities at the HL-LHC.

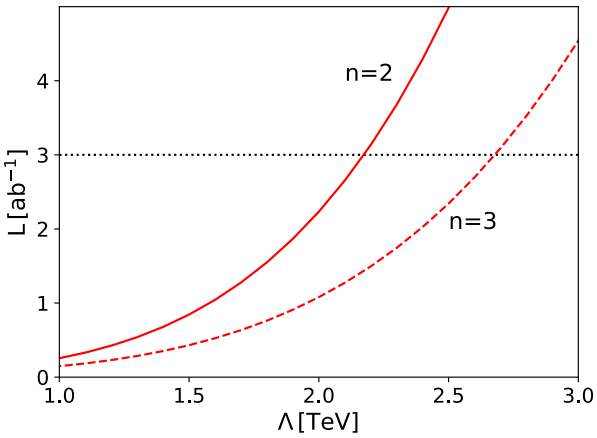

Figure 14: 95% CL sensitivity on the new physics scale Λ as a function of the LHC luminosity. We consider two form-factor scenarios: $n = 2$ (solid line) and $n = 3$ (dashed line).

2.3.2 Probing the form-factor

In Fig. 13, we present the transverse momentum distribution (p_{Th}) for the Higgs boson candidate from the $pp \to t\bar{t}h$ channel in the SM and the form-factor contribution. We consider two hypotheses $n = 2$ and $n = 3$ with the new physics scale $\Lambda = 2$ TeV. While it is challenging to probe the BSM effects at relatively small scales, these contributions can be effectively enhanced at the boosted regime. For instance, starting at $p_{Th} \sim 200$ GeV with $n = 2$ ($n = 3$), we observe a 5% (9%) effect. Moving to $p_{Th} \sim 400$ GeV, the new physics results in larger depletion of 18% (25%) with respect to the SM hypothesis.

Our relatively large event rate with the boosted $h \to b\bar{b}$ analysis, grants probes at large energy scales with relevant statistics. Hence, we explore the full profile of the p_{Th} distribution through a binned log-likelihood analysis. The new physics sensitivity is presented in Fig. 14. The HL-LHC, with 3 ab^{-1} of data, will be able to probe these new physics effects up to a scale of $\Lambda = 2.1$ TeV for $n = 2$ and $\Lambda = 2.7$ TeV for $n = 3$ at 95% CL. These results are complementary to the off-shell Higgs analyses, $gg \to h^* \to ZZ$. For the latter, assuming $n = 3$, the limits on the new physics scale are $\Lambda = 1.1$ TeV for the 4ℓ final state and $\Lambda = 2.1$ TeV for the $\ell\ell\nu\nu$ final state [95, 96].

	channel	c_i/Λ^2 [TeV^{-2}] 95% CL bounds	$\Lambda/\sqrt{c_i}$ [TeV] BSM scale
$c_{t\phi}$	$t\bar{t}h$ (this work)	$[-1.04, 1.00]$	1.0
	$h^* \to ZZ \to \ell\ell\nu\nu$ [96]	$[-2.8\ ,\ 1.5]$	0.6
	$h^* \to ZZ \to 4\ell$ [95]	$[-3.3\ ,\ 3.3]$	0.55
	Higgs comb. ATLAS [98]	$[-2.3\ ,\ 3.1]$	0.57
c_{tG}	$t\bar{t}h$ (this work)	$[-0.11\ ,\ 0.12]$	2.9
	$t\bar{t}$ CMS [99]	$[-0.24\ ,\ 0.07]$	2.1
form-factor $n = 2$	$t\bar{t}h$ (this work)	-	2.1
	$h^* \to ZZ \to \ell\ell\nu\nu$ [96]	-	1.5
	$h^* \to ZZ \to 4\ell$ [95]	-	0.8
form-factor $n = 3$	$t\bar{t}h$ (this work)	-	2.7
	$h^* \to ZZ \to \ell\ell\nu\nu$ [96]	-	2.1
	$h^* \to ZZ \to 4\ell$ [95]	-	1.1

Table 3: Summary results from the $t\bar{t}h$ studies for the Higgs-top coupling at high scales in terms of the dimension-6 operators and general form-factor scenarios. The results are shown at 95% CL, and we assume the HL-LHC at 14 TeV with 3 ab^{-1} of data. For comparison, we also show the results from off-shell h^* studies, the ATLAS Higgs combination with 139 fb^{-1}, and the CMS top pair bound with 35.9 fb^{-1}.

2.4 Summary and discussions

We studied the prospects to *directly* probe the Higgs-top coupling for new physics at high energy scales using the $pp \to t\bar{t}h$ process at the HL-LHC. We considered two beyond the SM scenarios, namely the SMEFT framework and a general Higgs-top form-factor, as discussed in Sec. 2.2. We presented in Sec. 2.3 the general phenomenological effects for these new physics contributions, showing that they could produce augmented new physics effects at high energy scales.

Focusing on the boosted Higgs regime in association with jet substructure techniques, we explored the largest Higgs branching fraction $h \to b\bar{b}$ along with the clean leptonic top-quark decays. The BSM effects were constrained through a shape analysis on the p_{Th} spectrum. We observed the potential sensitivity at the TeV-scale for new physics both in the EFT and form-factor scenarios. The chromomagnetic dipole operator was probed up to $\Lambda/\sqrt{c_{tG}} \approx 2.9$ TeV and the $\mathcal{O}_{t\phi}$ operator to $\Lambda/\sqrt{c_{t\phi}} \approx 1.0$ TeV, as shown in Sec. 2.3.1. The limits presented sub-leading differences between the linear and quadratic c_i/Λ^2 expansion, indicating that our phenomenological study satisfies the EFT expansion. Finally, when considering a more general Higgs-top quark form-factor in Sec. 2.3.2, we concluded that the HL-LHC is sensitive to new physics up to the scale $\Lambda = 2.1$ TeV for $n = 2$ and 2.7 TeV for $n = 3$ at 95% CL. Further details are summarized in Table 13. The $t\bar{t}h$ studies at high scales, which *directly* explore the Higgs-top Yukawa interaction, results in a competitive and complementary pathway for BSM sensitivity in comparison to the off-shell Higgs channels and the current ATLAS and CMS limits.

Some improvements in sensitivity can be anticipated by including other modes, such as $t\bar{t}(h \to \gamma\gamma)$, which would yield a cleaner signal but a lower rate [116]. In addition, we can increase our present $t\bar{t}(h \to b\bar{b})$ statistical sample by about a factor of six, if we include one leptonic decay plus one hadronic decay of the $t\bar{t}$. The analysis, however, would be more complex, with significantly larger QCD backgrounds [117]. Finally, while we adopt `MadGraph5_aMC@NLO` as our general Monte Carlo generator (that accounts for the signal EFT contributions at NLO QCD), we acknowledge some other recent important developments associated with the $t\bar{t}b\bar{b}$ background [118–120]. We leave those improvements to future work with realistic simulations.

CHAPTER III

BOOSTING NEW PHYSICS SEARCHES IN $t\bar{t}Z$ AND tZj PRODUCTION WITH ANGULAR MOMENTS

3.1 Introduction

Precision studies for top quark physics are a cornerstone for the LHC program. The large top quark mass indicates that it may have a special role in electroweak symmetry breaking (EWSB) [80–85, 121–123]. Thus, top quark precision measurements can display the first glimpse into new physics connected with EWSB. While the basic top quark properties (*e.g.*, mass, pair production cross-section, and W-helicity fractions) are well known and consistent with the Standard Model (SM) [124], its interaction with the Z boson is still weakly constrained.

The most promising *direct* probes for the top quark-Z boson interaction are via production at the LHC of a top pair and a Z boson $pp \to t\bar{t}Z$ and single top production in association with a Z boson and a jet $pp \to tZj$ [125]. The large production threshold of $2m_t + m_Z$ for $t\bar{t}Z$ and the small electroweak production rate for tZj require the sizable collision energy and luminosity provided by the LHC, making these probes unattainable at previous colliders. The most recent experimental measurements for the top quark-Z boson interaction are reported by ATLAS with 139.1 fb^{-1} [126] and CMS with 77.5 fb^{-1} [127], displaying good agreement with the theoretical calculations within the SM. Experimental projections indicate that the top quark electroweak interaction will be probed to great precision when going from the Run 2 dataset of 139 fb^{-1} to the projected high luminosity LHC (HL-LHC) with 3 ab^{-1} [128]. These analyses can ultimately shed light on well motivated

connections of the top quark to new physics.

In the present study, we show the possibility to boost the new physics sensitivity in the $t\bar{t}Z$ and $tZj/\bar{t}Zj$ processes at the LHC using the angular moments for the Z boson [129–135]. This proposal scrutinizes the hadronic structure of the processes under inspection through the full Z boson polarization information, using the leptons as spin analyzers for the underlying production dynamics. While this phenomenological probe is disregarded in the current experimental analyses, we show that the proposed method can be a key ingredient to access new physics contributions at higher precision.

We parametrize new physics effects in terms of the SM Effective Field theory (EFT) framework [57,58,136]. The EFT provides a well-defined approach to explore indirect effects from new theories as deformations from the SM structures. These new physics effects would generally manifest as subtle deviations in the standard physics observables.

The chapter is organized as follows. In Section 3.2, we present the SM angular moments for the $t\bar{t}Z$ and $tZj/\bar{t}Zj$ processes and quantify the higher order QCD effects. In Section 3.3, we present the relevant operators in the EFT framework up to dimension-six and calculate their new physics contributions to the observables under scrutiny. In Section 3.4, we show our detector level analysis and discuss the HL-LHC sensitivity to the corresponding Wilson coefficients. We draw our conclusion in Section 3.5.

3.2 Theoretical Framework

In the present manuscript, we show that the angular distribution in the $Z \to \ell^+\ell^-$ decay opens a gateway for precision studies in the $pp \to t\bar{t}Z$ and $tZj/\bar{t}Zj$ processes. In general,

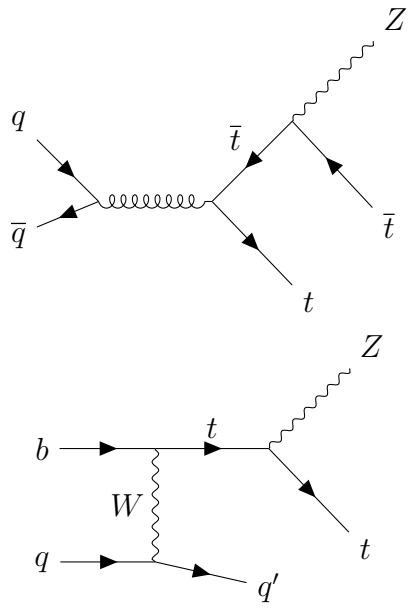

Figure 15: Representative set of Feynman diagrams for the $pp \to t\bar{t}Z$ (top) and $pp \to tZj$ (bottom) processes.

the differential cross-section for these processes can be written as [129, 130]

$$\begin{aligned}
&\frac{1}{\sigma}\frac{d\sigma}{d\cos\theta d\phi} = \\
&\frac{3}{16\pi}[1+\cos^2\theta + A_0\frac{1}{2}(1-3\cos^2\theta) + A_1\sin 2\theta\cos\phi \\
&+ A_2\frac{1}{2}\sin^2\theta\cos 2\phi + A_3\sin\theta\cos\phi + A_4\cos\theta \\
&+ A_5\sin^2\theta\sin 2\phi + A_6\sin 2\theta\sin\phi + A_7\sin\theta\sin\phi]\,,
\end{aligned} \tag{3.2.1}$$

where θ and ϕ are the polar and azimuthal angles of the ℓ^- lepton in the Z boson rest frame. The eight coefficients A_i, $i = [0, 7]$, correspond to the number of degrees of freedom for the polarization density matrix for a spin-1 particle. The angular coefficients A_i are frame dependent. We adopt the Collins-Soper frame in our study [137]. This is a typical frame choice in angular coefficient analyzes [138–140].

Our studies will focus on the top quark and Z boson interaction via top quark pair production in association with a Z boson $pp \to t\bar{t}Z$ and single top quark production in association with a Z boson and a jet $pp \to tZj/\bar{t}Zj$. See Fig. 15 for a representative set

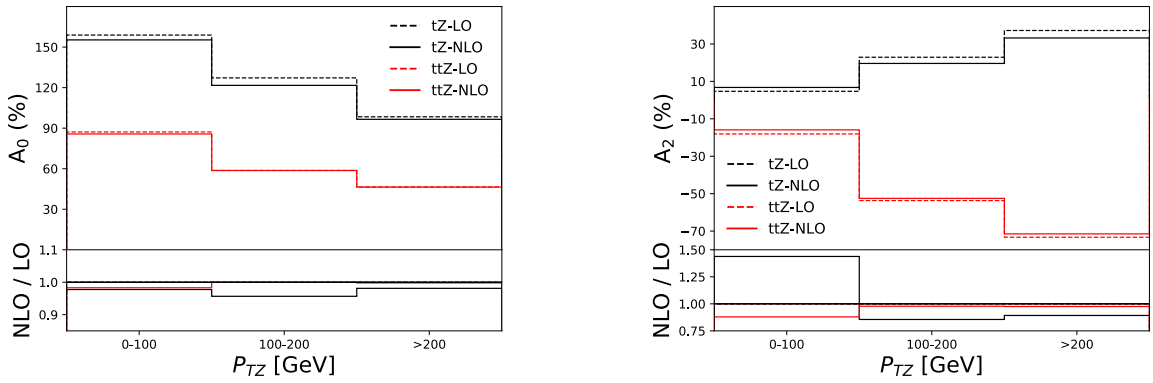

Figure 16: Angular coefficients A_0 (left panel) and A_2 (right panel) for top quark pair plus dilepton $pp \to t\bar{t}\ell^+\ell^-$ (black) and single top quark plus dilepton $pp \to t(\bar{t})\ell^+\ell^- j$ (red). The results are presented at LO (dashed line) and NLO (solid line). The processes are calculated at the parton level with $|\eta_\ell| < 4$, $p_{T\ell} > 5$ GeV, and $|m_{\ell\ell} - m_Z| < 10$ GeV. The renormalization and factorization scales are set to $\mu_R = \mu_F = 1/2 \sum_{i=1}^{n} \sqrt{m_i^2 + p_{T,i}^2}$.

of Feynman diagrams. We consider the semi-leptonic top pair decays and $Z \to \ell^+\ell^-$. The Monte Carlo analysis sums over all possible combinations of charged leptons $\ell^\pm = e^\pm, \mu^\pm$. Before analyzing the angular coefficients in the quest for new physics, we study in this section the stability of these terms to higher order effects.

Event generation for $pp \to t\bar{t}\ell^+\ell^-$ and $pp \to t(\bar{t})\ell^+\ell^- j$ processes is performed at leading order (LO) and next to leading order (NLO) QCD with MadGraph5_aMC@NLO [103]. We consider the LHC at $\sqrt{s} = 14$ TeV. Both the Z and γ^* intermediate states, associated to the dilepton final state, are accounted for. To isolate the higher order effects in our simulation, we perform a parton level study in this section, requiring only basic selections to the two charged leptons from the Z/γ^* decays, keeping the top quark pair stable. Leptons are defined with $|\eta_\ell| < 4$ and $p_{T\ell} > 5$ GeV. We demand a charged lepton pair, with same flavor and opposite sign, reconstructing the Z boson mass $|m_{\ell\ell} - m_Z| < 10$ GeV. The renormalization and factorization scales are dynamically defined as $\mu_R = \mu_F = 1/2 \sum_{i=1}^{n} \sqrt{m_i^2 + p_{T,i}^2}$. We adopt the parton distribution function NNPDF23 at NLO with $\alpha_s(m_Z) = 0.119$ [141].

	A_0	A_1	A_2	A_3	A_4	A_5	A_6	A_7
$t\bar{t}Z_{\rm LO}$	0.693	0.004	-0.412	0.000	-0.001	-0.002	0.002	0.001
$t\bar{t}Z_{\rm NLO}$	0.683	-0.003	-0.398	0.004	0.001	0.001	0.000	0.000
$t(\bar{t})Z_{\rm LO}$	1.464	0.001	0.117	0.041	0.000	-0.003	0.001	-0.001
$t(\bar{t})Z_{\rm NLO}$	1.416	-0.008	0.123	0.035	-0.005	-0.002	-0.006	-0.001

Table 4: Angular coefficients A_i for top pair plus dilepton $pp \to t\bar{t}\ell^+\ell^-$ and single top plus dilepton $pp \to t(\bar{t})\ell^+\ell^- j$ processes at LO and NLO QCD. The processes are calculated at the parton level with $|\eta_\ell| < 4$, $p_{T\ell} > 5$ GeV, and $|m_{\ell\ell} - m_Z| < 10$ GeV.

To extract the angular coefficients A_i from our Monte Carlo simulation, we observe that Eq. (3.2.1) is a spherical harmonic decomposition for the differential cross-section with real spherical harmonics $Y_{lm}(\theta, \phi)$ of order $l \leq 2$. Hence, we can access the angular coefficients, exploring the orthogonality relations for the spherical harmonics. The angular coefficients are projected out with

$$\begin{aligned} A_0 &= 4 - \left\langle 10\cos^2\theta \right\rangle, & A_1 &= \left\langle 5\sin 2\theta\cos\phi \right\rangle, \\ A_2 &= \left\langle 10\sin^2\theta\cos 2\phi \right\rangle, & A_3 &= \left\langle 4\sin\theta\cos\phi \right\rangle, \\ A_4 &= \left\langle 4\cos\theta \right\rangle, & A_5 &= \left\langle 5\sin^2\theta\sin 2\phi \right\rangle, \\ A_6 &= \left\langle 5\sin 2\theta\sin\phi \right\rangle, & A_7 &= \left\langle 4\sin\theta\sin\phi \right\rangle, \end{aligned} \tag{3.2.2}$$

where the weighted normalization is defined as

$$\langle f(\theta,\phi)\rangle \equiv \int_{-1}^{1} d\cos\theta \int_0^{2\pi} d\phi f(\theta,\phi)\frac{1}{\sigma}\frac{d\sigma}{d\cos\theta d\phi}\,. \tag{3.2.3}$$

In this definition, σ can represent any differential cross-section that is independent of the lepton kinematics.

In Table 4, we present the angular coefficients A_i at LO and NLO QCD. We observe that the angular distributions for the leptons are controlled by two leading terms, namely A_0 and A_2. The higher order corrections display relevant dependencies with the Z boson transverse

momentum, see Fig. 16. The other angular coefficients result in sub-leading effects. In particular, the coefficients A_{5-7} are zero at leading order. They are associated with the imaginary part of the amplitude, resulting in depleted contributions in the SM.

3.3 Effective Field Theory

The current LHC constraints point to a mass gap between the SM degrees of freedom and the new physics states. In this context, the new physics modes can be integrated out and be well parametrized by high dimension operators within the SM Effective Field Theory framework [57, 58, 90, 136]. In the present section, we study the effects of higher dimensional operators that influence the interaction between the top quark and neutral gauge bosons and are relatively unconstrained [61, 126, 127, 142–154]. Following the Warsaw basis [58], we focus on the operators

$$\begin{aligned}
\mathcal{O}_{tB} &= \left(\overline{Q}\sigma^{\mu\nu}t\right)\widetilde{\phi}B_{\mu\nu}\,,\\
\mathcal{O}_{tW} &= \left(\overline{Q}\sigma^{\mu\nu}\tau^I t\right)\widetilde{\phi}W^I_{\mu\nu}\,,\\
\mathcal{O}_{\phi t} &= \left(\phi^\dagger i\overleftrightarrow{D_\mu}\phi\right)\left(\bar{t}\gamma^\mu t\right)\,,\\
\mathcal{O}^{(1)}_{\phi Q} &= \left(\phi^\dagger i\overleftrightarrow{D_\mu}\phi\right)\left(\overline{Q}\gamma^\mu Q\right)\,,\\
\mathcal{O}^{(3)}_{\phi Q} &= \left(\phi^\dagger i\overleftrightarrow{D^I_\mu}\phi\right)\left(\overline{Q}\gamma^\mu\tau^I Q\right)\,,
\end{aligned} \tag{3.3.1}$$

where Q denotes the left-handed top-bottom doublet and t the right-handed top singlet. τ^I are the Pauli matrices, and the Higgs doublet is represented by ϕ and $\tilde{\phi} \equiv i\tau^2\phi$.

The BSM contributions to the top quark and Z boson interaction can be parametrized by the Wilson coefficients $(c_{\phi t}, c_{tZ}, c^I_{tZ}, c_{\phi Q})$. The last three coefficients are defined from the following linear combinations [127, 155]

$$c_{tZ} \equiv \mathrm{Re}\left(-\sin\theta_W c_{tB} + \cos\theta_W c_{tW}\right)\,, \tag{3.3.2}$$

$$c^I_{tZ} \equiv \mathrm{Im}\left(-\sin\theta_W c_{tB} + \cos\theta_W c_{tW}\right)\,, \tag{3.3.3}$$

$$c_{\phi Q} \equiv c^1_{\phi Q} - c^3_{\phi Q}\,, \tag{3.3.4}$$

where θ_W is the Weinberg angle.

Although we follow the EFT framework, it is illuminating to observe how these operators translate to the anomalous coupling approach [142]. In this context, the possible effects from physics beyond the SM are modeled by the extended Lagrangian for the $t\bar{t}Z$ interaction

$$\begin{aligned}\mathcal{L}_{t\bar{t}Z} =& e\bar{u}(p_t)[\gamma_\mu \left(C_{1,V} + \gamma_5 C_{1,A}\right) \\ &+ \frac{i\sigma^{\mu\nu}q_\nu}{M_Z}\left(C_{2,V} + i\gamma_5 C_{2,A}\right)]v(p_{\bar{t}})Z_\mu \,, \end{aligned} \tag{3.3.5}$$

where e is the electromagnetic coupling constant, $q_\nu = (p_t - p_{\bar{t}})_\nu$, and $\sigma_{\mu\nu} = \frac{i}{2}[\gamma_\mu, \gamma_\nu]$. In the Standard Model, the vector and axial couplings are respectively $C_{1,V}^{\mathrm{SM}} \approx 0.24$ and $C_{1,A}^{\mathrm{SM}} \approx -0.60$. In addition, the weak magnetic $C_{2,V}$ and electric dipole $C_{2,A}$ interactions are zero at tree level. Higher order corrections in the SM generate subleading contributions to these terms with $C_{2,V} \approx 10^{-4}$ [156] and $C_{2,A}$ being further suppressed, appearing only at three-loops [157, 158].

The EFT contributions in Eq. (3.3.1), which respect the SM symmetries, can be translated in terms of the anomalous couplings as [159]

$$\begin{aligned} C_{1,V} =& C_{1,V}^{\mathrm{SM}} + \frac{v^2}{2\Lambda^2 \sin\theta_W \cos\theta_W}\mathrm{Re}\left[-c_{\phi t} + \left(c_{\phi Q}^3 - c_{\phi Q}^1\right)\right], \\ C_{1,A} =& C_{1,A}^{\mathrm{SM}} + \frac{v^2}{2\Lambda^2 \sin\theta_W \cos\theta_W}\mathrm{Re}\left[-c_{\phi t} - \left(c_{\phi Q}^3 - c_{\phi Q}^1\right)\right], \\ C_{2,V} =& \frac{\sqrt{2}v^2}{2\Lambda^2 \sin\theta_W \cos\theta_W}\mathrm{Re}\left[-\sin\theta_w c_{tB} + \cos\theta_w c_{tW}\right], \\ C_{2,A} =& \frac{\sqrt{2}v^2}{2\Lambda^2 \sin\theta_W \cos\theta_W}\mathrm{Im}\left[-\sin\theta_w c_{tB} + \cos\theta_w c_{tW}\right]. \end{aligned} \tag{3.3.6}$$

In this form, it can be seen that the Wilson coefficient c_{tZ} generates the weak magnetic dipole moment and its imaginary counterpart c_{tZ}^I sources the electric dipole moment. At the same time, the coefficients $c_{\phi t}$ and $c_{\phi Q}$ induce anomalous neutral current interactions. Remarkably, the Wilson coefficients $c_{\phi Q}^3$ and $c_{\phi Q}^1$ only appear with an opposite sign, hence the associated production of top quark(s) and Z boson ($t\bar{t}Z$ and $tZj/\bar{t}Zj$) can only constrain the coefficient $c_{\phi Q}$ defined in Eq. (3.3.4).

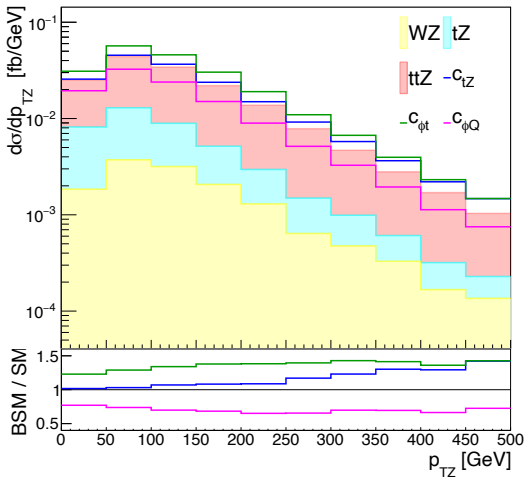

Figure 17: NLO differential cross-section as a function of p_{TZ} for the SM and illustrative new physics scenarios. The Wilson coefficients are turned on one at a time to $c_{tZ} = 1$ TeV^{-2} and $c_{\phi t} = c_{\phi Q} = 5$ TeV^{-2}. The new physics terms scale up to $\mathcal{O}(1/\Lambda^4)$ and the histograms are stacked. We show the ratio between the stacked BSM histograms and the SM in the bottom panel.

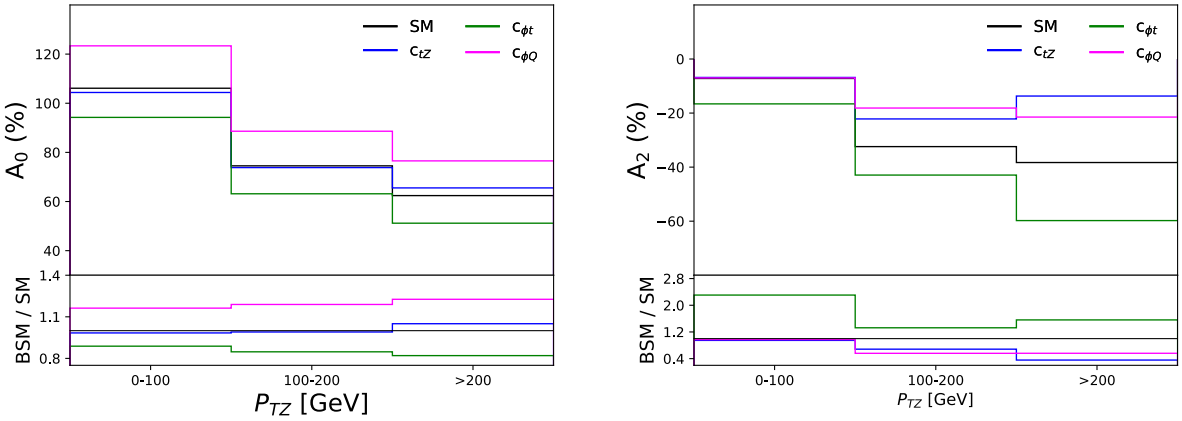

Figure 18: Angular coefficients A_0 (left panel) and A_2 (right panel) as a function of p_{TZ} for the SM and new physics hypotheses for the combined samples $t\bar{t}Z$, $t(\bar{t})Z$, and WZ. The Wilson coefficients are turned on one at a time to $c_{tZ} = 1$ TeV^{-2} and $c_{\phi t} = c_{\phi Q} = 5$ TeV^{-2}.

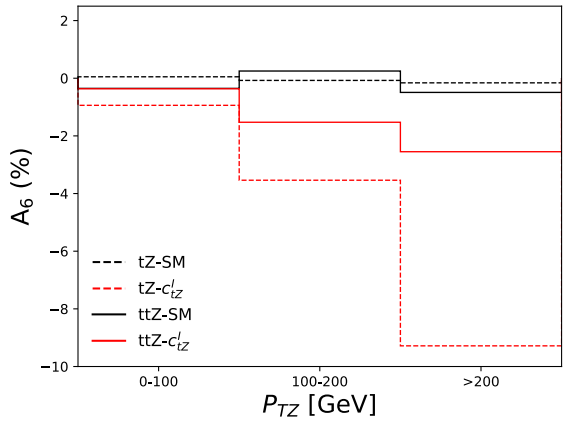

Figure 19: Angular coefficients A_6 as a function of the Z boson transverse momentum p_{TZ} for the SM (black) and BSM CP-violating hypothesis c_{tZ}^I (red). The results for the $t\bar{t}Z$ (solid) and $t(\bar{t})Z$ (dashed) processes are presented separately. The samples were generated at LO QCD and the Wilson coefficient is set to $c_{tZ}^I = 1$ TeV^{-2}.

3.4 Analysis

In our analysis, we focus on the associated production of top quark(s) and a Z boson ($t\bar{t}Z$ and $tZj/\bar{t}Zj$), considering the final state with the Z boson decaying leptonically and one top quark decaying semi-leptonically. To probe the HL-LHC sensitivity to new physics effects, we use MadGraph5_aMC@NLO with the UFO model `SMEFTatNLO` [160, 161]. This model file grants EFT studies at NLO QCD for the CP-conserving operators ($c_{\phi t}, c_{tZ}, c_{\phi Q}$). The CP-violating contributions for c_{tZ}^I are generated with the UFO model file `dim6top` [155], that provides EFT samples at LO. Spin correlation effects for the top quark pair decays are obtained with MadSpin package [162]. The leading background for this analysis arises from WZ production, which is also simulated with MadGraph. Parton shower, hadronization, and underlying event effects are accounted for with Pythia8 [163]. Detector effects are simulated with Delphes3 [164], using the default HL-LHC detector card [89]. We consider the LHC at $\sqrt{s} = 14$ TeV.

We start our detector level analysis, requiring three charged leptons. Leptons are defined

with $|\eta_\ell| < 4$ and $p_{T\ell} > 5$ GeV. We demand a charged lepton pair, with same flavor and opposite sign, reconstructing the Z boson mass $|m_{\ell\ell} - m_Z| < 10$ GeV. For the hadronic part of the event, we require three or more jets where one is b-tagged. Jets are defined with the anti-k_T jet algorithm with radius $R = 0.4$, $|\eta_j| < 4$, and $p_{Tj} > 30$ GeV.

In Fig. 17, we present the NLO differential cross-section as a function of the reconstructed Z boson transverse momentum for the SM and CP-conserving EFT operators ($c_{\phi t}, c_{tZ}, c_{\phi Q}$). Remarkably, the c_{tZ} contributions display augmented BSM effects at high energy scales. This can be understood by the extra momentum dependence arising from new physics. This is apparent, for instance, in the $C_{2,V}$ term of Eq. (3.3.5). In contrast, the other CP-conserving operators ($c_{\phi t}, c_{\phi Q}$) result in almost constant corrections to the SM rate across all energy bins.

The angular coefficients provide an extra phenomenological probe to these new physics effects. They work as spin analyzers for the hadronic structure. In Table 5, we display the angular coefficients A_i for the SM and new physics scenarios. To illustrate the distinctive BSM effects to the angular coefficients, we turn one Wilson coefficient at a time with strengths $c_{tZ} = c_{tZ}^I = 1$ TeV^{-2} and $c_{\phi t} = c_{\phi Q} = 5$ TeV^{-2}. The two leading angular coefficients that control the angular distributions in the SM, A_0 and A_2, present large BSM effects for the considered deformations in the EFT parameter space. Furthermore, while the SM and CP-conserving operators display depleted angular coefficient A_6, being zero at tree level, the CP-violating operator c_{tZ}^I presents a sizable contribution. The angular coefficient A_6 is sensitive to the imaginary part of the amplitude, arising from the CP-violating operator. In Figs. 18 and 19, we show that these angular coefficients result in relevant dependencies with the energy scale p_{TZ}. In particular, we observe augmented BSM contributions in the boosted regime for the c_{tZ}^I operator in Fig. 19. The uplifted new physics effects at high scales appear for both the $t\bar{t}Z$ and $tZj/\bar{t}Zj$ processes, being more pronounced for the latter.

To evaluate the sensitivity of these new BSM probes, we perform a bin-by-bin χ^2 analysis, exploring the differential cross-section and the angular coefficients A_i as a function of the

	SM_{NLO}	$c_{tZ} = 1$	$c_{\phi t} = 5$	$c_{\phi Q} = 5$	SM_{LO}	$c_{tZ}^I = 1$
σ [fb]	7.863	8.434	10.418	5.603	5.010	5.349
A_0	0.803	0.788	0.521	0.976	0.886	0.892
A_1	-0.003	0.001	-0.002	0.001	0.001	0.000
A_2	-0.265	-0.198	-0.459	-0.160	-0.226	-0.179
A_3	0.009	0.014	0.004	0.015	0.015	0.013
A_4	0.000	0.000	0.000	0.000	0.000	0.001
A_5	-0.001	-0.001	0.002	-0.002	-0.001	0.000
A_6	0.000	-0.003	-0.003	0.001	0.000	-0.013
A_7	-0.001	0.000	-0.002	-0.004	0.000	0.000

Table 5: Angular coefficient A_i for the SM and new physics hypotheses. The results account for the combination of all leading channel contributions: $pp \to t\bar{t}\ell^+\ell^-$, $pp \to t(\bar{t})\ell^+\ell^-$, and WZ. The Monte Carlo events are generated at NLO QCD for the CP-conserving operators $(c_{\phi t}, c_{tZ}, c_{\phi Q})$ and LO for the CP-violating one (c_{tZ}^I). The event generation includes parton shower, hadronization, and detector level effects. See the text for more details. The Wilson coefficients are turned on one at a time with the following strengths: $c_{tZ} = c_{tZ}^I = 1$ TeV^{-2} and $c_{\phi t} = c_{\phi Q} = 5$ TeV^{-2}. The new physics terms scale up to $\mathcal{O}(1/\Lambda^4)$.

transverse momentum of the Z boson p_{TZ}. The χ^2 function is defined as follows

$$\chi^2 = \sum_{ij} \frac{\left(\mathcal{O}_i^{BSM}(p_{TZ,j}) - \mathcal{O}_i^{SM}(p_{TZ,j})\right)^2}{(\delta\mathcal{O}_i(p_{TZ,j}))^2}\,, \tag{3.4.1}$$

where $\mathcal{O}_i(p_{TZ,j})$ are the observables considered in this analysis for distinct $p_{TZ,j}$ bins. We account for both the binned number of events $N(p_{TZ,j})$ and the angular moments $A_i(p_{TZ,j})$. For the errors $\delta\mathcal{O}_i(p_{TZ,j})$, we assume $\delta N = \sqrt{N^{SM} + (\epsilon_N N^{SM})^2}$ with systematic uncertainty $\epsilon_N = 10\%$ [126, 127]. For the angular coefficients, we estimate the statistical uncertainty associated with the measurement of each $A_i(p_{TZ,j})$, performing 100 pseudo-experiments. We consider a random set of $N(p_{TZ,j})$ Monte Carlo events to calculate $A_i(p_{TZ,j})$. We use the

		c_i/Λ^2 [TeV^{-2}]	$\Lambda/\sqrt{c_i}$ [TeV]
		95% C.L. bounds	BSM scale
c_{tZ}^I	linear in c_i/Λ^2	[-2.23, 2.23]	0.67
	quadratic in c_i/Λ^2	[-1.10, 1.12]	0.95
c_{tZ}	linear in c_i/Λ^2	[-4.63, 4.63]	0.47
	quadratic in c_i/Λ^2	[-1.39, 1.26]	0.89
$c_{\phi t}$	linear in c_i/Λ^2	[-4.00, 4.00]	0.5
	quadratic in c_i/Λ^2	[-3.06, 2.94]	0.58
$c_{\phi Q}$	linear in c_i/Λ^2	[-2.61, 2.61]	0.62
	quadratic in c_i/Λ^2	[-2.43, 2.83]	0.64

Table 6: 95% C.L. intervals for the dimension-six operators. The results are presented at linear and quadratic levels in c_i/Λ^2. The bounds for the CP-conserving operators $(c_{tZ}, c_{\phi Q}, c_{\phi t})$ are obtained with the observables $(N(p_{tZ}), A_0(p_{TZ}), A_2(p_{TZ}))$. For the operator c_{tZ}^I, we also account for the CP-sensitive observable $A_6(p_{TZ})$. We assume the HL-LHC at 14 TeV with 3 ab^{-1} of data.

standard deviation from the pseudo-experiments to infer the statistical uncertainty on the angular coefficients. The confidence level (C.L.) intervals are defined with

$$1 - \text{CL} \geq \int_{\chi^2}^{\infty} dx p_k(x)\,, \tag{3.4.2}$$

adopting the $\chi^2(c_i/\Lambda^2)$ distribution with k degrees of freedom $p_k(x)$. The CP-conserving effects are evaluated with SM and BSM events samples at NLO QCD. Since the CP-violating operator can only be generated at LO with the UFO model file `dim6top`, the analysis for this hypothesis accounts for SM and BSM $t\bar{t}Z$ and $tZj/\bar{t}Zj$ samples at LO, for consistency.

In Table 6, we present the 95% C.L. constraints on the Wilson coefficients, considering the effects of one BSM operator at a time. The results are presented up to linear and quadratic level on the new physics parameters c_i/Λ^2. To shed light on the extra sensitivity arising from the angular coefficients, we analyze the c_{tZ} and c_{tZ}^I results in Fig. 20 in three scenarios.

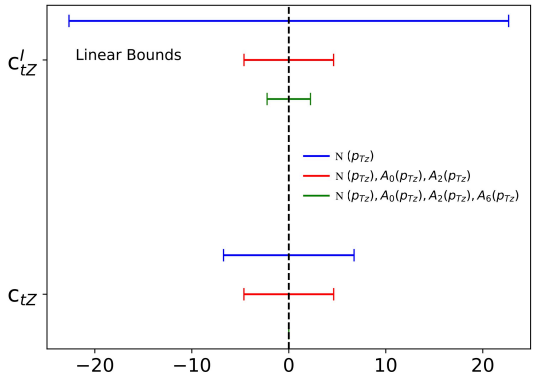

Figure 20: 95% C.L. intervals for c_{tZ}^I and c_{tZ} at linear level in c_i/Λ^2. The results are shown for three scenarios that differ by the used set of observables: *i*) $N(p_{p_{TZ}})$ (blue); *ii*) $N(p_{p_{TZ}}), A_0(p_{TZ}), A_2(p_{TZ})$ (red); and *iii*) $N(p_{p_{TZ}}), A_0(p_{TZ}), A_2(p_{TZ}), A_6(p_{TZ})$ (green). The latter scenario is only shown for the c_{tZ}^I, where A_6 displays appreciable sensitivity for the CP-odd effects. See also text and Fig. 19.

The first only explores the binned distribution for the transverse momentum of the Z boson $N(p_{TZj})$. The second also accounts for the angular coefficients as a function of the energy scale $A_0(p_{TZ,j})$ and $A_2(p_{TZ,j})$. The third one further includes $A_6(p_{TZ,j})$ as an extra probe. We observe that the extra information stored in the angular moments can strongly boost the sensitivity to the Wilson coefficients. Remarkably, while the analysis of the differential $N(p_{TZ})$ distribution results in no significant sensitivity for c_{tZ}^I at the linear level in the c_i/Λ^2 expansion, the addition of the angular coefficients A_i result in strong limits at the HL-LHC. In particular, this is due to the new physics effects from the imaginary part of the amplitude that can be probed by the angular coefficient A_6.

3.5 Conclusion

In this study, we present a method to augment the new physics sensitivity in searches with the $t\bar{t}Z$ and $tZj/\bar{t}Zj$ processes at the LHC. The proposal explores the accurate measurement of the angular moments for the Z boson, which probes with greater precision the underlying

production dynamics. We first access the next to leading order QCD effects for the angular coefficients A_i. We observe that the higher order effects can present relevant contributions. Going forward, we parametrize new physics effects in terms of the SM Effective Field theory framework. We observe that the SM and BSM samples display distinct angular coefficients A_i. Performing a realistic Monte Carlo study, we show that the angular moments can significantly boost the sensitivity to the Wilson coefficients. In particular, this approach can uncover blind directions to CP-odd operators, leading into sizable sensitivity at the HL-LHC. Remarkably, this proposal only relies on the lepton pair reconstruction, displaying small uncertainties. Hence, it can be promptly incorporated in the ATLAS and CMS analyses.

CHAPTER IV

NEUTRAL CURRENT NEUTRINO INTERACTIONS AT FASERν

4.1 Introduction

As the only neutral and uncolored fermions in the Standard Model (SM), neutrinos are perhaps some of the least well understood particles in nature. Precision measurements of neutrino interactions across a variety of energy scales are important in order to understand neutrino oscillations as well as to probe new physics in the neutrino sector. However, most experiments studying neutrinos from artificial sources are limited to maximum energies of a few hundred GeV. The exception is the Large Hadron Collider (LHC): As the highest energy particle collider ever built, the LHC is the source of the most energetic neutrinos created in a controlled laboratory environment. Proton-proton collisions typically lead to a large number of hadrons produced in the far-forward direction, which can inherit a significant fraction of the protons' momenta. The decays of these hadrons then lead to an intense and strongly collimated beam of high-energy neutrinos of all three flavors along the beam collision axis. While the possibility of probing neutrinos at the LHC was discussed as early as 1984 [41, 165–169], no LHC neutrino has been detected yet. This situation will change soon with the upcoming FASERν detector [9, 170], which is expected to detect thousands of neutrino interactions during Run 3 of the LHC.

One of the most basic measurements involving neutrinos is the scattering cross section of neutrinos off matter. Both charged current (CC) and neutral current (NC) scattering offer sensitive tests of the SM (for a review, see Ref. [171]). The majority of neutrino cross section measurements are from experiments using terrestrial sources at low energies, extending up to

neutrino energies of about 300 GeV [172,173]. Astrophysical neutrino cross sections have also been measured at IceCube [174,175], probing very high neutrino energies between $\sim$ 10 TeV and $\sim$ 1 PeV albeit with significant uncertainties. At the few 100 GeV to a few TeV scale, there are no precise measurements of neutrino scattering. FASERν offers an opportunity to study neutrinos at these energies. The ability of FASERν to measure CC neutrino scattering has been studied, but it is not known yet how well NC scattering could be measured with LHC neutrinos. In this work, we fill this gap by studying the capability of FASERν to determine the neutrino NC cross section at the LHC.

NC scattering is significantly more difficult to identify than its CC counterpart. While CC scattering produces an outgoing lepton that carries much of the original neutrino energy, neutrino NC interactions result only in a neutrino and any products of the recoiling nucleus. In FASERν, there are significant backgrounds to NC scattering from neutral hadron interactions within the detector. We simulate neutrino scattering and neutral hadron events at FASERν, and use a neural network to effectively separate signal from background using kinematic information of the final state. By applying another neural network, we show that the energy of the neutrino can be estimated with $\sim$ 50% uncertainty. Taken together, we find that FASERν will be able to measure the neutrino NC cross section as a function of neutrino energy.

The rest of this chapter is organized as follows. In Section 4.2, we provide an overview of FASERν and how it probes neutrino scattering. Section 4.3 describes our simulation of signal, background and the detector. Then, we detail our analysis procedure in Section 4.4. Section 4.5 contains the results of this analysis, including our estimate of the precision with which FASERν could measure the NC scattering cross section and our interpretation in terms of limits on neutrino non-standard interactions (NSI). We conclude in Section 4.6.

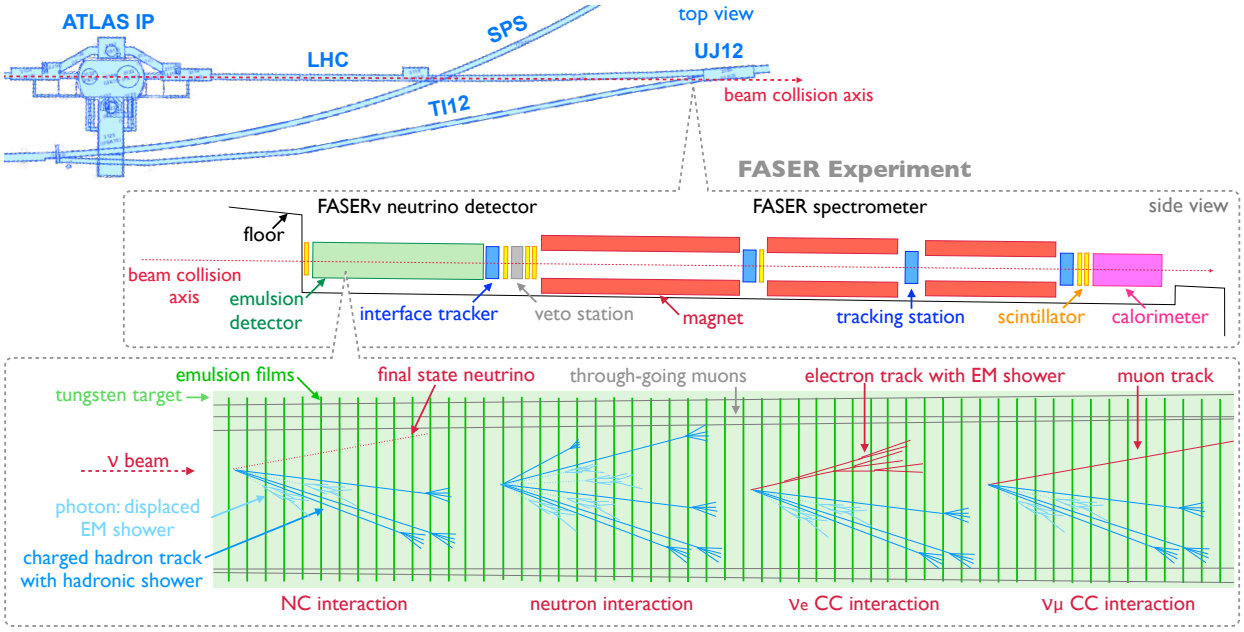

Figure 21: Location of the FASERν detector and event topology. **Top:** The FASER experiment is placed about 500 m downstream of the ATLAS interaction point in the previously unused side tunnel TI12, which connects the SPS with the LHC tunnel. **Center:** The detector is centered around the beam collision axis where the neutrino flux is maximal. It consists of the FASERν emulsion neutrino detector, followed by a magnetized spectrometer and a calorimeter. **Bottom:** The emulsion detector consists of tungsten plates interleaved with nuclear emulsion films. Both interactions of neutrinos and neutral hadrons lead to the appearance of a *neutral vertex* at which several charged particles emerge. Different types of events can be distinguished based on the event topology, as explained in the text.

4.2 Neutrino Interactions at FASERν

FASER [41, 176, 177] is a dedicated experiment at the LHC to both search for long-lived particles predicted by models of new physics [178–186], and to study interactions of high-energy neutrinos [9,170]. It is located in the far-forward direction, roughly 480 m downstream from the ATLAS interaction point (IP). At this location, the highly collimated neutrino beam produced at ATLAS, which is centered around the *beam collision axis*, intersects with the

side tunnel TI12, as shown in the upper part of Fig. 21. TI12 has previously served as an injector tunnel for LEP but remained unused during the LHC era. To maximize its sensitivity, a trench has been dug into the floor of TI12 such that the FASER apparatus can be aligned with the beam collision axis.

A schematic layout of the FASER detector is shown in the center part of Fig. 21. Located on the front is the FASERν neutrino detector. It is followed by the FASER spectrometer, consisting of magnets and three tracking stations. FASERν and the FASER spectrometer are connected by an interface tracking station, which allows a combined analysis of the emulsion and electronic detector components. In addition, the interface tracker can be used to time-stamp the event, which allows for a front veto to reject muon-associated background. At the end of FASER is an electromagnetic calorimeter.

The FASERν detector consists of emulsion plates that are interleaved with tungsten plates as a target. This configuration permits the reconstruction of tracks of charged particles passing through the detector with a sub-μm spatial resolution [187]. This allows observation of the event topology as shown in the lower part of Fig. 21.

Both neutrino and neutral hadron interactions are expected to produce several hadronic particles forming a collimated jet. This leads to a characteristic *neutral vertex* signature, with several outgoing tracks but no incoming track, that can be searched for. While most neutral hadrons escape undetected, charged hadrons will leave tracks and interact on a length scale of $\lambda_{\text{int}} \sim 10$ cm, initiating a hadronic shower. Neutral pions promptly decay into photons, which can be identified by their displaced electromagnetic showers. These showers typically occur within a radiation length $X_0 \sim 3.5$ mm in tungsten and point back to the neutral vertex.

It is further possible to distinguish different event types based on their topologies. CC neutrino interaction events contain an energetic charged lepton. While muons can be identified from tracks that do not interact further downstream in the detector, electrons lead to electromagnetic showers that emerge from a track connected to the neutral vertex. NC

interactions contain a neutrino in the final state, which escapes undetected and is expected to recoil against the hadronic activity, but no charged leptons. In contrast, neutral hadron interactions lead to a more uniform distribution of hadrons.

The high spatial resolution of emulsion detectors allows for the use of multiple Coulomb scatterings to estimate the momenta of charged tracks passing through the detector. Momentum measurements of final state charged particles can be used alongside other topological observables to estimate the energy of neutrinos. As shown in Ref. [9], an energy resolution of about 30% can be achieved for CC neutrino interactions, while results for NC neutrino interactions are presented in this study.

4.3 Simulation

The physics signal considered in this chapter is NC neutrino scattering. While all flavors of neutrinos can contribute to the signal, the majority of neutrinos passing through FASERν are muon neutrinos, supplemented by a sub-leading component of electron neutrinos. In this study, we use the fluxes and energy spectra of neutrinos passing through FASERν obtained in Ref. [9]. There it was found that muon neutrinos originate mainly from charged pion and kaon decays, electron neutrinos are primarily produced in neutral kaon, hyperon and D-meson decays, and tau neutrinos mainly come from D_s meson decay. All three neutrino flavors have spectra extending over a broad energy range with average energies between 600 GeV and 1 TeV.

The main background to neutrino NC events comes from high-energy neutral hadrons interacting with the detector. These neutral hadrons are produced by muons striking the tungsten within FASERν or the rock in front of it. The flux and energy spectra of muons have been estimated using `Fluka`, and are presented in the FASER technical proposal [177]. The expected muon rate is about $2 \cdot 10^4$ fb/cm^2, which has been validated with *in-situ* measurements. This corresponds to roughly $2 \cdot 10^9$ muons passing through FASERν during Run 3 of the LHC with a nominal integrated luminosity of 150 fb^{-1}. Positively charged

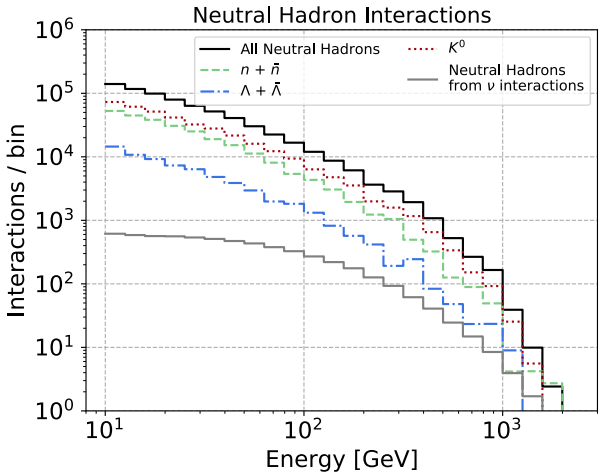

Figure 22: Expected energy spectrum of neutral hadrons interacting within the FASERν detector during LHC Run 3 with 150 fb^{-1} of luminosity.

muons have a softer energy spectrum than negatively charged muons and produce much fewer neutral hadrons, so in what follows we neglect them.

Using these results, we then estimate the rate and energy spectra of neutral hadrons. Using `Fluka` [188,189], we simulate muons striking a 25 cm $\times$ 25 cm $\times$ 1 m block of tungsten, preceded by a large volume of rock. The nuclear interaction length is approximately $\lambda_{\rm int} =$ 10 cm, so nearly all the neutral hadrons produced within FASERν interact. We find that the number of neutral hadrons at each energy is roughly independent of the longitudinal position within the detector. We obtain the spectra of hadrons interacting with the FASERν detector, which is shown in Fig. 22. We can see that the neutral hadron flux is dominated by neutral kaons, followed by neutrons. Neutral hadrons are also produced by neutrino NC (and CC) events themselves, but these are a subdominant contribution to the total flux.

With these fluxes, we simulate the interactions of both neutrinos and neutral hadrons with `Pythia 8` [106,190] using the `Monash` tune [107]. We use the nuclear parton distribution function `nCTEQ15` for tungsten [191,192]. Further nuclear effects in neutral hadron collisions are included with `Pythia`'s heavy ion module. For simplicity, all neutral hadrons have been simulated as neutrons. We have checked that different types of neutral hadrons forming our

background produce similar signatures in the FASERν detector.

To obtain a first understanding of the uncertainty associated with the simulation, we also simulate neutral hadron collisions with tungsten using `EPOS-LHC` [193] and `QGSJET-II-04` [194] as implemented in `CRMC` [195]. In addition, we generate neutrino interactions using `GENIE` [23, 24], following the settings presented in Ref. [9]. While `GENIE`'s simulation of deep inelastic scattering (DIS) events is based on `Pythia 6`, it also takes into account final state interaction effects. We find that the different simulations are in good agreement. However, we note that dedicated future efforts are needed to further validate and improve the simulation such that the associated uncertainties can be quantified and reduced.

In order to simulate the detector response, we perform a phenomenological detector simulation as follows. First, we choose a location for the primary interaction vertex within the detector from a random uniform distribution. In the next step, observable final states, such as charged tracks, photons, and electrons, are identified. Unobservable final state particles, such as neutrinos and neutral hadrons, are rejected. We also remove soft particles with energies below 300 MeV. We then assign a momentum to each observed particle using its energy and direction. While emulsion detectors can measure the directions of final state particles very accurately, we smear the energies (obtained either via the electromagnetic shower for electrons and photons or from multiple Coulomb scattering for tracks) according to the results obtained in Ref. [9]: We use a Gaussian smearing with width $\sigma_E/E = 50\%$ for showers and $\sigma_E/E = 46\%$ for charged particles. Finally, charged hadron tracks will often undergo secondary interactions, which will later be used to distinguish them from muons. The distance between primary and secondary interactions is sampled according to its exponential probability distribution. Both muons and charged hadrons that are produced without interacting again inside the detector are marked as muon candidates.

4.4 Analysis

As described previously, emulsion detectors such as FASERν are able to identify neutral vertices and also to record associated kinematic and topological features. In this section, we will present a neural network-based analysis to separate the NC neutrino interaction signal from the neutral hadron background and estimate the energy of the incoming neutrino. In the following, we will define a set of observables characterizing the interactions in Sec. 4.4.1, and then discuss their use in signal identification (Sec. 4.4.2) and neutrino energy estimation (Sec. 4.4.3).

4.4.1 Event observables

Due to its high spatial resolution, FASERν is able to precisely measure geometric variables, such as the multiplicities of tracks and photons and the directions, as well as to estimate kinematic quantities, such as charged particle momenta and energies of electromagnetic showers. We will now use these features to define a set of observables, which will subsequently be used as input for a multivariate analysis. Note that we will only consider tracks and showers with energy $E > 1$ GeV and an angle of $\theta < 45^\circ$ with respect to the incoming particle direction for the construction of these observables. This is to reduce the dependence of soft hadronic physics effects that might not be modeled accurately by MC simulators.

- The *charged track multiplicity* (n_{ch}) is the number of charged tracks originating from the neutral vertex. It is related to the hadronic energy in the event: $n_{\text{ch}} \sim \log(E_{\text{had}})$ [196]. Events considered in this study have $n_{\text{ch}} \geq 5$ charged tracks as required by the neutral vertex selection [9].

- Similarly, the *photon multiplicity* (n_γ) measures the number of identified photon-initiated electromagnetic showers that have been associated with the neutral vertex. The observed photons mainly originate from the prompt decays of neutral pions, making them a proxy for the pion multiplicity $n_\gamma \sim 2n_{\pi^0}$ and the hadronic energy

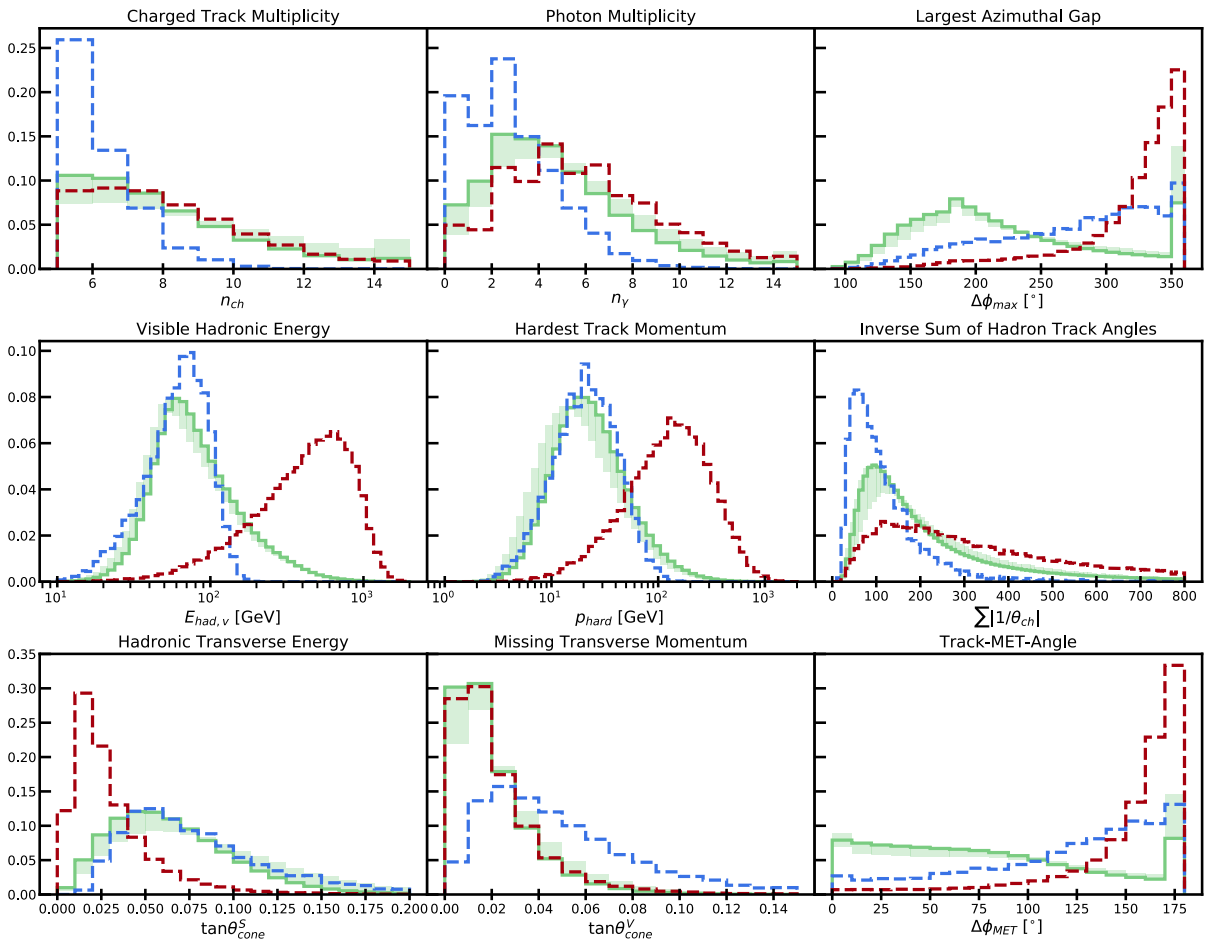

Figure 23: Normalized kinematic distributions for the observables defined in Sec. 4.4.1. The dashed lines show the distributions obtained with `Pythia 8` for the NC neutrino interaction signal at incoming neutrino energies of $E_\nu = 100$ GeV (blue) and $E_\nu = 1$ TeV (red). The solid green lines correspond to the distributions for the neutral hadron interactions simulated with `Pythia 8` for the expected energy spectrum presented in Fig. 22. The shaded region shows the range of predictions for the background distributions obtained from different generators: `Pythia 8`, `EPOS-LHC` and `QGSJET-II-04`.

$$n_{\mathrm{ch}} \sim \log(E_{\mathrm{had}}).$$

- The *visible hadronic energy* ($E_{\mathrm{had,v}}$) can be measured as the sum of reconstructed energies of visible particles, $E_{\mathrm{had,v}} = \sum E_{\mathrm{ch}} + \sum E_\gamma$, which includes both charged tracks

and photons (mainly from neutral pion decay). It is proportional to the true hadronic energy, $E_{\mathrm{had,v}} \sim E_{\mathrm{had}}$, which also includes additional long-lived neutral hadrons.

- Additionally, we consider the *momentum of the hardest track* (p_{hard}). It is closely related to the hadronic energy of the event $p_{\mathrm{hard}} \sim E_{\mathrm{had}}$.

- Another observable is the *inverse sum of track angles* ($\sum |1/\theta_{\mathrm{ch}}|$), where $\tan\theta_{\mathrm{ch}} = p_T/p_z$ is the slope of the individual tracks. More energetic events have hadron tracks with smaller angles and hence a larger value for this observable, $\sum |1/\theta_{\mathrm{ch}}| \sim E_{\mathrm{had}}$.

- The *scalar cone angle* ($\tan\theta^S_{\mathrm{cone}}$) is defined as the scalar sum of the momentum-weighted track angles, $\tan\theta^S_{\mathrm{cone}} = \sum p_i \tan\theta_i / \sum p_i = \sum p_{T,i} / \sum p_i$. It is proportional to the *hadronic transverse energy* (H_T) of the event, $\tan\theta^S_{\mathrm{cone}} \sim H_T/E_{\mathrm{had}}$.

- Additionally, the *vector cone angle* ($\tan\theta^V_{\mathrm{cone}}$) is defined as the vector sum of the individual track angles weighted by their momenta, with two components corresponding to the x and y directions. Using the tracks' transverse momenta, $\vec{p}_{T,i}$, it can be written as $\tan\theta^V_{\mathrm{cone}} = \sum \vec{p}_{T,i} / \sum p_i$. It is proportional to the *missing transverse momentum* ($\vec{\not{p}}_T$) of the event, $\tan\theta^V_{\mathrm{cone}} \sim \vec{\not{p}}_T/E_{\mathrm{had}}$. Larger values for the missing transverse energy , $|\vec{\not{p}}_T|$, are expected for NC neutrino events, in which the final state neutrino will carry away a sizable fraction of the incoming neutrino energy.

- The *largest azimuthal gap* ($\Delta\phi_{\mathrm{max}}$) is defined as the largest difference in azimuthal angle between two neighboring visible particles (charged tracks and photons) whose energy is $> 0.1E_{\mathrm{had,v}}$. This angle will be large for events in which a neutrino recoils against all of the hadronic activity ($\Delta\phi_{\mathrm{max}} > \pi$), and small for background events without a neutrino.

- Similarly, the *track MET angle* ($\Delta\phi_{\mathrm{MET}}$) is the azimuthal angle between the reconstructed missing transverse momentum, $\vec{\not{p}}_T$, and the nearest visible particle with en-

ergy $> 0.1E_{\mathrm{had,v}}$. This angle should be large for NC neutrino interaction events ($\Delta\phi_{\mathrm{MET}} > \pi/2$), and small for neutral hadron events.

In Fig. 23, we show the kinematic distributions for these observables. The dashed lines correspond to NC neutrino interactions with a neutrino energy of $E_\nu = 100$ GeV (blue) and 1 TeV (red). The solid green lines show the distributions for the neutral hadron background with the energy spectrum shown in Fig. 22. The shaded band corresponds to the range of predictions obtained from different generators, serving as a rough estimate of the background simulation uncertainty. We can see that the generator predictions are generally consistent and that the differences between different simulators are mild.

The most striking differences between the signal and background can be observed in the azimuthal angle features $\Delta\phi_{\mathrm{MET}}$ and $\Delta\phi_{\mathrm{max}}$. Large values for these observables are caused by the presence of a neutrino in the final state recoiling against hadrons. In contrast, neutral hadron interactions are expected to produce a more uniform angular distribution of charged tracks, leading to smaller values for these angles. Note that when calculating these observables, we only consider visible particles whose energy is larger than 10% of the visible hadronic energy. If only one track passes this energy threshold, $\Delta\phi_{\mathrm{max}} = 360^\circ$. We also note that most of the backgrounds at FASERν lie in the low energy range, $E \lesssim$ few 100 GeV. This explains why the background distributions are often similar to the $E_\nu = 100$ GeV curve but also implies that the energy content can be used to distinguish the neutral hadron background from NC signal with typical energies $E_\nu \sim$ TeV.

Comparing the distributions for the two considered beam energies, $E_\nu = 100$ GeV and 1 TeV, we can see that all observables are sensitive to the incoming neutrino energy. Not surprisingly, the largest differences are observed for track momentum-based observables: the visible hadronic energy, $E_{\mathrm{had,v}}$, and the momentum of the hardest track p_{hard}. However, complementary information is also provided by the other observables, motivating the multivariate analysis to obtain more robust results.

Note that here we assume that all incoming particles are moving parallel to the beam

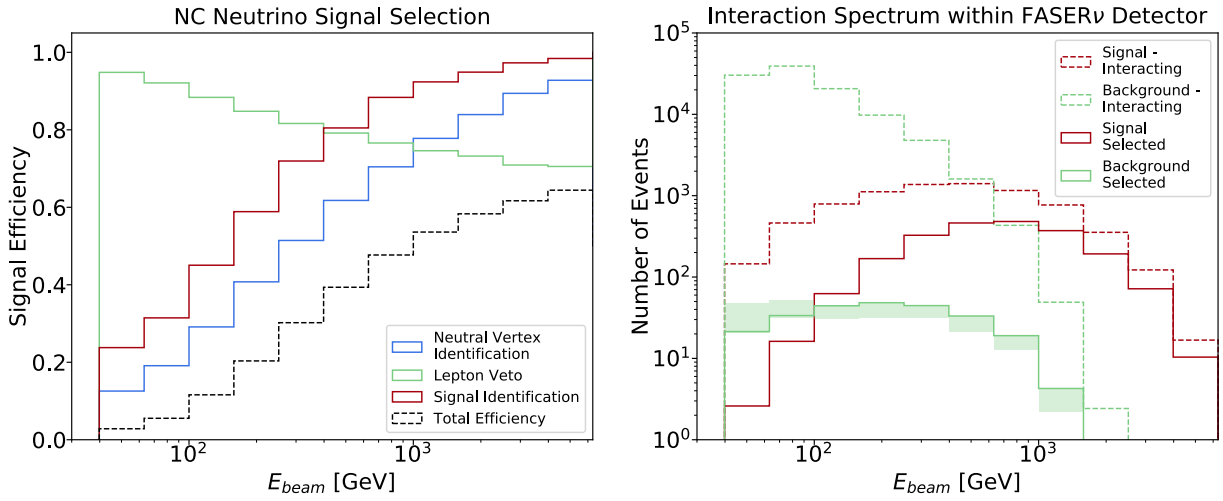

Figure 24: **Left:** Signal selection efficiencies as a function of beam energy. Each line indicates the fraction of events passing the following criteria sequentially: i) neutral vertex identification (blue) requiring ≥ 5 charged tracks, ii) lepton veto (green) requiring no electron candidate and no non-interacting charged track, and iii) signal identification (red) as performed by the NN classifier. The dashed black line shows the combined efficiency. **Right:** The energy spectra of particles interacting within the FASERν detector. We show the expected numbers of neutral hadron interactions (green) and NC neutrino interactions (red) with the FASERν detector during LHC Run 3 as dashed lines. The solid lines show the spectra for events passing the signal selection (including neutral vertex identification, lepton veto and signal identification). The uncertainty associated to the background generation is shown as a shaded band.

collision axis. In reality, the incoming neutrinos have an angular spread of $\theta \sim 0.5$ mrad, corresponding to the angular size of the detector. In addition, neutral hadrons, which are the result of scattering events occurring close to FASERν, will also have a small angle with respect to the beam axis of $\theta \lesssim 10$ mrad for energies $E > 100$ GeV, as shown in Ref. [9]. These incoming beam angles are smaller than typical values of $\tan\theta^{S,V}_{\text{cone}}$. However, small transverse momenta of incoming neutral hadrons and neutrinos can potentially distort the observable distributions, and should therefore be taken into account in a full experimental

analysis.

4.4.2 Signal identification

Let us now turn to the selection of NC neutrino interaction events. We first require the presence of a neutral vertex. Following Ref. [9], we demand the presence of ≥ 5 charged tracks with momentum $p > 1$ GeV and slope $\theta < 45°$ emerging from the vertex. The resulting neutral vertex identification efficiency for NC neutrino interactions is shown as the blue line in the left panel of Fig. 24. It is strongly suppressed at lower energies due to the typically lower charged particle multiplicity, but attains values of $> 80\%$ for neutrino energies $E_\nu > 1$ TeV.

In the second step, we veto all events containing a charged lepton candidate in the final state. Here each charged track with more than 5% of the event's visible hadronic energy that leaves the detector before interacting is considered a muon candidate. While designed to effectively eliminate the CC neutrino interaction background, it also reduces the acceptance rate for the NC neutrino interaction signal, especially for interactions occurring toward the end of the detector. The efficiency of NC events to pass the charged lepton veto is shown as the green line in the left panel of Fig. 24. At TeV energies, the efficiency is about 80%. The efficiency increases toward lower energies, mainly due to the typically lower multiplicity of charged tracks that could be potentially misidentified as muons. We assume that the fraction of CC events passing the lepton veto is negligible.

After removing CC neutrino interactions, we are left with the NC neutrino interaction signal and neutral hadron interaction backgrounds. In this work, we will separate the two samples using a neural network classifier, which uses the observables introduced in the previous section as input.

We simulate 100 times the expected Run 3 event rate for both the NC neutrino interaction signal and the neutral hadron interaction background using `Pythia 8`. We then train a neural network in `Keras` [197] to classify the event type as either signal or background. We use a

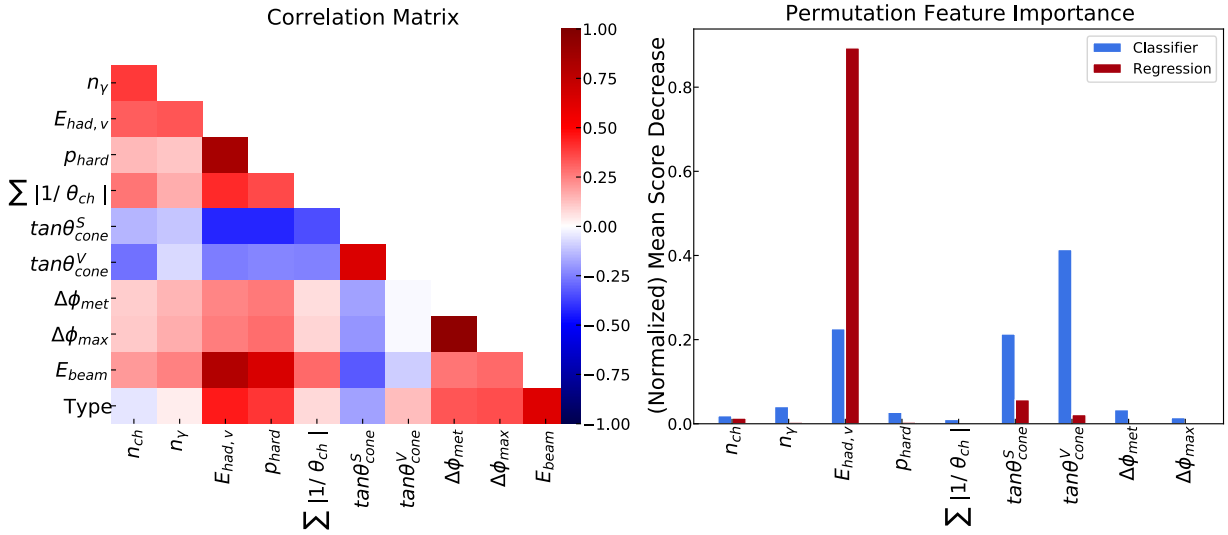

Figure 25: **Left:** Correlation matrix showing the linear relationship between observables presented in Sec. 4.4.1, the incoming particle energy (E_{beam}) and the event type (1 for NC neutrino interactions, 0 for neutral hadrons). **Right:** Permutation feature importance (the normalized mean score decrease for each of the observables) for the signal identification classifier (blue) and neutrino energy estimator (red) network. We use accuracy as the score metric for the classifier network and mean average percent error for the estimator. Scores decreases are normalized so that they sum to 1.

fully connected neural network with three hidden layers of 64 units and a sigmoid activation function, minimizing the binary cross-entropy loss by training with the `Adam` optimizer over 20 epochs. Our training employed a batch size of 256, a constant learning rate of 10^{-3}, and early stopping to avoid overtraining. These hyperparameters are the result of a coarse manual scan, and we did not perform an exhaustive optimization. It is likely that performance could be further improved with additional tuning.

The resulting signal identification efficiency is shown as the red line in the left panel of Fig. 24. The combined efficiency of vertex identification, lepton veto and signal identification is shown as the dashed black line. It is approximately 50% at TeV energies, but significantly reduced at lower energies, mainly due to the low neutral vertex detection efficiency.

In the right panel of Fig. 24 we show the energy spectra of NC neutrino interactions (red) and neutral hadron interactions (green). The dashed lines correspond to all interactions occurring within the detector. After applying all signal selection criteria, the event rates drop to the solid lines. We can see that the neural network classifier is able to identify the signal and sufficiently reduce the background. While the classification network was trained with `Pythia 8`, we have also tested it on data produced with `EPOS-LHC` and `QGSJET-II-04`, assuming the same incoming spectrum of neutral hadrons. The result is shown as a shaded band around the background line. We can see that uncertainties arising from the different simulation of neutral hadron interactions are small, and do not change the background rates significantly.

Before moving on, we further discuss the trained classifier network to understand which observables are most relevant for the signal identification. In the left panel of Fig. 25, we show the correlation matrix between different observables, the beam energy and the event type. Dark shaded bins correspond to stronger linear correlations, either positive (red) or negative (blue). We can see that the event type is most strongly correlated with the visible hadronic energy and the momentum of the hardest track. This is expected as the incoming neutrinos which interact with the detector tend to be harder than the neutral hadrons. We also see that the more energy associated with an event (larger E_{beam}, $E_{\text{had,v}}$, p_{hard}), the more tightly collimated its reaction products are (smaller cone angles θ_{cone}, larger azimuthal angles $\Delta\phi$). The full network, of course, has the ability to learn non-linear relationships.

In the right panel of Fig. 25, we show another common tool to analyse the network's performance: the *permutation feature importance*. It is obtained by randomly shuffling the values of one observable (say n_{ch}) between different events and recording the degradation in the final score obtained by the network. For the classifier network, the accuracy is taken as the score. Large decreases in the accuracy when randomizing a given observable indicate that the observable is important for network performance. The blue bars show the results for the event classification network. We can see that the most important variables for classification

are the hadronic energy and the cone angles, or, equivalently, $\not{p}_T$ and H_T. By contrast, when two observables provide the same information to the network, the permutation importance of each is low. This happens with the angular variables $\Delta\phi_{\text{max}}$ and $\Delta\phi_{\text{MET}}$: while they are clearly correlated with the event type, each variable gives the same information, so removing one alone does not significantly harm the network performance.

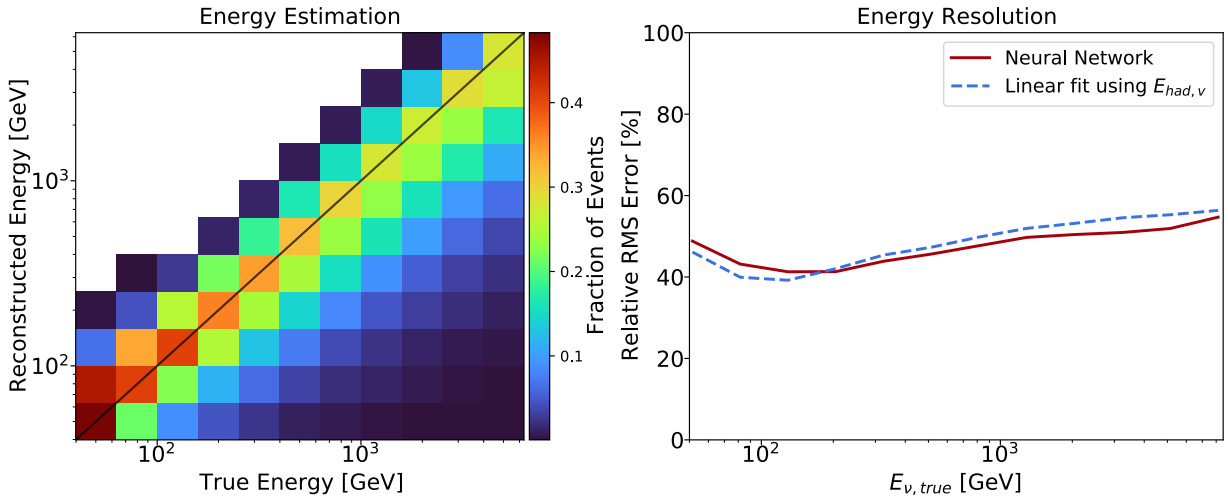

Figure 26: **Left:** Neutrino energy reconstruction for NC neutrino interaction events obtained by a neural network-based multivariate analysis using the observables defined in Sec. 4.4.1. **Right:** Relative RMS energy resolution using the neural network-based multivariate analysis (solid) and only the hadronic energy of the events (dashed).

4.4.3 Neutrino energy estimation

Having discussed the selection of NC neutrino interaction events, let us now turn to the estimation of the incoming neutrino's energy. In DIS neutrino interactions at FASERν, roughly half of the incoming neutrino energy is transferred to the nucleus on average. Since the final state neutrino escapes undetected, the observable hadronic final state is the only handle for energy reconstruction. The absence of an observable lepton results in degraded energy resolution compared to results obtained for CC neutrino interactions in Ref. [9].

As we have seen in Sec. 4.4.1, all observables considered are sensitive to the neutrino

energy, motivating the use of multivariate energy estimation. We simulate $6{\cdot}10^5$ NC neutrino interaction events that are uniformly distributed in $\log E_\nu$ using `Pythia 8`, and train a neural network to minimize the mean average percent error between the true and estimated energy. Here we use the same network architecture and hyperparameters as for the classification network, except the final layer has an identity map as its activation function.

The result of the energy estimation is shown in Fig. 26. The left panel shows the correlation between the reconstructed and true energy. With five bins per decade in energy, the leakage of events between bins is mild, indicating that the neutrino energy estimation for neutral current events is indeed possible. The right panel shows the RMS energy resolution

$$\text{relative RMS error} = \sqrt{\langle (E_{\nu,\text{reco}} - E_{\nu,\text{true}})^2 / E_{\nu,\text{true}}^2 \rangle} \tag{4.4.1}$$

as a function of energy. We obtain an energy resolution of about 50%.

As for the signal identification network, let us study which observables are most important for the energy estimation. In the left panel of Fig. 25, we see that the incoming particle energy E_{beam} is particularly well-correlated with the visible hadronic energy, though there is also a clear relationship with p_{hard}. In the permutation importance study for the energy estimation network shown by the red bars in the right panel, we use the increase in mean average percent error to quantify the impact of randomly permuting the values of one observable among events. $E_{\text{had,v}}$ is by far the dominant observable, suggesting that our network has learned the strong correlation between the visible hadronic energy and that of the incoming neutrino, and is relying heavily on the former to estimate the latter. This dependence arises regardless of the correlation between $E_{\text{had,v}}$ and the momentum of the hardest track, which is perhaps not surprising as p_{hard} is not as directly correlated with the neutrino energy. While the fraction of the neutrino energy that is transferred to the nucleus has an almost uniform distribution, we find that the visible hadronic energy still serves as an excellent proxy for the energy of the incoming neutrino. Motivated by this, we also show in the right panel of Fig. 26 the energy resolution that can be obtained by a linear fit to the visible hadronic

energy. The almost similar performance demonstrates the clear importance of the visible hadronic energy to neutrino energy estimation.

4.5 Results and Interpretation

4.5.1 NC cross section measurements

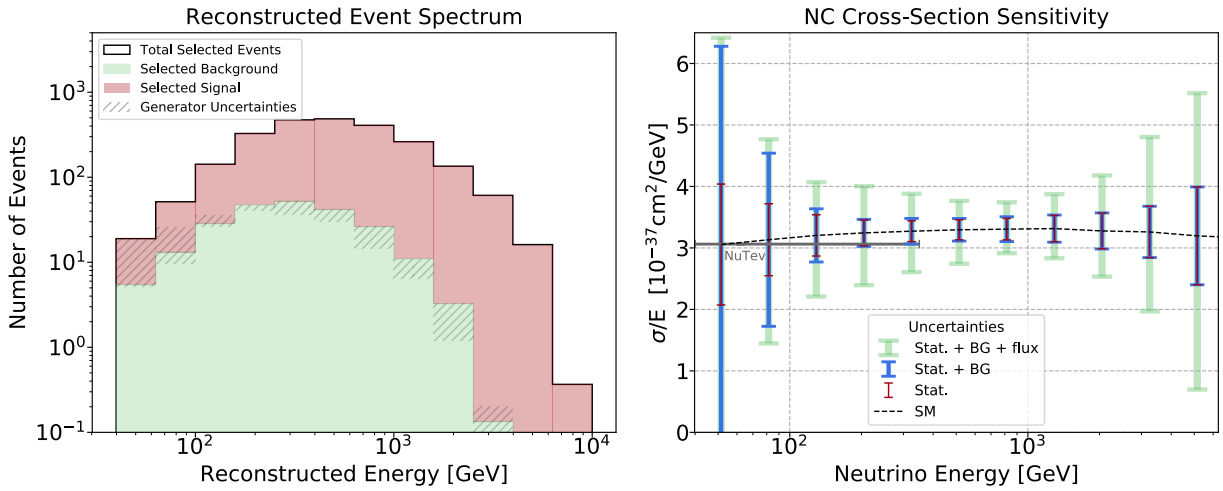

Figure 27: **Left:** Stacked histogram of events passing the event signal selection described in Sec. 4.4.2 as function of the reconstructed energy for LHC Run 3 with 150 fb^{-1} integrated luminosity. The red and green shaded regions show the NC neutrino interaction signal and the neutral hadron interaction background, respectively. The hatched region indicates the uncertainty arising from the simulation of neutral hadron interactions, corresponding to the range of predictions obtained by three different generators. **Right:** FASERν's estimated neutrino-tungsten NC cross section sensitivity. Existing constraints are shown in gray. The black dashed curve is the theoretical prediction for the DIS cross section, averaged over neutrinos and anti-neutrinos, per tungsten nucleus. The inner red error bars correspond to statistical uncertainties, the blue error bars additional take into account uncertainties associated with the simulation of the background, and the outer green error bars show the combined uncertainties with the neutrino production rate (which corresponds to the range of predictions obtained from different MC generators as obtained in Ref. [9]).

With the analysis described in the previous section, we proceed to discuss FASERν's expected physics sensitivity. In the left panel of Fig. 27, we show the expected number of NC neutrino signal (red) and neutral hadron background (green) events simulated with `Pythia 8` passing the event selection as a function of the reconstructed energy. As noted before, the signal dominates over the background for energies above about 100 GeV and reaches a signal to background ratio $\gtrsim 100$ for energies above 1 TeV. The hatched region shows the background simulation uncertainty, corresponding to the range of predictions obtained from three different event generators to simulate neutral hadron interactions using the same neutral hadron flux and energy spectrum.

Assuming no new physics contribution to neutrino production and propagation, the observed energy spectrum at FASERν can be used to measure the NC neutrino interaction cross section. We show FASERν's expected sensitivity to constraining the NC neutrino interaction cross sections with a tungsten nucleus in the right panel of Fig. 27. The black dashed line shows the SM prediction for the cross section, flux-weighted over neutrinos and anti-neutrinos. We also show the NuTeV neutrino-quark neutral current strength measurement [198] in gray, which had superior precision, $\mathcal{O}(1\%)$ with error bars that are too small to be visible, but used neutrinos that were less energetic than the bulk of the FASERν neutrino spectrum.

Several sources of uncertainties contribute to the measurement. In the following, we discuss these uncertainties and how they could be reduced in a full experimental analysis.

Statistical uncertainty During LHC Run 3 with a nominal integrated luminosity of 150 fb^{-1}, FASERν will collect roughly 7000 NC neutrino interactions. The corresponding statistical uncertainties in each energy bin are shown as thin red error bars.

Neutrino flux The neutrino flux uncertainty is associated with the modeling of forward particle production, which is mostly governed by non-perturbative physics and typically described by hadronic interaction models. Here we use the neutrino flux obtained

in Ref. [9], where the range of predictions obtained by different hadronic interactions models was used to estimate the neutrino flux uncertainties. We note that more efforts are needed, and indeed already ongoing, to both quantify and reduce these uncertainties. We show the neutrino flux uncertainty as the green error bars in Fig.27, and note that this is expected to be a dominating source of uncertainty.

In extracting limits on new physics, the flux uncertainty can be mitigated by taking the ratio of neutral current to charged current events. This technique has been used by previous experiments [10, 199–201] to measure the weak mixing angle.

Signal simulation As outlined in Ref. [170], there are a variety of uncertainties effecting the signal simulation, including (i) nuclear effects (such nuclear shadowing and anti-shadowing and EMC effect), (ii) the hadronization of final state partons, and (iii) the modeling of final state interactions in the tungsten target nuclei. Currently, there is no neutrino interaction generator that targets this high-energy DIS regime. While recent efforts on nuclear PDFs allow one to describe nuclear effects and their uncertainties [191, 192, 202–204], more dedicated efforts are needed to tune and improve the modeling of hadronization and final state interactions in existing generators and to quantify the uncertainties. In principle, data from previous neutrino experiments, such as DONuT or CHORUS, as well as FASERν's CC measurements could be helpful in this regard.

Uncertainties on the signal simulation will affect the distributions of observables and hence induce uncertainties in all parts of the analysis, including the neutral vertex identification efficiency, the signal identification efficiency, and the energy reconstruction performance. As no reliable estimates of these uncertainties are currently available, we do not attempt to quantify the impact of generator uncertainties on our final results.

Neutral hadron flux Analogous to the aforementioned uncertainty on the size of the signal, there are also uncertainties in the numbers of neutral hadrons impinging on

FASERν. The calculation of the neutral hadron flux takes the muon flux in front of FASERν as input and relies on the modeling of neutral hadron production from muons interacting with the detector and rock in front of it. The muon flux used in this study was obtained by the CERN STI group using a dedicated `Fluka` simulation, and it would not be unreasonable to allow for an $\mathcal{O}(1)$ uncertainty on the number of neutral hadrons [177]. Even such a large error, though, is expected to have a small impact on the final cross section uncertainty due to the efficiency of the classification network. The neutral hadron contamination of events that are classified as neutrino interactions is below 10–20% for energies above 200 GeV. Furthermore, at Run 3, FASER will directly measure the muon flux and energy spectrum, allowing for reduction of the uncertainty of the input for the neutral hadron calculation. In addition, the number of neutral hadron interactions in FASERν can be constrained directly using both measurements of a neutral hadron control sample, as well as charged hadrons which leave clearly visible tracks.

Background simulation As shown in Fig. 23, different generators for neutral hadron interactions produce variations in the distributions of the observables that are used for our analysis. This leads to an uncertainty on the rate of background events passing the event selection, as indicated by the hatched region in the left panel of Fig. 27. We have included the resulting uncertainty as blue error bars in the right panel of Fig. 27. While this uncertainty dominates the NC neutrino cross section sensitivity at low energies below 100 GeV, it only mildly affects the measurement at higher energies. These uncertainties can be further improved both using FASERν and measurements from dedicated beam dump experiments, such as DsTau [205] and NA61 [206].

Experimental Uncertainties While we have incorporated detector effects in our simulation, we do not include experimental uncertainties regarding the detector performance.

Energy estimation We have estimated the incoming neutrino energy with an error of

approximately 50% for events classified as neutrino neutral current events, as shown in Fig. 26. In an experimental analysis, a transfer matrix among the bins could be derived from the network performance. Then, the obtained energy distribution could be unfolded to obtain a better approximation of the incoming neutrino energies. At our level of precision, it is reasonable to assume that this matrix is approximately diagonal given the width of the energy bins, and we do not consider this uncertainty further.

Our results for the neutrino NC cross section are summarized in the right panel of Figure 27. The most significant source of uncertainty is the neutrino flux at higher energies and the background simulation at energies below 100 GeV. We note that statistical uncertainties could be reduced with a neutrino detector in the forward region of the HL-LHC, which has a nominal integrated luminosity of 3000 fb^{-1}. Such a detector could be placed in a future Forward Physics Facility [207] at the High Luminosity LHC.

4.5.2 Non-standard interactions

The neutrino neutral current cross section can be used to probe new interactions between neutrinos and quarks. Historically, the ratio of the neutral to charged current cross section has been considered as a measurement of the weak mixing angle, as it depends on $\sin^2\theta_w$. Since the weak mixing angle is measured very precisely by other facilities such as LEP [208], however, we choose to assume no deviations from precision electroweak physics in the SM, and instead place limits on BSM interactions. As fully $SU(2)\times U(1)$-symmetric interactions typically face strong constraints from processes involving charged leptons, we focus on the usual NSI [11]

$$\mathcal{L} \supset -\sqrt{2}G_F\sum_{f,\alpha,\beta}[\bar{\nu}_\alpha\gamma^\mu P_L\nu_\beta][\epsilon^{f,V}_{\alpha\beta}\bar{f}\gamma_\mu f + \epsilon^{f,A}_{\alpha\beta}\bar{f}\gamma_\mu\gamma^5 f] \tag{4.5.1}$$

where $f = u, d$ and $\alpha, \beta = e, \mu, \tau$. These interactions would interfere with Z exchange, affecting the neutrino neutral current cross section. Data on neutrino oscillations [209] and coherent neutrino-nucleus scattering [210] probe the vector couplings $\epsilon^{f,V}_{\alpha\beta}$ efficiently but are

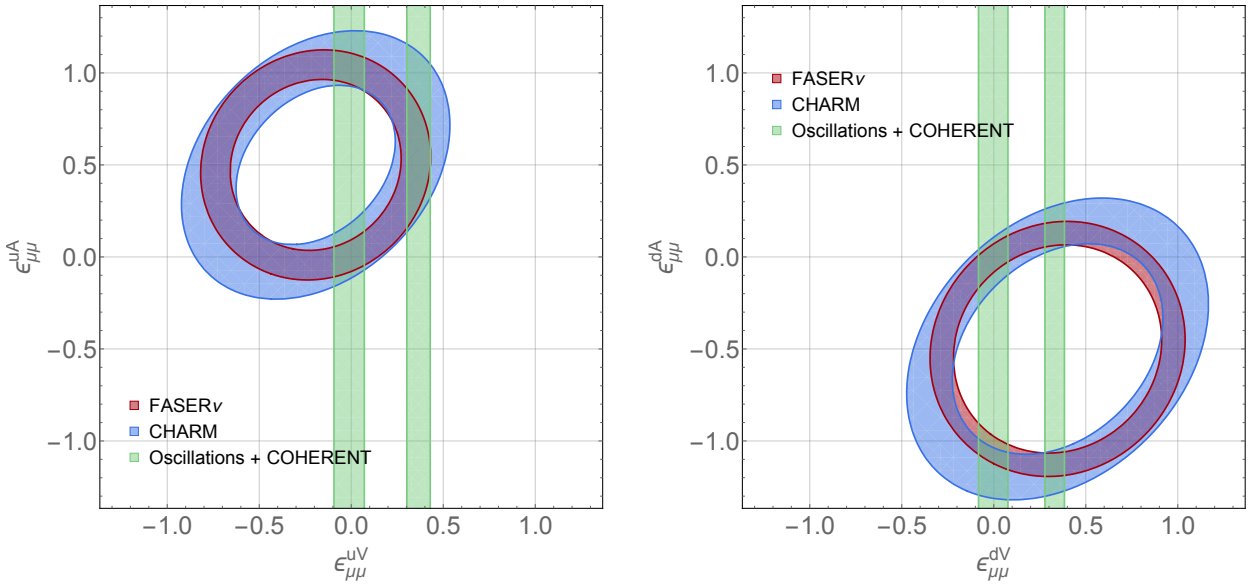

Figure 28: **Left:** Limits on neutrino NSI involving the up quark. The red ellipse indicates the expected 95% allowed region by FASERν , with limits from CHARM [10] (blue) shown for comparison. The one-dimensional allowed region from oscillation and COHERENT [11] is also shown (green). **Right:** Same as left plot but for NSI involving the down quark.

not sensitive to their axial counterparts that only couple to net spin. By contrast, high-energy experiments can probe NSI regardless of the underlying spin structure [211–213].

In passing, we remark that while the validity of any effective operator treatment breaks down at sufficiently high energies, the momentum transfers that we consider are of order $\sqrt{2m_N E_\nu} \lesssim v$, where $v = 246$ GeV is the electroweak vacuum expectation value. We will obtain limits on the NSI parameters that are less than $\mathcal{O}(1)$, corresponding to operator suppression scales above the electroweak scale. At even higher energies, of course, a full UV completion of the NSI should be considered [212]. It would be interesting to examine the sensitivity of FASERν neutrino NC scattering measurements to light mediators, where we would expect different kinematics from NC scattering in the SM.

To limit NSI, we anticipate a FASERν measurement of the neutrino neutral current cross section as in Fig. 28, in conjunction with a charged current cross section measurement [9]. We take the ratio of the neutral current to the charged current cross section assuming that

the flux uncertainties will largely cancel, with the main remaining considered sources of error being the statistics on the neutral current events and the uncertainty on the background. Following the discussion above, other uncertainties such as the neutral hadron flux and energy estimation are assumed to be subdominant in the cross section ratio. In particular, FASER will directly measure the muon flux and energy spectrum once it turns on which will reduce the neutral hadron flux uncertainties. By performing a χ^2 fit using the cross section ratio in each energy bin as input, we obtain the overall expected NSI sensitivity. Throughout, we make the simplifying assumption that all of the incoming neutrinos are muon (anti)neutrinos. Weaker bounds could, in principle, be obtained on NSIs involving electron neutrinos using the subdominant ν_e flux.

Our projected sensitivity is shown in Fig. 28. We also show the limits obtained from taking the ratio of the NC to CC cross-sections at CHARM [10], as well as the current bound on the vector NSI couplings from oscillation and COHERENT data [11]. We note that CHARM probes a different combination of the up and down quark NSIs because the limits come from neutrino scattering, whereas at FASERν we have a combined constraint from neutrinos and antineutrinos. In summary, we find that FASERν has the potential to provide competitive NSI sensitivity, particularly in the axial case where bounds from oscillation and coherent scattering experiments do not exist.

4.6 Outlook

While LHC neutrinos have never been directly detected, FASERν will provide the ability to probe their interactions for the first time. Measurements of neutrino cross sections at TeV-scale neutrino energies will fill a gap between lower energy laboratory experiments and astrophysical neutrino data. Neutral current scattering is significantly more difficult to observe than charged current scattering, owing to the final state neutrino that carries away much of the energy of the interaction. At FASERν, there is a significant background from neutral hadrons induced by muons from the LHC.

We have demonstrated that the neutral hadron background to neutrino neutral current scattering in FASERν can be significantly reduced for neutrino energies $\gtrsim$ 100 GeV. Furthermore, we have shown that the energy of the incoming neutrino can be estimated from the measured particles exiting the interaction vertex. The precision of our energy estimation procedure for neutral current scattering is comparable to that which could be obtained for charged current scattering. In both our handling of the background and our estimation of the neutrino energies, we have used neural networks to make maximal use of the available kinematic information in each event. We have identified areas where further work is warranted to maximize the power of a full experimental analysis, in particular, the improvement of simulation tools for neutrino DIS at TeV energies and the quantification of associated uncertainties.

The NC cross section measurement here would serve as a test of whether neutrinos interact as predicted by the SM, and can thus be used to test new couplings between neutrinos and quarks. We have interpreted our projected cross section measurements in terms of limits on neutrino NSIs, finding sensitivities that are competitive with other experiments. In particular, we obtain limits on axial NSIs, which are not constrained in any significant manner by oscillation or coherent scattering data.

As the most weakly interacting particles in the SM, there is still much to be learned about neutrinos. We have extended the potential of the LHC to test neutrino couplings by considering NC scattering at FASERν . Taken in the broader context of data from dedicated laboratory and astrophysical neutrino facilities, we hope that collider studies of neutral current scattering will lead to an increased understanding of the neutrino sector.

CHAPTER V

NEUTRINO ELECTROMAGNETIC PROPERTIES AND THE WEAK MIXING ANGLE AT THE LHC FORWARD PHYSICS FACILITY

5.1 Introduction

Neutrino properties are crucial to understanding our Universe and have been prime targets of particle physics experiments. The electromagnetic (EM) properties of neutrinos, in particular, can be tested in existing and future experiments. These measurements include the mass-dimension 4 neutrino millicharge, the mass-dimension 5 neutrino dipole moments, and the mass-dimension 6 neutrino charge radius. These properties can, for example, be used to determine whether neutrinos have a Dirac or Majorana nature [214, 215] and to probe new physics beyond the Standard Model (SM) [67]. These neutrino properties could be linked to intriguing experimental anomalies, including the NuTeV anomaly [216] and the Xenon 1T excess [217] (although the latter was determined most likely to be from an SM background [218]). Large neutrino dipole moments, for example, can also affect the mass gap of black holes [219, 220]. Interesting models were proposed to generate neutrino EM couplings much larger than the SM predictions [221–226] and to connect the anomalies to the neutrino properties [227]. Currently, the SM predictions of these properties are several orders of magnitude smaller than the present upper bounds, obtained from reactor neutrinos [228, 229], accelerator neutrinos [230–232], and solar neutrinos [218, 233–237], to name a few. For a connection between neutrino electromagnetic properties and CP phases, see Ref. [238].

The LHC provides one of the most exciting opportunities in studying high-energy neutrinos and tau neutrinos, given its high center-of-mass energy. The forward region at the

LHC, in particular, provides a large flux of neutrinos coming from meson decays [44]. The Forward Physics Facility (FPF) [39] at the LHC is ideally placed on studying these TeV energy neutrinos. Previously, interesting signatures from the neutrino dipole portal [239, 240], were studied at FPF [241] and FASER [186], but a proper analysis of the future capability of FPF on neutrino EM properties are sorely lacking at this moment.

In this chapter, we utilize the FPF to study interesting properties of neutrinos: the neutrino millicharge, magnetic moment, and charge radius. By looking at low recoil energy electron scattering and neutral current deep inelastic scattering (DIS) events, we show that we can reach competitive sensitivity for these properties. Most excitingly, we can set the world's leading limit on neutrino charge radius for the electron neutrino, while for the muon neutrino, we come within a factor of a few from the SM prediction. For the tau neutrino, FPF's limits on the magnetic moment are an order of magnitude better than the DONUT results [231] and bounds on millicharge and charge radius constitute some of the few existing measurements for the tau neutrino.

The neutrino interaction with the target material, investigated in this study, also depend sensitively on electroweak parameters. In this context, the precise measurement of the neutral current neutrino DIS rate can also be translated to a precise measurement of the weak mixing angle. This would allow one to test the anomalous result obtained by NuTeV [216].

The chapter is organized as follows. We briefly review neutrino EM properties in Sec. 5.2 and introduce the detectors under consideration at the FPF in Sec. 5.3. In Sec. 5.4, we discuss our signal characteristics. We present our results on the neutrino EM properties in Sec. 5.5 and discuss the measurement of the weak mixing angle in Sec. 5.6. We conclude in Sec. 5.7.

5.2 Neutrino EM Properties

The electric charge of neutrinos is zero in the SM. However, electromagnetic properties can arise at the quantum loop level (or via BSM physics) allowing electromagnetic interactions of

neutrinos with photons and charged particles. Considering neutrinos as massive fermions, the electromagnetic properties of neutrinos in the one-photon approximation can be assembled in the matrix element of the neutrino effective electromagnetic current [68, 69] as

$$\left\langle \nu_f(p_f)|j^{\mu}_{\nu,\mathrm{EM}}|\nu_i(p_i)\right\rangle = \overline{u}_f(p_f)\Lambda^{\mu}_{fi}(q)u_i(p_i), \tag{5.2.1}$$

where q is the four-momentum transferred to the photon. The vertex function $\Lambda^{\mu}_{fi}(q)$ is a 3×3 matrix in the neutrino mass eigenstates space that encodes the electromagnetic properties of neutrinos. We are interested in the ultra-relativistic limit where, at low-q^2, it simplifies to,

$$\Lambda^{\mu}_{fi}(q) = \gamma^{\mu}(Q_{fi} - \frac{q^2}{6}\left\langle r^2\right\rangle_{fi}) - i\sigma^{\mu\nu}q_{\nu}\mu_{fi} \tag{5.2.2}$$

with $f = i$ for diagonal and $f \neq i$ for transition electromagnetic properties. Note that in theories of massive neutrinos, the transition electromagnetic properties can be generated through mixing, even if the matrices in Eq. (5.2.2) are diagonal in the mass basis [242].

In this chapter, we conduct a phenomenological study of effective neutrino electromagnetic properties: the millicharge Q, the magnetic moment μ, and the charge radius $\langle r^2\rangle$ at the FPF. Effective here implies the possible inclusion of contributions coming from electric and anapole moments to the magnetic moment and charge radius [243], respectively. Also, the neutral current interaction we study here has no information on the outgoing neutrino flavor. Therefore, we implicitly assume a sum over all final state neutrino flavors [244, 245]. Note that when recasting the results obtained here for e.g. Majorana neutrinos have only transition magnetic moment and millicharge.

The electric neutrality of neutrinos in the SM is guaranteed by charge quantization [246, 247]. But in some BSM theories, neutrinos can have a very small electric charge [248] enabling it to couple to the photon. This BSM interaction can be described by an effective term in the Lagrangian $\mathcal{L} \supset Q_{\nu}(\bar{\nu}\gamma_{\mu}\nu)A^{\mu}$.

Neutrino magnetic moments, on the other hand, do arise in the SM at one loop level [249,

250]. The diagonal magnetic moment for a massive Dirac neutrino is given by

$$\mu_\nu \approx \frac{3eG_F}{8\sqrt{2}\pi^2} m_\nu \approx 3 \cdot 10^{-19} \mu_B \left(\frac{m_\nu}{1 \text{ eV}}\right). \tag{5.2.3}$$

where m_ν is the neutrino mass, e is the electric charge, G_F is the Fermi constant and $\mu_B = e/(2m_e)$ is the Bohr magneton. This very small value is beyond the scope of terrestrial and astrophysical probes currently. The values for transition magnetic moments for Majorana neutrinos are even smaller [251]. However, an additional contribution to the magnetic moment of neutrinos could arise from BSM physics [222, 224, 252]. In an effective field theory approach, this can be parametrized in terms of a higher dimensional operator $\mathcal{L} \supset \mu_\nu(\bar{\nu}\sigma_{\alpha\beta}\nu)F^{\alpha\beta}$ for Dirac neutrinos (for Majorana neutrinos one replaces $\bar{\nu}$ with $\bar{\nu}^c$ for only the left-handed neutrino fields (ν_L) above, and only transition moments are allowed).

Measuring the magnetic moment of neutrinos is important, as it can also in principle shed light on the Dirac vs. Majorana nature of neutrinos. Dirac neutrinos can have diagonal and transition magnetic moments, whereas Majorana neutrinos only have transition magnetic moments. Large transition magnetic moments for Majorana neutrinos could be realized in certain BSM models [253, 254], which are not too far from the current experimental limits, but the off-diagonal moments could be hard to measure, as we do not probe the outgoing neutrino flavor.

Neutrinos also have non-zero charge radii in the SM from radiative corrections given by [255, 256]

$$\left\langle r^2_{\nu_\ell} \right\rangle_{\text{SM}} = \frac{G_f}{4\sqrt{2}\pi^2} \left[3 - 2\log\frac{m_\ell^2}{m_W^2}\right]. \tag{5.2.4}$$

where m_ℓ are the lepton masses ($\ell = e, \mu, \tau$) and m_W is the W boson mass. The SM values are then found to be 4.1×10^{-33} cm^2 for ν_e, 2.4×10^{-33} cm^2 for ν_μ and 1.5×10^{-33} cm^2 for ν_τ. These values differ by at most one or two orders of magnitude from current terrestrial bounds, and hence testing the SM prediction of neutrino charge radius is a compelling challenge.

5.3 Detectors at the FPF

An unexpected but powerful source of light and weakly coupled particles can be found at the LHC [41]. In the forward direction, the LHC produces an intense and strongly collimated beam of neutrinos of all three flavors coming mainly from the decays of mesons produced at the interaction point. Currently, there are two experiments taking advantage of this opportunity: FASERν [44, 45] and SND@LHC [257, 258]. In particular, both experiments are expected to obtain about 20 tau neutrino interactions, which exceeds the number of events recorded by the DONuT [259] and OPERA [260] experiments.

Several improved neutrino detectors are planned for the HL-LHC era. They will be housed in the FPF [39, 40] along with an array of other detectors with a wide range of physics potential, to be located in a cavern 620 m downstream from the ATLAS interaction point. Our analysis focuses on two detector technologies at FPF which are sensitive to TeV range neutrino interactions: FLArE, which is a liquid argon time projection chamber, and FASERν2, which is an emulsion-based neutrino detector. In the following, we present the detector details relevant to the phenomenological study at hand:

- **FLArE**, the Forward Liquid Argon Experiment, is composed of a 10 tonne liquid argon time projection chamber with a fiducial volume of 1m $\times$ 1m $\times$ 7m [25]. Liquid argon time projection chambers are a proven technology for neutrino physics, having been used at Fermilab's Short-Baseline Neutrino Program [261] and at the future DUNE experiment [262]. They offer the dual advantage of very low energy thresholds of down to 30 MeV and excellent timing resolution, achieved through a light collection system. This will allow one to control possible muon induced backgrounds by vetoing events in coincidence with a muon track, which is critical to the feasibility of our study. FLArE is a 10 tonne detector. We also include in our study a larger 100 tonne detector, dubbed **FLArE-100**, with a fiducial volume of 1.6m $\times$ 1.6m $\times$ 30m. This is meant to illustrate how sensitivities would scale with target mass.

- **FASERν2** is an emulsion detector designed as a much larger successor to the approved FASERν detector [263]. In the HL-LHC era, FASERν2 is envisioned as a 10 tonne neutrino detector composed of emulsion layers interleaved with tungsten sheets acting as target material. Emulsion detectors are capable of detecting charged tracks with high spatial resolution. The major drawback of emulsion detectors is a lack of timing information associated with the recorded events. FASERν2 aims to mitigate this by introducing tracking layers between and at the end of the emulsion layers. Timing information can then be obtained by successfully matching the event in the emulsion and the tracker. This is helpful in the search for a coincident muon track, which can be used to reduce muon induced backgrounds. We assume that in FASERν2 all muon induced backgrounds can be eliminated with the help of timing information. The fiducial volume we consider is $0.5\ \text{m} \times 0.5\ \text{m} \times 2\ \text{m}$ [264]. Since the charged particle has to pass through a sufficient number of emulsion layers to leave a distinguishable track, a minimum particle momentum of 300 MeV [264] is required. This sets the energy threshold of the detector.

The two processes we study here are neutrino electron elastic scattering and neutral current DIS. The main backgrounds for the former are similar to those studied in Refs. [25, 265] and the latter was studied in the context of FASERν in Ref. [266]. Here we briefly summarize the relevant results.

A major source of similar backgrounds for both processes is muon-induced events. Muons passing through the detector can, for example, emit photons through bremsstrahlung or produce high energy neutral hadrons in inelastic scatterings. The photons could then pair convert to e^+e^- and if one of them is missed, it can mimic our electron scattering signal. Neutral hadron scattering, on the other hand, would look similar to the neutral current DIS neutrino interactions. In both cases, the inclusion of timing capabilities in the detectors allows vetoing such backgrounds by associating such events with the accompanying muon. For example, the currently operating FASER detector employs several scintillating veto layers

at its front, each of which has a muon detection efficiency of more than 99.99% [267]. In this chapter, we assume such muon-induced backgrounds can be reduced to negligible levels.

An irreducible source of backgrounds to both processes is SM contribution to neutral current neutrino scattering. For neutrino electron elastic scattering, we employ the use of kinematic cuts to enhance the signal to background ratio, as described in the next section. This is where a low energy threshold detector like FLArE is advantageous.

Throughout this work, we use the neutrino fluxes presented in Ref. [264] for the HL-LHC era. They were obtained using the event generator `SIBYLL 2.3d` [268–271] implemented via `CRMC` [195] which simulates the primary collision. Ref. [21] introduced a fast neutrino flux simulator which models the propagation and decay of long-lived hadrons within the SM in the forward direction at the LHC. Currently, there exist sizeable uncertainties on the neutrino flux. However, this is expected to be brought under control using the charged current scattering event rate once the detector starts to take data [44].

5.4 Neutrino EM Interaction Rate

The signature we investigate in our study is the excess (or deficit) of neutrino neutral current scattering events in the detectors with respect to the expected rate predicted by the SM in the absence of any neutrino EM properties.

We first consider the neutrino electron elastic scattering where the SM cross section, in terms of the electron recoil energy E_r, is given by [67, 272]

$$\left(\frac{d\sigma_{\nu_\ell e}}{dE_r}\right)_{\rm SM} = \frac{G_F^2 m_e}{2\pi}\Bigg[(g_V^\ell - g_A^\ell)^2\left(1-\frac{E_r}{E_\nu}\right)^2 + (g_V^\ell + g_A^\ell)^2 + \left((g_A^\ell)^2 - (g_V^\ell)^2\right)\frac{m_e E_r}{E_\nu^2}\Bigg] \tag{5.4.1}$$

with the standard vector and axial vector coupling constants g_A^ℓ and g_A^ℓ given by

$$g_V^\ell = 2\sin^2\theta_w - \frac{1}{2} + \delta_{\ell e}\ ,\ g_A^\ell = -\frac{1}{2} + \delta_{\ell e}\ . \tag{5.4.2}$$

Here G_F is the Fermi constant, θ_W is the weak mixing angle, and E_ν is the neutrino energy. For antineutrinos, one must replace g_A^ℓ by $-g_A^\ell$. There is an extra term for the electron neutrino coming from the exchange of the W boson, which is not present for muon and tau neutrinos. In the presence of non-negligible values for the neutrino electromagnetic properties, the event rate and distribution can be sufficiently distorted.

As detailed below, the most significant effect of including these BSM physics is in the event rate, especially at low recoil energies for the magnetic moment and millicharge. This motivates looking at E_r as the main kinematic variable in our study. One could also look at the recoil angle of the electron, as was studied in Ref. [25]. For neutrino electron scatterings at the energies of interest, so E_ν and $E_r \gg m_e$, the recoil angle is correlated with the recoil energy via $\cos\theta_r \approx 1 - m_e/E_r$. Although, this does not help to distinguish different neutrino electron scattering events but provides another handle to remove backgrounds coming from neutrino nuclear scattering events with a single particle recoiling in the final state. Since we will be imposing a strong kinematic cut on the electron recoil energy that suppresses the background sufficiently, we do not include the recoil angle of the electron as an additional observable. We note, however, the strong correlation between the recoil energy and the recoil angle of the electron can be used to improve energy resolution at small energies.

In some cases, it might be beneficial to also consider nuclear scattering, where one could benefit from higher event rates. As can be seen in Eq. (5.4.1), the neutral current scattering rate in the SM roughly scales proportionally to the target mass. If the new physics signal count decreases or doesn't increase commensurately, then moving to a heavier target will only degrade the sensitivity. This is the case with neutrino magnetic moment and millicharge, and hence we stick to electron scattering events for both of them. As we will see below, a charge radius essentially induces a shift in the vector coupling constant, g_V and hence we can expect higher rates of signal if we use a heavier target. We therefore also consider neutral current neutrino DIS in the charge radius case, which will result in significantly higher signal event rates and hence improve the bounds on $\langle r_{\nu_\ell}^2 \rangle$.

At leading order, the double differential cross section for neutral current neutrino-nucleon DIS is given by [273]

$$\frac{d\sigma(\nu N \to \nu X)}{dx\ dy} = \frac{2G_F^2 m_p E_\nu}{\pi} \frac{m_Z^4}{(Q^2+m_Z^2)^2} \times \sum_{q=u,d,s,c} \big[g_{q,L}^2[xf_q(x,Q^2) + xf_{\bar{q}}(x,Q^2)(1-y)^2] + g_{q,R}^2[xf_q(x,Q^2)(1-y)^2 + xf_{\bar{q}}(x,Q^2)]\big] \tag{5.4.3}$$

for neutrino scattering and

$$\frac{d\sigma(\overline{\nu} N \to \overline{\nu} X)}{dx\ dy} = \frac{2G_F^2 m_p E_\nu}{\pi} \frac{m_Z^4}{(Q^2+m_Z^2)^2} \times \sum_{q=u,d,s,c} \big[g_{q,L}^2[xf_q(x,Q^2)(1-y)^2 + xf_{\bar{q}}(x,Q^2)] + g_{q,R}^2[xf_q(x,Q^2) + xf_{\bar{q}}(x,Q^2)(1-y)^2]\big] \tag{5.4.4}$$

for anti-neutrino scattering, where X stands for the final states that are a byproduct of the DIS other than the neutrino. Here m_p is the mass of the target proton, m_Z is the Z boson mass, and $g_L^q, g_R^q = T^3 - Q_q \sin^2\theta_W$ are the left and right-handed neutral current couplings of the quarks with Q_q being the charge of the quarks in units of e. The differential cross section is expressed in terms of the DIS variables x, y and Q^2, where x is the partonic momentum fraction, $y = E_{\text{had}}/E_\nu$ is the fraction of neutrino's energy that is transferred to the hadronic system, and $Q^2 = 2m_p E_\nu xy$ is the squared 4-momentum transfer. Here E_ν is the incident neutrino energy, and E_{had} is all the energy contained in the hadronic system. The functions $f_q(x,Q^2)$ are the nucleon parton distribution function. Here we use nCTEQ15 which includes nuclear effects of the target nucleus [191].

5.4.1 Neutrino Magnetic Moment

The presence of a BSM contribution to the neutrino magnetic moment can lead to an excess in the number of electron recoil events, especially at low recoil energies. The differential cross section with respect to the electron recoil energy for the elastic scattering of a neutrino (or antineutrino) with incoming flavor ℓ and energy E_ν off an electron in the presence of a

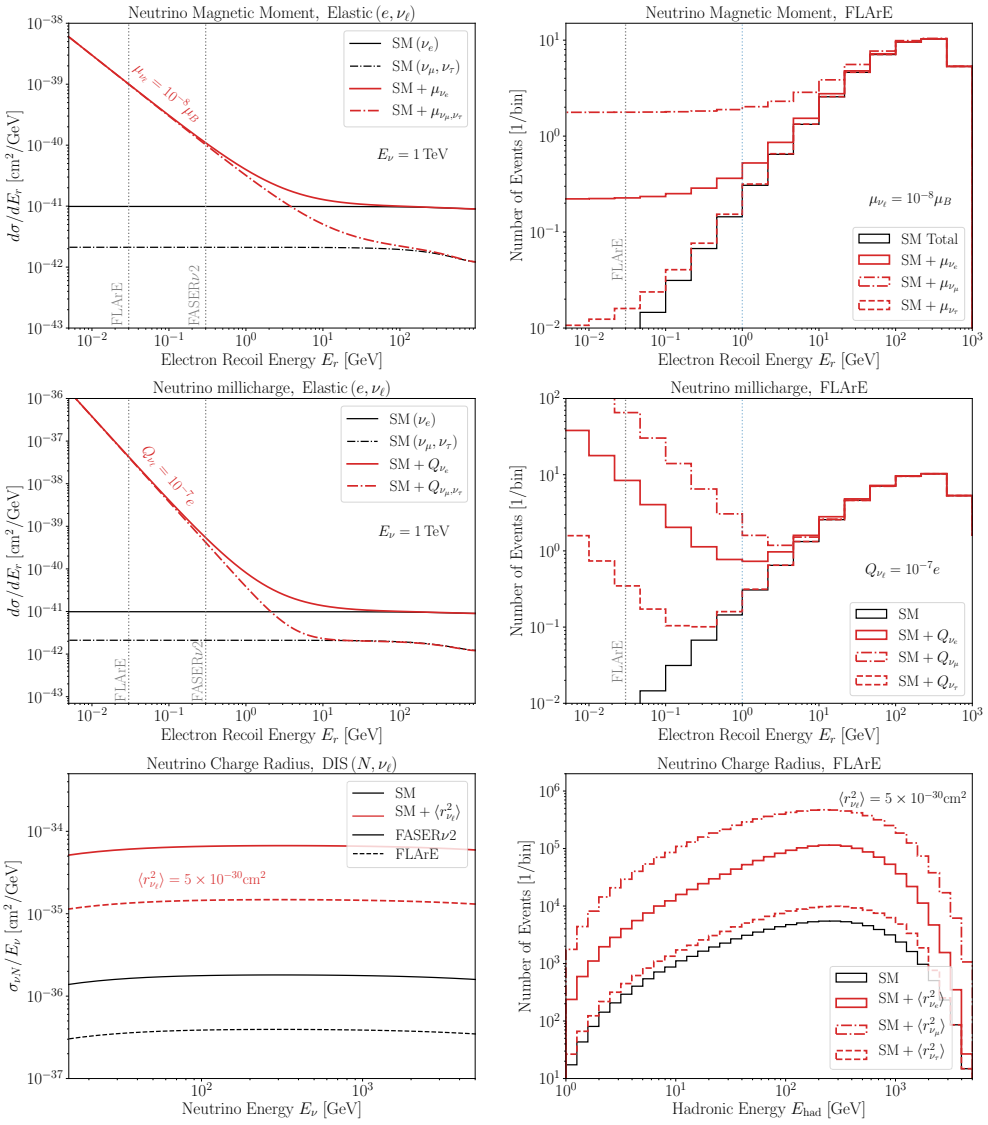

Figure 29: **Top and Middle Left:** Differential cross-section of neutrino elastic scattering on the electron as a function of electron recoil energy, corresponding to the incoming neutrino energy of 1 TeV. **Top and Middle Right:** The expected number of events at FLArE, considering the estimated neutrino flux at the FPF in the HL-LHC phase. The magnetic moment and millicharge electromagnetic contributions (red) exceed the SM background (black) at lower recoil energies. The FLArE and FASERν2 detector recoil energy thresholds of 30 and 300 MeV, as well as the 1 GeV upper cutoff, are indicated by vertical dotted lines. **Bottom Left:** Cross section of neutrino-nucleus deep-inelastic scattering in FASERν2 (solid) and FLArE (dashed) as a function of neutrino energy, within the SM (black) and in the presence of the charge radius. **Bottom Right:** Expected event rate at FLArE as a function of the energy of the hadronic system.

magnetic moment is given by [226, 274]

$$\left(\frac{d\sigma_{\nu_\ell e}}{dE_r}\right)_{\rm NMM} = \left(\frac{d\sigma_{\nu_\ell e}}{dE_r}\right)_{\rm SM} + \frac{\pi^2}{m_e^2}\left(\frac{1}{E_r} - \frac{1}{E_\nu}\right)\left(\frac{\mu_{\nu_\ell}}{\mu_{\rm B}}\right)^2, \tag{5.4.5}$$

where μ_{ν_ℓ} is the effective neutrino magnetic moment, and μ_B is the Bohr magneton. Note that the two contributions in Eq. (5.4.5) add incoherently in the cross section due to the following helicity argument [275]: in the ultra-relativistic limit, the SM weak interaction conserves the neutrino helicity while the helicity flips in the neutrino magnetic moment interaction. Hence, one is always guaranteed an excess of events in this case.

The two contributions in the cross section exhibit quite different dependencies in the electron recoil energy E_r, as illustrated in Fig. 29 top left panel for an incoming neutrino beam with 1 TeV energy. The signal cross section associated with the neutrino magnetic moment exceeds the SM background in the range,

$$E_r \lesssim 10 \text{ GeV} \times \left(\frac{\mu_{\nu_\ell}}{10^{-8}\,\mu_{\rm B}}\right)^2. \tag{5.4.6}$$

This leads to an increase in the elastic neutrino-electron events above the SM predicted value at low values of E_r. This can be seen as arising from the $1/E_r$ term in the BSM cross section expression. The lines for ν_e and $\nu_{\mu,\tau}$ look different due to the additional diagram coming from the W boson exchange that is only present for ν_e.

Given the neutrino flux at the FPF, the electron recoil energy spectrum at FLArE and FASERν2 detectors can be calculated. Fig. 29 top right panel shows the total expected event rate for a benchmark value of $\mu_{\nu_\ell} = 10^{-8}\ \mu_B$ for all three flavors at FLArE, as well as the SM event rate. The three flavors of neutrinos have different fluxes at FPF, resulting in distinct predictions for the event spectrum. The excess events in the low recoil energy bins serve as an experimental signature to look for neutrino magnetic moment.

5.4.2 Neutrino Millicharge

The FPF is an ideal environment to search for millicharged particles in the dark sector [276, 277] and can also be used to probe neutrino millicharge. The inclusion of a non-zero electric

charge for the neutrino changes the neutrino-electron elastic scattering cross section as [67, 242, 278]

$$\left(\frac{d\sigma_{\nu_\ell e}}{dE_r}\right)_{\rm NMC} = \left(\frac{d\sigma_{\nu_\ell e}}{dE_r}\right)_{\rm SM} + \left(\frac{d\sigma_{\nu_\ell e}}{dE_r}\right)_{\rm Int} + \left(\frac{d\sigma_{\nu_\ell e}}{dE_r}\right)_{\rm Quad}. \tag{5.4.7}$$

The first term is the above SM expression as before. The interference term is,

$$\left(\frac{d\sigma_{\nu_\ell e}}{dE_r}\right)_{\rm Int} = \frac{\sqrt{8\pi}G_F\alpha}{E_\nu^2 E_r}\left(\frac{Q_{\nu_\ell}}{e}\right)\left[g_V^\ell\big(2E_\nu^2 + E_r^2 - E_r(2E_\nu + E_r)\big) + g_A^\ell\big(E_r(2E_\nu - E_r)\big)\right] \tag{5.4.8}$$

with g_V^ℓ, g_A^ℓ defined as before, and the quadratic term is given by

$$\left(\frac{d\sigma_{\nu_\ell e}}{dE_r}\right)_{\rm Quad} = 4(\pi\alpha)^2\left(\frac{Q_{\nu_\ell}}{e}\right)^2\left[\frac{2E_\nu^2+E_r^2-2E_\nu E_r}{m_e E_r^2 E_\nu^2}\right], \tag{5.4.9}$$

where Q_{ν_ℓ} is the electric charge of the neutrino. For anti-neutrino, we replace g_A with $-g_A$ similar to the SM case. The presence of the interference term $\sim \big(Q_{\nu_\ell}/e\big)$ means we are now sensitive to the sign of the neutrino millicharge and depending on the value of Q_{ν_ℓ} we can expect an increase or decrease in the number of events. However, it turns out that, for the values of the millicharge that can be probed at the FPF, the quadratic term always dominates, therefore, an excess of events is expected. For a benchmark value of $Q_{\nu_\ell} = 10^{-7}e$ we see an even steeper increase in cross section at lower recoil energies than for the magnetic moment, as the quadratic term grows proportionally to $1/E_r^2$. This is shown in Fig. 29 middle left panel, while the middle right panel shows the event spectrum at FLArE.

Alternatively, neutrino millicharge can also be probed at FORMOSA [276], a proposed experiment located within the FPF to search for millicharged particles. If neutrino possesses a millicharge, then it will ionize the material and deposit energy as it passes through the detector, resulting in a scintillation signature. FORMOSA is a dedicated detector to detect low-charge scintillation signals consisting of an array of plastic scintillators with multiple layers, sensitive to low-energy deposits down to one single photoelectron. The mean ionization energy loss for a millicharged neutrino travelling through the plastic material can be estimated by Bethe-Bloch formula [279] that goes as $\langle dE/dx\rangle \sim (Q_\nu/e)^2 \times 5\,\text{MeV/cm}$, and

is quite insensitive to the neutrino energy and mass. The average number of photoelectrons produced within a scintillator bar $N_{\rm PE}$ is proportional to the ionization energy deposition, the bar length, and the scintillation light yield. To suppress the background noise in the photomultiplier tubes attached to the scintillation bars that collect the produced photoelectrons, the low-energy scintillation signal candidates are required to have multiple coincidences of hits. To detect a millicharged neutrino, at least one photoelectron in each layer of the scintillator must be observed. The detection probability $P = (1 - \exp(-N_{\rm PE}))^n$ follows the Poisson distribution, where n is the number of layers.

5.4.3 Neutrino Charge Radius

From Eq. (5.2.2), one sees that a non-zero value of charge radius amounts to a shift in the vector term of the neutrino vertex function. Within the SM, only diagonal charge radii are allowed, as generation lepton numbers are conserved. However, some BSM scenarios also allow for off-diagonal charge radii [280–282]. If we only consider diagonal elements in the flavor basis, it was shown in Ref. [250] that this amounts to a modification of the vector coupling constant in Eq. (5.4.2) as,

$$g_V^\ell \to g_V^\ell + \frac{2}{3} m_W^2 \langle r_{\nu_\ell}^2 \rangle \sin^2\theta_w. \tag{5.4.10}$$

This introduces additional linear and quadratic terms in $\langle r_{\nu_\ell}^2 \rangle$ to the cross section in Eq. (5.4.1). Therefore, similar to the neutrino millicharge case, we are sensitive to the sign of $\langle r_{\nu_\ell}^2 \rangle$. Also, note that the antineutrino charge radius contribution comes with a negative relative sign to the above shift [67]. For quarks, this shift is modified by the quark-to-electron electric charge ratio as,

$$g_V^q \to g_V^q - \frac{2}{3} Q_q m_W^2 \langle r_{\nu_\ell}^2 \rangle \sin^2\theta_w. \tag{5.4.11}$$

which modifies the left and right-handed neutral current couplings of the quarks $g_{L/R}^q = (g_V^q \pm g_A^q)/2$ in Eqs. (5.4.3) and (5.4.4).

In the bottom left panel of Fig. 29, we show the DIS cross section rates for a neutrino

scattering off the argon nucleus in the FLArE detector and tungsten nucleus in the FASERν2 detector as a function of the incoming neutrino energy, E_ν. FASERν2 with a target atom with a higher atomic number has more nucleons for the neutrino to scatter off and hence has a higher cross section value. In the presence of a non-zero charge radius, the cross section enhancement is almost uniform across the incoming neutrino energy range. In the bottom right panel, we show the event spectrum as a function of $E_{\rm had}$ at FLArE for a benchmark value of $\langle r^2_{\nu_\ell} \rangle = 5 \times 10^{-30}$ cm^2. At the neutrino energies available at FPF and the values of $\langle r^2_{\nu_\ell} \rangle$ we are sensitive to, it is the quadratic term that is dominant, and we observe an excess in events across the spectrum.

5.5 Sensitivity for Neutrino EM Properties

We are now ready to turn to our analysis. As described in the previous section, both the neutrino magnetic moment and neutrino millicharge would manifest themselves through an enhanced rate of neutrino-electron scattering events with low electron recoil energy. To isolate this effect, we select events within the energy range $E_{\rm thr} < E_r < 1$ GeV. Here we assume a lower energy threshold of $E_{\rm thr} = 30$ MeV for FLArE and 300 MeV for FASERν2. According to Refs. [25, 277], after applying these kinematic cuts, we expect less than $\mathcal{O}(1)$ neutrino-electron scattering events in the SM. Considering statistical uncertainties only, we then set limits on the neutrino magnetic moment and millicharge. Systematic uncertainties are expected to be under control since the neutrino-electron cross section is well understood and the neutrino fluxes can be constrained by the same experiment through a measurement of the event rate of neutrino charged current scattering.

We present projected sensitivity on neutrino magnetic moment and millicharge in the upper part of table 7. The upper bounds are given for different flavors at FASERν2, FLArE, and FLArE-100, considering an integrated luminosity of 3 ab^{-1} at HL-LHC. Note that the bounds are slightly sensitive to the sign of the neutrino millicharge due to the presence of the interference terms.

Neutrino EM Property		FASERν2	FLArE	FLArE-100
μ_{ν_ℓ} $[10^{-8}\mu_B]$	ν_e	1.78	1.35	0.73
	ν_μ	0.67	0.48	0.25
	ν_τ	10.7	6.59	3.08
Q_{ν_ℓ} $[10^{-8}e]$	ν_e	[-13.1 , 8.92]	[-4.03 , 3.21]	[-2.21 , 1.52]
	ν_μ	[-3.92 , 4.12]	[-0.96 , 1.27]	[-0.24 , 0.30]
	ν_τ	[-64.9 , 65.1]	[-17.9 , 17.9]	[-8.33 , 8.36]
$\langle r^2_{\nu_\ell}\rangle$ $[10^{-32}\text{cm}^2]$ Nuclear Scattering	ν_e	[-3.57 , 4.46]	[-3.47 , 4.29]	[-1.43 , 1.55]
	ν_μ	[-0.65 , 0.67]	[-0.62 , 0.64]	[-0.25 , 0.25]
	ν_τ	[-58.9 , 96.1]	[-41.3 , 78.4]	[-17.3 , 54.8]
$\langle r^2_{\nu_\ell}\rangle$ $[10^{-31}\text{cm}^2]$ Electron Scattering	ν_e	[-1.11 , 0.85]	[-1.62 , 1.10]	[-0.54 , 0.47]
	ν_μ	[-0.86 , 1.70]	[-1.03 , 1.79]	[-0.56 , 1.29]
	ν_τ	[-16.4 , 16.6]	[-14.5 , 14.8]	[-7.53 , 8.04]

Table 7: Projected 90% C.L. sensitivity on neutrino electromagnetic properties (μ_{ν_ℓ}, Q_{ν_ℓ}, $\langle r^2_{\nu_\ell}\rangle$) from FASER$\nu$2, FLArE, FLArE-100 detectors for all three flavors, assuming 3 ab^{-1} of integrated luminosity at HL-LHC. For completeness, we also show the charge radius bounds from electron scattering in the last row, which, as expected, are much weaker compared to those from nuclear scattering.

Unlike the other two neutrino properties, the effect of a neutrino charge radius is not confined to a specific energy region. Instead, we search for an increased neutrino neutral current event rate across the whole energy spectrum. For this, we consider both the electron scattering and nuclear scattering channel, where the latter will turn out to be more sensitive due to the significantly larger overall event rate. As this is essentially a precision measurement of the total neutral current scattering rate, it is subject to systematic uncertainties,

which we discuss below.

One major source of systematic uncertainties is associated with the neutrino flux. While the uncertainties on the LHC neutrino flux predictions are currently large [21, 283–285], a measurement of the charged current event rate will constrain the fluxes once the experiment starts taking data. In our analysis, we take this into account by considering the statistical uncertainty expected in the measurement of charged current events as a proxy for the uncertainty on the flux estimates.

Another source of uncertainty is associated with the modelling of the neutrino-nucleus interaction cross section. This includes for example parton distribution functions, quark mass effects, higher order radiative corrections, nuclear shadowing and anti-shadowing effects, the modelling of parton shower and hadronization inside the target nucleus, as well as final state interactions. As for the neutrino fluxes, measurement of charged current neutrino-nucleus interactions at the FPF will provide valuable input to constrain these uncertainties [39, 40] and we will neglect them for the purpose of this study.

Finally, there could be uncertainties arising from the experimental setup, for example, related to energy reconstruction, detection efficiency, particle identification, and event classification. Since the detector designs are still under development, the details on the detector performance are not yet available. However, this also leaves room to consider the signatures under discussion in this study as a benchmark for detector design and optimize them accordingly. In the following, we assume that detector-related uncertainties can be sufficiently reduced to be smaller than the statistical uncertainties of the measurement.

The projected sensitivity on neutrino charge radius, considering statistical uncertainties along with systematic uncertainty coming from the neutrino flux, are presented in the lower part of table 7. As expected, the bounds obtained from the electron scattering signature are much weaker compared to those from nuclear scattering.

The obtained sensitives to the neutrino EM properties are also presented in Fig. 30, alongside existing constraints and relevant benchmark scenarios. Here we show only the

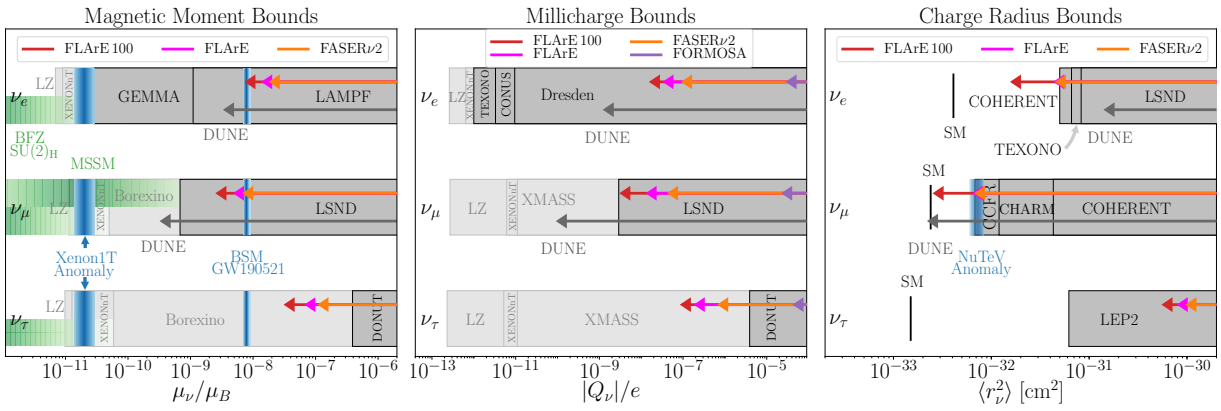

Figure 30: Comparison of experimental bounds on neutrino electromagnetic properties: effective magnetic moment (left), millicharge (middle), and charge radius (right). The projected sensitivity of FASERν2 (orange), FLArE (magenta), and FLArE-100 (red) shown alongside existing accelerator and reactor constraints (dark gray shaded), direct detection limits from solar neutrino flux (light gray shaded) and projections from other proposed searches (gray arrow). The blue-shaded regions correspond to the magnetic moment and charge radius values that explain the XENON1T, NuTeV anomaly, and gravitational waves signal from black hole mergers. The contribution of BSM benchmark models to large magnetic moments is presented in green. FLArE can set the world's leading laboratory-based limits on neutrino magnetic moment and millicharge for tau neutrino, and set the world's leading limit for electron neutrino charge radius. The limits on muon neutrino charge radius for FLArE come within a factor of a few from the SM prediction.

positive bounds, as the negative values are very similar in absolute value. A recent projection on the sensitivity for electron and muon neutrinos at DUNE, as obtained in Ref. [278], is also shown for comparison.

The left panel shows the results for the neutrino magnetic moment. Shown as dark gray shaded regions are current constraints obtained by purely laboratory experiments using reactor and accelerator neutrinos from GEMMA [228], TEXONO [229], LAMPF [232], LSND [230] and DONUT [231]. The light gray shaded region corresponds to measurements using solar neutrinos at Borexino [234], XENONnT [218,236,286] and LZ [236,237]. We can

see that FLArE will be able to provide the leading sensitivity to tau neutrino magnetic moment obtained using a pure laboratory measurement and constrain $\mu_{\nu_\tau} \lesssim 7 \times 10^{-8} \mu_B$. This is due to the large flux of tau neutrino at the LHC location compared with other laboratory neutrino sources.

Throughout the years, a variety of new physics models predicting large neutrino magnetic moments have been proposed [222, 223, 252]. Such scenarios have been revisited recently in Refs. [225, 226]. The authors conclude that models of Dirac neutrinos with large diagonal neutrino magnetic moments do not seem possible anymore unless one is willing to accept it to be fine-tuned. An example of such a scenario was found in Ref. [224] in a scan over the MSSM parameter space, where a muon magnetic neutrino magnetic moment as large as 10^{-9} μ_B was found. In contrast, for Majorana neutrinos, large transition moments can be realized, for example using a $SU(2)_H$ horizontal symmetry [253] or a BFZ model [254]. We illustrate those scenarios as the green region in Fig. 30. In addition, large neutrino magnetic moments have been considered as a solution to the XENON1T anomaly [217] and to explain the existence of black holes in the mass-gap region that have been detected in the gravitational wave event GW190521 [220]. The corresponding regions are marked in blue.

We present the results for neutrino millicharge in the middle panel of Fig. 30. As before, the dark-shaded regions show purely laboratory constraints from DONUT [231, 248], LSND [230, 248], Dresden-II [287], CONUS [288], TEXONO [289, 290], and GEMMA [290, 291]. Upper limits on neutrino millicharge have been also obtained using solar neutrinos by XMASS [292], XENONnT [218, 236, 286] and LZ [236, 237] as shown by the light gray shaded regions. Not included in this figure are additional constraints from astrophysical considerations, since they are subject to additional underlying assumptions and uncertainties compared to pure laboratory constraints. In particular, the neutrino millicharge can have an impact on astrophysical phenomena such as red giant or solar cooling [293], the rotation of magnetized neutron stars [294], and the arrival time of SN 1987A supernova neutrinos [295], resulting in approximate upper limits on the effective charge of electron neutrino in the range

$|Q_{\nu_e}| \lesssim 10^{-14} - 10^{-19}$. Even stronger constraints than astrophysical arguments on the electron neutrino millicharge can be obtained from electric charge conservation in neutron beta decay, along with the experimental bounds on the neutron charge and the non-neutrality of matter giving $|Q_{\nu_e}| \lesssim 10^{-21}e$ [293]. We find that FLArE is potentially capable of providing the most stringent laboratory-based limit on the effective electric charge of tau neutrino, with an upper limit of $|Q_{\nu_\tau}| \lesssim 10^{-7}e$.

Following the study of millicharged particles using the scintillator-based experiment [276, 296], we can expect to bound the neutrino millicharge at FORMOSA to $|Q_{\nu_e}| \lesssim 2.8 \times 10^{-5}e$, $|Q_{\nu_\mu}| \lesssim 2.2 \times 10^{-5}e$, and $|Q_{\nu_\tau}| \lesssim 4.1 \times 10^{-5}e$ with 90% C.L., corresponding to a scintillator detector with quadruple coincidence. These upper bounds on neutrino millicharge, which are weaker than FLArE results, are presented in the middle panel of Fig. 30. These projected sensitivities are almost independent of the neutrino flux, as the sensitivity is limited by the fact that below $Q_\nu \sim 5 \times 10^{-4}e$, the probability of photoelectron production drops significantly. The analysis of FORMOSA with 4 layers is considered almost background free. To demonstrate the sensitivity reach, we also assume zero background for a detector with triple coincidence and find the 90% C.L. upper bounds $|Q_{\nu_e}| \lesssim 0.8 \times 10^{-5}e$, $|Q_{\nu_\mu}| \lesssim 0.5 \times 10^{-5}e$, and $|Q_{\nu_\tau}| \lesssim 1.3 \times 10^{-5}e$. This background-free assumption can in principle be achieved, for example, by using better photomultiplier tubes (PMTs) that have less background noise.

The right panel shows the results for the neutrino charge radius. The dark gray shaded regions are current constraints obtained by purely laboratory experiments using reactor and accelerator neutrinos from COHERENT [287,297], CHARM-II [298], LSND [230], CCFR [299, 300], LEP2 [300], TEXONO [301]. FLArE can set the world's leading limit for electron neutrino and set highly competitive limits for muon neutrino where it comes within a factor of a few from the SM prediction. The deviation of the weak mixing angle from the SM observed by the NuTeV Collaboration [216] could also be interpreted as a measurement of the muon neutrino charge radius $\langle r^2_{\nu_\mu} \rangle = 4.20 \times 10^{-33}$ within 1σ error [300]. The 1σ preferred region

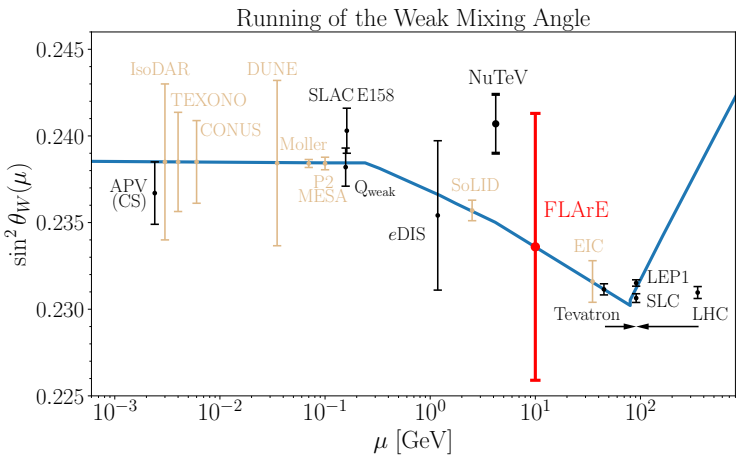

Figure 31: Scale dependence of the weak mixing angle in the $\overline{\rm MS}$ scheme, $\sin^2\theta_W(\mu)$, shown with the existing measurements (black), the expected sensitivity of experiments at FPF (red), and other future experiments (beige). The blue line corresponds to the SM prediction for the running of $\sin^2\theta_W$ with scale μ. For clarity, the Tevatron and LHC points are shifted horizontally on either side.

to explain the NuTeV anomaly is shown by the blue target region. For comparison, DUNE is expected to constrain $|\langle r^2_{\nu_\mu}\rangle| < 2\times10^{-33}$ cm^2 and $|\langle r^2_{\nu_e}\rangle| < 1\times10^{-31}$ cm^2, which is an order of magnitude weaker than the FLArE bound for the electron neutrino. The DUNE projection considered the electron scattering signature, which suffers from lower event rates. A measurement using nuclear scattering at DUNE does not seem promising due to the large nuclear uncertainties in the cross section for GeV energy neutrinos.

5.6 Measurement of the Weak Mixing Angle and the NuTeV Anomaly

The measurement of neutrino interactions at the energies accessible at the FPF provides an opportunity to measure precisely the electroweak parameters. The weak mixing angle, $\sin^2\theta_W$, is one key parameter that parameterizes several measurable observables in the electroweak sector of the SM. The value of $\sin^2\theta_W$ gets radiative corrections and depends on the renormalization prescription [302], where $\overline{\rm MS}$ (modified minimal subtraction) scheme is conventionally employed. One of the best measurements of the weak mixing

angle comes from Z-pole observables [279, 303] (Tevatron, LEP1, SLC, LHC) with an average value of $\sin^2\theta_W(m_Z)_{\overline{\rm MS}} = 0.23125(16)$, comparable to the SM value of $\sin^2\theta_W(m_Z)_{\overline{\rm MS}} = 0.23122(4)$ [279]. At relatively low energy scales, several experimental measurements of weak mixing angle exist (for a review, see Ref. [304]) including the electron-deep inelastic scattering [305] (eDIS), neutrino-nucleus scattering [216] (NuTeV), atomic parity violation [306–309] (APV on cesium), Moller scattering [310] (SLAC E158), elastic electron-proton scattering [311] ($Q_{\rm weak}$), and coherent elastic neutrino-nucleus scattering at COHERENT [312] and Dresden-II [313]. The precise measurement of the weak mixing angle at different energy scales provides a direct probe of new physics beyond the SM [304, 314, 315]. In particular, it will allow one to test the NuTeV anomaly [216]. Using neutrino scattering, the collaboration measured a value of $\sin^2\theta_W$ that was 3σ above the SM prediction at a scale of ~ 4 GeV. A measurement at FPF will shed more light on the running of the weak mixing angle at a similar energy scale. Any change in the weak mixing angle from the SM value, $\sin^2\theta_W \to \sin^2\theta_W + \Delta\sin^2\theta_W$, will result in a shift in the vector coupling constant,

$$g_V^q \to g_V^q - 2Q_q\Delta\sin^2\theta_W. \tag{5.6.1}$$

The phenomenological consequences of this shift are therefore very similar to the study of neutrino charge radius presented in the previous section. We perform a similar analysis to obtain the FLArE expected sensitivity to the weak mixing angle and constrain $\Delta\sin^2\theta_W < 0.0077$ at 68% C.L. The estimate for sensitivity to $\sin^2\theta_W$ in the $\overline{\rm MS}$ scheme at the scale $\mu \sim Q \sim 10$ GeV, which is the typical momentum transfer for a TeV scale energy neutrino at FLArE, is shown in Fig. 31, along with the existing constraints and the running of the coupling predicted by the SM [279, 302, 316]. For comparison, we also show the projected sensitivities to the weak mixing angle from future experiments including DUNE [317], EIC [318], Moller at JLAB [310, 319], MESA-P2 [320], SoLID at JLAB [321], IsoDAR at Yemilab [322], and reactors [323–326] (TEXONO, CONUS).

A precise measurement of the weak mixing angle requires good control over various sys-

tematic uncertainties. These are analogous to the measurement of the neutrino charge radius through nuclear scattering, and we refer the reader to the previous section for a more detailed discussion. As before, we have considered statistical uncertainties as well as uncertainties associated with flux normalization as constrained by charged current measurements in our sensitivity estimate. It is worth noting that the measurement of the weak mixing angle provides a well-motivated benchmark for detector performance requirements that should be considered during detector design.

5.7 Conclusion

The immense flux of neutrinos in the forward region of the LHC provides an excellent opportunity for neutrino physics. This neutrino beam is a powerful source of the most energetic human-made neutrinos for all three flavors. The proposed neutrino detectors at the FPF, FASERν2 and FLArE, can use this neutrino beam to set stringent constraints on neutrino electromagnetic properties and measure the weak mixing angle to percent level precision.

In this chapter, we have presented a detailed phenomenological study on the potential of the FPF experiments to probe the neutrino electromagnetic properties: magnetic moment, millicharge and charge radius. All these scenarios result in an excess of neutral current events that can be observed at these detectors. We first look at neutrino-electron elastic scattering, where in the presence of neutrino magnetic moment and millicharge the excess events are at low electron recoil energies. Focusing on this kinematic region and taking advantage of the huge tau neutrino flux, FPF can set the strongest laboratory-based limits on neutrino magnetic moment and millicharge for tau neutrinos. For neutrino charge radius, better constraints are obtained by looking at the neutral current neutrino DIS process, where the heavier target results in an increased event rate over neutrino-electron elastic scattering. By looking for excess events across the entire spectrum, FPF can set the world's leading limits on the neutrino charge radius for electron neutrinos and, for muon neutrinos, FPF can come

within a factor of a few from the SM prediction. We have summarized our results in table 7 and Fig. 30.

An important test of the SM is the measurement of electroweak parameters at different energy scales. FPF has the potential to measure the weak mixing angle with a precision of about 3% at an energy scale of $\mu \sim 10$ GeV. In Fig. 31, we show the scale dependence of the weak mixing angle along with the FPF measurement, which considers both statistical and flux uncertainties. This is an important test of the SM, especially in light of the NuTeV anomaly. The ability to measure the weak mixing angle with high precision sets an important benchmark for the design of the FPF neutrino detectors.

CHAPTER VI

NEUTRINO UP-SCATTERING VIA THE DIPOLE PORTAL AT FORWARD LHC DETECTORS

6.1 Introduction

The discovery of neutrino flavor oscillations [327] has firmly established the existence of non-zero neutrino masses and mixing. While neutrino mixing parameters have been measured with increasing precision in recent years, much remains unknown about the neutrino sector. Notably, the generation of neutrino masses and mixing requires physics beyond the Standard Model (SM). In these extensions, the SM neutrino fields typically acquire additional interactions. In particular, in most extensions of the SM that account for neutrino mass generation, neutrinos acquire magnetic moments through loop effects [214, 249]. The sizes of these magnetic moments can be related to the neutrino masses themselves in specific models. Searches for neutrino magnetic moments are thus of great importance as our understanding of the neutrino sector continues to grow. In this work, we investigate the ability of LHC neutrino detectors to observe signatures of neutrino magnetic dipole interactions.

From a theoretical perspective, in many neutrino mass models yielding the observed neutrino masses and mixings, the predicted magnetic moments of neutrinos are imperceptibly small; for a review, see Ref. [67]. However, it is possible to construct theories with relatively large neutrino magnetic moments that are consistent with neutrino mass generation [226].

More troubling, perhaps, are strong experimental constraints on neutrino magnetic moments from terrestrial experiments [228, 234] and stellar evolution [328, 329]. These can be evaded, nevertheless, in the case of a significant magnetic dipole interaction between the

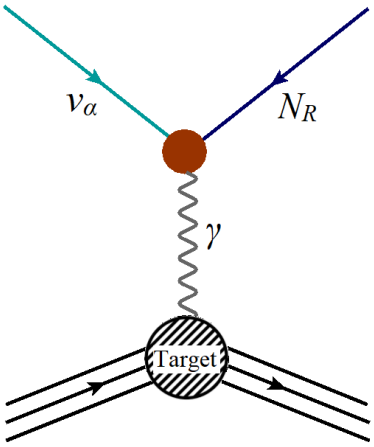

Figure 32: Neutrino up-scattering process arising from dipole portal to HNL.

SM neutrino and heavier *additional* neutrinos. Sterile neutrinos with dipole couplings to the active neutrinos have in fact received renewed attention recently [14,15,240,330–334] in light of the MiniBooNE [335] and XENON1T [217] anomalies, where they have been employed as explanations for observed excesses. Sterile neutrinos can have dipole interactions with strengths that are orders of magnitude above limits on active neutrino transition magnetic moments. Because of kinematic considerations, most laboratory and astrophysical tests for active-sterile neutrino magnetic moments do not apply for larger sterile neutrino masses. For instance, searches involving solar neutrinos typically only probe sterile neutrino masses at the MeV scale.

By contrast, the LHC produces a large flux of TeV-energy mesons at high rapidity, many of which produce neutrinos in their decays. These neutrinos can be used to test for sterile neutrinos up to the GeV scale due to their high energies [186]. Specifically, a sterile neutrino N_R can be produced through the magnetic dipole operator via active neutrino up-scattering, most commonly the electron scattering channel $\nu + e \to N_R + e$. Furthermore, the N_R with a dipole interaction decays characteristically to photons, $N_R \to \nu + \gamma$. Both the production and decay of sterile neutrinos interacting through the dipole coupling differ from those in theories with other interactions between active and sterile states, e.g. the standard fermion portal scenario with renormalizable $\nu - N_R$ mixing through the Higgs. The distinct phenomenology

of sterile neutrinos with magnetic dipole couplings to their active counterparts, together with the higher mass reach that should be achievable in LHC collisions, motivates us to consider search possibilities for such neutrinos at the LHC.

Specifically, the dedicated FASERν [44] and SND@LHC [258] neutrino detectors have recently been approved to collect data during Run 3 at the LHC, making use of the large neutrino flux that emerges at high rapidity from TeV-scale pp collisions. The purpose of this chapter is to evaluate the extent to which forward neutrino detectors at the HL-LHC can be used to search for N_R with magnetic dipole couplings. We will show that new parameter space will be tested for sterile neutrinos in the MeV-GeV mass range, for dipole couplings with characteristic suppression scales in excess of 1000 TeV. While the potential of an upgraded FASERν experiment at the HL-LHC in searching for sterile neutrinos has been considered in Ref. [186], we consider liquid argon facilities with lower detection thresholds, in addition to considering sterile neutrinos coupling to individual flavors and using updated neutrino flux estimates. The sensitivities we will obtain are competitive with limits from other sources of high energy neutrinos such as IceCube [16]. Thus, collider neutrino experiments offer probes of new neutrino states with magnetic dipole couplings in regions that are unlikely to be tested directly in the near future. Additionally, we will demonstrate that HL-LHC neutrino detectors can approach probing active-sterile neutrino magnetic moments that could be responsible for the MiniBooNE excess.

The rest of this chapter is organized as follows. In the next section, we introduce theories of sterile neutrinos with magnetic dipole interactions, providing historical context and enumerating existing constraints. We then describe the HL-LHC neutrino detectors that can be used to search for these sterile neutrinos. Subsequently, we discuss the neutrino-electron up-scattering signal and relevant backgrounds. We use the kinematic properties of N_R production and the SM neutrino scattering backgrounds to construct an analysis and evaluate the LHC reach. Finally, we conclude.

6.2 Motivation

Searches for neutrino magnetic moments were initiated seven decades ago [336], even before the discovery of the neutrino. These searches began to receive more attention three decades ago when an apparent time variation of the solar neutrino flux was detected by the chlorine radio-chemical solar neutrino experiment [337, 338]. Subsequently, several reactor based experiments (such as KRASNOYARSK [339], ROVNO [340], MUNU [341], TEXONO [342], and GEMMA [228]), accelerator based experiments (such as LAPMF [232] and LSND) and solar neutrino experiments (such as Borexino [234]) have searched for neutrino magnetic moments by studying $\nu_e - e$ scattering. Moreover, the investigation of neutrino magnetic moments has become even more exciting and relevant today since it has the potential to address multiple recently observed anomalies, notably the excess of electron recoil events at XENON1T [217] (see Refs. [14, 226, 240] for explanations), the muon $g-2$ anomaly [343] (see Ref. [227] for explanation) and the MiniBooNE anomaly [335] (see Refs. [15,330–334] for explanations). However, it is important to note that interpretations of the XENON1T excess and MiniBooNE anomaly via transition magnetic moments between the active neutrinos become questionable due to stringent astrophysical limits, $|\mu_\nu| \leq 1.5 \times 10^{-12}\mu_B$ (95% CL), from red giants and horizontal branch stars [344–346]. These limits arise from plasmon decays within stars into two neutrinos leading to additional energy loss which affects stellar evolution [328,329]. While these limits can be evaded by adding further neutrino interactions such that the neutrinos are trapped inside stars [226], here we restrict ourselves to the single BSM interaction from the magnetic dipole operator, and take astrophysical limits seriously. Nevertheless, these limits can be relaxed for sterile neutrinos with dipole interactions with the active neutrinos, if the sterile neutrinos are sufficiently heavy that plasmons do not have enough phase space to decay back to them. For this reason, we focus on relatively heavy sterile neutrinos with transition magnetic moments involving their active counterparts.

At the effective field theory level, an active to sterile neutrino transition magnetic moment

can be described by an operator of the form

$$\mathcal{L}_{dipole} \supset \frac{1}{2}\mu_\nu^\alpha \bar{\nu}_L^\alpha \sigma^{\mu\nu} N_R F_{\mu\nu} \tag{6.2.1}$$

where μ_ν^α denotes the strength of the active to sterile transition neutrino magnetic moment, $F^{\mu\nu}$ indicates the electromagnetic field strength tensor, ν_L^α and N_R represent left-handed (active) and right-handed (sterile) neutrino fields respectively, and α is a flavor index.

The Lagrangian term (cf. Eq. 6.2.1) for the "neutrino dipole portal" is valid up to a cut-off energy scale Λ, where the active to sterile transition magnetic moment μ_ν^α is anticipated to be of order $1/\Lambda$. It is worth noting that Eq. 6.2.1 is not $SU(2)_L$ gauge invariant. Therefore, an interpretation of μ_ν^α above the electroweak scale requires a Higgs insertion so that the neutrino dipole interaction described in Eq. 6.2.1 is really a dimension-6 operator, i.e, $\mu_\nu^\alpha \sim \frac{ev_{EW}}{\Lambda^2}$. To describe the new physics associated with the operator in Eq. 6.2.1 above the EW scale, one can write the $SU(2)_L$ invariant possibilities

$$\mathcal{L}_{dipole} \supset \frac{c_B}{\Lambda^2} g' B_{\mu\nu} \bar{L}_L^\alpha \tilde{H} \sigma^{\mu\nu} N_R + \frac{c_W}{\Lambda^2} g W_{\mu\nu}^a \bar{L}_L^\alpha \sigma^a \tilde{H} \sigma^{\mu\nu} N_R \tag{6.2.2}$$

where the gauge couplings associated with $SU(2)_L$ and $U(1)_Y$ are g and g' respectively, $W_{\mu\nu}^a$ and $B_{\mu\nu}$ denote the $SU(2)_L$ and $U(1)_Y$ field strength tensors, Λ is the cutoff scale, and σ^a are Pauli matrices. After EW symmetry breaking (with the Higgs vacuum expectation value v_{EW}), these operators lead to flavor-specific neutrino magnetic moments of the form

$$\mu_\nu = \frac{\sqrt{2} e v_{EW}}{\Lambda^2} \left(c_B + c_W\right). \tag{6.2.3}$$

Now, in general, in order to achieve large transition magnetic moments in various ultraviolet extensions of the SM, one would expect large contributions to active neutrino masses since both the magnetic moment and mass operators are chirality-flipping. The typical induced Dirac mass term $m_{\mu N}$ goes as $\mu_\nu \Lambda^2$, or equivalently

$$\frac{\mu_\nu}{\mu_B} \sim \frac{2 m_e m_{\nu N}}{\Lambda^2} \tag{6.2.4}$$

In the absence of any additional symmetries, one would thus require substantial fine-tuning to get large neutrino magnetic moments while being consistent with the measured active

neutrino masses. In order to generate neutrino magnetic moments, at least some of the particles within the loop must be electrically charged. Typically, experimental searches disfavor such new charged particles of mass below ~ 100 GeV. A naive estimate from Eq. 6.2.4 suggests that for a new physics scale Λ of 100 GeV, a neutrino magnetic moment $\mu_\nu = 10^{-11}\mu_B$ corresponds to a neutrino mass of 0.1 MeV, which is six orders of magnitude higher than the observed active neutrino masses.

In order to avoid this conundrum, Voloshin suggested [221] a new $SU(2)_\nu$ symmetry which transforms ν into ν^c. As a Lorentz scalar, the neutrino mass operator is symmetric and thus forbidden under this new exchange symmetry, while the neutrino magnetic moment operator, a Lorentz tensor, is anti-symmetric and thus allowed under the $SU(2)_\nu$ symmetry. It is quite important to mention that this new symmetry is hard to implement [222], since this new $SU(2)_\nu$ symmetry does not commute with the Standard Model. Several aspects of model-building are summarized in Refs. [14,15,222,226,253]. A slightly different mechanism dubbed "spin-symmetry" has also been used to enhance the dipole moment μ_ν while suppressing new physics contributions to the active neutrino mass contribution, as prescribed in Refs. [226, 254,347]. This is another unique way to achieve large transition magnetic moments between active and sterile neutrinos. For the rest of our analysis, we shall be agnostic regarding the potential link between the magnetic moment and neutrino masses.

Here, we investigate a promising method of detecting active to sterile transition neutrino magnetic moments by looking at electron recoils from neutrino up-scattering at the forward LHC detectors. Intriguingly, for large μ_ν, the heavy neutral lepton (HNL) scattering rate ($\propto 1/E_{rec}$) gets enhanced at low electron recoil. With recoil energy thresholds that can be below 100 MeV for liquid argon, the forward LHC detectors are ideal places for searching for neutrino magnetic moments. We now briefly describe these detectors before turning to our analysis.

6.3 Neutrino Detectors at the LHC

We consider a future FPF [39, 207, 348, 349] located 620 m downstream from the ATLAS interaction point (IP), and two possible neutrino detectors at the FPF site, following Ref. [25]. We assume that the FPF detectors would be centered around the collision axis in ATLAS. We expect that including the beam crossing angle would lead to only a mild reduction in the neutrino flux, as has been studied previously [21] for other forward detectors including FASERν and SND@LHC. For all detectors, we assume an integrated luminosity of 3000 fb^{-1}.

The first, FASERν2, would be an emulsion detector similar to but larger than the currently approved FASERν detector [44] in the TI12 tunnel 480 m from the IP. The main strength of emulsion detectors is the spatial precision with which charged tracks can be reconstructed. Photons also convert to e^+e^- pairs leading to electromagnetic showers, but neutral hadrons such as neutrons are not visible. While emulsion detectors do not have timing capabilities, we assume that timing layers could be placed between the emulsion plates to gain temporal resolution. This is necessary in order to veto backgrounds induced by muons, and such a design is being incorporated in SND@LHC [258]. In order to pass through enough plates to create a signature, we require electrons to have a minimum energy of 300 MeV. We take a detector made of tungsten that has transverse dimensions 0.5 m x 0.5 m and is 2 m in depth along the collision axis, i.e. a mass of approximately 10 tonnes.

Liquid argon detectors offer lower detection thresholds and better timing capabilities than emulsion detectors and have been employed in current and future neutrino experiments, e.g. in the case of the Short-Baseline Neutrino Program at Fermilab [261] and DUNE [262]. Thus, we also consider a liquid argon detector, FLArE. We consider 10 and 100 tonne versions of this detector, with dimensions 1 m x 1 m x 7 m and 1.6 m x 1.6 m x 30 m respectively. Consistent with previous studies in liquid argon detectors [25, 264, 350, 351], we take a threshold of 30 MeV for charged tracks. Because the neutrinos impinging on the FPF are quite collimated around the beam axis, it should be noted that the number of

interactions in FLArE-100 relative to that in FLArE-10 does not scale completely with the detector mass. In particular, more energetic neutrinos tend to emerge at higher rapidity, and so the neutrino flux increases up to an angle of approximately $\Lambda_{\rm QCD}/E_p$ where E_p is the proton energy, which corresponds to a rapidity of $\eta \approx 10$. At larger angles from the beam axis, the neutrino flux tends to be smaller and consists of less energetic neutrinos [21]. For detectors centered on the beam axis, then, the largest number of interactions per unit mass is expected for denser detectors, i.e. FASERν2.

We emphasize the importance of timing information to reduce muon-induced backgrounds. In particular, muons can emit photons through bremsstrahlung which subsequently undergo pair conversion. If one of the resulting e^+/e^- is missed, the event would mimic our neutrino-electron scattering process. With timing, however, these events could be associated with the accompanying muon and vetoed. MicroBooNE [352], which uses the same Liquid Argon Time Projection Chamber as would be used in FLArE, can achieve a time resolution of $\mathcal{O}$(ns). For further details see Ref. [25], which discusses the prospects for rejecting backgrounds from muons for a single electron recoil signature in the context of dark matter detection, as well as Ref. [39].

6.4 Signal

With the addition of the dipole portal (Eq. 6.2.1) to the SM Lagrangian, the N_R can be produced in neutrino scattering via photon exchange, $\nu_L^\alpha e^- \to N_R e^-$ as shown in Fig. 32. The up-scattering results in a single EM shower from the recoiling electron with no other visible tracks. The differential cross-section for this process is given by [14, 240]

$$\frac{d\sigma(\nu_L^\alpha e^- \to N_R e^-)}{dE_{rec}} = \alpha \left(\mu_\nu^\alpha\right)^2 \left[\frac{1}{E_{rec}} - \frac{1}{E_\nu} + M_N^2 \frac{E_{rec} - 2E_\nu - M_e}{4E_\nu^2 E_{rec} M_e} + M_N^4 \frac{E_{rec} - M_e}{8E_\nu^2 E_{rec}^2 M_e^2}\right], \quad (6.4.1)$$

where E_ν is the energy of the incoming neutrino, E_{rec} is the energy of the outgoing electron, and M_e and M_N are the electron and N_R masses, respectively. The first term in Eq. 6.4.1

results in an enhancement in signal cross-section at low recoil energies, a characteristic feature of neutrino magnetic moment interactions that we utilize here to differentiate signal from background.

In addition to the recoil energy, the angle of the outgoing electron could also be considered as an observable. However, in the kinematic region of interest where the outgoing electron is relativistic, its recoil energy and angle are strongly correlated. Ref. [25] found that this angle could be used to discriminate against neutrino nuclear interaction backgrounds in dark matter scattering, but we will find below that an energy cut is sufficient.

The relatively heavy mass of the sterile neutrino means that eventually it will decay into an active neutrino and a photon, potentially leading to another signal. The decay length of N_R in the lab frame is given by [15, 186]

$$l_{decay} = \frac{16\pi}{\mu_\nu^2 M_N^4}\sqrt{E_N^2 - M_N^2}. \tag{6.4.2}$$

where E_N is the energy of the outgoing N_R. Depending on the coupling and mass of the N_R, it can decay promptly or at a displaced location within the detector. We define l_{prompt} to be the minimum decay length for the decay vertex to appear displaced, and hence distinguishable from the production vertex. Using the decay length l_{decay}, detector length $l_{detector}$, and l_{prompt} we define 3 regions of interest:

- $l_{decay} > l_{detector}$: N_R decays outside the detector and the decay vertex is not observable. The signature is the single electron recoil in the production process.

- $l_{prompt} < l_{decay} < l_{detector}$: The decay vertex is sufficiently displaced from the production vertex and results in "double-bang" events [16, 19, 353] where both vertices in coincidence provide the signal signature.

- $l_{decay} < l_{prompt}$: The decay occurs promptly, leading to an electron and photon produced at the same point. Note that the photon travels a distance of the order of one mean free path before pair-converting into a visible e^+e^- pair.

We take l_{prompt} to be the mean free path λ for pair production by the photon in the detector material, which is closely related to the radiation length [327, 354]. For FASERν2 (FLArE) which is made out of liquid argon (tungsten), this distance is 4.5 mm (18 cm). We assume that the decay will appear displaced if the decay length of N_R is more than the mean free path of photons in the detector material. Conversely, if the N_R lifetime is shorter than λ, the tracks produced when the photon undergoes pair conversion will not be sufficiently distant from the production vertex to conclusively determine that the photon originated at a different location than the electron recoil.

Of the possible signatures above, we choose to focus on those with a single electron track emerging from the production vertex, with no other nearby activity in the detector. The SM background for this signature at FPF detectors has been considered previously and found to be small [25]. We allow for the double-bang possibility where in addition to the electron emanating from the N_R production point, the N_R decays to a photon at a displaced location within the detector. Such a requirement could be imposed on top of the single electron recoil search and should have lower background than a search for N_R production alone. On the other hand, we ignore events where the N_R decays promptly, which could have different backgrounds than the ones we consider in the next section.

We also note that neutrino up-scattering off electrons is not the only possible production mechanism at these detectors. The active neutrino can also undergo *quasi-elastic scattering* off a proton in the nucleus, $\nu_L^\alpha p \to N_R p$. The ejected proton from the nucleus will leave a single charged track in the detector. Coherent scattering off the nucleus, $\nu_L^\alpha X_Z^A \to N X_Z^A$ via photon exchange, is also possible. The low momentum transfer favored by the massless mediator in such reactions makes the nuclear recoil of these heavier targets more difficult to detect. It may be possible, however, to search for N_R production in these channels if the N_R decays inside the detector [186]. Because our focus is on signatures involving visible up-scattering, we do not consider these alternate production mechanisms. Having described the signal, we now turn to a description of the SM backgrounds to electron recoil events.

6.5 SM Backgrounds

$$\frac{d\sigma(\nu_\alpha e^- \to \nu_\alpha e^-)}{dE_{rec}} = \frac{G_F^2 m_e}{2\pi}\left[(g_V^\alpha + g_A^\alpha)^2 + (g_V^\alpha - g_A^\alpha)^2(1 - \frac{E_{rec}}{E_\nu})^2 + ((g_A^\alpha)^2 - (g_V^\alpha)^2 m_e \frac{E_{rec}}{E_\nu^2})\right] , \tag{6.5.1}$$

$$\text{with} \quad g_V^e = 2\sin^2\theta_w + \frac{1}{2} \ , \ g_A^e = \frac{1}{2}, \quad g_V^{\mu,\tau} = 2\sin^2\theta_w - \frac{1}{2} \ , \ g_A^{\mu,\tau} = -\frac{1}{2}. \tag{6.5.2}$$

The couplings are different for ν_e to include charged current interactions. Unlike Eq. 6.4.1 for scattering through the dipole operator, which is enhanced at low recoil energy due to the massless photon mediator, the SM background is approximately independent of the recoil energy for E_{rec} much smaller than E_ν. In the left panel of Fig. 33, we show the differential cross-section $d\sigma/dE_{rec}$ for the signal and background for three benchmark values of μ_{ν_α}, taking a fixed incoming neutrino energy of 1 TeV and $M_N = 10^{-1}$ GeV. The SM background has a flat distribution, whereas the signal shows the characteristic enhancement at low recoil energies. This also illustrates the advantage of having a detector with a lower energy threshold like FLArE (30 MeV).

We take the forward neutrino flux expected at the LHC from Ref. [21]. We do not consider systematic uncertainties in the flux, given that it can be measured independently from CC interactions [44]. Despite a lower flux of ν_es relative to ν_μ expected in the forward direction, the dominant contribution to the background comes from ν_e CC scattering due to the larger rates for CC interactions. The signal rates, on the other hand, depend only on the total incoming ν flux as the cross-section is the same for all 3 flavors. The number of background and signal events as a function of the electron recoil energy is obtained by convoluting the incoming neutrino flux with the respective differential cross-sections and the detector geometry. The minimum incoming neutrino energy, E_ν^{min}, required to produce an electron with recoil energy E_{rec} is given by [14],

$$E_\nu^{min}(E_{rec}) = \frac{1}{2}\left[E_{rec} + \sqrt{E_{rec}^2 + 2m_e E_{rec}}\right] \times \left(1 + \frac{M_N^2}{2m_e E_{rec}}\right) \tag{6.5.3}$$

	SM backgrounds			$\mu_{\nu_e} = 10^{-7}\mu_B$			$\mu_{\nu_\mu} = 10^{-8}\mu_B$			$\mu_{\nu_\tau} = 10^{-7}\mu_B$		
Detector	no cuts	loose	strong	no cuts	loose	strong	no cuts	loose	strong	no cuts	loose	strong
FASERν2	86	2.5	0.1	480	134.1	39	30	8.6	2.5	12.7	3.6	1.0
FLArE-10	51	2	0.1	320.5	144	79.6	22.3	10.4	5.9	13.1	5.9	3.3
FLArE-100	332	15	1.0	2285	1037	575.7	165.1	78.2	44.6	126.1	57.2	31.8

Table 8: SM background and signal events with and without kinematic cuts at FPF detectors. Here, the SM background includes only the neutrino induced backgrounds from scattering off electrons (both NC interactions for all 3 flavors, and CC interactions for ν_e), as described in the text. Signal events are for $\mu_{\nu_e} = 10^{-7}\mu_B$, $\mu_{\nu_\mu} = 10^{-8}\mu_B$ and $\mu_{\nu_\tau} = 10^{-7}\mu_B$, and $M_N = 10^{-1}$ GeV. Loose (strong) cuts correspond to $E_{thresh} < E_{rec} < 10$ (1) GeV. Only signal events where the N_R does not decay promptly are considered.

where the SM background corresponds to $M_N = 0$. The right panel of Fig. 33 shows the expected number of SM background and signal + background events per bin for $\mu_{\nu_\alpha} = 10^{-8}\mu_B$ and $M_N = 10^{-1}$ GeV at FLArE-10. It is the excess events at lower recoil energies that constitute the signature for our BSM scenario. We are prevented from going to very low recoil energies, $E_{rec} \leq 30$ (300) MeV, due to detector thresholds in FASERν2 (FLArE) but, as shown below, are still able to probe a large portion of the parameter space that is currently unconstrained.

Our background consists of SM interactions, with no incoming charged tracks and a single outgoing electron. These can result from photons emitted through bremsstrahlung off of muons produced either at the ATLAS interaction point or through collisions with the LHC infrastructure [25], when one of the electron/positron tracks from the photon pair conversion is missed. Similarly, muons can directly produce e^+e^- pairs when scattering. These background events can be effectively vetoed by the timing capabilities of the detectors in the FPF [207]. In what follows we ignore such muon-induced backgrounds.

The other main source of background is neutrino interactions, which can give the same single electron recoil as our signal. This includes neutral current (NC) neutrino interactions via the Z for all flavors, and ν_e charged current (CC) interactions via the W. The SM neutrino differential cross-section is given by [226]

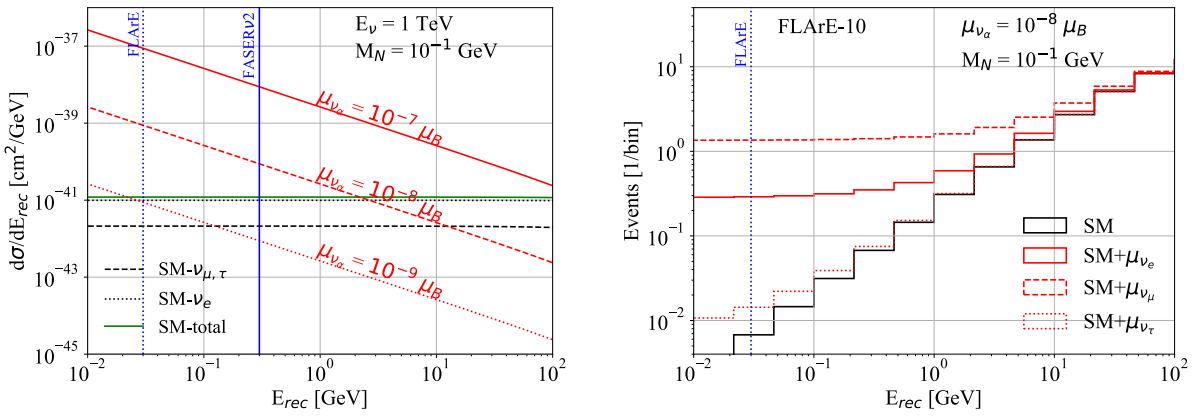

Figure 33: *Left*: $d\sigma/dE_{rec}$ for the SM background components (black) and total (green), and signal (red) for various benchmark values of the dipole magnetic moment μ_{ν_α}, with $E_\nu = 1$ TeV and $M_N = 10^{-1}$ GeV. The differential cross-section is the same for all 3 flavors. The solid (dotted) vertical blue lines show the anticipated detector thresholds at FASERν (FLArE) of 300 (30) MeV. The signal cross-section is enhanced at low recoil energies, making FLArE a more promising detector with its lower energy threshold. *Right*: Expected number of events for SM background (black), and signal + background (red) at FLArE-10 for ν_e (solid), ν_μ (dashed), and ν_τ (dotted). For all the signal lines, we use $\mu_{\nu_\alpha} = 10^{-8}\mu_B$ and $M_N = 10^{-1}$ GeV.

Backgrounds can also arise from electron neutrino charged current interactions with nuclei. These interactions include quasi-elastic, resonant, and deep inelastic scattering. Quasi-elastic scattering events can reproduce our signature of interest, but the outgoing electron energy is quite large because it is comparable to the incoming neutrino energy. Since the dipole portal interaction favors low momentum transfer in $\nu e \to N_R e$, the outgoing electron for our signal tends to be much less energetic than in the ν_e quasielastic scattering backgrounds. Furthermore, as our signal consists of a single EM shower with no additional visible activity, significant portions of the resonant and deep inelastic scattering backgrounds are removed by the requirement that there be only one outgoing track. Ref. [186] considered single electron recoils from all types of ν_e nuclear charged current events, finding that with

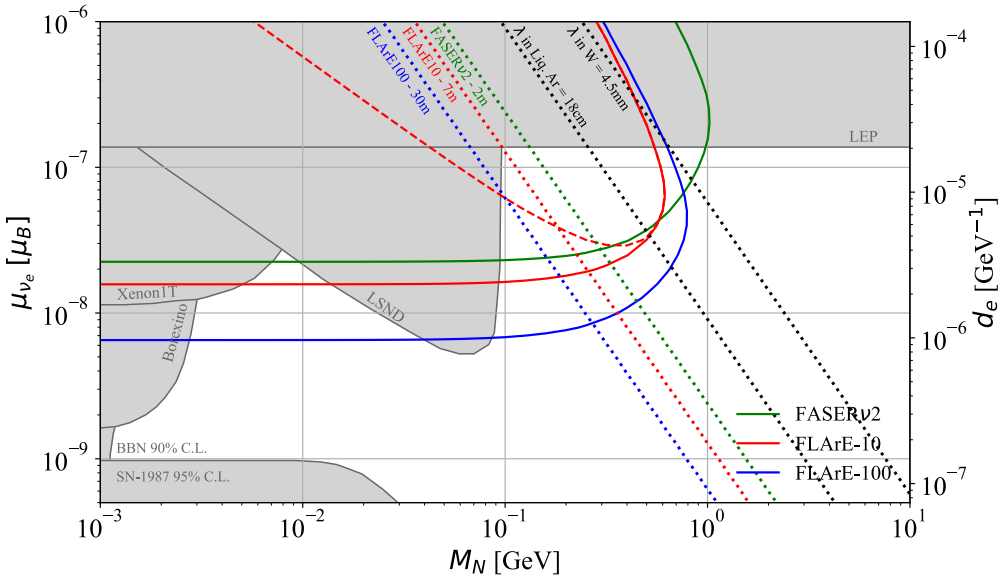

Figure 34: Projected sensitivity at 90% C.L. for μ_{ν_α} at FASERν2 (green solid), FLArE-10 (red solid), FLArE-100 (blue solid) for 3 ab^{-1} luminosity after applying the strong cuts in the text. The gray shaded region indicates current constraints coming from terrestrial experiments such as Borexino [12–14], XENON1T [14], LSND [15], MiniBooNE [15], CHARM-II [16,17], NOMAD [15,18], and LEP [15] as implemented in [19]. Astrophysical constraints from SN-1987 [15] and BBN [14] are also shown. The dotted lines are for constant decay lengths of N_R in the lab frame, corresponding to various lengths of interest. The colored dotted lines show $l_{decay} = l_{detector}$ for various detectors assuming $E_N = 100$ GeV, and the black dotted lines show $l_{decay} = \lambda$ in various detector materials. For comparison, we also show the 90% C.L. line coming from considering only double bang events at FLArE-10 (red dashed line), assuming zero background. The brown shaded box is the Region Of Interest (ROI) where N_R can explain the MiniBooNE anomaly [20].

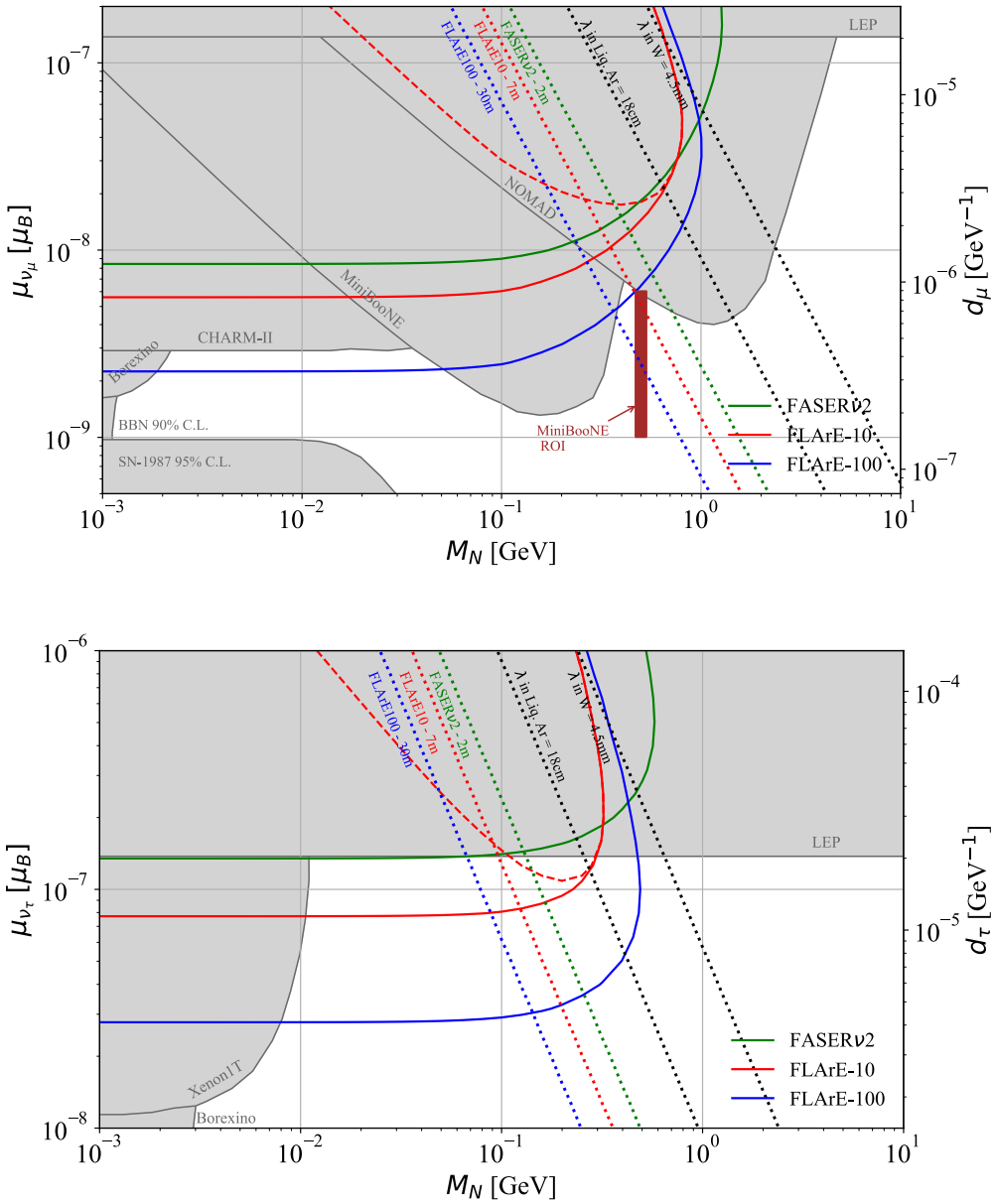

Figure 35: Same as Fig. 34 but for ν_μ (top) and ν_τ (bottom).

cuts on the electron kinematics and a veto on additional activity, these backgrounds can be brought down to $\mathcal{O}(10)$ events over the entire HL-LHC. Compared to Ref. [186], we will employ tighter upper bounds on the electron energy, of order 1 GeV. With these cuts, we expect that ν_e nuclear scattering backgrounds can be reduced to very small levels without an angular requirement, and do not consider them further. Similarly, neutrino neutral current interactions with nuclei that produce photons or pions have the potential to reproduce our signal if a photon is misidentified as an electron; we expect these backgrounds to be smaller than those from charged current interactions. A detailed experimental analysis would require further study of these subdominant neutrino-nucleus backgrounds.

6.6 Results

Motivated by the right panel of Fig. 33 we employ a simple cut and count analysis. By placing an upper cut on the recoil energy of the electron we focus on a range of E_{rec} where the signal is most enhanced. We define loose (strong) cuts as $E_{threshold} < E_{rec} < 10$ (1) GeV with the FASERν2 threshold at 300 MeV, and FLArE threshold at 30 MeV. In Table 8 we present the effect of these cuts on the expected number of background and signal events at FASERν2, FLArE-10, and FLArE-100 detectors for various benchmark values of μ_{ν_α} at $M_N = 10^{-1}$ GeV. Here we only consider signal events where the N_R does not decay promptly as mentioned above. We see a 2–3 order of magnitude suppression of the SM backgrounds whereas the signal count is suppressed by at most an order of magnitude. This simple but effective analysis strategy results in competitive bounds on the neutrino dipole transition magnetic moment at FASERν2, and FLArE-10 (100) detectors.

We show our results for ν_e, ν_μ, and ν_τ in Figs. 34 and 35 in the $M_N - \mu_{\nu_\alpha}$ plane. The sensitivity reach at 90% CL obtained using the strong cuts defined above are shown for FASERν2 (solid green), FLArE-10 (solid red), and FLArE-100 (solid blue). This corresponds to a background-free search for FASERν2 and FLArE-10, and 1 background event for FLArE-100. For all three neutrino flavors, FPF detectors can probe parameter space that is currently

unconstrained. Below $M_N \sim 10^{-1}$ GeV the sensitivities are approximately independent of M_N because the only dependence of Eq. 6.4.1 on the N_R mass is in terms suppressed by powers of M_N^2/s; with incoming TeV-scale neutrinos, the CM energy $\sqrt{s} = \sqrt{m_e^2 + 2E_\nu m_e}$ can typically reach around a GeV. We find that the FPF detectors can reach down to dipole coupling strengths of a few $10^{-9}\mu_B$ for μ_{ν_e}, $\sim 10^{-9}\mu_B$ for μ_{ν_μ}, and a few $10^{-8}\mu_B$ for μ_{ν_τ}. Starting at $M_N \sim 10^{-1}$ GeV, the sensitivity weakens. This is because when M_N is larger than $\sqrt{s}$ it becomes kinematically impossible to produce the N_R [14]; the actual value of M_N that can be produced for a given E_ν is slightly lower than $\sqrt{s}$ after requiring the electron to have a minimum energy to be detectable [240].

In principle, the electron recoil from N_R production can be searched for in isolation. However, if the N_R decays inside the detector, the coincident photon could provide a striking signature. To show the effects of N_R decay, we plot 90% exclusion contours assuming a background-free search for double bang events in FLArE-10 (dashed red) in Figs. 34 and 35. These lines overlap with the solid red contours from the single electron recoil search at N_R masses near the kinematic threshold because the N_R lifetime is typically smaller than the detector size. In this case, all electrons produced through the up-scattering of neutrinos to N_R are accompanied by a later photon from the N_R decay. To guide the eye, we show where the N_R lab frame lifetime equals the detector depth, $l_{decay} = l_{detector}$, assuming that it was produced with energy 100 GeV. This energy is typical of the incoming neutrinos; for our signal of interest, the collision is elastic and the outgoing electron is much less energetic than the neutrino, so the N_R energy is approximately equal to E_ν. We show these sample N_R lab frame lifetime contours for FASERν2 (dotted green), FLArE-10 (dotted red), and FLArE-100 (dotted blue).

We also plot lines corresponding to $l_{decay} = \lambda$ (dashed black) for tungsten and liquid argon, again taking a fixed N_R energy of 100 GeV. This allows us to see the three separate regions of $M_N - \mu_{\nu_\alpha}$ space where the N_R decay is prompt, displaced, or unobservable. For instance, in the case of FLArE-10 (red lines), $l_{decay} > l_{detector}$ is the region to the left of the dashed red line

where N_R decays outside the detector and the decay vertex is not visible. Between the dashed red line and the dashed black line corresponding to $\lambda = 18$ cm, $l_{prompt} < l_{decay} < l_{detector}$. Here, the decay vertex is sufficiently displaced to be differentiated from the production vertex. To the right of this dashed black line, the decay of N_R is prompt and the signal would contain an electron and photon. Since we do not consider such events, we see a loss in sensitivity at large dipole moments and masses where the typical N_R lifetime is smaller than λ in the detector material.

We proceed to compare our limits to existing bounds on the dipole portal [1]. The gray shaded region in Figs. 34 and 35 shows current constraints from terrestrial experiments as shown in Ref. [19]. Borexino [12–14] constrained modifications to the electron recoil spectrum from solar neutrinos scattering through magnetic dipole interactions. XENON1T [14, 356] placed constraints on the dipole portal from neutrino interactions with nuclei, and CHARM-II [16, 17] studied elastic scattering of ν_μ, $\overline{\nu}_\mu$ off electrons to place constraints on μ_{ν_μ}. LSND and MiniBooNE [15, 20, 230] placed bounds on $\mu_{\nu_{e,\mu}}$ from N_R decays producing photons which could appear as single tracks for small opening angles; the curves shown are 95% CL limits. Similarly, the NOMAD constraint [15, 18, 357] comes from a search for single photon production. Unlike searches for N_R production through up-scattering including the FPF limits that are the subject of this work, constraints from searches for N_R decay typically get weaker at low M_N because the N_R lifetime in the detector frame must be comparable to the detector size. Going beyond neutrino experiments, LEP [15, 358–361] places a limit on our scenario of interest from monophoton searches. Finally, there are astrophysical and cosmological bounds, notably from Supernova 1987A [15] which excluded a portion of the parameter space based on the rate of energy loss associated with N_R production. We note the existence of recent work suggesting that this bound may be affected by modeling of

[1] During the preparation of this manuscript, Ref. [355] appeared which placed constraints on flavor-universal neutrino magnetic moments, based on recently released CENNS 10 and COHERENT data. Limits from coherent neutrino-nucleus scattering are complementary to our results at low N_R masses.

supernovae [362]. Other astrophysical bounds come from BBN [14], as the N_R can affect the expansion rate of the universe during nucleosynthesis and hence the different abundances for heavier elements [2].

For the case of a dipole coupling between N_R and ν_μ, we also show the region of parameter space which could explain the MiniBooNE anomaly [20] as the brown shaded box in the top panel of Fig. 35. A 100 ton liquid argon detector at the FPF would nearly probe the relevant region of interest. We also note that the FPF neutrino detectors will be able to narrow the gap between neutrino-based searches and supernova constraints in the low mass region for dipole couplings to electron and muon neutrinos.

To place our study of neutrino magnetic moments at the forward LHC detector in a more global context, we mention below projected sensitivities at certain future proposed experiments. Ref. [19] projected bounds at DUNE from searches for N_R decay to photons within the near (far) detector for $\nu_{e,\,\mu}$ (ν_τ), with or without an accompanying signal from proximate N_R production. Similarly, the expected bounds from N_R decay at the Fermilab Short-Baseline Neutrino program (for magnetic moments with $\nu_{e,\,\mu}$ only) and SHIP [364] have been computed [15]. In addition, the double-bang signature from N_R production and decay has been investigated in the context of IceCube [16]. All of these limits are complementary to ours. Unlike those based on pure up-scattering, they get somewhat less constraining for light N_R due to the requirement that the N_R decay inside the detector. Additional future constraints are possible at low N_R masses, below roughly 10 MeV. In particular, SuperCDMS [365] could limit the dipole portal by considering solar neutrinos up-scattering off nuclei to sterile states [366]. Borexino and Super-Kamiokande also constrain the dipole portal for light N_R due to the possibility of solar neutrinos up-scattering within the Earth and then decaying within neutrino detectors [367–369]. Finally, Ref. [370] studies transi-

[2]During the preparation of this work, PandaX-4T released results [363] which provide the leading DM-nucleon spin-independent cross-section limits. These could be recast to place further bounds on neutrino magnetic moments.

tion neutrino magnetic moments using future coherent elastic neutrino-nucleus scattering (CEνNS) or elastic neutrino-electron scattering (EνES) experiments. A particular strength of the present analysis is that competitive new limits can be achieved across a wide range of N_R masses, both for light N_R due to the lack of a requirement for the N_R to decay near its production point, and for heavy N_R because of the high energies of LHC neutrinos.

6.7 Conclusions

The existence of nonzero neutrino magnetic moments is implied by neutrino masses, and the need for BSM physics in the neutrino sector suggests the importance of searches for magnetic moments in the neutrino sector that could be larger than the typical expectation given the neutrino mass scale. In particular, in the presence of heavy right-handed neutrinos, dipole interactions between the active neutrinos and new states face relatively few constraints due to kinematic limits on the production of the sterile states. In this work, we have demonstrated the capability of neutrino detectors at the LHC to search for these couplings.

Magnetic dipole interactions between active and sterile neutrinos affect neutrino scattering at low momentum transfer. We have studied the ability of the proposed FPF neutrino detectors FASERν2 and FLArE to constrain these interactions through neutrino-electron scattering. We find that HL-LHC forward neutrino detectors can test significantly smaller dipole interactions than current limits for all three flavors. Below 10 – 100 MeV, the searches here will help to close the gap between oscillation searches and supernova bounds. In the case of interactions with the muon neutrino, FLArE-100 could also approach sensitivity to new states that could explain the MiniBooNE excess through the dipole portal. We emphasize the importance of low detection thresholds; FLArE often performs better than FASERν2 with similar assumed detector masses, due to a much lower electron threshold which can make up for a mildly smaller number of events.

Neutrino electromagnetic interactions are interesting from both a theoretical and experimental standpoint, and we have demonstrated the utility of LHC neutrino detectors to search

for them. The unique energy spectrum of neutrinos in the forward region of the LHC enables stronger probes than from existing facilities. We expect that more opportunities remain in testing new physics with SM neutrino processes at the LHC.

CHAPTER VII

DISCOVERING DARK MATTER AT THE LHC THROUGH ITS NUCLEAR SCATTERING IN FAR-FORWARD EMULSION AND LIQUID ARGON DETECTORS

7.1 Introduction

A primary goal of high-energy colliders is to produce dark matter (DM) particles. If DM is heavy with a mass near the weak scale, its signature is missing transverse energy, which has been studied in detail for decades. If DM is light, however, such searches are typically ineffective (as are conventional direct detection searches), and alternative search strategies, experiments, and facilities are needed.

In this study, we consider extremely simple models of light DM in which the Standard Model (SM) is supplemented by a dark photon [371] that decays to pairs of DM particles through $A' \to \chi\chi$. For dark photons with typical loop-suppressed couplings $\varepsilon \sim 10^{-4} - 10^{-3}$ and $m_{A'}, m_\chi \sim \text{MeV} - \text{GeV}$, the DM annihilates through $\chi\chi \to A'^{(*)} \to f\bar{f}$ in the early universe, yielding the correct thermal relic density. This model is representative of a broad class of hidden sector theories in which the correct amount of DM is produced through thermal freeze-out within the standard cosmology [372–377], just as in the case of weak-scale DM. In this scenario, however, the DM is light. As a result, at colliders, the dark photons and DM are dominantly produced along the beampipe in the far-forward region, escape through holes in collider detectors, and evade all conventional collider searches.

To remove such "blind spots" from the Large Hadron Collider (LHC) physics program, a number of experiments are currently planned for the far-forward region. FASER [41,176,177,

181] has been completely constructed, and FASERν [9,170,378] and SND@LHC [257] are also being prepared to take data when Run 3 of the LHC begins in 2022. For the High Luminosity-LHC (HL-LHC) era, a Forward Physics Facility (FPF) is under study [207, 348, 349]. The FPF would house a suite of far-forward experiments, including possibly FASER2 [379], targeting new long-lived particles that decay visibly in the detector; FORMOSA [276], a milli-charged particle detector; FASERν2 [263, 380], a 10-tonne emulsion detector; SND2, a successor to SND@LHC; and FLArE [25], a proposed liquid argon time projection chamber (LArTPC) with an active volume of 10 tonnes (FLArE-10) to 100 tonnes (FLArE-100). FASERν2, SND2, and FLArE will detect millions of TeV-energy neutrinos, providing a wealth of SM measurements, but they also have the potential to search for light DM and other new particles.

Here we evaluate the prospects for discovering light DM at FASERν2 and FLArE through DM-nuclear scattering in the HL-LHC era. This work complements Ref. [25], which focused on the prospects for observing elastic DM-electron interactions in these detectors; Refs. [182, 184], which explored the potential of FASER to probe inelastic DM; Ref. [186], which studied the scatterings of unstable, but very long-lived, heavy neutral leptons at FASERν2; and Ref. [28], which investigated leptophobic DM scattering at SND@LHC.[1] We assume these experiments are located in a new cavern that is under study for the FPF, which would place the fronts of these detectors approximately 620 m from the ATLAS interaction point (IP), and we consider 14 TeV pp collisions and the expected HL-LHC integrated luminosity of 3 ab^{-1}. Alternative locations for the FPF that are ~ 150 m closer or farther from the IP do not change the prospects much, provided, of course, that they are large enough to house the detectors we consider.

We begin by defining the light DM models in Sec. 7.2 and specifying the detectors in Sec. 8.3. We then consider the dominant processes contributing to DM-nuclear scattering,

[1] See also Refs. [22, 27, 381–392] for studies employing a similar DM search technique at proton beam fixed-target experiments.

including elastic scattering ($\chi p \to \chi p$), resonant pion production ($\chi N \to \chi N \pi$), and deep inelastic scattering (DIS) ($\chi N \to \chi X$) in Secs. 8.4.2, 7.5, and 7.6, respectively. For each of these signals, we devise simple kinematic cuts to differentiate the DM signal from the neutrino-induced SM background.

In Sec. 7.7, we then combine all of these DM-nuclear probes with the DM-electron signals investigated in Ref. [25]. We find that DM-nuclear scattering and DM-electron scattering are quite complementary, with nuclear scattering more powerful for relatively high masses $m_\chi \gtrsim 100$ MeV and electron scattering more sensitive for low masses $m_\chi \lesssim 10$ MeV. By combining DM-nuclear and DM-electron scattering, FASERν2 and FLArE can cover the cosmologically-favored parameter space, where the χ thermal relic density is at or below $\Omega_{\rm DM}$, for a wide range of DM masses between MeV $\lesssim m_\chi \lesssim$ GeV. In Sec. 7.7, we also compare the sensitivity of FASERν2 and FLArE to non-LHC experiments that have discovery potential for invisibly decaying dark photons and light DM [393, 394]. Our conclusions are presented in Sec. 8.6.

7.2 Invisibly-Decaying Dark Photon Models

In this section, we describe two popular benchmark models in which light DM interacts with the SM through an invisibly decaying dark photon mediator. Given its coupling to electrically charged particles and quarks, in particular, the dark photon efficiently mediates scattering between DM and nuclei, making these models an interesting test case for our study.

The dark photon, A', is a massive gauge boson that arises when the SM is supplemented with a new broken U(1)$_D$ symmetry. For light GeV-scale dark photons, the dark photon Lagrangian is

$$\mathcal{L} \supset -\frac{1}{4} F'_{\mu\nu} F'^{\mu\nu} + \frac{1}{2} m_{A'}^2 A'_\mu A'^\mu + A'_\mu \left(\varepsilon \, e \, J^\mu_{EM} + g_D \, J^\mu_D \right), \tag{7.2.1}$$

where $F'_{\mu\nu}$ is the dark photon's field strength, $m_{A'}$ is the dark photon mass, ε is the kinetic mixing parameter, J^μ_{EM} and J^μ_D are the SM electromagnetic and U(1)$_D$ currents, respectively,

and $g_D \equiv \sqrt{4\pi\alpha_D}$ is the U(1)$_D$ gauge coupling.

For the DM candidates, χ, we will examine two popular examples: Majorana fermion DM and complex scalar DM. The corresponding Lagrangians are

$$\mathcal{L} \supset \begin{cases} \frac{1}{2}\overline{\chi} i\gamma^\mu \partial_\mu \chi - \frac{1}{2} m_\chi \overline{\chi}\chi \quad \text{(Majorana fermion DM)} \\ \\ |\partial_\mu \chi|^2 - m_\chi^2 |\chi|^2 \quad \text{(complex scalar DM)} \ , \end{cases} \tag{7.2.2}$$

where m_χ is the DM mass. The $U(1)_D$ currents associated with these models are

$$J_D^\mu = \begin{cases} \frac{1}{2}\overline{\chi}\gamma^\mu\gamma^5\chi \quad \text{(Majorana fermion DM)} \\ \\ i\chi^* \overset{\leftrightarrow}{\partial^\mu} \chi \quad \text{(complex scalar DM)} \ . \end{cases} \tag{7.2.3}$$

These two DM models have many similarities, but also some key differences. We discuss them in turn, beginning with the Majorana fermion case. As noted in Sec. 8.1, an attractive feature of these light DM models is the fact that the observed DM relic density can be easily obtained through thermal freeze-out. For $m_{A'} > 2m_\chi$, Majorana fermion DM annihilates in the early universe through $\chi\chi \to A'^{(*)} \to f\bar{f}$ with cross section

$$\sigma v \propto \alpha\, v^2\, \frac{\varepsilon^2\, \alpha_D\, m_\chi^2}{m_{A'}^4} = \alpha\, v^2\, \frac{y}{m_\chi^2} \ , \tag{7.2.4}$$

where we have assumed $m_{A'} \gg m_\chi$ and $y \equiv \varepsilon^2 \alpha_D (m_\chi/m_{A'})^4$ [375]. As evident from Eq. (7.2.4), the annihilation is P-wave, and so bounds from cosmic microwave background (CMB) temperature anisotropies on late-time DM annihilation are not very constraining in these models [395, 396]. In addition, the scattering of Majorana fermion DM in direct detection experiments is also velocity-suppressed at the non-relativistic energies relevant for these searches, and so direct detection null results also do not set strong limits.

For complex scalar DM, the annihilation cross section is, in fact, similar to that for Majorana fermion DM. Equation (7.2.4) still applies, and so the complex scalar DM model also evades CMB bounds. In contrast to the Majorana fermion case, however, the non-relativistic scattering of complex scalar DM in matter is not velocity-suppressed. Direct

detection null results are therefore a significant constraint on this model. These bounds may be evaded, however, if a small mass splitting is introduced to make the DM scattering transition inelastic [397].

In this work, we will present our results in the (m_χ, y) plane. As we will see, at the relativistic energies relevant for the LHC, the DM-nuclear interactions for Majorana fermion and complex scalar DM are very similar, and so the results we derive will be almost imperceptibly different in the (m_χ, y) plane. We will therefore simply present the Majorana fermion DM results. At the same time, to understand the cosmological significance of these results, we will also present "thermal targets," the regions of parameter space where the thermal relic density is identical to the observed DM abundance. These differ slightly for the Majorana fermion and complex scalar DM models, and so we will present both, using the relic density predictions of Ref. [398].

To reduce the parameter space to two dimensions, we will present results for $\alpha_D = 0.5$ and $m_{A'} = 3m_\chi$ throughout this work. These represent relatively conservative choices in terms of characterizing the experimental prospects for testing the thermal freeze-out hypothesis, at least in the regime $m_{A'} \gg m_\chi$. Of course, if $m_{A'} - 2m_\chi \ll m_{A'}$, the annihilation rate is resonantly enhanced, and the corresponding thermal targets occur at smaller couplings and can be much more challenging to probe at colliders [399–401].

7.3 Detectors and Simulation

7.3.1 Benchmark Detectors

The benchmark detectors we consider are identical to those studied in Ref. [25], except that they are now assumed to be housed in the "new cavern" FPF, placing them 620 m from the ATLAS IP. We review their most salient characteristics here; for more details, see Ref. [25].

FASERν2 [263] is envisioned to be a larger version of FASERν [170], currently being built for LHC Run 3. The FASERν2 benchmark detector we consider here is a 10-tonne

rectangular tungsten-emulsion detector with location and size given by

$$\text{FASER}\nu 2: \; L = 620 \text{ m}\,, \; \Delta = 2 \text{ m}\,, \; S_T = (0.5 \text{ m} \times 0.5 \text{ m})\,, \tag{7.3.1}$$

where L is the distance from the IP to the front of the detector, and Δ and S_T are the longitudinal and transverse dimensions of the tungsten target. At the ATLAS IP during the HL-LHC, it is expected that the beam half-crossing angle will vary by as much as 250 μrad, moving the beam collision axis horizontally by as much as 15 cm at the detector location. Given the detector's transverse dimensions and the $\sim$ 20 cm spread of the DM signal and neutrino background [21], the crossing angle will have little effect on our results; for simplicity, we assume that the detector is always centered on the beam collision axis.

We will assume that tracks down to momenta of 300 MeV can be detected and that the emulsion is exchanged periodically so that the track density remains manageable. This requires changing the detector every 30 fb^{-1} or so, or less if a sweeper magnet is available to bend away muons produced at the IP.

The main disadvantage of emulsion detectors for this DM search is the lack of timing, which makes it difficult to reject muon-induced backgrounds. To remedy this, it is necessary to augment the tungsten-emulsion detector with interleaved electronic tracker layers, which would provide event time information. This design follows the successful example of the OPERA experiment [402], and an analogous design is being implemented for SND@LHC [403]. We will, therefore, assume that muon-induced backgrounds can be rejected by vetoing events in coincidence with a high-energy muon track. It is important to note, however, that all of our FASERν2 sensitivities depend on this assumption, and if muon-induced backgrounds are difficult to reject in emulsion detectors, liquid argon technology may be preferable for dark matter detection.

For FLArE, we consider two sizes with physical dimensions

$$\text{FLArE-10 (10 tonnes)}: \qquad L = 620 \text{ m}, \; \Delta = 7 \text{ m}, \quad S_T = (1 \text{ m} \times 1 \text{ m})\,, \tag{7.3.2}$$

$$\text{FLArE-100 (100 tonnes)}: \quad L = 620 \text{ m}, \; \Delta = 30 \text{ m}, \; S_T = (1.6 \text{ m} \times 1.6 \text{ m})\,, \tag{7.3.3}$$

where, as above, L is the distance from the IP to the front of the detector, Δ and S_T are the longitudinal and transverse dimensions of the active volume, and we assume that the detector is centered on the beam collision axis.

Particle kinetic energy thresholds for LArTPC detectors typically lie in the 10-100 MeV range. For protons, we will consider two kinetic energy thresholds: a conservative value of 50 MeV, as is considered in the DUNE Conceptual Design Report [404], and a more optimistic choice of 20 MeV. Concerning the latter, we note that the ArgoNeuT experiment has already achieved thresholds for such short proton tracks down to 21 MeV [405,406]. For other particles, including shower-like objects (electrons, photons, neutral pions) and charged pions, we will assume a 30 MeV kinetic energy threshold, which is broadly consistent with Refs. [404–406]. In contrast to emulsion detectors, LArTPCs have good active event timing capabilities, particularly when equipped with a light collection system [407,408], and we will assume that vetoing events with a coincident muon is sufficient to remove all muon-induced backgrounds.

7.3.2 Expected Neutrino Fluxes

A crucial ingredient for the estimation of background rates is the flux of neutrinos passing through the different detectors. We use the dedicated forward physics event generator `Sibyll 2.3c` [268–270], as implemented in the CRMC simulation package [195], to simulate the primary collisions. We then use the fast neutrino flux simulation introduced in Ref. [21] to simulate the propagation of SM hadrons through the LHC beam pipe and magnets and their decays into neutrinos.

The results are presented in Fig. 36 for the HL-LHC with an integrated luminosity of 3 ab^{-1}, assuming no beam crossing angle. The upper panels show the numbers of neutrinos passing through the detectors. Unsurprisingly, detectors with a larger cross sectional area will have more neutrinos passing through them. The lower panels show the numbers of charged current (CC) and neutral current (NC) DIS neutrino interactions in the detectors,

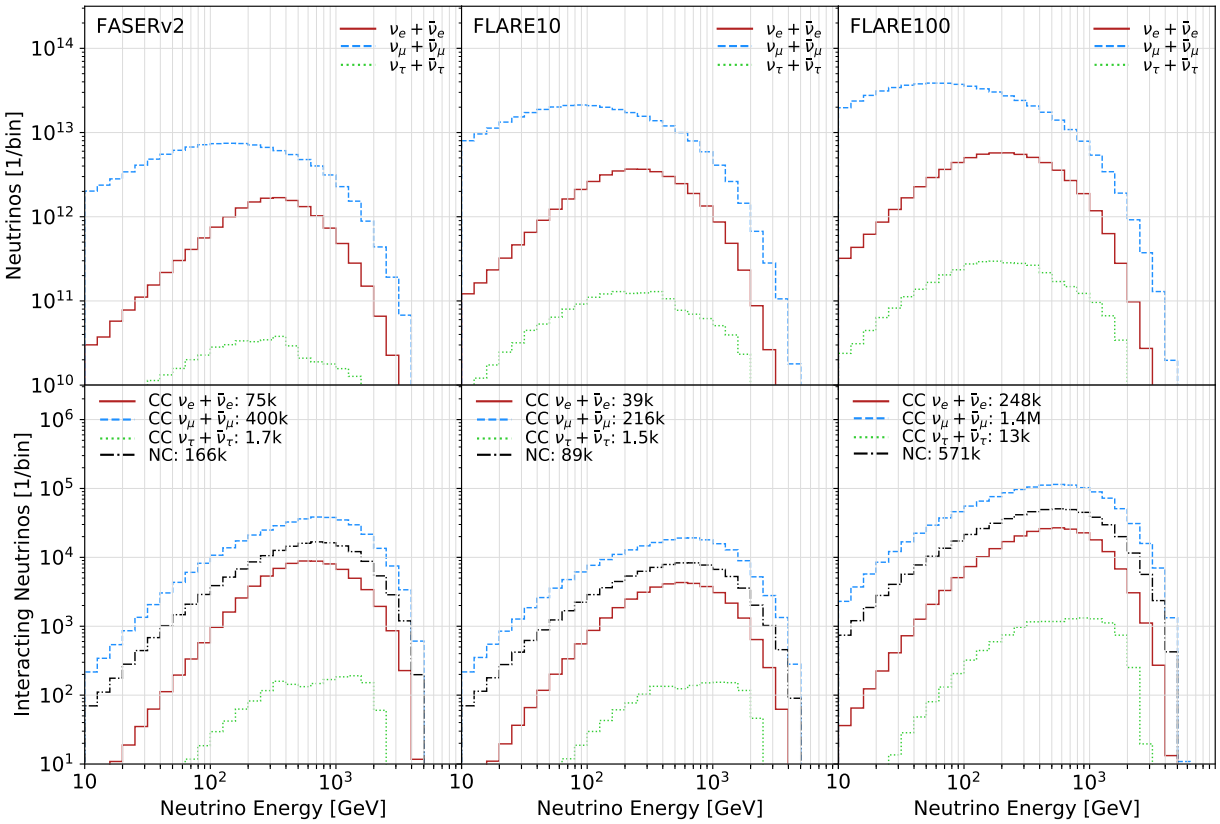

Figure 36: The number of neutrinos passing through the detector (top) and interacting in the detector (bottom), for FASERν2 (left), FLArE-10 (center), and FLArE-100 (right) during the HL-LHC era. The detector geometries and locations are described in the text. These results assume 14 TeV pp collisions and an integrated luminosity of $\mathcal{L} = 3$ ab^{-1} and are estimated using `Sibyll 2.3d` and the fast neutrino flux simulation introduced in Ref. [21].

where we use the neutrino interaction cross sections from Ref. [9]. Note that the event rate is larger for FASERν2 than FLArE-10, despite the two detectors having the same mass. This is because the neutrino beam is strongly collimated around the beam collision axis, and so a narrow detector with more mass close to the beam axis, such as FASERν2, will observe a larger event rate. During the HL-LHC era, we expect about 3.9×10^4 electron neutrino, 2.2×10^5 muon neutrino, and 1.5×10^3 tau neutrino CC interactions in the FLArE-10 detector. In addition, we expect about 8.9×10^4 NC neutrino interactions. The average energy of these interacting neutrinos is about 600 GeV.

	CCQE						CCRES						NCEL	NCRES
Detector	ν_e	$\bar{\nu}_e$	ν_μ	$\bar{\nu}_\mu$	ν_τ	$\bar{\nu}_\tau$	ν_e	$\bar{\nu}_e$	ν_μ	$\bar{\nu}_\mu$	ν_τ	$\bar{\nu}_\tau$	all	all
FASERν2	57	50	570	355	1.9	1.6	170	183	1.6k	1.1k	5.4	5.1	170	1.3k
FLArE-10	43	40	425	260	2.0	1.6	120	140	1.2k	860	5.6	5.1	130	940
FLArE-100	325	290	3.3k	2k	20	15	930	980	9.2k	6.8k	54	50	980	6.5k

Table 9: Expected event rates for charged current quasi-elastic (CCQE), charged current resonant (CCRES), neutral current elastic (NCEL), and neutral current resonant (NCRES) interactions of neutrinos in the FASERν2, FLArE-10, and FLArE-100 detectors. The results for CC interactions are given for each neutrino flavor separately, while, for the NC events, all the contributions are summed up.

In addition to the total neutrino interaction rates that, for each flavor, are dominated by DIS, we also provide in table 9 the expected number of events for several exclusive scattering channels. These include both CC quasi-elastic and NC elastic scatterings (denoted in the table by CCQE and NCEL, respectively), as well as the relevant resonant pion production channels (CCRES and NCRES). We estimate them by convoluting the above neutrino fluxes with the cross sections simulated with `GENIE` [23,24]. As can be seen, in total approximately 3000 CCQE and CCRES and 1000 NCEL and NCRES events are expected in FLArE-10 during the entire HL-LHC era, and the scattering rate is about 30% larger for FASERν2, and a factor of $7-8$ larger for FLArE-100. These events are mainly due to interactions of the muon neutrinos, while electron neutrinos are responsible for about 10% of the event rates, and tau neutrinos give subdominant contributions.

As discussed in Ref. [21], the neutrino fluxes predicted by different commonly-used event generators are somewhat different, indicating a flux uncertainty of about a factor of 2. This situation will improve in the coming years, given dedicated theoretical efforts to reduce these uncertainties; see, e.g., Ref. [283]. In addition, measurements of the energy spectra of CC neutrino interactions at FASERν and SND@LHC during LHC Run 3 and later in

the FPF neutrino detectors will provide direct measurements of the neutrino fluxes. In the following, we, therefore, assume that the neutrino flux uncertainties are dominated by statistical uncertainties.

7.3.3 Signal Modeling

Given our chosen benchmark scenario with $m_{A'} = 3\,m_\chi$, the DM particles originate from the decays of on-shell dark photons produced at the ATLAS IP. We simulate the flux of DM particles through the far-forward detectors with the geometries and locations given in Eqs. (7.3.1), (7.3.2), and (7.3.3), normalizing the number of events to the total integrated luminosity of $\mathcal{L} = 3$ ab^{-1} anticipated for the HL-LHC era. The dark photons produced in rare π^0 and η decays are obtained by employing the `CRMC` simulation package [195] and the dedicated `EPOS-LHC` Monte Carlo tool [193]. In addition, we include dark photon production by dark bremsstrahlung, using the Fermi-Weizsacker-Williams approximation, following the discussion in Refs. [22, 41, 409].

A rich variety of DM-nuclei scattering processes can be studied with the far-forward detectors. To organize the discussion, in the following, we will divide them into distinct categories in a way similar to neutrino interactions; see Ref. [171] for a review. We first study the case of elastic DM-nucleon scattering, which leads to events with single proton charged tracks in the detector. Next, we consider the exclusive inelastic processes of resonant pion production produced through DM-nucleon interactions. Finally, we consider DM-induced DIS, which is most relevant at high-momentum transfer.

7.4 Elastic Scattering

7.4.1 Signal

Here we consider elastic DM-nucleon scattering and the associated signature of a single proton track in the detector with no additional visible charged tracks emerging from the

interaction vertex. As mentioned above, we will also assume that there is no through-going muon in the detector that could be associated with the DM-induced event. When presenting the results, we will further require that the proton momentum, p_p, be above a minimum value defined by the energy threshold of the detector (see Sec. 8.3) and below a maximum value that we chose to maximize the signal to background ratio, $S/\sqrt{B}$.

The single proton signature is most directly associated with elastic scatterings of DM off protons, $\chi p \to \chi p$. The relevant differential cross section is [384, 410]

$$\frac{d\sigma(\chi p \to \chi p)}{dQ^2} = \frac{4\pi\varepsilon^2\alpha\alpha_D Q^2}{(E_\chi^2 - m_\chi^2)(m_{A'}^2 + Q^2)^2}\left[A(Q^2) + \left(\frac{E_\chi}{Q} - \frac{Q}{4m_N}\right)^2 (\tilde{F}_{1,p}^2 + \tau\tilde{F}_{2,p}^2)\right], \quad (7.4.1)$$

where E_χ is the incoming DM energy, $Q^2 = 2m_p(E_p - m_p)$ is the squared four-momentum transfer with E_p the outgoing proton energy and m_p the proton mass, and

$$A(Q^2) = \begin{cases} \left[\frac{1}{4}\tilde{F}_{1,p}^2\left(1-\frac{1}{\tau}\right) + \frac{1}{4}\tilde{F}_{2,p}^2(1-\tau) + \tilde{F}_{1,p}\tilde{F}_{2,p}\right]\left(\tau + \frac{m_\chi^2}{m_p^2}\right) \text{ (Majorana fermion DM)} \\ -\frac{1}{4}\left(\tilde{F}_{1,p} + \tilde{F}_{2,p}\right)^2\left(\tau + \frac{m_\chi^2}{m_p^2}\right) \text{ (complex scalar DM)}\,, \end{cases} \quad (7.4.2)$$

with $\tau = Q^2/(4m_p^2)$. The proton form factors can be expressed as

$$\tilde{F}_{1,p}(Q^2) = \frac{1+\mu_p\tau}{1+\tau}G_D(Q^2)\,, \qquad \tilde{F}_{2,p}(Q^2) = \frac{\mu_p - 1}{1+\tau}G_D(Q^2)\,, \quad (7.4.3)$$

where $\mu_p = 2.793$, and $G_D(Q^2) = (1 + Q^2/M^2)^{-2}$, with $M = 0.843\,\text{GeV}$.

As advertised in Sec. 7.2, the scattering cross sections for Majorana fermion and complex scalar DM have the same high-energy limit. This is evident upon inspection of Eqs. (7.4.1) and (7.4.2), which reveals that the first term proportional to $A(Q^2)$ in Eq. (7.4.1) is negligible compared to the second term for large E_χ. The projected exclusion bounds presented below are therefore valid for both the Majorana fermion and complex scalar DM scenarios. We also note that the integrated cross section becomes independent of the DM energy at large E_χ.

Additional signal events could arise from elastic DM scatterings off neutrons, $\chi n \to \chi n$, in which the outgoing neutron re-scatters before leaving the nucleus and produces a final-state proton. The relevant cross section for this process can be obtained from Eqs. (7.4.1)

and (7.4.2) by replacing the proton mass and form factors with the quantities appropriate for neutrons [384]. However, because the dark photon mediator couples to electric charge, its coupling to neutrons vanishes in the limit of zero momentum transfer. Therefore, for the models considered here, elastic DM-neutron scattering is considerably suppressed relative to elastic DM-proton scattering. Similarly, inelastic DM scattering followed by the absorption of all charged tracks and neutral pions inside the nucleus, besides a single outgoing proton, contributes subdominantly to the total DM signal event rate. We have verified this using `GENIE`, under the assumption that the impact of nuclear final-state interactions (FSI) on such particles in DM-induced events can be well approximated by their impact on neutrino events with the same momentum transfer to the nucleus.

In addition to the outgoing proton's energy, its direction can also be observed. Angular cuts were found in Ref. [25] to be useful in separating DM-electron scattering from neutrino-electron scattering, but they are less useful here. In DM-electron scattering, the additional discriminating power was related to the mass hierarchy between the target electron and the incoming DM particles, $m_e \ll m_\chi$. For the DM-nuclear scattering considered here, however, $m_\chi \lesssim m_p$ in the parameter space of interest, and so the DM particles behave similarly to essentially massless neutrinos. In the following, we will therefore focus only on the energy cut.

Elastic scatterings $\chi p \to \chi p$ generally lead to low visible energy depositions due to the strong form factor suppression for large momentum transfers, $Q^2 \gtrsim 1$ GeV^2. As a result, we will typically set the maximum outgoing proton momentum, $p_p^{\max}$, to values below 1 GeV. The DM detection prospects for this signature improve with softer lower limits on the outgoing proton momentum. For this reason, FLArE can be more sensitive than FASERν2 if the FLArE proton kinetic energy threshold, $E_{k,p}$, can be lowered to 20 MeV, as discussed in Sec. 7.3.1. Below, we present in detail the estimated sensitivity reach and background estimates for both types of detectors.

7.4.2 Neutrino-Induced Backgrounds

The dominant neutrino-induced backgrounds to DM-nucleon elastic scattering come from neutral current elastic scatterings (NCEL) of all three neutrino flavors that produce the outgoing proton in the final state, $\nu p \to \nu p$. Additional background events can be induced by deep inelastic neutrino scatterings (NCDIS) and resonant pion production processes (NCRES), in which, occasionally, most of the outgoing particles are absorbed in the nucleus due to FSI. We assume below that outgoing electrons and muons can be sufficiently discriminated from protons so that CC neutrino interactions can be neglected in the background discussion.

In table 10, we present the total background event rates obtained with `GENIE` for FASERν2, FLArE-10, and FLArE-100. In the case of liquid argon detectors, we impose a selection cut on the minimum proton kinetic energy of either $E_{k,p} > 20$ or 50 MeV, corresponding to the assumed proton detection thresholds discussed in Sec. 7.3.1. The latter condition corresponds to a minimum proton momentum of $p_p \gtrsim 300$ MeV, which we also require in the analysis for the emulsion detector. We also cut on the maximum proton momentum, $p_p < p_p^{\rm max} = 1$ GeV, and for the more optimistic proton threshold in FLArE, $E_{k,p} > 20$ MeV, we additionally study a more aggressive upper momentum cut, $p_p^{\rm max} = 500$ MeV. Finally, in each case, we veto on events containing any additional charged tracks or neutral pions emerging from the nucleus, besides the single proton, that have energies above their corresponding detection thresholds; see Sec. 8.3. As can be seen, in the HL-LHC era, the expected number of background events can be roughly 100 events for FLArE-10 and 1000 events for FLArE-100.

The number of background events in FASERν2 is between those in the two liquid argon detectors. The surprisingly large number of expected background events in FASERν2 when compared with FLArE-10, which has a similar mass, is mainly driven by the additional impact of neutrino-induced NCRES events that mimic the single proton signal. The outgoing pions produced in these events often have energies corresponding to the mass difference

Elastic $\chi p \to \chi p$		ν-induced backgrounds	DM: $m_\chi = 100$ MeV, $\varepsilon = 6 \times 10^{-4}$
FASERν2	$p_p > 300$ MeV, $p_p < 1$ GeV	310	34
FLArE-10	$E_{k,p} > 20$ MeV, $p_p < 500$ MeV	100	37
	$E_{k,p} > 20$ MeV, $p_p < 1$ GeV	125	42
	$E_{k,p} > 50$ MeV, $p_p < 1$ GeV	120	23
FLArE-100	$E_{k,p} > 20$ MeV, $p_p < 500$ MeV	810	260
	$E_{k,p} > 20$ MeV, $p_p < 1$ GeV	1050	310
	$E_{k,p} > 50$ MeV, $p_p < 1$ GeV	1010	165

Table 10: Neutrino-induced background and DM signal events for the single proton signature for several choices of selection cuts on the outgoing proton momentum p_p. We assume 14 TeV pp collisions with integrated luminosity 3 ab^{-1}. The cuts on the minimum proton momentum are dictated by the assumed experimental thresholds, as discussed in Sec. 7.3.1. The maximum proton momentum is set to 1 GeV for FASERν2. For FLArE-10 and FLArE-100, we also consider an additional case with $p_p < 500$ MeV. The DM signal corresponds to the benchmark scenario with parameters $(m_\chi, \varepsilon) = (100 \text{ MeV}, 6 \times 10^{-4})$, $m_\chi = m_{A'}/3$, and $\alpha_D = 0.5$, and takes into account the efficiency factors (see text).

between the dominant Δ resonance and the proton, $E_\pi \sim m_\Delta - m_p \sim 300$ MeV. As a result, such events often lead to pions below the detectability threshold, while the outgoing proton can remain visible. This effect is significantly more pronounced in FASERν2 than in FLArE. A detailed treatment of this background will also depend on the position of the interaction in the tungsten layer, which we leave for future studies with more detailed detector simulations.

For completeness, we also present in table 10 the number of DM signal events obtained for a benchmark scenario with $m_\chi = m_{A'}/3 = 100$ MeV, $\varepsilon = 6 \times 10^{-4}$ ($y = 2.2 \times 10^{-9}$), and $\alpha_D = 0.5$ for three sets of cuts and different detectors. Both in this table and in the subsequent analysis, the number of DM signal events has been additionally rescaled by a finite signal detection efficiency. This is due to the impact of FSI on the outgoing proton that can affect the DM-induced event reconstruction in the detector. We have estimated this efficiency as a function of the momentum of the final-state proton produced in the initial interaction inside the nucleus by studying elastic scatterings of neutrinos with `GENIE`. The value of the signal efficiency factor that we use in our analysis typically varies between 50% and 70%, and it depends on the energy of the outgoing proton and the analysis type. As can be seen, for FLArE-10 and FLArE-100 with the lower limit $E_{k,p} > 20$ MeV, the DM signal can yield a 30% to 40% excess over the neutrino background. In contrast, for FASERν2, even though the DM scattering rate is somewhat larger than in FLArE-10, the prospects for probing DM are limited by larger backgrounds.

In the left panel of Fig. 37, we show the signal-to-background ratio S/B as a function of $p_p^{\max}$ for the FLArE-10 detector. We present results for the above-mentioned benchmark scenario and also for one with $(m_\chi, \varepsilon) = (264\ \text{MeV}, 10^{-3})$ ($y = 6.2 \times 10^{-9}$). As evident from Fig. 37, the DM search favors lower values of $p_p^{\max}$. This is expected for DM scatterings mediated by the dark photon A', which is much lighter than the Z boson mediating neutrino NC scatterings. For a similar discussion for FLArE and DM-electron scattering, see Ref. [25]. As is apparent from Eq. (7.4.1), the lower the A' mass, the lower the typical momentum exchange in the $\chi p \to \chi p$ reaction, which also leads to a lower characteristic momentum

of the outgoing proton. In particular, for $m_{A'} \lesssim 100$ MeV, it would become necessary to require $p_p^{\max} \lesssim 300$ MeV or even lower to obtain $S/B \sim 1$. This, however, goes beyond the FLArE and FASERν2 capabilities that we assume in our study. On the other hand, the DM scattering rate can become much higher for increasing mediator mass, in which case a larger momentum exchange is allowed. This can be seen for the case of $m_{A'} = 3m_\chi = 792$ MeV also shown in the plot. The surprisingly large values of S/B obtained for this benchmark scenario are related to the efficient A' production in the proton bremsstrahlung process for $m_{A'}$ close to the ρ and ω resonances.

Last but not least, we note that, if systematic uncertainties are negligible relative to statistical uncertainties, the significance of the signal is more closely characterized by $S/\sqrt{B}$ than S/B. As $p_p^{\max}$ increases, the background rate increases, but this increase is milder for $\sqrt{B}$ than for B, and the dependence on the maximum momentum cut is milder for the ratio $S/\sqrt{B}$ than for S/B. For this reason, the projected exclusion bounds shown below are roughly independent of the precise value of $p_p^{\max}$.

7.4.3 Sensitivity Reach

In the right panel of Fig. 37, we present the expected projected 90% CL exclusion bounds for the three detectors under study. We see that, with just the elastic scattering signature, FLArE-10 will probe most of the thermal relic target for the complex scalar DM model with $m_\chi \gtrsim 100$ MeV. For the Majorana fermion DM case, FLArE-10 will only probe the small part of the thermal target region where DM production is enhanced by ω and ρ resonances in the dark photon bremsstrahlung process. The detection prospects could be further improved in the larger FLArE-100 experiment. The expected exclusion bounds for FASERν2 are similar to FLArE-10. We reiterate, however, that, as noted in Sec. 7.3.1, this assumes that muon-induced backgrounds can be eliminated for FASERν2.

We also show the impact of different cuts on the proton kinetic energy, $E_{k,p} > 50$ MeV, and maximum outgoing proton momentum, $p_p^{\max} < 1$ GeV. We see that the reach is better

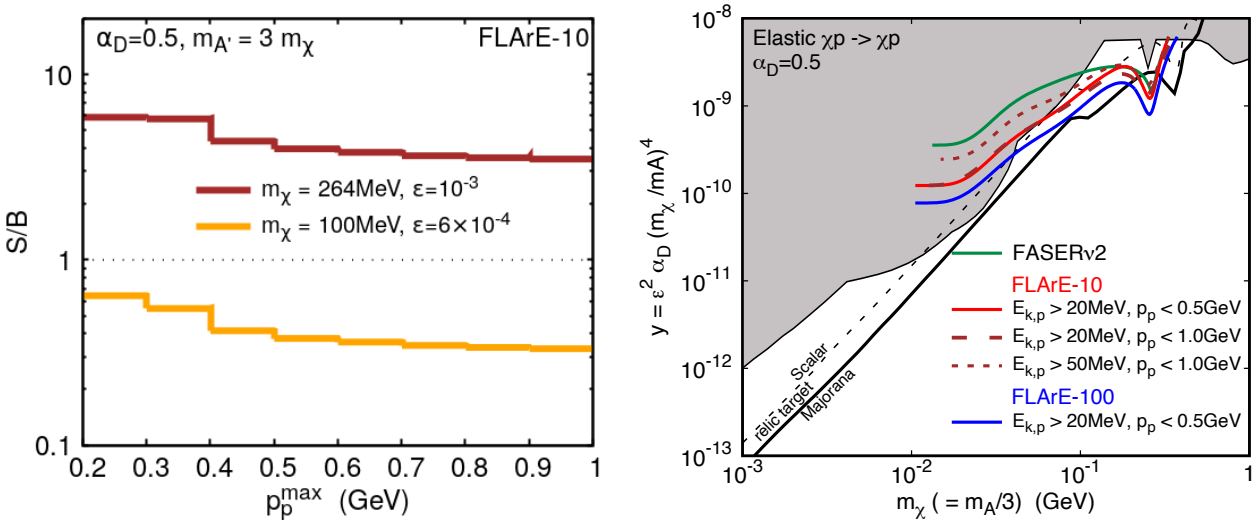

Figure 37: *Left*: The signal-to-background ratio S/B for the elastic scattering signature for FLArE-10 and the two DM benchmark scenarios indicated as a function of the maximum momentum of the outgoing proton $p_p^{\max}$. The expected number of neutrino-induced background events for selected values of $p_p^{\max}$ can be found in table 10, and we assume the detectability threshold of $E_{k,p} > 20$ MeV for the proton kinetic energy. *Right*: The projected 90% CL exclusion bounds for the elastic scattering signature for FASERν2 with 300 MeV $\lesssim p_p \lesssim$ 1 GeV (green), FLArE-10 (red), and FLArE-100 (blue) with the proton energy and momentum cuts indicated. Current bounds exclude the gray-shaded region; see Sec. 7.7 for details. The thermal relic targets for the Majorana fermion DM and complex scalar DM models are also shown.

in the low-mass region for the lower proton kinetic energy threshold. However, the improved reach mainly corresponds to a region in the parameter space that is already excluded by existing bounds. On the other hand, the expected bound at higher masses is only slightly sensitive to changes of our lower kinetic energy and upper momentum cuts. As a result, the presented sensitivity reach for $m_\chi \gtrsim 100$ MeV only mildly depends on the final FLArE capabilities in the considered range of $E_{k,p}$ and p_p. When we present combined results for different types of searches in Sec. 7.7, we will therefore just present results for the cuts $E_{k,p} > 20$ MeV, $p_p < 0.5$ GeV .

7.5 Resonant Pion Production

7.5.1 Signal

The next signal of interest is $\chi 1\pi^0$ events, in which a single neutral pion is produced through DM-nucleus scattering with no other mesons or charged leptons emerging from the vertex. Such events are produced by DM-induced resonant pion production, $\chi N \to \chi N \pi^0$, which we model using the `BdNMC` DM simulation tool [22]. `BdNMC` accounts for incoherent pion production via excitation of the Δ resonance, which is expected to be the leading contributor to this process. In addition, $\chi 1\pi^0$ events can also result from DM elastic scatterings off protons followed by FSI. We include this effect in our analysis, although it only mildly affects our final results. When treating the elastic scattering contribution, we assume that the impact of FSI can be modeled using neutrino interactions, as was discussed in Sec. 8.4.2.

In our analysis, we do not differentiate events based on the number of final-state nucleons, including protons, that emerge from the nucleus. This is to mitigate the strong dependence of the number of expected signal events on the assumed FSI model. This inclusive approach is consistent with similar analyses performed by the K2K [411], MicroBooNE [412] and MiniBooNE [413] Collaborations.

The neutral pion in the final state will immediately decay into two photons with momenta

typically above the visibility threshold of 30 MeV characteristic for the liquid-argon detectors. In contrast, for FASERν2, the reach will partially be limited by the requirement that photons have an energy of at least 300 MeV to be visible. As discussed above, in the resonant pion production events, we typically observe $E_\pi \sim 300$ MeV from the Δ resonance, which would only be moderately altered by the presence of heavier resonances and FSI. We illustrate this in the left panel of Fig. 38, in which we show the resonant event distribution as a function of the energy of the final-state neutral pion E_{π^0} for two benchmark DM models with $m_\chi = m_{A'}/3 = 10$ and 100 MeV, and for neutrino-induced NCRES background events. The plot has been obtained for the liquid argon detector. As can be seen, in the case of neutrinos, in which the aforementioned effects going beyond the simple Δ resonance and parton level interactions are taken into account, the resulting distribution is more smeared than for DM. Notably, in both cases, the photons produced in π^0 decays will typically be above 30 MeV.

The characteristic energy of the pions produced through resonant scatterings translates into a relatively weak dependence of the sensitivity reach on the upper energy threshold, which is similar to the elastic DM-nucleon scattering search discussed in Sec. 8.4.2. As a result, we will employ a single cut on the maximum pion energy given by $E_{\pi^0} < 1$ GeV. Increasing this limit has a minimal impact on the number of DM-induced resonant pion production events, while it could adversely affect the sensitivity by increasing the number of neutrino-induced backgrounds from DIS events.

Similar to the discussion in Sec. 8.4.2, here we also do not discuss the possible impact of the angular cuts on the derived exclusion bounds. We note, however, that the pion angular distribution, as well as the invariant mass reconstruction of the photon pair, could play an important role in further distinguishing such events from neutrino-induced backgrounds producing single electrons in the final state due to the scatterings off electrons or nuclei; see Ref. [27] for a similar discussion for MiniBooNE. Below, for simplicity, we assume that such backgrounds can be rejected in the analysis.

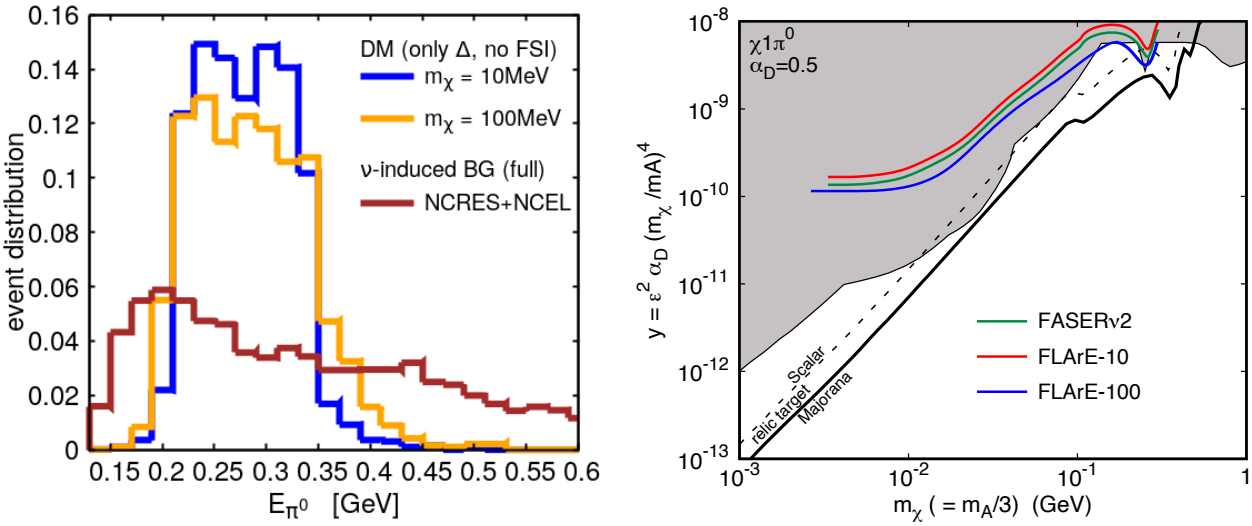

Figure 38: *Left*: The event distribution as a function of the pion energy for $\chi 1\pi^0$ signal events and neutrino-induced backgrounds in the liquid argon detectors. The DM results are shown for two benchmark masses $m_\chi = m_{A'}/3 = 10$ MeV (blue) and 100 MeV (yellow) for the complex scalar DM model. They have been obtained with the `BdNMC` code [22] that takes into account the dominant pion production via production of the Δ resonance. We also show the relevant results for neutrino-induced backgrounds from NCRES and NCEL events (brown histogram). This was obtained using the far-forward LHC neutrino energy spectrum and full `GENIE` [23, 24] simulations with further resonances and final-state interactions of hadrons taken into account. *Right*: The colorful solid lines correspond to the projected 90% CL exclusion bounds in the DM-nuclei scattering $\chi 1\pi^0$ signature for FASERν2 (green), FLArE-10 (red), and FLArE-100 (blue). Current bounds and thermal relic targets are as in Fig. 37.

$\chi\mathbf{1}\pi^{\mathbf{0}}$	ν-induced backgrounds			
Detector	$E_{\pi^0} < 170$ MeV	300 MeV	1 GeV	2 GeV
FASERν2	–	–	150	170
FLArE-10	9	90	220	230
FLArE-100	70	740	1750	1850

Table 11: Neutrino-induced background events in the search for $\chi 1\pi^0$-type events (see the text for details) as a function of the maximum threshold for the outgoing pion energy. The minimum threshold energy for the outgoing photon is set to 300 MeV and 30 MeV for the emulsion and liquid argon detectors, respectively.

7.5.2 Neutrino-Induced Backgrounds

The dominant neutrino-induced backgrounds for the $\chi 1\pi^0$ events are due to NCRES scatterings. We also study subdominant contributions associated with the coherent pion production processes (COHERENT), in which the neutrino scatters off the entire nucleus, and the elastic scatterings NCEL followed by the FSI that generate the outgoing neutral pion. We model all these backgrounds using `GENIE`. We provide the total expected number of background events for the three detectors in Table 11 for four choices of the π^0 upper energy threshold: $E_{\pi^0} < 170$ MeV, 300 MeV, 1 GeV, and 2 GeV. As can be seen, increasing the energy threshold above 1 GeV has a very mild impact on the number of background events. We require that the events do not contain any charged pions or other mesons above the visibility thresholds discussed in Sec. 8.3.

Focusing now on the pion energy cut of $E_{\pi^0} \lesssim 1$ GeV, we see that we expect roughly 200 background events in both FASERν2 and FLArE-10, and roughly 2000 such events in FLArE-100. Interestingly, the number of background events is now smaller in FASERν2 than for FLArE-10. This is the opposite effect to the one discussed in Sec. 8.4.2, in which increasing the lower energy threshold resulted in a larger number of NCRES events mimicking

NCEL ones in the detector. For this reason, we now observe a relatively lower number of NCRES events that will be reconstructed in the emulsion detector as $\chi 1\pi^0$-like events. As far as liquid argon detectors are concerned, the number of background events in this search is larger, although of a similar order, than for the previously discussed search based on elastic scattering events.

7.5.3 Sensitivity Reach

In the right panel of Fig. 38, we present the expected projected 90% CL exclusion bounds based on the $\chi 1\pi^0$ search. As can be seen, the expected bounds are weaker than the ones based on DM elastic scattering shown in Fig. 37. This is primarily due to the smaller scattering cross section. Once we limit the DM signal rate to only NC (A' exchange) scatterings off protons with single π^0 production and no charged pions in the final state, the relevant cross section is suppressed relative to elastic scattering by more than an order of magnitude for small mediator masses, $m_{A'} \lesssim 100$ MeV [22]. The suppression factor becomes smaller, of order a factor of a few, for heavier dark photons. The signal rate is further suppressed by signal efficiencies resulting from FSI and event reconstruction. We estimate them to be of the order of 25% for FLArE and between 10% and 15% for FASERν2. In the latter case, this efficiency also takes into account the aforementioned energy cut of $E_\gamma \gtrsim 300$ MeV, which is larger than in LArTPC detectors. In the end, we find that the resonant pion signature is less promising than both the electron and single proton signatures.

7.6 Deep Inelastic Scattering

7.6.1 Signal

The last signature that we consider is DM-nuclear scattering at high momentum transfer. Because light DM will be produced with TeV-scale energies in the direction of the FPF, the maximum accessible momentum transfer in nuclear scattering is tens of GeV. Above the

QCD scale, deep inelastic scattering leads to a relatively high-energy nuclear recoil, which can subsequently produce multiple charged tracks. In this regime, a partonic treatment is appropriate, and the outgoing hadrons are easily above detector thresholds.

We consider the DIS process $\chi N \to \chi X$ in the models of Sec. 7.2. The double differential cross section is given by

$$\frac{d\sigma(\chi N \to \chi X)}{dx\ dy} = 2\pi\varepsilon^2\alpha\alpha_D \frac{2m_p E_\chi}{(Q^2 + m_{A'}^2)^2} \sum_{q=u,d,s,c} Q_q^2\ B(y)\left[x f_q(x,Q^2) + x f_{\bar{q}}(x,Q^2)\right], \quad (7.6.1)$$

where $Q^2 = 2m_p E_\chi xy$, x is the parton momentum fraction, $y = 1 - E'_\chi/E_\chi$ is the fraction of the incoming DM energy transferred to the nucleon in the lab frame, f_q is the quark parton distribution function, Q_q is the quark electric charge, and

$$B(y) = \begin{cases} 1 + (1-y)^2 & \text{(Majorana fermion DM)} \\ 2(1-y) & \text{(complex scalar DM)}\ . \end{cases} \quad (7.6.2)$$

As the scattering takes place through a light mediator, it is not surprising that low momentum transfer is favored regardless of the χ spin. Furthermore, the functions $B(y)$ for Majorana fermion and complex scalar DM in Eq. (7.6.2) are identical up to $\mathcal{O}(y^2)$. Because the cross section is dominated by the small y region, then, the DIS signal strength is approximately the same for these two models. This motivates the choice previously mentioned in Sec. 7.2 to only show results for the Majorana fermion DM scenario.

To estimate the scattering signal, we convolute these cross sections with the nCTEQ15 parton distribution functions [191] for tungsten and argon nuclei, imposing a minimum cut of $Q^2 > 1$ GeV^2. When the parton hadronizes, of course, multiple charged tracks and photons, which yield electromagnetic showers, are produced. We do not simulate this hadronization nor the reconstruction of the hadronic energy and transverse momentum from these objects, though other works have demonstrated the use of track-level information to search for similar signals [266, 414]. Instead, we simply take the outgoing parton energy and transverse momentum as proxies for the energy and transverse momentum of the recoiling

hadronic system,

$$E_{\rm had} = yE_\chi \quad \text{and} \quad p_{T,\rm had}^2 = Q^2(1-y) = 2m_p E_\chi xy(1-y)\ . \tag{7.6.3}$$

We expect both $E_{\rm had}$ and $p_{T,\rm had}$ to grow with increasing Q^2. In principle, there are more detailed kinematic variables involving the visible tracks from the scattered nucleon that could be accessed by doing a full simulation. However, since the hadronic part of each event depends only on the outgoing parton momentum and hadron interaction modeling, we do not anticipate that further kinematic considerations would provide significant additional discriminating power between the signal and neutrino background.

The left panel of Fig. 39 shows the two-dimensional distribution of the quantities in Eq. (7.6.3) for DIS in one of our benchmark DM scenarios at FLArE-10. The distribution is qualitatively similar at FASERν2. The signal events are clustered at lower energies and transverse momenta than the background, consistent with the preference for low momentum transfer in light DM scattering. Despite the preference for low momentum transfer, there is still a significant number of events with energetic nuclear recoils. We see the most events at $E_{\rm had}$ of several GeV and low $p_{T,\rm had}$, and expect that such events would have multiple tracks emerging from a vertex with no incoming track. A more detailed study of the detection efficiency, including the effects of hadronization and FSI, would be interesting. For instance, the efficiency would depend on the number of tracks and hence the hadron multiplicity, which tends to grow with the center-of-mass energy W of the recoiling hadronic system. W is related to the momentum transfer and partonic momentum fraction through $W^2 = m_p^2 + Q^2(1-x)/x$. The EMC experiment measured the charged hadron multiplicity in muon DIS, finding that several charged tracks were typical for $W > 4$ GeV [415]. We have checked that a cut of $W > 2$ GeV, which would avoid the resonant scattering region with fewer tracks, does not change our results significantly. In addition, as our signal is clustered at values of $p_{T,\rm had}/E_{\rm had}$ corresponding to angles of several degrees, it would be useful to examine technologies for measuring multiple hadronic tracks in the forward direction in liquid argon for FLArE. While there can be difficulties measuring such tracks using wire planes

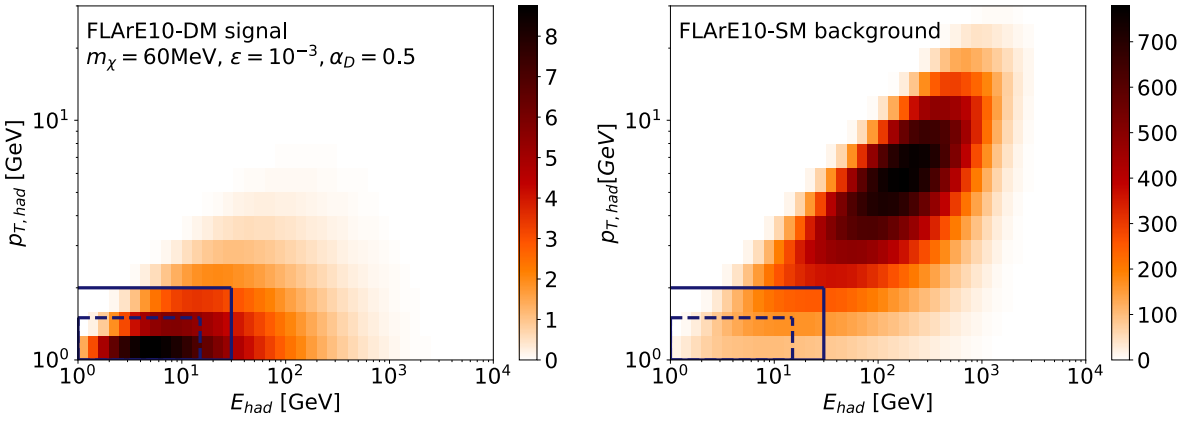

Figure 39: Expected number of DIS events in the $(E_{\rm had}, p_{T,\rm had})$ plane for one benchmark Majorana DM scenario (left) and SM NC neutrino background (right) at FLArE-10. Most of the signal events are at low $E_{\rm had}$ and low $p_{T,\rm had}$, motivating our choice of cuts. The dashed (solid) box shows the strong (loose) cuts of 1 GeV $< E_{\rm had} <$ 15 (30) GeV and 1 GeV $< p_{T,\rm had} <$ 1.5 (2.0) GeV used in our analysis.

if the planes are oriented parallel to the track direction, the patterns of charge deposition can be used to obtain three-dimensional information [416], as has been demonstrated by MicroBooNE for neutrino event identification [417] and cosmic ray rejection [418].

7.6.2 Neutrino-Induced Backgrounds

The main background to DM DIS is neutrino scattering. NC neutrino scattering would produce a nuclear recoil with significant energy carried away by the outgoing neutrino, just as in our signal. CC neutrino scattering, by contrast, would result in a high-energy outgoing lepton. We assume that the detector would have sufficient efficiency that the neutrino CC backgrounds could be rendered very small.

There are also backgrounds from muon interactions, which can be eliminated by requiring that there is no charged track leading into the vertex [9]. Muon interactions can also produce neutral hadrons, which travel for distances on the order of 10 cm before scattering. These neutral hadron events can mimic the signal. Although neutral hadron backgrounds are

problematic in a pure emulsion detector [9, 266], as mentioned in Sec. 7.3.1, we assume that an active muon veto will remove these events at FASERν2 or FLArE [25]. By using timing to remove a small area around each muon interaction, we expect that neutral hadron scattering could be reduced to negligible levels without significant impact on the signal.

The differential NC neutrino scattering cross section at high energy is [273]

$$\frac{d\sigma(\nu N \to \nu X)}{dx\ dy} = \frac{2G_F^2 m_p E_\nu}{\pi} \frac{m_Z^4}{(Q^2+m_Z^2)^2} \times \sum_{q=u,d,s,c} \left[g_{q,L}^2 [x f_q(x,Q^2) + x f_{\bar{q}}(x,Q^2)(1-y)^2] + g_{q,R}^2 [x f_q(x,Q^2)(1-y)^2 + x f_{\bar{q}}(x,Q^2)] \right] \tag{7.6.4}$$

in terms of the partonic momentum fraction x and the fractional neutrino energy loss $y = 1 - E'_\nu/E_\nu = E_{\rm had}/E_\nu$. The momentum transfer is $Q^2 = 2m_p E_\nu xy$. Here, $g_{q,L}, g_{q,R} = T^3 - Q\sin^2\theta_W$ are the NC couplings of the quarks. For anti-neutrinos, the cross section is

$$\frac{d\sigma(\bar{\nu} N \to \bar{\nu} X)}{dx\ dy} = \frac{2G_F^2 m_p E_\nu}{\pi} \frac{m_Z^4}{(Q^2+m_Z^2)^2} \times \sum_{q=u,d,s,c} \left[g_{q,L}^2 [x f_q(x,Q^2)(1-y)^2 + x f_{\bar{q}}(x,Q^2)] + g_{q,R}^2 [x f_q(x,Q^2) + x f_{\bar{q}}(x,Q^2)(1-y)^2] \right]. \tag{7.6.5}$$

As the momentum transfer Q^2 is generally small compared to m_Z^2, the neutrino scattering cross sections are proportional to the CM energy or, equivalently, the energy of the incoming neutrino.

The typical Q^2 is perhaps the most striking difference between light DM DIS and neutrino NC scattering. In principle, the momentum transfer $2E_\chi m_N$ in DM scattering can be as high as tens of GeV. However, for scattering through a light mediator, smaller momentum transfers are typically preferred, as the scattering cross section goes as $1/Q^4$ in the limit of vanishing mediator mass. On the other hand, neutrino scattering proceeds through the Z, which is heavy compared to the typical momentum transfer. Consequently, the neutrino NC scattering cross section grows linearly with the partonic CM energy $\sqrt{\hat{s}}$.

We proceed to investigate the kinematics further to discriminate between signal and background, showing the hadronic energy and transverse momentum for the neutrino background

DIS	ν-induced backgrounds			DM: $m_\chi = 60$ MeV, $\varepsilon = 10^{-3}$			DM: $m_\chi = 188$ MeV, $\varepsilon = 10^{-3}$		
Detector	no cuts	loose cuts	strong cuts	no cuts	loose cuts	strong cuts	no cuts	loose cuts	strong cuts
FASERν2	154k	7.4k	2.9k	700	335	210	440	170	100
FLArE-10	82k	5k	2k	380	185	116	250	95	55
FLArE-100	528k	38k	15k	2.3k	1.1k	748	1.5k	615	361

Table 12: The effects of the energy and momentum cuts in Eq. (7.6.6) on the numbers of SM neutrino NC background and DM DIS signal events. Two different benchmark DM scenarios are shown. The "no cuts" columns include only a Q^2 requirement and no cuts on the hadronic transverse momentum or energy.

in the right panel of Fig. 39. Motivated by these kinematic distributions, we consider two sets of cuts on $E_{\rm had}$ and $p_{T,\rm had}$:

$$\begin{aligned} \text{Strong cuts:} \quad & 1\ \text{GeV} < E_{\rm had} < 15\ \text{GeV}\,, \qquad 1\ \text{GeV} < p_{\rm T,had} < 1.5\ \text{GeV} \\ \text{Loose cuts:} \quad & 1\ \text{GeV} < E_{\rm had} < 30\ \text{GeV}\,, \qquad 1\ \text{GeV} < p_{\rm T,had} < 2.0\ \text{GeV} \quad . \end{aligned} \tag{7.6.6}$$

The effects of these cuts on the background and signal are shown in table 12. We see that the background can be reduced by over an order of magnitude while keeping 1/4 to 1/2 of the DM DIS signal.

7.6.3 Sensitivity Reach

Having examined the kinematics of the signal and background events, we present the expected projected 90% CL exclusion bounds for DM DIS searches at FASERν2 and FLArE in Fig. 40. Considering statistical uncertainties only, the former set of cuts in Eq. (7.6.6) yields the strongest projected exclusions. The figure shows the reach of the different detectors, as well as the effects of the hadronic energy and transverse momentum cuts in the case of FLArE-10. In contrast to the lower energy signatures in Secs. 8.4.2 and 7.5, the typical deposited energy is well above the thresholds for both emulsion and liquid argon detectors. The relative performances of FASERν2 and FLArE thus depend mostly on the detector mass and geometry, as well as on their background rejection and event identification capabilities. Here, we focus on the former, while assuming 100% signal detection efficiency for both types

of experiments. Of the two 10-tonne detectors, the more compact FASERν2 provides better sensitivity to light DM scattering because it has more mass at large rapidity where the DM flux is higher. In addition, the numbers of events for FLArE-100 in Table 12 do not scale fully with the detector mass, when compared to its 10-tonne analog. Similar effects were observed for DM-electron scattering [25].

As discussed above, the DIS limits are very similar for the Majorana fermion and complex scalar DM models, and we have used the former to draw the projected exclusion lines. To guide the interpretation of the limits, we also show the thermal relic targets in each of these scenarios, assuming standard thermal cosmology. We see that DIS searches can probe dark photon scenarios yielding the correct thermal relic density for DM masses above approximately 200 MeV. The expected sensitivity reach can then also partially cover the resonance region, in which the intermediate dark gauge boson in DM annihilations mixes with the SM vector mesons ρ and ω, i.e., $2m_\chi \approx m_{\rho,\omega}$, especially for complex scalar DM. By contrast, the reach of DM DIS is relatively limited at low masses. This is because the growth of the DIS cross section at small mediator masses is limited by our minimum momentum transfer cut of 1 GeV. Nevertheless, DM DIS searches at FPF detectors offer the potential to probe dark photon scenarios that are viable from the standpoint of thermal cosmology and that are otherwise unconstrained.

Finally, we note from Table 12 that with the full HL-LHC dataset, there will be thousands of background events even with kinematic cuts. It will thus be important to reduce uncertainties from systematics such as the neutrino flux and signal/background modeling, which we have not considered here, in a full experimental analysis. We assume that they can be suppressed so that the analysis will be dominated by statistical uncertainties. For instance, as has been suggested previously [25], measuring the neutrino flux at other detectors or in other kinematic regions could help constrain the background normalization. If statistical uncertainties dominate, then since the number of signal events scales with y^2, the limit on y associated with a fixed significance $S/\sqrt{B}$ improves as $\mathcal{L}^{-1/4}$. The impact of this

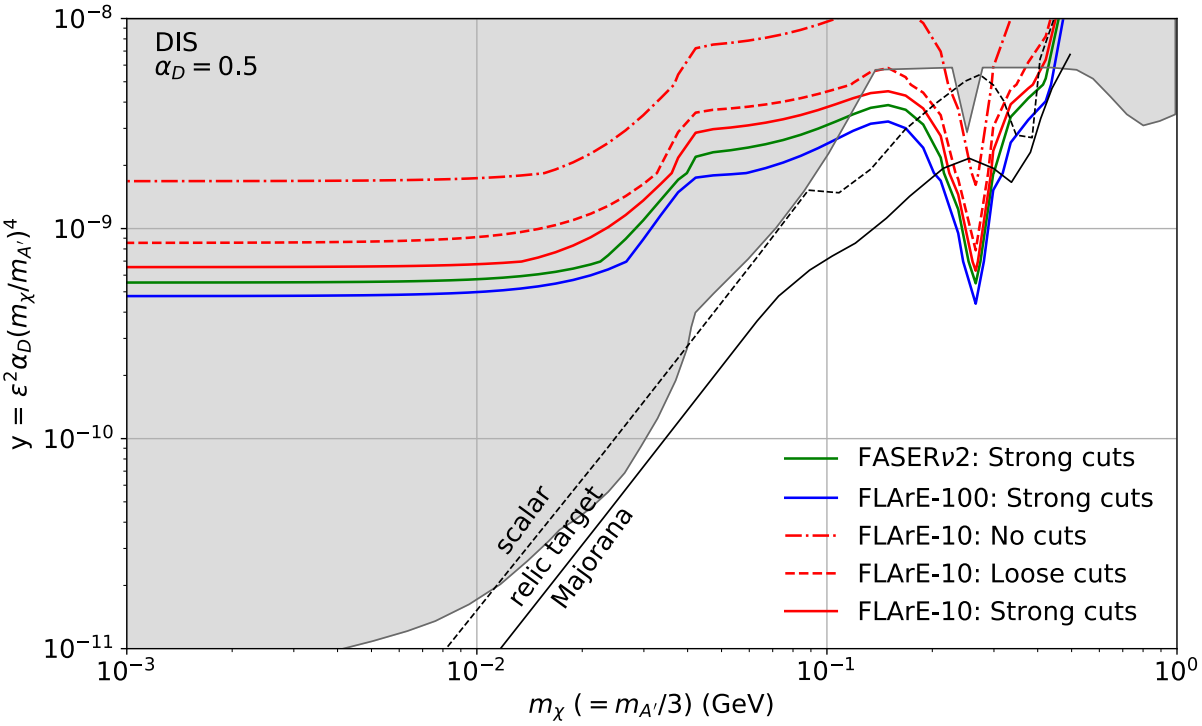

Figure 40: The projected 90% CL exclusion bounds for the DIS signature in the Majorana fermion DM model at various detectors. For FLArE-10 we show the limits with and without the kinematic cuts, whereas for FASERν2 and FLArE-100 we show only the best limits corresponding to the strong cuts. The thermal relic targets for Majorana fermion DM (black solid) and complex scalar DM (black dashed), and current bounds (gray shaded region) are also shown.

mild dependence is that new parameter space can be probed with a relatively small amount of data. We will consider the effect of luminosity on the reach more completely in the next section, where we combine the results of this section and the previous two to obtain the overall FPF reach in searches for light DM-nuclear scattering.

7.7 Combined Sensitivity Reach

In this section, we combine all of our previous results on DM-nucleus scattering processes, including elastic scattering (Sec. 8.4.2), resonant pion production (Sec. 7.5), and DIS (Sec. 7.6), as well as the results previously obtained [25] for the DM search based on scatterings off the electrons.

These are shown for FLArE-10 in Fig. 41. In general, since the scattering cross sections grow for small mediator mass and we have taken a fixed mass ratio $m_{A'}/m_\chi$, the limits are strongest at low m_χ. The flattened sensitivity at the left of the plot arises from the minimum momentum transfer for each process considered. For elastic scattering and resonant production, these come from experimental considerations on the visibility of the outgoing proton or pion. We see that the low thresholds of liquid argon detectors allow for the ability to probe new parameter space at $m_\chi \lesssim 200$ MeV. For DIS, the Q^2 cutoff to ensure the validity of our partonic treatment limits the sensitivity at small masses, but the inherently harder nature of DIS can lead to stronger bounds at higher DM mass.

Figure 41 also shows that elastic scattering and DIS are the most sensitive nuclear scattering probes at low and high masses, respectively. Resonant pion production is never the strongest signature in this model. The sensitivity reach from DM-electron scattering, derived previously in Ref. [25], is also shown, and can be seen to be competitive with the best nuclear signatures at moderate and high masses, and even stronger at low masses.

In Fig. 41, we also show the thermal relic targets for Majorana fermion and complex scalar DM, as well as current and projected results from other experiments. Existing bounds from null results are shown as the gray shaded region. These include results from BaBar [419],

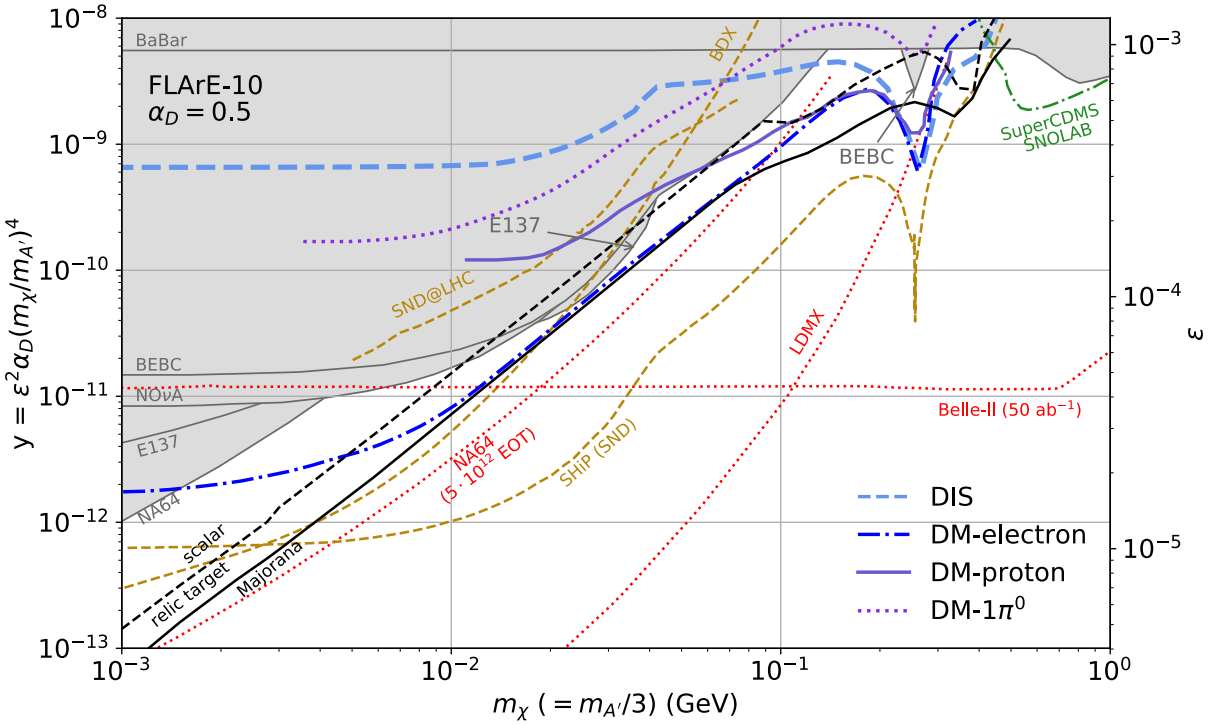

Figure 41: The projected 90% CL exclusion bounds for Majorana fermion DM from DM-nucleus elastic scattering, resonant pion production, and DIS (this work), along with DM-electron scattering from Ref. [25] at FLArE-10. In the gray shaded region, we also show the strongest existing constraints from BaBar, NA64, NOνA, E137, and BEBC, as implemented in Refs. [26, 27]. Projected reaches from other experiments are shown in brown for beam dump/collider experiments and in red for missing momentum-type searches. The green contour shows the projected bound on Majorana fermion DM from SuperCDMS; see text for more details.

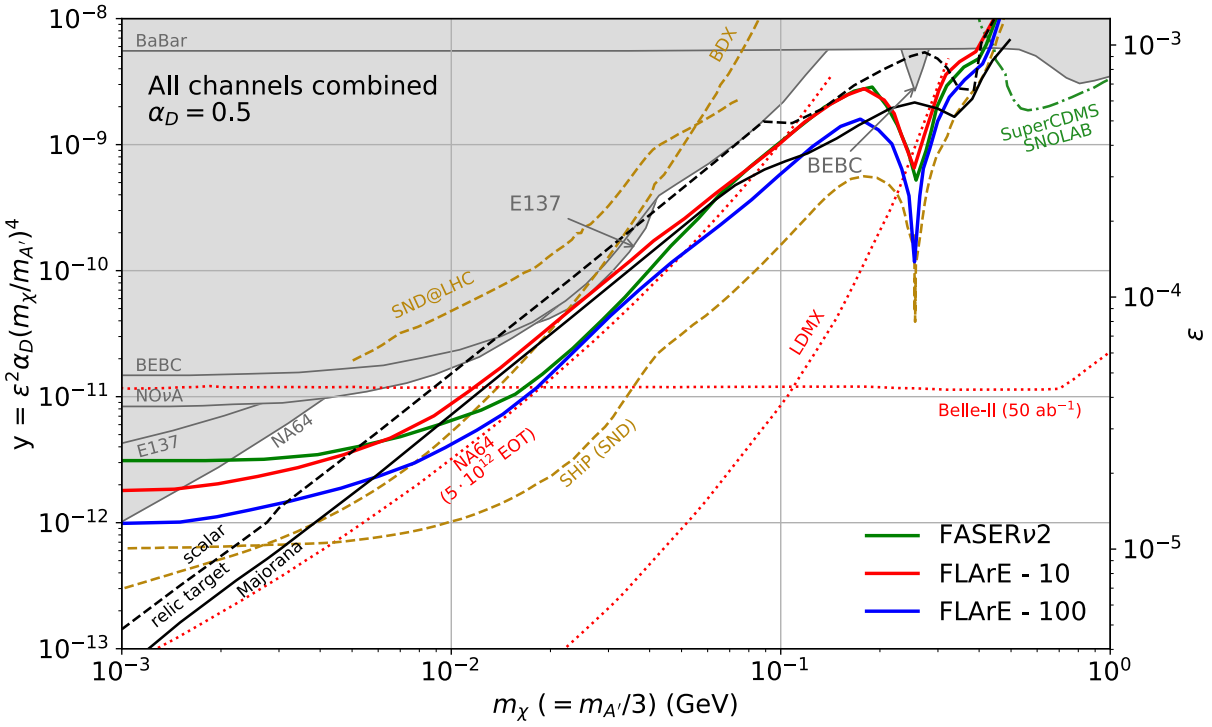

Figure 42: The projected 90% CL exclusion bounds combining all channels for the FASERν2, FLArE-10, and FLArE-100 detectors at the HL-LHC with 3 ab^{-1} of integrated luminosity. At lower DM mass the DM-electron signature is the best, whereas, at higher masses, DIS provides the most stringent limits. Existing constraints and projected reaches from other experiments are as in Fig. 41.

MiniBooNE [27], and NA64 [420], as well as recasts of searches at BEBC [421], CHARM-II [422], E137 [423,424], LSND [382], and NOνA [425], as derived by the authors of Refs. [26, 426]. Projected sensitivities of future experiments are shown in the dashed and dotted colored contours. We also note that future short baseline neutrino experiments such as ICARUS could also be sensitive to DM scattering [26]. The brown contours are projected sensitivities from searches for DM that is produced at a collider or beam dump and then subsequently scatters in a downstream detector, a signature similar to what we have considered in this work. These include BDX [427], SND@LHC [403], and SND@SHiP [428]. The red contours are projected sensitivities of future missing momentum-type searches, including NA64 [429], LDMX [398, 430], and Belle-II [431]. Last, the green contour shows the projected sensitivity of SuperCDMS to the Majorana fermion DM model [393, 398, 430]. The region probed by SuperCDMS is at higher masses than are probed by FLArE-10. For the complex scalar DM model, direct detection limits can be more constraining, but they can also be evaded by the introduction of a small mass splitting between the DM states so that the scattering is inelastic.

Figure 42 then shows the best limits from each of the detectors in Sec. 8.3. As for FLArE-10 in Fig. 41, the best limits arise from electron scattering and nuclear DIS in the low and high mass ranges, respectively. Both FASERν2 and FLArE-10 will probe the relic target for the complex scalar DM model for DM masses between several MeV and a few hundred MeV. FLArE-100 could provide a similar reach for the Majorana fermion DM model. Altogether, the detectors we have studied are able to probe a wide swath of the cosmologically-favored parameter space for both the Majorana fermion and complex scalar DM models.

Finally, to estimate the time scales on which forward LHC searches could start to achieve new sensitivity to light DM, we show the 90% projected exclusion bounds at FLArE-10 for a selection of integrated luminosities in Fig. 43. Again, the best limits from all processes (elastic proton scattering, resonant pion production, DIS, and electron scattering) have been used. With around 30 fb^{-1} of data, these searches can begin to test thermal DM scenarios

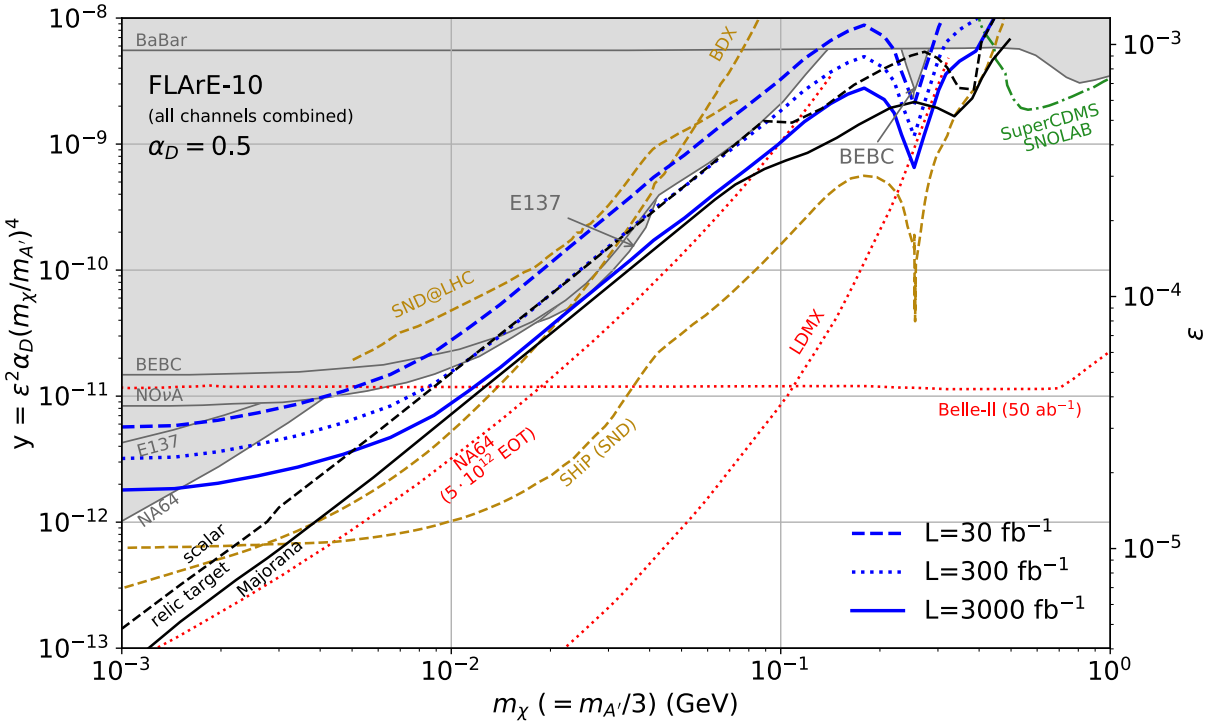

Figure 43: The projected 90% CL exclusion bounds for the FLArE-10 detector combining all channels for the three integrated luminosities indicated. New parameter space will start to be probed even for an integrated luminosity of order 30 fb^{-1}. Existing constraints and projected reaches from other experiments are as in Fig. 41.

that are thus far unconstrained. In addition, the 5σ discovery reach as a function of m_χ is a factor of approximately 1.6 in y above the projected exclusion bounds. As a result, DM can be discovered at the 5σ level with 3000 fb^{-1} for DM masses of 3 – 10 MeV and 50 – 300 MeV.

7.8 Conclusions

The search for terrestrial DM production is a major component of the physics programs of particle accelerator and collider facilities. This avenue is especially useful in the case of sub-GeV DM, where traditional direct detection experiments lose sensitivity. Such light DM at the LHC would be dominantly produced at high rapidities beyond the reach of the

general-purpose detectors, motivating dedicated experiments in the far-forward direction. In this work, we have studied potential DM scattering signals in forward detectors at the HL-LHC, as would be possible at the FPF. Our focus has been on interactions between DM and nuclei, complementing previous work on DM-electron scattering.

We have considered detectors based on both emulsion and liquid argon technology. With the use of timing information, it would be possible to reject muon-induced backgrounds, including those from neutral hadron interactions. We thus expect that the dominant backgrounds will be from neutrino scattering. Indeed, the scattering processes that we have considered are analogous to SM processes with neutrinos: elastic scattering, resonant pion production, and DIS. For each of these processes, we have estimated the DM signal and neutrino background, investigating the differences due to kinematics and incorporating the effects of nuclear FSI as appropriate. We find that for DM scattering through a light mediator, it is possible to mitigate neutrino backgrounds with kinematic cuts favoring events with low momentum transfer. This strategy is effective because the heavier weak gauge bosons cause neutrino backgrounds to prefer high Q^2 scattering. Similar considerations apply to other signatures, and it would be interesting to study whether additional sensitivity could be obtained with other processes. These include coherent scattering, coherent pion production, and multiple meson production.

Looking at benchmark models with light DM interacting through the minimal dark photon portal, we find new sensitivity in the MeV to GeV mass range. With either complex scalar or Majorana fermion DM, the searches here would test regions of parameter space in which the observed relic density is obtained through thermal freeze-out. As the characteristic energies of the processes that we have studied are different, they have complementary sensitivities. When these searches are combined with those for DM-electron scattering, FASERν2 and FLArE-10 could cover the relic target for complex scalar DM for DM masses between several MeV and several hundred MeV. FLArE-100 would provide sensitivity to the relic target in a similar mass range for Majorana DM, which is not probed by current experiments.

All of these experiments cover much of the parameter space in which the thermal relic density does not overclose the Universe, and they have the potential to provide direct evidence for DM interactions, in contrast to missing momentum-based searches at accelerator and beam dump facilities. Notably, currently unconstrained regions of parameter space can start to be probed with even the first $\mathcal{O}(30)$ fb^{-1} of integrated luminosity at the HL-LHC.

The forward region of the LHC offers exciting possibilities to study physics within and beyond the Standard Model. The FPF would extend the reach of the LHC, providing qualitatively new discovery potential in well-motivated theories of light dark sectors. In addition to electron scattering, a suite of nuclear scattering searches at the FPF detectors can be performed to improve our understanding of the nature of DM. In searching for DM and beyond, further exploration of the unique environment provided by the far-forward region at the LHC is warranted to fully leverage collider probes of new physics.

CHAPTER VIII

HADROPHILIC DARK SECTORS AT THE FORWARD PHYSICS FACILITY

8.1 Introduction

Searches for new particles and dark matter (DM) are primary physics drivers at the Large Hadron Collider (LHC). Traditional searches for the classic missing p_T signature at the LHC main detectors have sensitively searched for particles with weak-scale masses and $\mathcal{O}(1)$ couplings to Standard Model (SM) particles, but are less effective for light and weakly coupled new particles, including long-lived particles (LLPs) and DM. Recently it has been appreciated that new experiments in the far-forward region at the LHC can provide a powerful probe of new light particles. These experiments exploit the large forward flux of pions and other SM particles, which, if they decay to new light particles, can create a large forward flux of LLPs and DM. Light new physics species can also be produced in the far-forward region of the LHC in other types of interactions, including proton-proton bremsstrahlung and the Drell-Yan process. The recent detection of TeV neutrino candidates in the forward region [432] also opens a new window on neutrinos at colliders, which may be used to probe both SM and beyond the SM (BSM) phenomena [9, 39, 403].

In evaluating any proposal for new physics at the MeV to GeV mass scale, one must carefully consider all of the existing constraints from particle and nuclear experiments carried out over the last 60 years. To do this requires a model framework. The dark photon model has been discussed at length in the literature. It is theoretically attractive and contains within it phenomenologically-viable benchmark scenarios of light thermal DM. Of particular relevance

for this study, previous studies in the dark photon framework have established the potential for forward experiments to detect both LLPs [41,181] and light thermal DM [25,264]. At the same time, the experimental signatures of a given dark sector model are, to a large extent, determined by the interactions of the mediator with the SM. To more fully evaluate the physics potential of proposed experiments, then, a variety of phenomenologically distinct mediators must be examined. Since the LHC is a pp collider, it is natural to consider mediators with hadrophilic couplings, i.e., sizable couplings to quarks, but suppressed couplings to leptons. Although such models are challenging to test at electron facilities (e.g., Belle-II [433], NA64 [434], LDMX [430], and SENSEI [435]), one might suspect that they can be sensitively probed at proton facilities, such as the LHC.

In this work we study the prospects for probing two dark sector models with hadrophilic vector boson mediators. The first model is based on a gauged $\mathrm{U}(1)_B$ baryon number symmetry (see, e.g., Refs. [384, 385, 436–438]). This model is perhaps the first example of a hadrophilic model one might consider, since it has sizable couplings to quarks and (loop-)suppressed couplings to all leptons. The model suffers from gauge anomalies, however, which potentially lead to stringent constraints from rare FCNC and Z boson decays [439,440]. We will evaluate the prospects for discovering new physics in this model, carefully respecting all anomaly constraints, as well as those from other experimental searches. We note that anomaly-free extensions of the SM with a local $\mathrm{U}(1)_B$ symmetry and DM have been constructed in Refs. [441–444], which focus on the case of new particle masses above the weak scale.

As a second example we consider a model with a $\mathrm{U}(1)_{B-3L_\tau}$ vector boson mediator. (In the rest of this chapter, we will use the modest abbreviation of $\mathrm{U}(1)_{B-3\tau}$ for this symmetry.) With the addition of a right-handed neutrino, this symmetry is anomaly free and therefore evades the most stringent rare decay constraints present in the $\mathrm{U}(1)_B$ model. This model is also hadrophilic, in the sense that couplings to electrons, muons, and their accompanying neutrinos are suppressed. However, the presence of τ and ν_τ couplings brings with it both

additional constraints from neutrino nonstandard interactions (NSI), and also new opportunities for signals involving the 3rd generation leptons. A goal of this study is to incorporate all these new constraints and see what discovery prospects remain.

We will consider both current and proposed far-forward experiments. In the last two years, the magnetic spectrometer and tracking detector FASER [177], and the two emulsion detectors FASERν [170] and SND@LHC [257] have been approved. FASER has been fully constructed, and all three are expected to begin taking data when Run 3 starts in 2022. For the High Luminosity LHC (HL-LHC) era, detectors under consideration include upgrades of these detectors (FASER2, FASERν2, and Advanced SND), as well as the Forward Liquid Argon Experiment (FLArE) [25].[1] A new facility, the Forward Physics Facility (FPF) [39, 446], has been proposed to accommodate these experiments.

Remarkably, we will find that all of these detectors have discovery prospects for the hadrophilic models we consider. The possible signals include DM deep inelastic scattering (DIS) and elastic scattering, enhanced predictions for neutrino neutral current (NC) scattering, an excess of tau neutrinos in the forward region, and the visible decay of the dark mediators into SM final states. Notably, the visible decays include final states, such as $\pi^+\pi^-\pi^0$, $\pi^0\gamma$, K^+K^-, and K_SK_L, that could conceivably appear in FASER at LHC Run 3; such states are inaccessible at FASER in dark photon models. The signals are diverse and require a similarly diverse set of experiments to find them, and when combined, the experiments probe parameter space even beyond the DM thermal targets. These models therefore add to the broad physics portfolio of the FPF, complementing other studies of long-lived particle searches, collider-produced TeV-energy neutrinos, new probes of QCD, and high-energy astroparticle physics [39].

The chapter is organized as follows. In Sec. 8.2 we introduce the two hadrophilic dark sector models based on the $\mathrm{U}(1)_B$ and $\mathrm{U}(1)_{B-3\tau}$ gauge symmetries and discuss the production

[1] As a potential upgrade of milliQan [445], a fifth experiment, FORMOSA [276], has also been proposed to carry out dedicated searches for milli-charged particles and similar signatures.

and decays of the vector boson mediator, the DM thermal relic abundance, and the existing constraints for each model. Next, we present our assumptions regarding the performance of FASER, FASER2, SND@LHC, FASERν2, and FLArE in Sec. 8.3. In Sec. 8.4 we outline our methodology for estimating the sensitivity of these far-forward detectors to the new physics signatures predicted in these hadrophilic models. Our main results are contained in Sec. 8.5, and our conclusions and outlook are presented in Sec. 8.6.

8.2 Models of Hadrophilic Physics

8.2.1 Models

With the motivation outlined in Sec. 8.1, we begin in this section by describing the two representative hadrophilic dark sector models based on the anomalous $\mathrm{U}(1)_B$ and anomaly-free $\mathrm{U}(1)_{B-3\tau}$ gauge symmetries.[2] Since the new gauge group is Abelian, the new vector gauge boson generically mixes with the SM photon through a kinetic mixing term $F_{\mu\nu}V^{\mu\nu}$, where $F_{\mu\nu}$ and $V_{\mu\nu}$ are the field strengths of the SM photon and new gauge boson, respectively. In the physical mass basis, the Lagrangian of the vector boson mediator V_μ is

$$\mathcal{L} \supset -\frac{1}{4}V_{\mu\nu}V^{\mu\nu} + \frac{1}{2}m_V^2 V_\mu V^\mu + V_\mu(J^\mu_{\mathrm{SM}} + J^\mu_\chi) \ , \tag{8.2.1}$$

where m_V is the vector boson mass, J^μ_{SM} is a current composed of SM fields, and J^μ_χ is the current for the dark matter particle χ.

The SM current is

$$J^\mu_{\mathrm{SM}} = g_V[J^\mu_B - 3x(\overline{\tau}\gamma^\mu\tau + \overline{\nu}_\tau\gamma^\mu P_L\nu_\tau)] + \varepsilon\, e\, J^\mu_{\mathrm{EM}} \ , \tag{8.2.2}$$

[2]The cancellation of gauge anomalies in the $\mathrm{U}(1)_{B-3\tau}$ model requires the introduction of a right-handed neutrino with $B-3\tau$ charge of -3. In this study we assume that the right handed neutrino is somewhat heavier than the vector boson mediator, which can be achieved by coupling it to the dark Higgs field that spontaneously breaks $\mathrm{U}(1)_{B-3\tau}$. In principle the heavy neutrino mass could reside anywhere in the range below m_V/g_V. Depending on its mass and mixing with SM neutrinos there could be additional signatures beyond the core phenomenology outlined below. These are beyond the scope of our study, but see Ref. [186] for the sub-GeV case and far-forward searches.

where $g_V \equiv \sqrt{4\pi\alpha_V}$ is the new U(1) gauge coupling, J_B^μ and $J_{\rm EM}^\mu$ are the baryon number and electromagnetic currents, respectively, ε is the kinetic mixing parameter, and $x = 0$ (1) for the $\mathrm{U}(1)_B$ ($\mathrm{U}(1)_{B-3\tau}$) model.

To specify J_χ^μ, we must choose the DM candidate χ. We will study both complex scalar DM and Majorana fermion DM in this work, with Lagrangians

$$\mathcal{L} \supset \begin{cases} |\partial_\mu \chi|^2 - m_\chi^2 |\chi|^2 \,, & \text{complex scalar} \\ \\ \dfrac{1}{2}\overline{\chi} i\gamma^\mu \partial_\mu \chi - \dfrac{1}{2} m_\chi \overline{\chi}\chi \,, & \text{Majorana fermion} \,, \end{cases} \tag{8.2.3}$$

where m_χ is the DM mass. The associated currents, J_χ^μ in Eq. (8.2.1), are

$$J_\chi^\mu = g_V Q_\chi \begin{cases} i\chi^* \overset{\leftrightarrow}{\partial^\mu} \chi \,, & \text{complex scalar} \\ \\ \dfrac{1}{2}\overline{\chi}\gamma^\mu\gamma^5\chi \,, & \text{Majorana fermion} \,, \end{cases} \tag{8.2.4}$$

where Q_χ is the charge of the DM under the new gauge symmetry. As we will discuss below, both complex scalar and Majorana fermion DM exhibit velocity-suppressed P-wave annihilation to SM final states, implying that bounds from precision measurements of the cosmic microwave background anisotropies [395, 396] are easily satisfied in these models. Furthermore, Majorana DM features momentum-dependent scattering in the non-relativistic regime, making it challenging to probe with DM direct detection experiments. This is not the case for complex scalar DM, and, as we will see, direct detection experiments place strong constraints on such DM for masses above the GeV scale. However, it is important to note that these constraints can also be evaded in a straightforward way by introducing a small mass splitting, which renders the scattering transition inelastic [397, 447, 448].

The full parameter space of these models is, then, specified by 5 parameters:

$$m_V,\ g_V,\ \varepsilon,\ m_\chi,\ \text{and}\ Q_\chi \,. \tag{8.2.5}$$

To reduce the parameter space, as is commonly done in the literature, we will assume a

kinetic mixing parameter of typical one-loop size,

$$\varepsilon = \frac{e\, g_V}{16\pi^2} \ . \tag{8.2.6}$$

This is the parametric size of the kinetic mixing generated by loops of SM particles charged under both electromagnetism and the new gauge symmetry. The kinetic mixing depends, in general, on the details of the UV physics and therefore cannot be determined unambiguously, but we neglect such effects here; see also Ref. [449] for further discussion of this issue. Throughout our study we will also adopt another common convention,

$$m_V = 3m_\chi \ , \tag{8.2.7}$$

so that DM annihilation proceeds to SM particles through a virtual s-channel vector boson mediator.

Given the assumptions of Eqs. (8.2.6) and (8.2.7), the resulting parameter space may be specified by the three parameters

$$m_V, \ g_V, \ \text{and} \ Q_\chi \ . \tag{8.2.8}$$

We will present our results in the (m_V, g_V) plane with various choices for Q_χ. Since the new symmetries are Abelian, the charge Q_χ may be any real number. When presenting our results below, we will consider two choices for coupling hierarchies. As a first scenario, we will consider DM and SM particles to have comparable interaction strengths with the vector boson mediator, fixing

$$Q_\chi = \begin{cases} 1 \, , \ \mathrm{U}(1)_B \ \text{models} \\ \\ 3 \, , \ \mathrm{U}(1)_{B-3\tau} \ \text{models} \ . \end{cases} \tag{8.2.9}$$

In the $B-3\tau$ model, we have fixed the DM charge to be opposite that of the ν_τ, $Q_\chi = -Q_\tau$. As a second, qualitatively distinct, scenario, we consider the case in which the DM coupling to the vector boson mediator has a fixed value,

$$\alpha_\chi \equiv \frac{g_V^2 Q_\chi^2}{4\pi} = 0.01 \ \text{or} \ 0.5 \ . \tag{8.2.10}$$

Given that we will be considering vector boson mediators with weak couplings to the SM, that is, values of $g_V \sim 10^{-8} - 10^{-2}$, Eq. (8.2.10) implies very large DM charges Q_χ. This may appear unnatural, but there is nothing wrong in principle, since the expansion parameter α_χ remains perturbative. Ideas for achieving such large coupling hierarchies for two U(1) gauge symmetries have been presented in Ref. [398].

Finally, although we do not consider them in this work, viable models of hadrophilic scalar mediators can also be constructed; see, e.g., Refs. [450–452]. However, for the incident DM energies in the TeV range relevant for FPF experiments, scalar-mediated DM-nuclear scattering rates are typically suppressed by several orders of magnitude in comparison to vector boson-mediated scattering rates; see also Ref. [398] for a comparison of vector boson- and scalar-mediated DM scattering in the ultra-relativistic regime. For this reason, scalar-mediated DM scattering can be better probed by low- and medium-energy experiments [451]. On the other hand, experiments such as FASER and FASER2 can have powerful sensitivity to visible decays of the long-lived scalar mediator in these models, as has been demonstrated in Ref. [453].

8.2.2 Production and Decay of the Vector Boson Mediator

In our simulations, we model the production of light dark vector bosons in the far-forward region of the LHC by employing the `FORESEE` package [453]. We thereby include dark vector boson production by light meson decays, proton bremsstrahlung,[3] and the Drell-Yan process. We observe that typically the production of dark vector bosons in light meson decays dominates if kinematically allowed. For the dark vector bosons heavier than the η meson, the most important production mode is due to bremsstrahlung, while the Drell-Yan process

[3]The modeling of dark vector boson production via proton bremsstrahlung in `FORESEE` is based on the Fermi-Weizsacker-Williams approximation presented in Refs. [22, 409]. Recently, Ref. [454] studied this process using an alternative model of nucleon interactions based on Pomeron exchange, finding production rates that are smaller by a factor of a few. These estimates provide a sense of the theoretical uncertainty inherent in this process.

starts to dominate for $m_V > 1.5$ GeV.

We then consider various decay final states of the dark vector bosons. In particular, the partial decay width for $V \to \chi\chi^*$ is

$$\Gamma_{\chi\chi^*} = \kappa \frac{\alpha_\chi m_V}{12} \left(1 - \frac{4m_\chi^2}{m_V^2}\right)^{3/2}, \tag{8.2.11}$$

where $\kappa = 1$ and 2 for complex scalar and Majorana DM, respectively. The partial decay width into hadrons and other SM particles is taken from the `DarkCast` package [455], which used data-driven methods to estimate the hadronic width. An alternative description has also recently been implemented in `Herwig 7`; see Ref. [456].

In Fig. 44, we present the corresponding decay branching fractions for both of the models assuming the Q_χ charge as in Eq. (8.2.9). In the case of the $U(1)_B$ model, LLP decays into lepton pairs are always subdominant, since they appear only at the loop level through the vector boson mixing with the photon. In contrast, the invisible branching fraction of $V \to \chi\chi^*$ is close to unity for light vector boson masses up to the ω-resonance region, $m_V \approx m_\omega \simeq 782$ MeV. This leads to an intense flux of DM particles, which can be detected via DM scatterings, as we will discuss in Secs. 8.4.1 and 8.4.2. For heavier dark vector bosons, decays into light hadrons start to play an important role and can lead to additional signatures in the detectors, as we will see in Sec. 8.4.5.

For the $B - 3\tau$ model with the dark charge set to $Q_\chi = 3$, we obtain $\mathrm{BR}(V \to \chi\chi^*) \sim (10 - 20)\%$ up to the tau threshold, above which $V \to \tau^+\tau^-$ decays become kinematically allowed. The remaining decay rate for lighter dark vector bosons is dominantly into tau neutrinos, $V \to \nu_\tau \overline{\nu}_\tau$. As will be discussed in Sec. 8.4.4, this can contribute to the total ν_τ flux measured at the FPF. The decays into hadrons also become important for certain values of m_V, especially around the ω- and ϕ-resonance regions.

8.2.3 Thermal Relic Abundance

Thermal targets, that is, the regions of parameter space where DM annihilates in the early Universe through thermal freezeout to the correct relic density, provide an important stan-

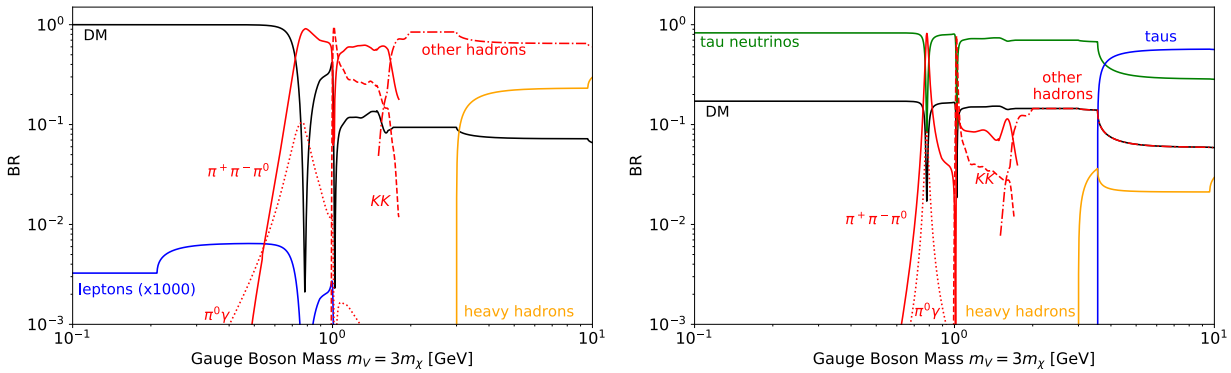

Figure 44: Decay branching fractions of the B (left) and $B-3\tau$ (right) gauge bosons for fixed $Q_\chi = 1$ and 3, respectively. The "heavy hadrons" contour includes charm and bottom hadrons, and the red contours correspond to all other hadrons. Among them, we explicitly show the dominant branching fractions into $\pi^0\pi^+\pi^-$, $\pi^0\gamma$, and kaon pairs $KK = K^+K^- + K_SK_L$. Here we assume loop-induced couplings of the bosons to charged leptons of the first two generations of size $g_\ell = g_V\,(e/4\pi)^2$. The relevant contour for boson decays into e^+e^- or $\mu^+\mu^-$, shown in the left panel, has been multiplied by a factor of 1000 for visibility. The DM is taken to be a scalar, with the decay width given in Eq. (8.2.11).

dard by which to judge the sensitivity of collider searches. These have been determined in the $\mathrm{U}(1)_B$ model with fixed $\alpha_\chi = 0.5$ in Ref. [398]. Here we determine, for the first time, the thermal targets for the $\mathrm{U}(1)_B$ model with fixed Q_χ and for the $\mathrm{U}(1)_{B-3\tau}$ model described above.

The dark matter annihilation cross section can be written in the standard resonance form,

$$\sigma_{\rm ann}(s) = \kappa\,\frac{16\pi}{s\beta_\chi^2}\,\frac{(2s_V+1)}{(2s_\chi+1)^2}\,\frac{s\;\Gamma_{\chi\chi^*}(s)\;\Gamma_{\rm SM}(s)}{(s-m_V^2)^2+m_V^2\Gamma_V^2}\,, \tag{8.2.12}$$

where $\beta_\chi(s) = (1-4m_\chi^2/s)^{1/2}$, $s_V = 1$, $s_\chi = 0$, and $\Gamma_{\chi\chi^*}(s)$ and $\Gamma_{\rm SM}(s)$ are the partial decay widths for V decaying into dark matter and SM particles, respectively, with the replacement $m_V \to \sqrt{s}$.

The thermally-averaged cross section is, then, [457]

$$\langle \sigma_{\rm ann} v \rangle = \frac{\kappa}{2} \frac{\int_{4m_\chi^2}^{\infty} \sqrt{s}(s-4m_\chi^2)\, \sigma_{\rm ann}(s)\, K_1(\sqrt{s}/T)\, ds}{8 m_\chi^4 T K_2^2(m_\chi/T)} \,, \tag{8.2.13}$$

where v is the relative velocity of the annihilating dark matter particles, and K_i is the modified Bessel function of order i. To determine the thermal target regions of parameter space, we require

$$\langle \sigma_{\rm ann} v \rangle = 4 \times 10^{-26}\ {\rm cm}^3\ {\rm s}^{-1} \,, \tag{8.2.14}$$

which reproduces the observed DM relic abundance for the masses we consider [458].

The thermal targets are presented below in Figs. 45 and 46. Their shapes can be understood as follows. In the $\mathrm{U}(1)_{B-3\tau}$ models, annihilation to tau neutrinos is allowed throughout the m_V range. The thermally-averaged cross section has the parametric dependence

$$\langle \sigma_{\rm ann} v \rangle \sim \frac{\kappa g_V^4 Q_\chi^2}{m_V^2} \sim \frac{\kappa g_V^2 \alpha_\chi}{m_V^2} \,, \tag{8.2.15}$$

and so in the $(\log m_V, \log g_V)$ plane, the thermal targets have slope 1 for the models with fixed α_χ shown in Fig. 45, and slope 1/2 for the models with fixed Q_χ shown in Fig. 46. The discrepancy between the complex scalar and Majorana fermion cases results from the fact that in the complex scalar case, there are both DM and anti-DM particles, whereas in the Majorana case, DM is its own anti-particle, which impacts the annihilation rate through the parameter κ's appearance in Eqs. (8.2.12) and (8.2.13).

For the $\mathrm{U}(1)_B$ models, the thermal target slopes are similar to those for the $\mathrm{U}(1)_{B-3\tau}$ models for $m_V \gtrsim 1$ GeV. The required couplings g_V are greater because the annihilation to tau neutrinos is absent. As m_V drops below 1 GeV, the cross section to hadrons decreases rapidly, and without a large leptonic annihilation channel, the required g_V increases rapidly to maintain a fixed $\langle \sigma_{\rm ann} v \rangle$. This continues until m_V drops below m_π, at which point all hadronic channels shut off, and only the loop-suppressed annihilation to light leptons is allowed. The curve moves further up for masses $m_V/3 = m_\chi < m_e$ where only the high velocity tail of the thermal DM population can annihilate into electrons, which needs to be

compensated by a larger coupling. However, even though only a small fraction of DM can annihilate into electrons, this is still more efficient than the annihilation into 3 photons. The latter process, $\chi\chi \to 3\gamma$ [459, 460], was found to be negligible for our study.

The resonance structure seen in all cases arises from resonant mixing of the dark gauge boson V with the SM vector mesons ρ, ω, and ϕ. In the case of DM annihilation, these resonances occur at masses $2m_V/3 = 2m_\chi = m_{\rho,\phi,\omega}$, whereas for V production, these resonances occur at $m_V = m_{\rho,\phi,\omega}$.

8.2.4 Existing Constraints

Light hadrophilic mediators have a rich phenomenology, giving rise to constraints from previous searches, as well as search opportunities at FPF experiments. Below, we summarize the various laboratory experimental constraints on light hadrophilic gauge bosons following the discussion of Ref. [461]. The resulting limits are shown in Figs. 45 and 46 as dark gray shaded regions.

Invisible Mediator Decays The focus of this study are hadrophilic mediators with a sizable branching fraction into dark matter. This decay leads to missing energy signatures which have been searched for by various experiments. The most sensitive constraints have been obtained by the search for the decay $\pi^0 \to \gamma V$ at NA62 [462] and LESB [463]; the search for the decay $\pi^0, \eta, \eta' \to \gamma V$ at Crystal Barrel [464]; the search for the decay $K^+ \to \pi^+ V$ at E949 [465] as discussed in Ref. [384, 466]; the search for the mixing induced invisible decays of the J/Ψ by BES [467] and the Υ by BaBar [468] as discussed in Ref. [384]; and the monojet search $pp \to V + \text{jet}$ at CDF [469] as discussed in Ref. [470].

Visible Mediator Decays If the couplings of the hadrophilic mediator to the SM and dark sector have similar size, decays into visible final states are possible. If the coupling is sufficiently large, the decays of the mediator occur promptly in the detector and

can be searched for via a bump hunt. Bounds have been obtained by the search for the decay $\eta' \to V\gamma \to \pi^0\gamma\gamma$ at GAMS-2000 [471] and the search for the non-electromagnetic contribution to the decay $\Upsilon(1S) \to jj$ by ARGUS [472], as discussed in Ref. [473]. In addition, there are bounds from searches for displaced decays of LLPs from NuCAL [474].

DM and Neutrino Scattering The hadrophilic mediator is copiously produced in beam dump experiments. The decay $V \to \chi\chi^*$ then leads to a dark matter beam. The MiniBooNE collaboration has searched for the scattering of χ in their downstream neutrino detector [475, 476]. Recently, even stronger bounds on coherent scatterings of leptophobic DM have been obtained with the Coherent CAPTAIN-Mills (CCM) liquid argon (LAr) detector [477]. Similarly, the decay $V \to \nu_\tau \overline{\nu}_\tau$ leads to an increased tau neutrino flux, which can be constrained using measurements from DONuT [172], as discussed in Ref. [461].

Indirect Probes A hadrophilic mediator can also be constrained indirectly through its contribution to the low-energy neutron-lead scattering cross section [478], as discussed in Ref. [479]. Additionally, a new gauge boson with couplings to tau leptons can be constrained by the measurement of the $Z \to \tau\tau$ decay width at LEP [173], as discussed in Ref. [480].

In addition, there are other constraints that are somewhat more model dependent. These are the anomaly constraints and the constraints from neutrino NSIs, which are shown as light gray shaded regions in Figs. 45 and 46, and which we now describe:

Anomaly Constraints As mentioned above, the dark vector boson in the $\mathrm{U}(1)_B$ model couples to a non-conserved SM current. Invisible decays of such a vector boson are then constrained by enhanced bounds from missing energy searches in rare Z decays and flavor-changing meson decays $K \to \pi V$ and $B \to KV$. We implement them following Refs. [439, 440], assuming that anomalies associated with the new gauge group are

canceled by heavy fermions that do not receive masses from electroweak symmetry breaking. If these anomalies were canceled by fermions with Yukawa couplings to the Higgs, the invisible decay constraints would not apply, but there would be severe LHC constraints on the additional fermions.

Neutrino NSI For the $U(1)_{B-3\tau}$ model, additional constraints arise from studying neutrino oscillations, both in vacuum and in the matter background of the Sun and Earth. These have been precisely measured by a variety of neutrino experiments. A global fit to these neutrino oscillations measurements simultaneously constrains the oscillation parameters and NSI between neutrinos and matter. We present these bounds following Ref. [481].[4] We note, however, that these constraints are model dependent and could be weakened in the presence of additional new physics.

Direct Detection Further bounds on hadrophilic DM can arise from direct detection (DD) searches [384]. These, however, depend sensitively on the detailed structure of the DM interaction and do not apply to Majorana DM and to inelastic scalar DM if the mass gap between the dark species is large enough to suppress upscatterings of non-relativistic DM particles. We stress this in the following when presenting the current DD bounds on spin-independent DM-nuclei scattering from the CRESST-III [484], DarkSide-50 [485], and Xenon 1T [356, 486] experiments. We show these bounds assuming that $\Omega_\chi h^2 \simeq 0.12$ [487] in the entire reach plot and that a non-standard cosmological scenario affects the DM relic density for points in the parameter space away from the thermal target lines.

Cosmology & Astrophysics Further indirect probes arise from possible contributions of light dark vector bosons to the number of relativistic degrees of freedom in the early Universe, $\Delta N_{\rm eff}$. We present them below following Refs. [488, 489]. Additional bounds

[4] An alternative study, which obtained slightly stronger constraints, was performed in Ref. [482] using the global fit results obtained in Ref. [483].

could arise from an enhanced supernova cooling rate of SN1987A, as discussed, for example, in Refs. [490–496]. Such constraints typically probe very small couplings outside the regions of interest for this study. In addition, they are also dependent on a number of astrophysical assumptions, which may weaken the constraints or possibly even remove them altogether; see, e.g., Ref. [497]. In the following, we do not show these bounds explicitly in our sensitivity reach plots, as a detailed study for the models considered here is beyond the scope of our analysis.

8.3 Detectors

We perform our analysis for the on-axis far-forward detectors that will operate either during LHC Run 3 or the HL-LHC era. In the latter case, we focus on the proposed FPF, which begins at a distance $L = 620$ m away from the ATLAS Interaction Point [39]. In particular, we study the expected future sensitivity of the 10-tonne emulsion detector FASERν2, a proposed successor to the FASERν experiment that will take data during LHC Run 3 [9, 170], as well as the 10- and 100-tonne fiducial mass liquid-argon time projection chamber (LArTPC) detectors FLArE-10 and FLArE-100 [25]. The relevant detector geometries are

$$\begin{aligned}
\text{FASER}\nu\text{2:}&\quad \Delta = 2\text{ m}, \quad S_T = (0.5\text{ m} \times 0.5\text{ m}),\\
\text{FLArE-10:}&\quad \Delta = 7\text{ m}, \quad S_T = (1\text{ m} \times 1\text{ m}),\\
\text{FLArE-100:}&\quad \Delta = 30\text{ m}, \quad S_T = (1.6\text{ m} \times 1.6\text{ m}),
\end{aligned}$$

where Δ is the length of the detector, and S_T denotes its transverse size.

Both types of detectors have excellent capabilities to reconstruct the low-energy nuclear scattering signals created by both neutrinos and hadrophilic DM, and also to disentangle DM-induced events from the more energetic neutrino scatterings. For these searches, however, it is also important that they be able to reject backgrounds induced by high-energy muons that pass through the facility and interact with the surrounding rock and infrastructure. To veto these muons, it is highly beneficial to collect time information about the events. In the

case of FASERν2, this would likely require interleaving the emulsion layers with additional electronic detectors. For FLArE, on the other hand, the required time resolution can be more easily obtained by employing an additional light collection system; see Ref. [25] for further discussion.

Throughout this chapter, we use the neutrino fluxes for the FPF as presented in Ref. [264]. These fluxes were obtained using the event generator `SIBYLL 2.3d` [268–271] as implemented in `CRMC` [195] to simulate the primary collision, and the fast neutrino flux simulation presented in Ref. [21] to model the propagation and decay of long-lived SM hadrons in the forward LHC infrastructure.

In addition to the aforementioned scattering detectors, we will also present sensitivities for the LLP signature of the vector boson mediator decaying to visible SM final states. To this end, we will focus on FASER [176, 177] and FASER2, cylindrical detectors with length Δ and radius R, where [181]

$$\begin{aligned} \text{FASER:}\ \ &\Delta = 1.5 \text{ m}, \quad R = 10 \text{ cm}, \quad \mathcal{L} = 150 \text{ fb}^{-1}\,, \\ \text{FASER2:}\ \ &\Delta = 5 \text{ m}, \quad\ \ R = 1 \text{ m}, \quad\ \ \mathcal{L} = 3 \text{ ab}^{-1}\,. \end{aligned}$$

FASER will take data during LHC Run 3 and will be positioned in the far-forward region at a distance $L = 480$ m away from the ATLAS IP. For FASER2 we assume the relevant parameters for the HL-LHC era and the FPF location. Above, we have also provided the relevant integrated luminosities. The multiple collisions that occur in each bunch crossing (pile-up) are accounted for in determining the flux of V.

Throughout the study, we assume perfect detection efficiency for all the events that pass the selection criteria. The probability of passing such criteria depends on the geometrical acceptance of the detectors, energy and other kinematic cuts, as well as on the final state interactions inside the nucleus that we take into account in the case of the elastic scattering. We discuss the relevant cuts for different signatures below.

We will also include in our plots the expected sensitivities of the SND@LHC detector [258] to DM scattering in the $\mathrm{U}(1)_B$ model, as determined in Ref. [28]. For the elastic DM

Signature	DM DIS	DM Elastic	ν NC DIS	ν_τ CC DIS	LLP decays
Section	Sec. 8.4.1	Sec. 8.4.2	Sec. 8.4.3	Sec. 8.4.4	Sec. 8.4.5
Models	$U(1)_B$, $U(1)_{B-3\tau}$	$U(1)_B$, $U(1)_{B-3\tau}$	$U(1)_{B-3\tau}$	$U(1)_{B-3\tau}$	$U(1)_B$, $U(1)_{B-3\tau}$
Production	$pp \to V \to \chi\chi$ 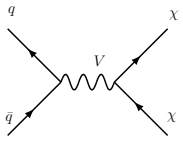	$pp \to V \to \chi\chi$ 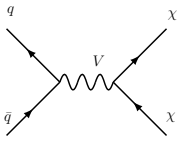	$pp \to D_s \to \nu_\tau$ 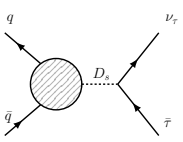	$pp \to V \to \nu_\tau \bar{\nu}_\tau$ 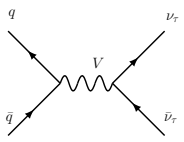	$pp \to V$ 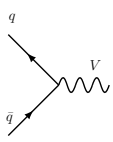
Detection	$\chi N \to \chi X$ 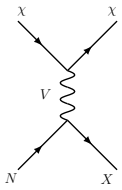	$\chi p \to \chi p$ 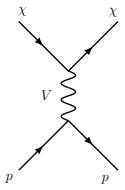	$\nu_\tau N \to \nu_\tau X$ 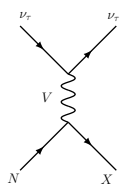	$\nu_\tau N \to \tau X$ 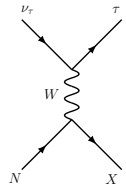	$V \to$ hadrons 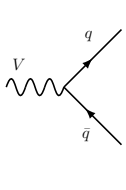
Rate scales as	$g_V^6 Q_\chi^2 \sim g_V^4 \alpha_\chi$	$g_V^6 Q_\chi^2 \sim g_V^4 \alpha_\chi$	g_V^4	g_V^2	$g_V^2 e^{-g_V^2 m_V^2}$ or g_V^4
Background	$\nu\ N \to \nu\ X$	$\nu\ p \to \nu\ p$	$\nu\ N \to \nu\ X$	$D_s \to \nu_\tau \tau$	None

Table 13: The signatures studied. In the first three rows, the name of the signature, the subsection in which it is discussed, and the relevant new physics models are given. In the 4th and 5th rows, we show the Feynman diagrams for some example production and detection processes, respectively. The production processes shown are not necessarily the dominant ones. The 6th row shows the dependence of the signal rate on the model parameters, and the 7th row lists the dominant SM backgrounds.

scattering signature, this analysis assumed that backgrounds from muon-induced hadrons and photons can be rejected and that the number of neutrino-induced events can also be suppressed to a negligible level. In the DIS regime, the analysis estimated that pure neutrino-induced backgrounds could be reduced to $\mathcal{O}(1000)$ events, and the sensitivity curves were taken to be $N = 100$ DM signal event contours.

8.4 Signatures

The hadrophilic models we are considering produce a diverse array of new physics signatures. These are shown in table 13, where we list which models are relevant for each signature, the dominant production and detection processes that determine the signal rates, the dependence of these rates on the model parameters, and the dominant SM backgrounds. As can be seen,

the FPF experiments will be sensitive to direct signals generated by both the dark vector boson and DM, as well as to neutrino-induced signals. We now discuss them all in detail.

8.4.1 DM Deep Inelastic Scattering

We first consider DM DIS off nuclei, $\chi N \to \chi X$. At large momentum transfer, DM DIS produces a significant hadronic recoil with multiple charged tracks. The main background is SM neutrino NC interactions. Due to the light mediator, DM scattering prefers lower momentum transfer than the neutrino background, which proceeds through Z-boson exchange. Our discussion of this signature closely follows that in Ref. [264].

The differential cross section for complex scalar DM DIS in the models of Sec. 8.2 is given by

$$\frac{d\sigma(\chi N \to \chi X)}{dx\ dy} = 4\pi\alpha_\chi\alpha_V \frac{2m_p E_\chi}{(Q^2+m_{A'}^2)^2} \times \sum_{q=u,d,s,c} (1-y)\left[x f_q(x,Q^2) + x f_{\bar{q}}(x,Q^2)\right], \quad (8.4.1)$$

where x is the parton momentum fraction, $y = 1 - E'_\chi/E_\chi$ is the fraction of the incoming DM energy transferred to the nucleon in the lab frame, $Q^2 = 2m_p E_\chi xy$ is the squared momentum transfer, and f_q is the quark parton distribution function. We use the nCTEQ15 parton distribution functions [191] for tungsten and argon and integrate Eq. (8.4.1) requiring $Q^2 > 1$ GeV^2 to obtain the expected numbers of DM DIS events in the FPF detectors. We also require the energy transferred to the hadronic system to be 1 GeV $< E_{\rm had} <$ 15 GeV, where $E_{\rm had} = yE_\chi$, and the total transverse momentum of the recoiling hadrons to be 1 GeV $< p_{T,\rm had} <$ 1.5 GeV, where $p_{T,\rm had}^2 = Q^2(1-y)$. For the background, we calculate the expected numbers of neutrino NC scattering events satisfying the same cuts on Q^2, $E_{\rm had}$, and $p_{T,\rm had}^2$. Our cuts favor softer hadronic recoils, eliminating much of the neutrino NC background. Our projected sensitivities assume perfect detector efficiency and consider only statistical uncertainties. A previous study [264] of DM DIS at FLArE found that some experimentally motivated cuts did not have a large effect on the signal, but a full study remains to be performed.

8.4.2 DM-Nucleon Elastic Scattering

The light DM particles produced in the far-forward region at the LHC can also be discovered via their elastic scatterings with nucleons, which lead to single proton tracks visible in the detector. We treat this signature following Ref. [264], in which we have also studied the relevant neutrino-induced backgrounds. In particular, when presenting the sensitivity contours, we require the momentum of the outgoing proton to be within the range 300 MeV $< p_p <$ 1 GeV in FASERν2, and for FLArE we require $p_p < 1$ GeV and the proton's kinetic energy to satisfy $E_{k,p} > 20$ MeV. We also reject events in which other visible tracks emerge from the vertex. After these cuts, we expect $\sim$ 100, 1000, and 300 background events during the entire HL-LHC run for FLArE-10, FLArE-100, and FASERν2, respectively.

The elastic scattering cross section for the complex scalar DM interacting with the neutron or proton via the hadrophilic gauge boson is

$$\frac{d\sigma(\chi p \to \chi p)}{dQ^2} = \frac{4\pi\alpha_\chi\alpha_V Q^2}{(E_\chi^2 - m_\chi^2)(m_V^2+Q^2)^2} \times \Big\{ A(Q^2) + \left(\frac{E_\chi}{Q} - \frac{Q}{4m_N}\right)^2 \Big[(\tilde{F}^B_{1,N})^2 + \tau (\tilde{F}^B_{2,N})^2 \Big] \Big\}, \tag{8.4.2}$$

where $Q^2 = 2\,m_N\,(E_N - m_N)$ is the squared four-momentum transfer in terms of the nucleon mass m_N ($N = n, p$) and the outgoing nucleon energy E_N, and E_χ corresponds to the incident DM energy. The term proportional to $A(Q^2)$, which contributes negligibly to the cross section at high energies, is given by

$$A(Q^2) = -\frac{1}{4}\,(\tilde{F}^B_{1,N} + \tilde{F}^B_{2,N})^2 \,\left(\tau + \frac{m_\chi^2}{m_p^2}\right), \tag{8.4.3}$$

with $\tau = Q^2/(4m_p^2)$. In contrast to the case of a vanilla dark photon mediator, the neutron and proton form factors are identical in this case and given by

$$\tilde{F}^B_{1,N}(Q^2) = \frac{1 + (\mu_p + \mu_n)\,\tau}{1+\tau}\, G_D(Q^2)\ , \tag{8.4.4}$$

$$\tilde{F}^B_{2,N}(Q^2) = \frac{\mu_p + \mu_n - 1}{1+\tau}\, G_D(Q^2)\ , \tag{8.4.5}$$

where $\mu_p = 2.793$, $\mu_n = -1.913$, and $G_D(Q^2) = (1 + Q^2/M^2)^{-2}$, with $M = 0.843\,\text{GeV}$. The differential elastic scattering cross section becomes form-factor suppressed at large mo-

mentum transfers, and the total elastic cross section is dominated by the contribution from $Q^2 \lesssim m_V^2$.

In the following, we include scatterings off both protons and neutrons. For protons, we include the efficiency factors $\sim (50-70)\%$ related to the final-state interactions (FSI) of protons, as in Ref. [264]. For neutrons, we include similar efficiency factors in the range $(15-30)\%$, which have been obtained as a function of the outgoing neutron momentum by studying neutrino interactions in `GENIE` [23, 24]. In this case, the neutron re-scatterings inside the nucleus can lead to an outgoing proton with momentum within the aforementioned cuts and with no other detectable tracks. We find that scatterings of DM off neutrons can contribute up to 25% to the total elastic event rate.

8.4.3 Enhanced Neutrino Neutral Current Scattering

When a new mediator couples to neutrinos, NC scattering $\nu N \to \nu X$ receives an additional contribution from the mediator. The signature is identical to that for DM DIS. However, as NC scattering depends only on the couplings of the mediator to quarks and neutrinos, there is no dependence on m_χ or Q_χ, unlike the case of DM scattering. In particular, for the $B-3\tau$ mediator, the total ν_τ NC cross section becomes

$$\begin{aligned}\frac{d\sigma(\nu N \to \nu X)}{dx\, dy} = \frac{m_p E_\nu}{4\pi} \times \sum_{q=u,d,s,c} \Big\{ & c_L^2 \left[x f_q(x,Q^2) + x(1-y)^2 f_{\bar{q}}(x,Q^2) \right] \\ & + c_R^2 \left[x(1-y)^2 f_q(x,Q^2) + x f_{\bar{q}}(x,Q^2) \right] \Big\} ,\end{aligned} \tag{8.4.6}$$

where

$$c_{L/R} = \frac{(g_W\, g_{\nu,L})(g_W\, g_{q,L/R})}{\cos^2\theta_W (Q^2 + m_Z^2)} + \frac{1}{4} \frac{(g_V^2 Q_\nu Q_q)}{(Q^2 + m_V^2)} \, . \tag{8.4.7}$$

Here g_W is the SM weak coupling, $g_{\nu,L} = \frac{1}{2}$, and $g_{q,L} = \frac{1}{2} - \frac{2}{3}\sin^2\theta_W$ for up-type quarks and $-\frac{1}{2} + \frac{1}{3}\sin^2\theta_W$ for down-type quarks. The second term in $c_{L,R}$ is the contribution from the new $B-3\tau$ mediator with charges $Q_\nu = -3$ (3) for ν_τ ($\bar{\nu}_\tau$), and $Q_q = \frac{1}{3}$ for all quarks. The interference term is proportional to $Q_\nu Q_q$, and so carries opposite signs for ν_τ and $\overline{\nu}_\tau$ NC scattering [498]. At the FPF where we expect almost equal fluxes of ν_τ and $\bar{\nu}_\tau$, this implies

a small contribution from the interference term after cancellations. Nevertheless we use the complete expression above in our analysis.

For small m_V, the BSM contribution to NC scattering prefers low recoil energy, similar to DM DIS and unlike the weak boson-mediated SM process, whose cross section grows with momentum transfer. We calculate the number of additional NC events expected at the FPF with Eq. (8.4.6), using the same parton distribution functions and minimum Q^2 cut as in Sec. 8.4.1. Because of the small relative flux of tau neutrinos compared to muon and electron neutrinos, the impact of the light mediator on the total NC cross section must be significant to provide a sizable effect relative to the SM NC background.

In testing whether an excess of NC events is observable, we consider only statistical uncertainties and neglect systematic uncertainties. For simplicity, we also assume perfect detection efficiency for NC interactions; the inclusion of realistic detection efficiencies [266] would not substantially change the positions of the limits from excess NC events in Figs. 45 and 46, relative to the other signatures that we consider. We note that the main systematic uncertainty in the NC cross section measurement, the neutrino flux, can be constrained by measurements of charged current (CC) interactions. We find a statistically significant effect from the BSM contribution to NC scattering when the coupling to mass ratio of the new interaction is comparable to that of the weak interaction, $g_V/m_V \gtrsim g_W/m_W \approx 10^{-2}$ GeV^{-1}.

8.4.4 Excess of Tau Neutrino Flux

In the case of the gauged $B-3\tau$ scenario, the hadrophilic mediator decays into tau neutrinos with a sizable branching fraction.[5] As discussed in Ref. [461], this opens another opportunity to probe this model via their contribution to the LHC tau neutrino flux. In the SM, tau neutrinos are mainly produced via $D_s \to \nu\tau$ and subsequent τ decays, which occurs in

[5]Additional ν_τ flux can be produced via V decays into tau leptons for $m_V \gtrsim 2\,m_\tau$. However, the corresponding expected sensitivity lies in a region of parameter space that is already excluded, as shown in Sec. 8.5.

roughly one in 10^5 collisions at the LHC. This means that even rare BSM processes could lead to sizable contributions to the tau neutrino flux. The relevant detection channel in this case is via ν_τ CC scatterings off nuclei. The displaced decays of the outgoing boosted tau lepton must then be identified in the detector, requiring excellent spatial resolution.

An important issue that arises when searching for signs of new physics is the large uncertainty on the normalization of the SM tau neutrino flux [21, 283]. Although future efforts are expected to reduce these uncertainties, we will follow a different approach. In contrast to tau neutrinos from charm and tau decays, which have a broader angular spread, tau neutrinos from light mediator decays are more centered around the beam collision axis. In this study, we use this feature and perform a shape analysis of the ν_τ angular distribution, which does not rely on knowledge of the neutrino flux normalization. We focus on the FLArE-10 design, whose 1 m $\times$ 1 m cross sectional area is sufficiently large to capture this effect. More precisely, we define five concentric rectangular bins centered around the beam collision axis and corresponding to the distance between d and $d + 10$ cm away from it, where $d = 0, 10, 20, 30, 40$ cm. In practice, the most important contribution to the BSM-induced excess of ν_τs is from the two most central bins, i.e., at distances up to $d \lesssim 20$ cm away from the beam collision axis.

8.4.5 Visible Decays of the Dark Vector Boson

In the following, we study the decay signature using the `FORESEE` package [453] with the lifetimes modeled with `DarkCast` [455] and the spectrum of light hadrons obtained from EPOS-LHC [193]. We assume 100% detection efficiency for all visible final states. We present the results for both FASER and FASER2. In the analysis, we require the total energy of the visible products of the vector boson decays to be at least 100 GeV. This cut has a minor impact on the BSM signal events, but suppresses possible SM backgrounds to a negligible level [176,177]. Visibly decaying dark vector bosons could also appear in secondary production processes due to DM scatterings occurring right in front of or even inside the

detector [184]. We neglect the impact of such processes below, as we do not expect them to improve the sensitivity reach of the FPF detectors in the models under study.

8.5 Results

In Fig. 45, we present the results of our analysis for both the $U(1)_B$ and $U(1)_{B-3\tau}$ models in the (m_V, g_V) plane. In the plots, we fix the DM coupling to $\alpha_\chi = 0.01$ and 0.5 in the upper and lower panels, respectively, and we keep a constant mass ratio between the dark sector particles, $m_V = 3\, m_\chi$. In dark gray, we show the existing constraints, as discussed in Sec. 8.2.4, while the black solid (dashed) lines correspond to the relic density targets for the complex scalar (Majorana) DM. We stress that, although the anomaly bounds, shown in light gray in the left panels for the $U(1)_B$ case, can be avoided in modified versions of this simplified scenario, this often leads to further constraints due to additional couplings of the dark vector bosons that are introduced in the model to make it anomaly-free. An example is shown in the right panels for the anomaly-free $U(1)_{B-3\tau}$ model, where the NSI constraints cover a good portion of the parameter space shown in the plot.

In Fig. 45, we also present the expected 90% CL exclusion bounds in searches for DM scatterings off nuclei in the elastic (dark red) and DIS (light red) channels for FLArE-10 (solid), FLArE-100 (dash-dotted), and FASERν2 (dotted). As is clear from the plot, the elastic scattering probe is stronger for light DM and mediator masses below 1 GeV, which favor interactions with low momentum exchange. For $m_V \gtrsim 1$ GeV, the elastic scattering rate is suppressed by the form factor and the cut on the outgoing proton momentum $p_p \lesssim 1$ GeV. In this higher mass range, the search based on DIS processes provides the best reach. For comparison, we also show the expected reach of the SND@LHC detector [28] with the assumptions noted in Sec. 8.3.

For the $U(1)_B$ model with fixed $\alpha_\chi = 0.01$ shown in the upper left panel of Fig. 45, we expect that future searches at the FPF will cover almost the entire remaining allowed region in the parameter space above the Majorana and complex scalar relic target lines, in which

DM is not thermally overproduced in the early Universe. This corresponds to vector boson masses between 1 and 3 GeV. For the simple complex scalar DM model, additional stringent bounds for $m_\chi \gtrsim 200$ MeV can arise from past DM DD searches, which are indicated in the plots by the very light gray shaded regions and cover the region within the sensitivity of FLArE and FASERν2. However, these limits can be evaded in the inelastic scalar DM case and are not relevant for Majorana DM. For lower masses, (a few) MeV $\lesssim m_V \lesssim 1$ GeV, the expected FLArE and FASERν2 bounds extend beyond current constraints from the CCM, MiniBooNE, and NA62 experiments. Here, the searches at the FPF would probe regions in the parameter space that are otherwise partially excluded only by anomaly-induced rare K and Z decays.

Next, we consider the $\mathrm{U}(1)_{B-3\tau}$ model with fixed $\alpha_\chi = 0.01$ shown in the upper right panel of Fig. 45. Since the model is free of gauge anomalies, the stringent constraints from rare Z and meson decays present in the $\mathrm{U}(1)_B$ model are absent in this case. On the other hand, the additional bounds from neutrino NSI cover much of the model parameter space. Nevertheless, we observe that the FPF detectors can still explore a portion of the currently allowed parameter space, especially in the ω and ϕ resonance regions, $m_V \sim m_\omega, m_\phi$, and the corresponding part of the relic target line for complex scalar DM. In this model, additional sensitivity arises from dark vector boson-mediated scattering of tau neutrinos in the DIS regime; see Sec. 8.4.3. The relevant expected bounds, which are indicated by the light purple lines in the plots, impact parameter regions that are already excluded by past searches. We note that the actual exclusion bound in the DIS channel should be derived using the combined excess signal rates for both DM and BSM neutrino scatterings over the expected SM backgrounds. Instead, in the plot, we have presented the expected bounds for each separately to allow for independent discussion of the impact of different new physics effects.

For larger values of α_χ, the relic target lines shift downwards relative to the FPF sensitivity contours from DM scattering. This is dictated by the different parametric dependence of the annihilation cross section and the number of DM scattering events in the FPF ex-

periments on the coupling constants, $\langle \sigma v \rangle \sim g_V^2 \alpha_\chi$ and $N_{\rm ev} \sim g_V^4 \alpha_\chi$, respectively. As a result, in the lower panel of Fig. 45 obtained for $\alpha_\chi = 0.5$, we observe that both FLArE and FASERν2 will only partially cover the thermal target lines for the U(1)$_B$ model. Instead, in the U(1)$_{B-3\tau}$ case, they will typically probe regions in the parameter space predicting subdominant fractions of thermally-produced χ DM.

Thus far we have considered scenarios in which the vector boson mediator couples much more strongly to DM than to SM particles, $Q_\chi \gg 1$. In Fig. 46 we consider the different scenario in which the vector boson mediator couples with comparable strength to complex scalar DM and SM particles, with Q_χ fixed according to Eq. (8.2.9). As can be seen, for both the $U(1)_B$ and $U(1)_{B-3\tau}$ models, FLArE-10 can cover the entire relic target line in a wide vector boson mass range between 1 MeV and 10 GeV. As in the previous scenarios depicted in Fig. 45, significant portions of these regions are already constrained by either anomaly-induced or NSI bounds, as well as by the other past searches indicated in the plots. However, we emphasize that for the case of inelastic scalar DM in the U(1)$_B$ model, to which DD constraints do not apply, FLArE-10 will be able to test an interesting open region of parameter space for vector boson mass of order several GeV that is consistent with the observed DM abundance.

Fig. 46 also highlights the rich phenomenology present in scenarios with comparable DM and SM couplings to the vector boson mediator. Along with the scattering searches relevant for DM and BSM neutrino interactions, additional prospects arise at very small couplings from FPF searches for visible decays of the long-lived vector boson mediator; see Sec. 8.2.2. In particular, for m_V between several hundred MeV and a GeV and coupling $10^{-8} \lesssim g_V \lesssim 10^{-5}$, such displaced decays into visible final states, primarily light hadrons, can be detected at both FASER and FASER2. The dominant branching fraction in this case is into three pions, $\pi^0\pi^+\pi^-$, which leads to a striking signature consisting of a photon pair accompanied by two oppositely charged tracks.

We present the relevant expected 90% CL exclusion bounds on LLP decays for FASER

(dark blue) and FASER2 (light blue) in the plots. These correspond to the region of parameter space with $m_V \sim m_\omega$ or m_ϕ. Here, both the dark vector boson production via proton bremsstrahlung and its decay branching fractions into light hadrons are enhanced. The expected exclusions shown in the plot are bounded from below by the production rate of the dark vector bosons being too low, and from above by the V lifetime being too small for the boson to decay in the detectors. In the $\mathrm{U}(1)_B$ model, further sensitivity at FPF experiments can be obtained for $m_V \lesssim 10$ MeV due to loop-induced dark vector boson decay into an e^+e^- pair. This scenario is, however, already constrained by the past beam-dump search in NuCal and by the anomaly-induced bounds.

Last but not least, in the $\mathrm{U}(1)_{B-3\tau}$ model, further constraints arise due to the dominant dark vector boson decays into tau neutrinos. These can generate an excess flux of ν_τs over the expected SM production rates, which can be detected via their CC scatterings in the detector, as described in Sec. 8.4.4. The corresponding expected sensitivity is indicated by the green contour in the right panel of Fig. 46. For $m_V \lesssim 2$ GeV, this sensitivity is greater than from the DM and BSM neutrino searches. In particular, it allows one to constrain the currently allowed region of the parameter space of the model close to the ω- and ϕ-resonance regions. In this case, the increased flux of ν_τs could also further contribute to the aforementioned NC DIS signal rate due to BSM tau neutrino interactions. To isolate the impact of various new physics effects, we do not take this into account when presenting relevant expected bounds, which should thus be considered conservative. We stress that the dominant expected bound in the corresponding region of the parameter space is, in any case, due to excess CC ν_τ scatterings.

8.6 Conclusions

While the ability of the LHC to search for TeV-scale DM is well known, recently proposed dedicated experiments at high rapidity can significantly enhance the potential of the LHC to probe light DM. Beyond the minimal portal extensions of the SM that allow for light DM

and an associated mediator, new gauge groups represent a well-motivated class of possible dark sector models. In this chapter, we have explored the use of the FPF to study such U(1) theories leading to hadrophilic dark sectors. In particular, these remain beyond the reach of experiments focusing on BSM electron couplings, while they can more straightforwardly be studied at the LHC.

The suite of FPF experiments provides a comprehensive set of tests of these theories in different regions of parameter space. DM produced in pp collisions can scatter in the FASERν2 and FLArE detectors through the new light vector boson; we have considered both elastic and deep inelastic scattering. Furthermore, if the mediator has a significant decay branching ratio to SM states, the FASER2 LLP detector can search for the visible decay products. In fact, already at Run 3, the FASER detector will begin to test hadrophilic U(1) theories at couplings substantially lower than existing bounds. These hadrophilic models therefore motivate near-term searches at FASER for new LLP signatures

$$V \to \pi^0\gamma,\, \pi^+\pi^-\pi^0,\, K^+K^-,\, K_S K_L\ , \tag{8.6.1}$$

which are not motivated by dark photon models for FASER in Run 3. Finally, if neutrinos are also charged under the new gauge symmetry, additional signatures are possible in the scattering detectors. We have demonstrated that with a symmetry under which tau neutrinos are charged, the ν_τ flux and NC cross section are both enhanced, leading to potential deviations in ν_τ CC and NC scattering rates.

These results for $\mathrm{U}(1)_B$ and $\mathrm{U}(1)_{B-3\tau}$ models should be considered as illustrative of the complementarity of forward LHC experiments in searching for light dark sectors, particularly between LLP and scattering detectors. In both of these theories, the FPF can test broad regions in the coupling-gauge boson mass plane, including significant expanses over which the observed DM relic density could be obtained through standard thermal freezeout. For our benchmark scenario with scalar DM, $m_V = 3m_\chi$ and low values of the dark charge Q_χ given by Eq. (8.2.9), FPF searches can probe well below the thermal relic target lines in each model for nearly all gauge boson masses between 1 MeV and 10 GeV. Throughout our

results, the strongest searches tend to be those based on DM elastic scattering and DIS, with distinct additional reach possible from LLP searches when the mediator can decay to SM final states. For the $B-3\tau$ model, searches for an increased ν_τ flux would also test new space.

The models that we have studied face strong indirect constraints, notably from rare invisible decays and neutrino oscillations, but we emphasize that FPF searches can test couplings that are smaller than these formidable existing bounds. In addition, in the GeV mass range, these searches provide constraints that are complementary to those from spin-independent DD, the latter only being applicable in the case of elastic scalar DM.

Though we have chosen to focus on two possible gauge groups with a handful of coupling and mass assumptions, the general interplay between the DM scattering, LLP and neutrino searches is likely to persist for other theories and parameter choices. To determine the gain provided by the FPF in a particular theory, the reach of these searches must be compared against those from other bounds. As we have seen, U(1) theories that are not anomaly-free typically face rare meson decay constraints, while those with nonzero lepton charges can encounter NSI bounds. For models with couplings to 1st and 2nd generation leptons, additional limits from beam dump and neutrino experiments would likely need to be considered as well.

Forward LHC detectors offer a distinct perspective on light hidden sectors, allowing for searches for light DM and its associated mediators in an otherwise inaccessible kinematic regime. The results here underscore the utility of different types of forward detectors, as could be provided at the FPF. The multi-pronged approach to uncovering physics beyond the SM that is enabled by such a facility, along with other uses such as measurements of SM neutrino interactions and tests of QCD, bolsters the physics case for the FPF.

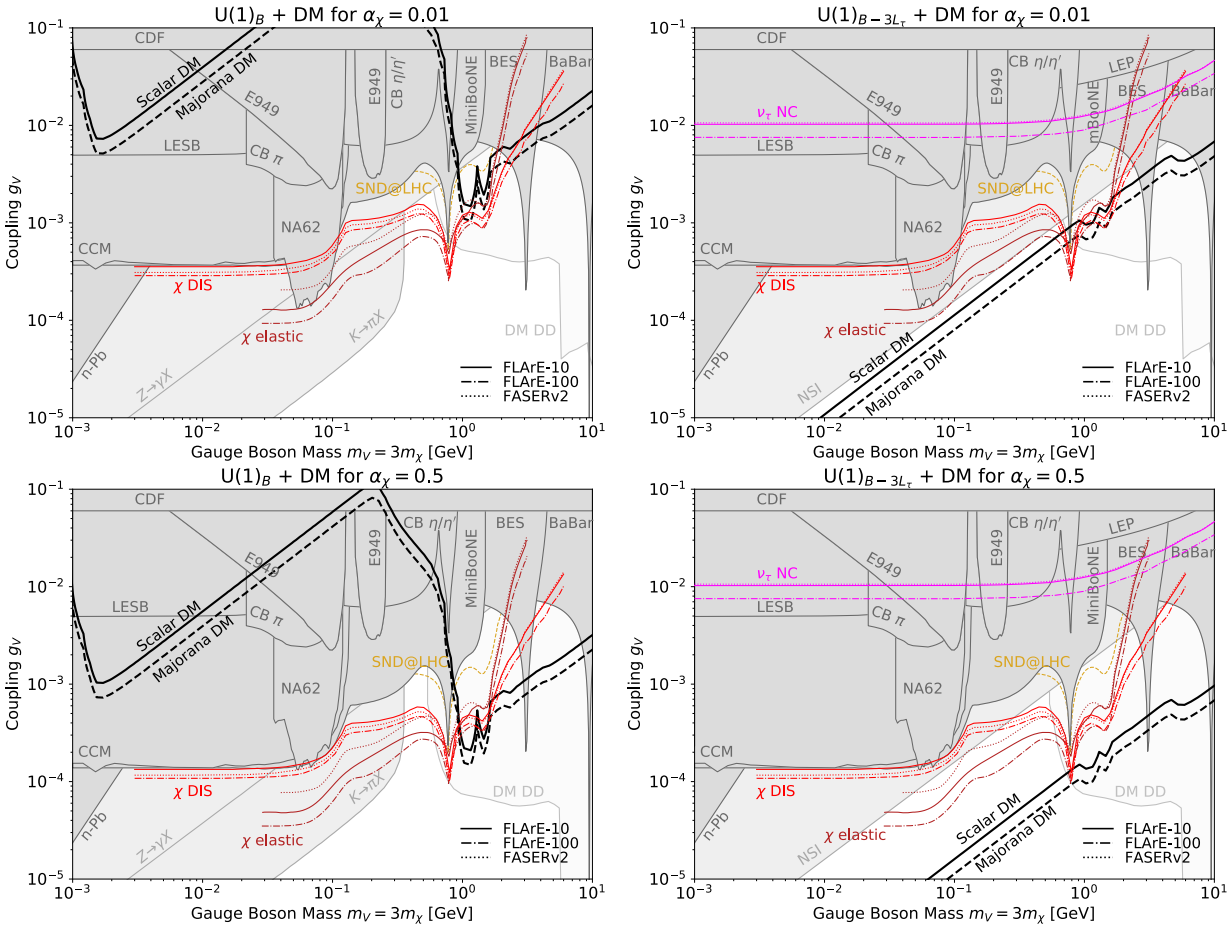

Figure 45: The (m_V, g_V) parameter space of hadrophilic DM models with U(1)$_B$ (left) and U(1)$_{B-3\tau}$ (right) gauge boson mediators coupling to complex scalar DM, for dark matter coupling $\alpha_\chi = 0.01$ (top) and 0.5 (bottom), and $m_V = 3m_\chi$. The black contours are the thermal relic targets for complex scalar and Majorana DM; DM is thermally overproduced below these contours. The light (dark) red lines correspond to 90% CL exclusion bounds from DM DIS (elastic) scatterings off nuclei for FLArE-10, FLArE-100, and FASERν2, as indicated. The dotted brown contours are the sensitivity contours for SND@LHC [28]. In the right panels, the light purple contours are the projected sensitivity contours from probing the V-induced BSM NC interactions of tau neutrinos. In both panels, the dark gray shaded regions are excluded by current bounds. The light gray shaded regions in the left (right) panels correspond to the anomaly-induced K and Z decays (NSI bounds). The very light gray shaded regions are constraints from DM DD; these do not apply to Majorana and inelastic scalar DM (see Sec. 8.2.4).

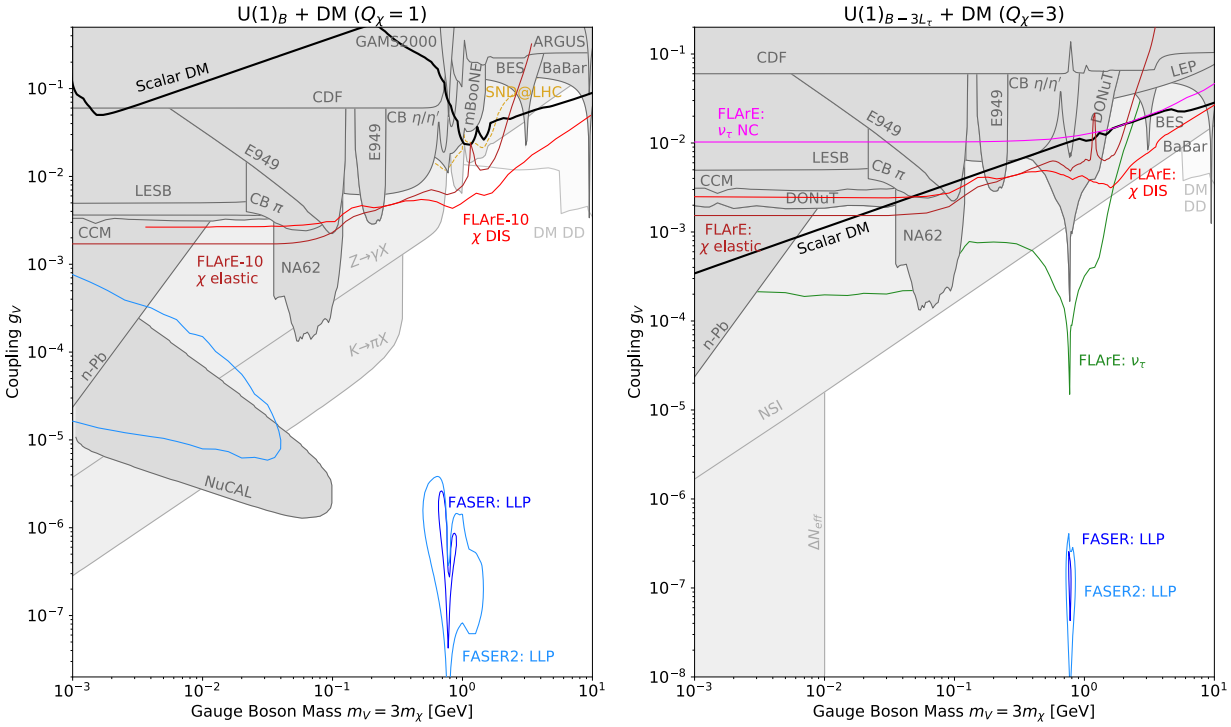

Figure 46: Same as Fig. 45, but for only the FLArE-10 detector, complex scalar DM, and fixed charges $Q_\chi = 1$ (left) and $Q_\chi = -Q_\tau = 3$ (right), resulting in a floating α_χ. Additional expected exclusion bounds from probing displaced V decays to SM final states in FASER (FASER2) are shown with dark (light) blue lines. In the right panel, the green contour is the sensitivity contour from probing excess CC scatterings of ν_τ.

CHAPTER IX

Conclusion

There is a growing body of evidence to go beyond the SM to explain nature. This comes in the form of many experimental observations, anomalies, and also from theoretical considerations. The search for BSM physics is the focus of this dissertation. Here we have adopted a phenomenological approach where we test well motivated BSM theories in new settings; this can be in newly proposed experiments, Chapters IV to VIII, or new ways to study the results coming from existing experiments, Chapters II and III. In each chapter we had presented the new model we wanted to explore, the experimental requirements, expected signature in the detectors, as well as the analysis and results. We now briefly summarize these conclusions.

In Chapter II, we look at the Yukawa coupling between the Higgs boson and the top quark, work done in Ref. [499]. The unprecedented precision that the HL-LHC era offers makes this study promising. Working within the SMEFT framework we focus on $\mathcal{O}_{t\phi}$ and $\mathcal{O}_{tG}$, two dimension 6 operators that contribute to the $t\bar{t}h$ process. We also consider a general expression for the Higgs-top form factor. The new physics effects can be enhanced in the boosted Higgs regime and combining this with jet substructure techniques allow us to place tight constraints on the Wilson coefficients, and hence the scale of the new physics. We show that we can probe the $\mathcal{O}_{t\phi}$ operator up to $\Lambda/\sqrt{c_{t\phi}} \approx 1.0$ TeV, and $\mathcal{O}_{tG}$ operator up to $\Lambda/\sqrt{c_{tG}} \approx 2.9$ TeV. Depending on the exact form of Higgs-top form factor, the HL-LHC is sensitive to new physics up to $\Lambda = 2.1$ TeV (n=2), and $\Lambda = 2.7$ TeV (n=3).

In Chapter III, we continue our exploration of collider physics by focussing on top quark and Z boson interactions [500]. The channels considered were $t\bar{t}Z$ and $tZj/\bar{t}Zj$ processes

where the angular moments (A_i) of the Z boson decay products (l^+l^-) can be used to probe the dynamics of this process. We first present the A_i values for these processes at NLO in QCD. Then within the SMEFT framework, we focus on operators that contribute to these processes: $\mathcal{O}_{tZ}$, $\mathcal{O}_{\phi t}$, $\mathcal{O}_{\phi Q}$ which are CP conserving, and $\mathcal{O}_{tZ}^I$ which is CP violating. By making use of the new A_i observables, we were able to enhance new physics searches in these channels. We demonstrated how the new physics scale could be probed up to ≈ 0.5 TeV in each of the case. We also observed that certain A_i coefficients are very sensitive to CP violating operators like $\mathcal{O}_{tZ}^I$ enabling one to open up otherwise blind directions in this analysis.

In the remaining chapters, we look at the physics potential in the forward direction at the LHC. Chapter IV focuses on the challenges facing neutral current neutrino interaction studies at the FASERν detector [266]. Collider neutrinos are the most energetic neutrinos made by humans and fall in the energy range between low energy lab experiments and astrophysical sources. We use machine learning techniques to identify neutral current neutrino interactions from their very similar looking neutral hadron backgrounds. By training neural networks on kinematic information from each event, we were able to distinguish signal from background, and also estimate the energy of the incoming neutrino. This is especially challenging as there is missing energy in the final state, carried away by the neutrino. By identifying and reconstructing these interactions, we can make a measurement of neutral current neutrino cross section which can then be compared with the SM prediction. One can also recast this cross section measurement to constrain neutrino non-standard interaction (NSI) which are comparable with existing bounds from other experiments.

We continue exploring neutrinos at the LHC in the forward direction in the next two chapters. SM neutrinos do not interact with photon at the tree level as it is electrically neutral. But one can imagine BSM scenarios that may give the neutrino a non-zero magnetic moment, millicharge, or charge radius. In Chapter V, we explore this possibility at FLArE and FASERν2 detectors [501]. Introducing these electromagnetic properties for neutrinos

induces couplings with photon. This modifies the neutrino interaction rates in the detector, and with proper kinematic cuts we are able to constrain the electromagnetic properties of neutrinos. The significant flux of tau neutrinos allow us to place the strongest lab based bounds on tau neutrino magnetic moment and millicharge. For the muon neutrino charge radius, we can probe values very close to the SM value. We also show that the weak mixing angle can be measured to a 3% precision at an energy scale of 10 GeV. One can also introduce a heavy neutral lepton that couples to the SM neutrino via a dipole portal, as presented in Chapter VI [241]. Neutrinos can interact within the detector and up-scatter to these heavier states. Due to the high energy of the incoming neutrinos, we can produce heavy states to up to a GeV. This again modifies the interaction rates and can be used to place constraints on the mass and coupling strength of heavy neutral leptons in the forward detectors.

The forward detectors at LHC can also serve as DM detectors. We first take up the dark photon DM model in Chapter VIII [264]. For DM with mass in the MeV - GeV range, it is possible to dominantly produce dark matter in the forward direction for suitable values of ϵ, kinetic mixing. In such a scenario, the dark matter can leave scattering signatures in the forward detectors. By looking at various scattering signatures; DM-e scattering, deep inelastic scattering (DIS) etc., we place constraints in the M_χ vs. ϵ plane and find that new parameter space for these models can be probed by the forward detectors. Since the LHC is a hadron collider, we also looked at hadrophilic models of DM, where the vector mediator can have enhanced couplings to quarks but suppressed couplings to leptons. We consider two such models with a $U(1)_B$, and $U(1)_{B-3L_\tau}$ vector mediator in Chapter VIII [265]. Apart from DM-e scattering and DIS signatures, the latter model can also result in other signatures coming from an enhanced ν_τ flux that can be used to probe new parameter space in these hadrophilic models. Taken together, these neutrino and DM studies advertising the great versatility and potential of the forward detectors at LHC.

REFERENCES

[1] **LHC Higgs Cross Section Working Group** Collaboration, J. R. Andersen *et al.*, "Handbook of LHC Higgs Cross Sections: 3. Higgs Properties," arXiv:1307.1347 [hep-ph].

[2] S. Dittmaier *et al.*, "Handbook of LHC Higgs Cross Sections: 2. Differential Distributions," arXiv:1201.3084 [hep-ph].

[3] J. Ellis, "Topics in Higgs Physics," *CERN Yellow Rep. School Proc.* **2** (2018) 1, arXiv:1702.05436 [hep-ph].

[4] **ATLAS** Collaboration, G. Aad *et al.*, "Measurements of differential cross-sections in four-lepton events in 13 TeV proton-proton collisions with the ATLAS detector," *JHEP* **07** (2021) 005, arXiv:2103.01918 [hep-ex].

[5] I. Esteban, M. C. Gonzalez-Garcia, M. Maltoni, T. Schwetz, and A. Zhou, "The fate of hints: updated global analysis of three-flavor neutrino oscillations," *JHEP* **09** (2020) 178, arXiv:2007.14792 [hep-ph].

[6] D. H. Rogstad and G. S. Shostak, "Gross Properties of Five Scd Galaxies as Determined from 21-CENTIMETER Observations," **176** (Sept., 1972) 315.

[7] G. Bertone and D. Hooper, "History of dark matter," *Rev. Mod. Phys.* **90** (2018) no. 4, 045002, arXiv:1605.04909 [astro-ph.CO].

[8] D. Clowe, M. Bradac, A. H. Gonzalez, M. Markevitch, S. W. Randall, C. Jones, and D. Zaritsky, "A direct empirical proof of the existence of dark matter," *Astrophys. J. Lett.* **648** (2006) L109–L113, arXiv:astro-ph/0608407.

[9] **FASER** Collaboration, H. Abreu *et al.*, "Detecting and Studying High-Energy Collider Neutrinos with FASER at the LHC," *Eur. Phys. J. C* **80** (2020) no. 1, 61, arXiv:1908.02310 [hep-ex].

[10] **CHARM** Collaboration, J. Allaby *et al.*, "A Precise Determination of the Electroweak Mixing Angle from Semileptonic Neutrino Scattering," *Z. Phys. C* **36** (1987) 611.

[11] P. Coloma, I. Esteban, M. Gonzalez-Garcia, and M. Maltoni, "Improved global fit to Non-Standard neutrino Interactions using COHERENT energy and timing data," *JHEP* **02** (2020) 023, arXiv:1911.09109 [hep-ph].

[12] W. Grimus, M. Maltoni, T. Schwetz, M. A. Tortola, and J. W. F. Valle, "Constraining Majorana neutrino electromagnetic properties from the LMA-MSW solution of the solar neutrino problem," *Nucl. Phys. B* **648** (2003) 376–396, arXiv:hep-ph/0208132.

[13] **Borexino** Collaboration, M. Agostini *et al.*, "Limiting neutrino magnetic moments with Borexino Phase-II solar neutrino data," *Phys. Rev. D* **96** (2017) no. 9, 091103, arXiv:1707.09355 [hep-ex].

[14] V. Brdar, A. Greljo, J. Kopp, and T. Opferkuch, "The neutrino magnetic moment portal: cosmology, astrophysics, and direct detection," *Journal of Cosmology and Astroparticle Physics* **2021** (Jan, 2021) 039–039. http://dx.doi.org/10.1088/1475-7516/2021/01/039.

[15] G. Magill, R. Plestid, M. Pospelov, and Y.-D. Tsai, "Dipole Portal to Heavy Neutral Leptons," *Phys. Rev. D* **98** (2018) no. 11, 115015, arXiv:1803.03262 [hep-ph].

[16] P. Coloma, P. A. N. Machado, I. Martinez-Soler, and I. M. Shoemaker, "Double-Cascade Events from New Physics in Icecube," *Phys. Rev. Lett.* **119** (2017) no. 20, 201804, arXiv:1707.08573 [hep-ph].

[17] **CHARM II** Collaboration, T. Mouthuy *et al.*, "A New determination of the electroweak mixing angle from muon-neutrino electron scattering," in *4th Les Rencontres de Physique de la Vallee d'Aoste: Results and Perspectives in Particle Physics*. 1990.

[18] S. N. Gninenko and N. V. Krasnikov, "Limits on the magnetic moment of sterile neutrino and two photon neutrino decay," *Phys. Lett. B* **450** (1999) 165–172, arXiv:hep-ph/9808370.

[19] T. Schwetz, A. Zhou, and J.-Y. Zhu, "Constraining active-sterile neutrino transition magnetic moments at dune near and far detectors," arXiv:2105.09699 [hep-ph].

[20] **MiniBooNE** Collaboration, A. A. Aguilar-Arevalo *et al.*, "A Search for Electron Neutrino Appearance at the $\Delta m^2 \sim 1eV^2$ Scale," *Phys. Rev. Lett.* **98** (2007) 231801, arXiv:0704.1500 [hep-ex].

[21] F. Kling and L. J. Nevay, "Forward neutrino fluxes at the LHC," *Phys. Rev. D* **104** (2021) no. 11, 113008, arXiv:2105.08270 [hep-ph].

[22] P. deNiverville, C.-Y. Chen, M. Pospelov, and A. Ritz, "Light dark matter in neutrino beams: production modelling and scattering signatures at MiniBooNE, T2K and SHiP," *Phys. Rev. D* **95** (2017) no. 3, 035006, arXiv:1609.01770 [hep-ph].

[23] C. Andreopoulos *et al.*, "The GENIE Neutrino Monte Carlo Generator," *Nucl. Instrum. Meth.* **A614** (2010) 87–104, arXiv:0905.2517 [hep-ph].

[24] C. Andreopoulos, C. Barry, S. Dytman, H. Gallagher, T. Golan, R. Hatcher, G. Perdue, and J. Yarba, "The GENIE Neutrino Monte Carlo Generator: Physics and User Manual," arXiv:1510.05494 [hep-ph].

[25] B. Batell, J. L. Feng, and S. Trojanowski, "Detecting Dark Matter with Far-Forward Emulsion and Liquid Argon Detectors at the LHC," *Phys. Rev. D* **103** (2021) no. 7, 075023, arXiv:2101.10338 [hep-ph].

[26] L. Buonocore, C. Frugiuele, and P. deNiverville, "Hunt for sub-GeV dark matter at neutrino facilities: A survey of past and present experiments," *Phys. Rev. D* **102** (2020) no. 3, 035006, arXiv:1912.09346 [hep-ph].

[27] **MiniBooNE DM** Collaboration, A. A. Aguilar-Arevalo *et al.*, "Dark Matter Search in Nucleon, Pion, and Electron Channels from a Proton Beam Dump with MiniBooNE," *Phys. Rev. D* **98** (2018) no. 11, 112004, arXiv:1807.06137 [hep-ex].

[28] A. Boyarsky, O. Mikulenko, M. Ovchynnikov, and L. Shchutska, "Searches for new physics at SND@LHC," arXiv:2104.09688 [hep-ph].

[29] **ATLAS** Collaboration, G. Aad *et al.*, "Observation of a new particle in the search for the Standard Model Higgs boson with the ATLAS detector at the LHC," *Phys. Lett. B* **716** (2012) 1–29, arXiv:1207.7214 [hep-ex].

[30] **CMS** Collaboration, S. Chatrchyan *et al.*, "Observation of a New Boson at a Mass of 125 GeV with the CMS Experiment at the LHC," *Phys. Lett. B* **716** (2012) 30–61, arXiv:1207.7235 [hep-ex].

[31] **Planck** Collaboration, P. A. R. Ade *et al.*, "Planck 2013 results. I. Overview of products and scientific results," *Astron. Astrophys.* **571** (2014) A1, arXiv:1303.5062 [astro-ph.CO].

[32] V. C. Rubin and J. Ford, W. Kent, "Rotation of the Andromeda Nebula from a Spectroscopic Survey of Emission Regions," **159** (Feb., 1970) 379.

[33] D. Clowe, A. Gonzalez, and M. Markevitch, "Weak lensing mass reconstruction of the interacting cluster 1E0657-558: Direct evidence for the existence of dark matter," *Astrophys. J.* **604** (2004) 596–603, arXiv:astro-ph/0312273.

[34] **SNO** Collaboration, Q. R. Ahmad *et al.*, "Measurement of the rate of $\nu_e + d \to p + p + e^-$ interactions produced by ^{8}B solar neutrinos at the Sudbury Neutrino Observatory," *Phys. Rev. Lett.* **87** (2001) 071301, arXiv:nucl-ex/0106015.

[35] **Super-Kamiokande** Collaboration, Y. Fukuda *et al.*, "Evidence for oscillation of atmospheric neutrinos," *Phys. Rev. Lett.* **81** (1998) 1562–1567, arXiv:hep-ex/9807003.

[36] E. Komatsu, K. M. Smith, J. Dunkley, C. L. Bennett, B. Gold, G. Hinshaw, N. Jarosik, D. Larson, M. R. Nolta, L. Page, D. N. Spergel, M. Halpern, R. S. Hill, A. Kogut, M. Limon, S. S. Meyer, N. Odegard, G. S. Tucker, J. L. Weiland, E. Wollack, and E. L. Wright, "Seven-year wilkinson microwave anisotropy probe (wmap*) observations: Cosmological interpretation," *The Astrophysical Journal Supplement Series* **192** (jan, 2011) 18. https://dx.doi.org/10.1088/0067-0049/192/2/18.

[37] G. Hinshaw, D. Larson, E. Komatsu, D. N. Spergel, C. L. Bennett, J. Dunkley, M. R. Nolta, M. Halpern, R. S. Hill, N. Odegard, L. Page, K. M. Smith, J. L. Weiland, B. Gold, N. Jarosik, A. Kogut, M. Limon, S. S. Meyer, G. S. Tucker, E. Wollack, and E. L. Wright, "Nine-year wilkinson microwave anisotropy probe (wmap) observations: Cosmological parameter results," *The Astrophysical Journal Supplement Series* **208** (sep, 2013) 19. https://dx.doi.org/10.1088/0067-0049/208/2/19.

[38] "LHC Machine," *JINST* **3** (2008) S08001.

[39] L. A. Anchordoqui *et al.*, "The Forward Physics Facility: Sites, experiments, and physics potential," *Phys. Rept.* **968** (2022) 1–50, arXiv:2109.10905 [hep-ph].

[40] J. L. Feng *et al.*, "The Forward Physics Facility at the High-Luminosity LHC," *J. Phys. G* **50** (2023) no. 3, 030501, arXiv:2203.05090 [hep-ex].

[41] J. L. Feng, I. Galon, F. Kling, and S. Trojanowski, "ForwArd Search ExpeRiment at the LHC," *Phys. Rev. D* **97** (2018) no. 3, 035001, arXiv:1708.09389 [hep-ph].

[42] **FASER** Collaboration, A. Ariga *et al.*, "Technical Proposal for FASER: ForwArd Search ExpeRiment at the LHC," arXiv:1812.09139 [physics.ins-det].

[43] **FASER** Collaboration, A. Ariga *et al.*, "Letter of Intent for FASER: ForwArd Search ExpeRiment at the LHC," arXiv:1811.10243 [physics.ins-det].

[44] **FASER** Collaboration, H. Abreu *et al.*, "Detecting and Studying High-Energy Collider Neutrinos with FASER at the LHC," *Eur. Phys. J. C* **80** (2020) no. 1, 61, arXiv:1908.02310 [hep-ex].

[45] **FASER** Collaboration, H. Abreu *et al.*, "Technical Proposal: FASERnu," arXiv:2001.03073 [physics.ins-det].

[46] **FASER** Collaboration, H. Abreu *et al.*, "First Direct Observation of Collider Neutrinos with FASER at the LHC," arXiv:2303.14185 [hep-ex].

[47] P. W. Anderson, "Plasmons, gauge invariance, and mass," *Phys. Rev.* **130** (Apr, 1963) 439–442. https://link.aps.org/doi/10.1103/PhysRev.130.439.

[48] P. W. Higgs, "Broken symmetries and the masses of gauge bosons," *Phys. Rev. Lett.* **13** (Oct, 1964) 508–509. https://link.aps.org/doi/10.1103/PhysRevLett.13.508.

[49] F. Englert and R. Brout, "Broken symmetry and the mass of gauge vector mesons," *Phys. Rev. Lett.* **13** (Aug, 1964) 321–323. https://link.aps.org/doi/10.1103/PhysRevLett.13.321.

[50] G. S. Guralnik, C. R. Hagen, and T. W. B. Kibble, "Global Conservation Laws and Massless Particles," *Phys. Rev. Lett.* **13** (1964) 585–587.

[51] S. L. Glashow, "Partial Symmetries of Weak Interactions," *Nucl. Phys.* **22** (1961) 579–588.

[52] S. Weinberg, "A Model of Leptons," *Phys. Rev. Lett.* **19** (1967) 1264–1266.

[53] J. R. Ellis, M. K. Gaillard, and D. V. Nanopoulos, "A Phenomenological Profile of the Higgs Boson," *Nucl. Phys. B* **106** (1976) 292.

[54] **Particle Data Group** Collaboration, "Review of particle physics," *Phys. Rev. D* **86** (Jul, 2012) 010001. https://link.aps.org/doi/10.1103/PhysRevD.86.010001.

[55] S. Weinberg, "Baryon and Lepton Nonconserving Processes," *Phys. Rev. Lett.* **43** (1979) 1566–1570.

[56] E. Ma, "Pathways to naturally small neutrino masses," *Phys. Rev. Lett.* **81** (1998) 1171–1174, arXiv:hep-ph/9805219.

[57] W. Buchmuller and D. Wyler, "Effective Lagrangian Analysis of New Interactions and Flavor Conservation," *Nucl. Phys. B* **268** (1986) 621–653.

[58] B. Grzadkowski, M. Iskrzynski, M. Misiak, and J. Rosiek, "Dimension-Six Terms in the Standard Model Lagrangian," *JHEP* **10** (2010) 085, arXiv:1008.4884 [hep-ph].

[59] J. Ellis, M. Madigan, K. Mimasu, V. Sanz, and T. You, "Top, Higgs, Diboson and Electroweak Fit to the Standard Model Effective Field Theory," arXiv:2012.02779 [hep-ph].

[60] J. J. Ethier, F. Maltoni, L. Mantani, E. R. Nocera, J. Rojo, E. Slade, E. Vryonidou, and C. Zhang, "Combined SMEFT interpretation of Higgs, diboson, and top quark data from the LHC," arXiv:2105.00006 [hep-ph].

[61] I. Brivio, S. Bruggisser, F. Maltoni, R. Moutafis, T. Plehn, E. Vryonidou, S. Westhoff, and C. Zhang, "O new physics, where art thou? A global search in the top sector," *JHEP* **02** (2020) 131, arXiv:1910.03606 [hep-ph].

[62] T. Corbett, O. J. P. Eboli, D. Goncalves, J. Gonzalez-Fraile, T. Plehn, and M. Rauch, "The Higgs Legacy of the LHC Run I," *JHEP* **08** (2015) 156, arXiv:1505.05516 [hep-ph].

[63] A. Biekötter, D. Gonçalves, T. Plehn, M. Takeuchi, and D. Zerwas, "The global Higgs picture at 27 TeV," *SciPost Phys.* **6** (2019) no. 2, 024, arXiv:1811.08401 [hep-ph].

[64] B. Pontecorvo, "Mesonium and anti-mesonium," *Sov. Phys. JETP* **6** (1957) 429.

[65] B. Pontecorvo, "Inverse beta processes and nonconservation of lepton charge," *Zh. Eksp. Teor. Fiz.* **34** (1957) 247.

[66] Z. Maki, M. Nakagawa, and S. Sakata, "Remarks on the unified model of elementary particles," *Prog. Theor. Phys.* **28** (1962) 870–880.

[67] C. Giunti and A. Studenikin, "Neutrino electromagnetic interactions: a window to new physics," *Rev. Mod. Phys.* **87** (2015) 531, arXiv:1403.6344 [hep-ph].

[68] B. Kayser, "Majorana Neutrinos and their Electromagnetic Properties," *Phys. Rev. D* **26** (1982) 1662.

[69] J. F. Nieves, "Electromagnetic Properties of Majorana Neutrinos," *Phys. Rev. D* **26** (1982) 3152.

[70] **WMAP** Collaboration, G. Hinshaw *et al.*, "Five-Year Wilkinson Microwave Anisotropy Probe (WMAP) Observations: Data Processing, Sky Maps, and Basic Results," *Astrophys. J. Suppl.* **180** (2009) 225–245, arXiv:0803.0732 [astro-ph].

[71] F. Zwicky, "Republication of: The redshift of extragalactic nebulae," *General Relativity and Gravitation* **41** (Jan., 2009) 207–224.

[72] H. Andernach and F. Zwicky, "English and spanish translation of zwicky's (1933) the redshift of extragalactic nebulae," 2017.

[73] M. S. Roberts, "A High-Resolution 21-CM Hydrogen-Line Survey of the Andromeda Nebula," **144** (May, 1966) 639.

[74] D. N. Schramm and G. Steigman, "Relic Neutrinos and the Density of the Universe," **243** (Jan., 1981) 1.

[75] J. R. Primack, "Dark matter and structure formation," in *Midrasha Mathematicae in Jerusalem: Winter School in Dynamical Systems*. 7, 1997. arXiv:astro-ph/9707285.

[76] M. Davis, J. Huchra, D. W. Latham, and J. Tonry, "A survey of galaxy redshifts. II. The large scale space distribution.," **253** (Feb., 1982) 423–445.

[77] C. T. Hill and E. H. Simmons, "Strong Dynamics and Electroweak Symmetry Breaking," *Phys. Rept.* **381** (2003) 235–402, arXiv:hep-ph/0203079. [Erratum: Phys.Rept. 390, 553–554 (2004)].

[78] D. Buttazzo, G. Degrassi, P. P. Giardino, G. F. Giudice, F. Sala, A. Salvio, and A. Strumia, "Investigating the near-criticality of the Higgs boson," *JHEP* **12** (2013) 089, arXiv:1307.3536 [hep-ph].

[79] F. Bezrukov and M. Shaposhnikov, "Why should we care about the top quark Yukawa coupling?," *J. Exp. Theor. Phys.* **120** (2015) 335–343, arXiv:1411.1923 [hep-ph].

[80] M. Carena, M. Olechowski, S. Pokorski, and C. E. M. Wagner, "Radiative electroweak symmetry breaking and the infrared fixed point of the top quark mass," *Nucl. Phys. B* **419** (1994) 213–239, arXiv:hep-ph/9311222.

[81] G. Panico and A. Wulzer, "The Discrete Composite Higgs Model," *JHEP* **09** (2011) 135, arXiv:1106.2719 [hep-ph].

[82] O. Matsedonskyi, G. Panico, and A. Wulzer, "Light Top Partners for a Light Composite Higgs," *JHEP* **01** (2013) 164, arXiv:1204.6333 [hep-ph].

[83] A. Pomarol and F. Riva, "The Composite Higgs and Light Resonance Connection," *JHEP* **08** (2012) 135, arXiv:1205.6434 [hep-ph].

[84] B. Bellazzini, C. Csáki, and J. Serra, "Composite Higgses," *Eur. Phys. J. C* **74** (2014) no. 5, 2766, arXiv:1401.2457 [hep-ph].

[85] G. Panico and A. Wulzer, *The Composite Nambu-Goldstone Higgs*, vol. 913. Springer, 2016. arXiv:1506.01961 [hep-ph].

[86] **ATLAS** Collaboration, G. Aad *et al.*, "Combined measurements of Higgs boson production and decay using up to 80 fb^{-1} of proton-proton collision data at $\sqrt{s} = 13$ TeV collected with the ATLAS experiment," *Phys. Rev. D* **101** (2020) no. 1, 012002, arXiv:1909.02845 [hep-ex].

[87] **ATLAS** Collaboration, M. Aaboud *et al.*, "Observation of Higgs boson production in association with a top quark pair at the LHC with the ATLAS detector," *Phys. Lett. B* **784** (2018) 173–191, arXiv:1806.00425 [hep-ex].

[88] **CMS** Collaboration, A. M. Sirunyan *et al.*, "Observation of $t\bar{t}H$ production," *Phys. Rev. Lett.* **120** (2018) no. 23, 231801, arXiv:1804.02610 [hep-ex].

[89] M. Cepeda *et al.*, "Report from Working Group 2: Higgs Physics at the HL-LHC and HE-LHC," *CERN Yellow Rep. Monogr.* **7** (2019) 221–584, arXiv:1902.00134 [hep-ph].

[90] T. Appelquist and J. Carazzone, "Infrared Singularities and Massive Fields," *Phys. Rev. D* **11** (1975) 2856.

[91] A. Azatov, C. Grojean, A. Paul, and E. Salvioni, "Taming the off-shell Higgs boson," *Zh. Eksp. Teor. Fiz.* **147** (2015) 410–425, arXiv:1406.6338 [hep-ph].

[92] C. Englert and M. Spannowsky, "Limitations and Opportunities of Off-Shell Coupling Measurements," *Phys. Rev. D* **90** (2014) 053003, arXiv:1405.0285 [hep-ph].

[93] M. Buschmann, D. Goncalves, S. Kuttimalai, M. Schonherr, F. Krauss, and T. Plehn, "Mass Effects in the Higgs-Gluon Coupling: Boosted vs Off-Shell Production," *JHEP* **02** (2015) 038, arXiv:1410.5806 [hep-ph].

[94] D. Goncalves, T. Han, and S. Mukhopadhyay, "Off-Shell Higgs Probe of Naturalness," *Phys. Rev. Lett.* **120** (2018) no. 11, 111801, arXiv:1710.02149 [hep-ph]. [Erratum: Phys.Rev.Lett. 121, 079902 (2018)].

[95] D. Gonçalves, T. Han, and S. Mukhopadhyay, "Higgs Couplings at High Scales," *Phys. Rev. D* **98** (2018) no. 1, 015023, arXiv:1803.09751 [hep-ph].

[96] D. Gonçalves, T. Han, S. Ching Iris Leung, and H. Qin, "Off-shell Higgs couplings in $H^* \to ZZ \to \ell\ell\nu\nu$," *Phys. Lett. B* **817** (2021) 136329, arXiv:2012.05272 [hep-ph].

[97] F. Maltoni, E. Vryonidou, and C. Zhang, "Higgs production in association with a top-antitop pair in the Standard Model Effective Field Theory at NLO in QCD," *JHEP* **10** (2016) 123, arXiv:1607.05330 [hep-ph].

[98] **ATLAS Collaboration** Collaboration, "A combination of measurements of Higgs boson production and decay using up to 139 fb^{-1} of proton–proton collision data at $\sqrt{s} = 13$ TeV collected with the ATLAS experiment," tech. rep., CERN, Geneva, Aug, 2020. http://cds.cern.ch/record/2725733.

[99] **CMS** Collaboration, A. M. Sirunyan *et al.*, "Measurement of the top quark polarization and $t\bar{t}$ spin correlations using dilepton final states in proton-proton collisions at $\sqrt{s} = 13$ TeV," *Phys. Rev. D* **100** (2019) no. 7, 072002, arXiv:1907.03729 [hep-ex].

[100] D. Liu, I. Low, and C. E. M. Wagner, "Modification of Higgs Couplings in Minimal Composite Models," *Phys. Rev. D* **96** (2017) no. 3, 035013, arXiv:1703.07791 [hep-ph].

[101] A. Banerjee, S. Dasgupta, and T. S. Ray, "Chasing the Higgs shape at HL-LHC," arXiv:2105.01093 [hep-ph].

[102] V. Punjabi, C. F. Perdrisat, M. K. Jones, E. J. Brash, and C. E. Carlson, "The Structure of the Nucleon: Elastic Electromagnetic Form Factors," *Eur. Phys. J. A* **51** (2015) 79, arXiv:1503.01452 [nucl-ex].

[103] J. Alwall, R. Frederix, S. Frixione, V. Hirschi, F. Maltoni, O. Mattelaer, H. S. Shao, T. Stelzer, P. Torrielli, and M. Zaro, "The automated computation of tree-level and next-to-leading order differential cross sections, and their matching to parton shower simulations," *JHEP* **07** (2014) 079, arXiv:1405.0301 [hep-ph].

[104] C. Degrande, G. Durieux, F. Maltoni, K. Mimasu, E. Vryonidou, and C. Zhang, "Automated one-loop computations in the SMEFT," arXiv:2008.11743 [hep-ph].

[105] R. Goldouzian, J. H. Kim, K. Lannon, A. Martin, K. Mohrman, and A. Wightman, "Matching in $pp \to t\bar{t}W/Z/h+$ jet SMEFT studies," arXiv:2012.06872 [hep-ph].

[106] T. Sjöstrand, S. Ask, J. R. Christiansen, R. Corke, N. Desai, P. Ilten, S. Mrenna, S. Prestel, C. O. Rasmussen, and P. Z. Skands, "An introduction to PYTHIA 8.2," *Comput. Phys. Commun.* **191** (2015) 159–177, arXiv:1410.3012 [hep-ph].

[107] P. Skands, S. Carrazza, and J. Rojo, "Tuning PYTHIA 8.1: the Monash 2013 Tune," *Eur. Phys. J. C* **74** (2014) no. 8, 3024, arXiv:1404.5630 [hep-ph].

[108] P. Artoisenet, R. Frederix, O. Mattelaer, and R. Rietkerk, "Automatic spin-entangled decays of heavy resonances in Monte Carlo simulations," *JHEP* **03** (2013) 015, arXiv:1212.3460 [hep-ph].

[109] L. A. Harland-Lang, A. D. Martin, P. Motylinski, and R. S. Thorne, "Parton distributions in the LHC era: MMHT 2014 PDFs," *Eur. Phys. J. C* **75** (2015) no. 5, 204, arXiv:1412.3989 [hep-ph].

[110] M. R. Buckley and D. Goncalves, "Boosting the Direct CP Measurement of the Higgs-Top Coupling," *Phys. Rev. Lett.* **116** (2016) no. 9, 091801, arXiv:1507.07926 [hep-ph].

[111] M. Cacciari, G. P. Salam, and G. Soyez, "FastJet User Manual," *Eur. Phys. J. C* **72** (2012) 1896, arXiv:1111.6097 [hep-ph].

[112] J. M. Butterworth, A. R. Davison, M. Rubin, and G. P. Salam, "Jet substructure as a new Higgs search channel at the LHC," *Phys. Rev. Lett.* **100** (2008) 242001, arXiv:0802.2470 [hep-ph].

[113] T. Plehn, G. P. Salam, and M. Spannowsky, "Fat Jets for a Light Higgs," *Phys. Rev. Lett.* **104** (2010) 111801, arXiv:0910.5472 [hep-ph].

[114] **ATLAS Collaboration** Collaboration, "Technical Design Report for the ATLAS Inner Tracker Pixel Detector," Tech. Rep. CERN-LHCC-2017-021. ATLAS-TDR-030, CERN, Geneva, Sep, 2017. https://cds.cern.ch/record/2285585.

[115] **CMS Collaboration** Collaboration, "Using associated top quark production to probe for new physics within the framework of effective field theory," tech. rep., CERN, Geneva, 2020. https://cds.cern.ch/record/2725399.

[116] J. Brehmer, F. Kling, I. Espejo, and K. Cranmer, "MadMiner: Machine learning-based inference for particle physics," *Comput. Softw. Big Sci.* **4** (2020) no. 1, 3, arXiv:1907.10621 [hep-ph].

[117] **ATLAS** Collaboration, M. Aaboud *et al.*, "Search for the standard model Higgs boson produced in association with top quarks and decaying into a $b\bar{b}$ pair in pp collisions at $\sqrt{s} = 13$ TeV with the ATLAS detector," *Phys. Rev. D* **97** (2018) no. 7, 072016, arXiv:1712.08895 [hep-ex].

[118] T. Ježo, J. M. Lindert, N. Moretti, and S. Pozzorini, "New NLOPS predictions for $t\bar{t}+b$ -jet production at the LHC," *Eur. Phys. J. C* **78** (2018) no. 6, 502, arXiv:1802.00426 [hep-ph].

[119] A. Denner, J.-N. Lang, and M. Pellen, "Full NLO QCD corrections to off-shell tt¯bb¯ production," *Phys. Rev. D* **104** (2021) no. 5, 056018, arXiv:2008.00918 [hep-ph].

[120] G. Bevilacqua, H.-Y. Bi, H. B. Hartanto, M. Kraus, M. Lupattelli, and M. Worek, "$t\bar{t}b\bar{b}$ at the LHC: on the size of corrections and b-jet definitions," *JHEP* **08** (2021) 008, arXiv:2105.08404 [hep-ph].

[121] K. Agashe, G. Perez, and A. Soni, "Collider signals of top quark flavor violation from a warped extra dimension," *Phys. Rev. D* **75** (Jan, 2007) 015002. https://link.aps.org/doi/10.1103/PhysRevD.75.015002.

[122] A. L. Kagan, G. Perez, T. Volansky, and J. Zupan, "General minimal flavor violation," *Phys. Rev. D* **80** (Oct, 2009) 076002. https://link.aps.org/doi/10.1103/PhysRevD.80.076002.

[123] T. Ibrahim and P. Nath, "Chromoelectric dipole moment of the top quark in models with vectorlike multiplets," *Phys. Rev. D* **84** (Jul, 2011) 015003. https://link.aps.org/doi/10.1103/PhysRevD.84.015003.

[124] P. D. Group, "Review of Particle Physics," *Progress of Theoretical and Experimental Physics* **2020** (08, 2020) , https://academic.oup.com/ptep/article-pdf/2020/8/083C01/34673722/ptaa104.pdf. https://doi.org/10.1093/ptep/ptaa104. 083C01.

[125] U. Baur, A. Juste, L. H. Orr, and D. Rainwater, "Probing electroweak top quark couplings at hadron colliders," *Phys. Rev. D* **71** (2005) 054013, arXiv:hep-ph/0412021.

[126] **ATLAS** Collaboration, G. Aad *et al.*, "Measurements of the inclusive and differential production cross sections of a top-quark-antiquark pair in association with a Z boson at $\sqrt{s} = 13$ TeV with the ATLAS detector," *Eur. Phys. J. C* **81** (2021) 737, arXiv:2103.12603 [hep-ex].

[127] **CMS** Collaboration, A. M. Sirunyan *et al.*, "Measurement of top quark pair production in association with a Z boson in proton-proton collisions at $\sqrt{s} = 13$ TeV," *JHEP* **03** (2020) 056, arXiv:1907.11270 [hep-ex].

[128] **CMS Collaboration** Collaboration, "Anomalous couplings in the tt+Z final state at the HL-LHC," tech. rep., CERN, Geneva, 2018. https://cds.cern.ch/record/2652018.

[129] K. Hagiwara, K.-i. Hikasa, and N. Kai, "Parity-odd asymmetries in w-jet events at hadron colliders," *Phys. Rev. Lett.* **52** (Mar, 1984) 1076–1079. https://link.aps.org/doi/10.1103/PhysRevLett.52.1076.

[130] E. Mirkes and J. Ohnemus, "W and Z polarization effects in hadronic collisions," *Phys. Rev. D* **50** (1994) 5692–5703, arXiv:hep-ph/9406381.

[131] D. Goncalves and J. Nakamura, "Role of the Z polarization in the $H \to b\bar{b}$ measurement," *Phys. Rev. D* **98** (2018) no. 9, 093005, arXiv:1805.06385 [hep-ph].

[132] D. Goncalves and J. Nakamura, "Boosting the $H \to$ invisibles searches with Z boson polarization," *Phys. Rev. D* **99** (2019) no. 5, 055021, arXiv:1809.07327 [hep-ph].

[133] S. Banerjee, R. S. Gupta, J. Y. Reiness, and M. Spannowsky, "Resolving the tensor structure of the Higgs coupling to Z-bosons via Higgs-strahlung," *Phys. Rev. D* **100** (2019) no. 11, 115004, arXiv:1905.02728 [hep-ph].

[134] S. Banerjee, R. S. Gupta, O. Ochoa-Valeriano, M. Spannowsky, and E. Venturini, "A fully differential SMEFT analysis of the golden channel using the method of moments," *JHEP* **06** (2021) 031, arXiv:2012.11631 [hep-ph].

[135] S. Banerjee, R. S. Gupta, J. Y. Reiness, S. Seth, and M. Spannowsky, "Towards the ultimate differential SMEFT analysis," *JHEP* **09** (2020) 170, arXiv:1912.07628 [hep-ph].

[136] I. Brivio and M. Trott, "The Standard Model as an Effective Field Theory," *Phys. Rept.* **793** (2019) 1–98, arXiv:1706.08945 [hep-ph].

[137] J. C. Collins and D. E. Soper, "Angular distribution of dileptons in high-energy hadron collisions," *Phys. Rev. D* **16** (Oct, 1977) 2219–2225. https://link.aps.org/doi/10.1103/PhysRevD.16.2219.

[138] **ATLAS** Collaboration, G. Aad *et al.*, "Measurement of the angular coefficients in Z-boson events using electron and muon pairs from data taken at $\sqrt{s} = 8$ TeV with the ATLAS detector," *JHEP* **08** (2016) 159, arXiv:1606.00689 [hep-ex].

[139] **ATLAS** Collaboration, M. Aaboud *et al.*, "Measurement of the Drell-Yan triple-differential cross section in pp collisions at $\sqrt{s} = 8$ TeV," *JHEP* **12** (2017) 059, arXiv:1710.05167 [hep-ex].

[140] **CMS** Collaboration, V. Khachatryan *et al.*, "Angular coefficients of Z bosons produced in pp collisions at $\sqrt{s} = 8$ TeV and decaying to $\mu^+\mu^-$ as a function of transverse momentum and rapidity," *Phys. Lett. B* **750** (2015) 154–175, arXiv:1504.03512 [hep-ex].

[141] **NNPDF** Collaboration, R. D. Ball, V. Bertone, S. Carrazza, L. Del Debbio, S. Forte, A. Guffanti, N. P. Hartland, and J. Rojo, "Parton distributions with QED corrections," *Nucl. Phys. B* **877** (2013) 290–320, arXiv:1308.0598 [hep-ph].

[142] R. Röntsch and M. Schulze, "Constraining couplings of top quarks to the z boson in $t\bar{t}$ + z production at the lhc," *Journal of High Energy Physics* **2014** (Jul, 2014) . http://dx.doi.org/10.1007/JHEP07(2014)091.

[143] R. Röntsch and M. Schulze, "Probing top-Z dipole moments at the LHC and ILC," *JHEP* **08** (2015) 044, arXiv:1501.05939 [hep-ph].

[144] A. Buckley, C. Englert, J. Ferrando, D. J. Miller, L. Moore, M. Russell, and C. D. White, "Constraining top quark effective theory in the LHC Run II era," *JHEP* **04** (2016) 015, arXiv:1512.03360 [hep-ph].

[145] M. Schulze and Y. Soreq, "Pinning down electroweak dipole operators of the top quark," *Eur. Phys. J. C* **76** (2016) no. 8, 466, arXiv:1603.08911 [hep-ph].

[146] O. Bessidskaia Bylund, F. Maltoni, I. Tsinikos, E. Vryonidou, and C. Zhang, "Probing top quark neutral couplings in the Standard Model Effective Field Theory at NLO in QCD," *JHEP* **05** (2016) 052, arXiv:1601.08193 [hep-ph].

[147] **CMS** Collaboration, A. M. Sirunyan *et al.*, "Measurement of the cross section for top quark pair production in association with a W or Z boson in proton-proton collisions at $\sqrt{s} = 13$ TeV," *JHEP* **08** (2018) 011, arXiv:1711.02547 [hep-ex].

[148] C. Englert and M. Russell, "Top quark electroweak couplings at future lepton colliders," *Eur. Phys. J. C* **77** (2017) no. 8, 535, arXiv:1704.01782 [hep-ph].

[149] C. Degrande, F. Maltoni, K. Mimasu, E. Vryonidou, and C. Zhang, "Single-top associated production with a Z or H boson at the LHC: the SMEFT interpretation," *JHEP* **10** (2018) 005, arXiv:1804.07773 [hep-ph].

[150] F. Maltoni, L. Mantani, and K. Mimasu, "Top-quark electroweak interactions at high energy," *JHEP* **10** (2019) 004, arXiv:1904.05637 [hep-ph].

[151] G. Durieux, A. Irles, V. Miralles, A. Peñuelas, R. Pöschl, M. Perelló, and M. Vos, "The electro-weak couplings of the top and bottom quarks — Global fit and future prospects," *JHEP* **12** (2019) 98, arXiv:1907.10619 [hep-ph]. [Erratum: JHEP 01, 195 (2021)].

[152] B. Ravina, E. Simpson, and J. Howarth, "Observing $t\bar{t}Z$ spin correlations at the LHC," *Eur. Phys. J. C* **81** (2021) no. 9, 809, arXiv:2106.09690 [hep-ph].

[153] R. Rahaman, "On two-body and three-body spin correlations in leptonic $t\bar{t}Z$ production and anomalous couplings at the LHC," arXiv:2204.12152 [hep-ph].

[154] R. K. Barman and A. Ismail, "Constraining the top electroweak sector of the SMEFT through Z associated top pair and single top production at the HL-LHC," arXiv:2205.07912 [hep-ph].

[155] D. Barducci *et al.*, "Interpreting top-quark LHC measurements in the standard-model effective field theory," arXiv:1802.07237 [hep-ph].

[156] J. Bernabeu, D. Comelli, L. Lavoura, and J. P. Silva, "Weak magnetic dipole moments in two Higgs doublet models," *Phys. Rev. D* **53** (1996) 5222–5232, arXiv:hep-ph/9509416.

[157] A. Czarnecki and B. Krause, "On the dipole moments of fermions at two loops," *Acta Phys. Polon. B* **28** (1997) 829–834, arXiv:hep-ph/9611299.

[158] W. Hollik, J. I. Illana, S. Rigolin, C. Schappacher, and D. Stockinger, "Top dipole form-factors and loop induced CP violation in supersymmetry," *Nucl. Phys. B* **551** (1999) 3–40, arXiv:hep-ph/9812298. [Erratum: Nucl.Phys.B 557, 407–409 (1999)].

[159] J. Aguilar-Saavedra, "A Minimal set of top anomalous couplings," *Nucl. Phys. B* **812** (2009) 181–204, arXiv:0811.3842 [hep-ph].

[160] J. Alwall, R. Frederix, S. Frixione, V. Hirschi, F. Maltoni, O. Mattelaer, H.-S. Shao, T. Stelzer, P. Torrielli, and M. Zaro, "The automated computation of tree-level and next-to-leading order differential cross sections, and their matching to parton shower simulations," *Journal of High Energy Physics* **2014** (Jul, 2014) . http://dx.doi.org/10.1007/JHEP07(2014)079.

[161] C. Degrande, G. Durieux, F. Maltoni, K. Mimasu, E. Vryonidou, and C. Zhang, "Automated one-loop computations in the smeft," 2020.

[162] P. Artoisenet, R. Frederix, O. Mattelaer, and R. Rietkerk, "Automatic spin-entangled decays of heavy resonances in monte carlo simulations," *Journal of High Energy Physics* **2013** (Mar, 2013) . http://dx.doi.org/10.1007/JHEP03(2013)015.

[163] T. Sjostrand, S. Mrenna, and P. Z. Skands, "A Brief Introduction to PYTHIA 8.1," *Comput. Phys. Commun.* **178** (2008) 852–867, arXiv:0710.3820 [hep-ph].

[164] S. Ovyn, X. Rouby, and V. Lemaitre, "DELPHES, a framework for fast simulation of a generic collider experiment," arXiv:0903.2225 [hep-ph].

[165] A. De Rujula and R. Ruckl, "Neutrino and muon physics in the collider mode of future accelerators," in *SSC Workshop: Superconducting Super Collider Fixed Target Physics*, pp. 571–596. 5, 1984.

[166] F. Vannucci, "Neutrino physics at LHC/SSC," Tech. Rep. LPNHE-93-03, Paris 6. Lab. Phys. Nucl. Théor. Hautes Enérg., Paris, Aug, 1993. https://cds.cern.ch/record/253670.

[167] A. De Rujula, E. Fernandez, and J. J. Gomez-Cadenas, "Neutrino fluxes at future hadron colliders," *Nucl. Phys.* **B405** (1993) 80–108.

[168] H. Park, "The estimation of neutrino fluxes produced by proton-proton collisions at $\sqrt{s} = 14$ TeV of the LHC," *JHEP* **10** (2011) 092, arXiv:1110.1971 [hep-ex].

[169] S. Buontempo, G. M. Dallavalle, G. De Lellis, D. Lazic, and F. L. Navarria, "CMS-XSEN: LHC Neutrinos at CMS. Experiment Feasibility Study," arXiv:1804.04413 [physics.ins-det].

[170] **FASER** Collaboration, H. Abreu *et al.*, "Technical Proposal: FASERnu," arXiv:2001.03073 [physics.ins-det].

[171] J. Formaggio and G. Zeller, "From eV to EeV: Neutrino Cross Sections Across Energy Scales," *Rev. Mod. Phys.* **84** (2012) 1307–1341, arXiv:1305.7513 [hep-ex].

[172] **DONuT** Collaboration, K. Kodama *et al.*, "Final tau-neutrino results from the DONuT experiment," *Phys. Rev. D* **78** (2008) 052002, arXiv:0711.0728 [hep-ex].

[173] **Particle Data Group** Collaboration, M. Tanabashi *et al.*, "Review of Particle Physics," *Phys. Rev.* **D98** (2018) no. 3, 030001.

[174] **IceCube** Collaboration, M. Aartsen *et al.*, "Measurement of the multi-TeV neutrino cross section with IceCube using Earth absorption," *Nature* **551** (2017) 596–600, arXiv:1711.08119 [hep-ex].

[175] M. Bustamante and A. Connolly, "Extracting the Energy-Dependent Neutrino-Nucleon Cross Section above 10 TeV Using IceCube Showers," *Phys. Rev. Lett.* **122** (2019) no. 4, 041101, arXiv:1711.11043 [astro-ph.HE].

[176] **FASER** Collaboration, A. Ariga *et al.*, "Letter of Intent for FASER: ForwArd Search ExpeRiment at the LHC," arXiv:1811.10243 [physics.ins-det]. https://cds.cern.ch/record/2642351. Submitted to the CERN LHCC on 18 July 2018.

[177] **FASER** Collaboration, A. Ariga *et al.*, "Technical Proposal for FASER: ForwArd Search ExpeRiment at the LHC," arXiv:1812.09139 [physics.ins-det].

[178] J. L. Feng, I. Galon, F. Kling, and S. Trojanowski, "Dark Higgs bosons at the ForwArd Search ExpeRiment," *Phys. Rev.* **D97** (2018) no. 5, 055034, arXiv:1710.09387 [hep-ph].

[179] F. Kling and S. Trojanowski, "Heavy Neutral Leptons at FASER," *Phys. Rev.* **D97** (2018) no. 9, 095016, arXiv:1801.08947 [hep-ph].

[180] J. L. Feng, I. Galon, F. Kling, and S. Trojanowski, "Axionlike particles at FASER: The LHC as a photon beam dump," *Phys. Rev.* **D98** (2018) no. 5, 055021, arXiv:1806.02348 [hep-ph].

[181] **FASER** Collaboration, A. Ariga *et al.*, "FASER's physics reach for long-lived particles," *Phys. Rev.* **D99** (2019) no. 9, 095011, arXiv:1811.12522 [hep-ph].

[182] A. Berlin and F. Kling, "Inelastic Dark Matter at the LHC Lifetime Frontier: ATLAS, CMS, LHCb, CODEX-b, FASER, and MATHUSLA," *Phys. Rev.* **D99** (2019) no. 1, 015021, arXiv:1810.01879 [hep-ph].

[183] **FASER** Collaboration, A. Ariga *et al.*, "FASER: ForwArd Search ExpeRiment at the LHC," arXiv:1901.04468 [hep-ex].

[184] K. Jodłowski, F. Kling, L. Roszkowski, and S. Trojanowski, "Extending the reach of FASER, MATHUSLA, and SHiP towards smaller lifetimes using secondary particle production," *Phys. Rev. D* **101** (2020) no. 9, 095020, arXiv:1911.11346 [hep-ph].

[185] F. Kling and S. Trojanowski, "Looking forward to test the KOTO anomaly with FASER," *Phys. Rev. D* **102** (2020) no. 1, 015032, arXiv:2006.10630 [hep-ph].

[186] K. Jodłowski and S. Trojanowski, "Neutrino beam-dump experiment with FASER at the LHC," arXiv:2011.04751 [hep-ph].

[187] T. Nakamura *et al.*, "The OPERA film: New nuclear emulsion for large-scale, high-precision experiments," *Nucl. Instrum. Meth. A* **556** (2006) 80–86.

[188] A. Ferrari, P. R. Sala, A. Fassò, and J. Ranft, *FLUKA: A multi-particle transport code (program version 2005)*. CERN Yellow Reports: Monographs. CERN, Geneva, 2005. http://cds.cern.ch/record/898301.

[189] T. Böhlen, F. Cerutti, M. Chin, A. Fassò, A. Ferrari, P. Ortega, A. Mairani, P. Sala, G. Smirnov, and V. Vlachoudis, "The FLUKA Code: Developments and Challenges for High Energy and Medical Applications," *Nucl. Data Sheets* **120** (2014) 211–214.

[190] T. Sjostrand, S. Mrenna, and P. Z. Skands, "PYTHIA 6.4 Physics and Manual," *JHEP* **05** (2006) 026, arXiv:hep-ph/0603175 [hep-ph].

[191] K. Kovarik *et al.*, "nCTEQ15 - Global analysis of nuclear parton distributions with uncertainties in the CTEQ framework," *Phys. Rev.* **D93** (2016) no. 8, 085037, arXiv:1509.00792 [hep-ph].

[192] A. Kusina *et al.*, "nCTEQ15 - Global analysis of nuclear parton distributions with uncertainties," *PoS* **DIS2015** (2015) 041, arXiv:1509.01801 [hep-ph].

[193] T. Pierog, I. Karpenko, J. M. Katzy, E. Yatsenko, and K. Werner, "EPOS LHC: Test of collective hadronization with data measured at the CERN Large Hadron Collider," *Phys. Rev.* **C92** (2015) 034906, arXiv:1306.0121 [hep-ph].

[194] S. Ostapchenko, "Monte Carlo treatment of hadronic interactions in enhanced Pomeron scheme: I. QGSJET-II model," *Phys. Rev.* **D83** (2011) 014018, arXiv:1010.1869 [hep-ph].

[195] C. Baus, T. Pierog, and R. Ulrich, "Cosmic Ray Monte Carlo (CRMC),". https://web.ikp.kit.edu/rulrich/crmc.html.

[196] J. F. Grosse-Oetringhaus and K. Reygers, "Charged-Particle Multiplicity in Proton-Proton Collisions," *J. Phys. G* **37** (2010) 083001, arXiv:0912.0023 [hep-ex].

[197] F. Chollet *et al.*, "Keras." https://github.com/fchollet/keras, 2015.

[198] G. P. Zeller, *A Precise measurement of the weak mixing angle in neutrino - nucleon scattering*. PhD thesis, Northwestern U., 2002.

[199] M. Holder *et al.*, "Measurement of the Neutral to Charged Current Cross-Section Ratio in Neutrino and anti-neutrino Interactions," *Phys. Lett. B* **71** (1977) 222.

[200] **CCFR, E744, E770** Collaboration, K. S. McFarland *et al.*, "A Precision measurement of electroweak parameters in neutrino - nucleon scattering," *Eur. Phys. J. C* **1** (1998) 509–513, arXiv:hep-ex/9701010.

[201] **NuTeV** Collaboration, G. Zeller *et al.*, "A Precise Determination of Electroweak Parameters in Neutrino Nucleon Scattering," *Phys. Rev. Lett.* **88** (2002) 091802, arXiv:hep-ex/0110059. [Erratum: Phys.Rev.Lett. 90, 239902 (2003)].

[202] K. J. Eskola, P. Paakkinen, H. Paukkunen, and C. A. Salgado, "EPPS16: Nuclear parton distributions with LHC data," *Eur. Phys. J.* **C77** (2017) no. 3, 163, arXiv:1612.05741 [hep-ph].

[203] **NNPDF** Collaboration, R. Abdul Khalek, J. J. Ethier, and J. Rojo, "Nuclear parton distributions from lepton-nucleus scattering and the impact of an electron-ion collider," *Eur. Phys. J.* **C79** (2019) no. 6, 471, arXiv:1904.00018 [hep-ph].

[204] R. Abdul Khalek, J. J. Ethier, J. Rojo, and G. van Weelden, "nNNPDF2.0: quark flavor separation in nuclei from LHC data," *JHEP* **09** (2020) 183, arXiv:2006.14629 [hep-ph].

[205] **DsTau** Collaboration, S. Aoki *et al.*, "DsTau: Study of tau neutrino production with 400 GeV protons from the CERN-SPS," *JHEP* **01** (2020) 033, arXiv:1906.03487 [hep-ex].

[206] **NA49-future Collaboration** Collaboration, M. Gazdzicki, Z. Fodor, and G. Vesztergombi, "Study of Hadron Production in Hadron-Nucleus and Nucleus-Nucleus Collisions at the CERN SPS," Tech. Rep. CERN-SPSC-2006-034. SPSC-P-330, CERN, Geneva, Nov, 2006. http://cds.cern.ch/record/995681. revised version submitted on 2006-11-06 12:38:20.

[207] J. L. Feng, F. Kling, *et al.*, *Forward Physics Facility*, Aug., 2020. https://doi.org/10.5281/zenodo.4059893.

[208] **ALEPH, DELPHI, L3, OPAL, LEP Electroweak** Collaboration, S. Schael *et al.*, "Electroweak Measurements in Electron-Positron Collisions at W-Boson-Pair Energies at LEP," *Phys. Rept.* **532** (2013) 119–244, arXiv:1302.3415 [hep-ex].

[209] L. Wolfenstein, "Neutrino Oscillations in Matter," *Phys. Rev. D* **17** (1978) 2369–2374.

[210] J. Barranco, O. Miranda, and T. Rashba, "Probing new physics with coherent neutrino scattering off nuclei," *JHEP* **12** (2005) 021, arXiv:hep-ph/0508299.

[211] W. Altmannshofer, M. Tammaro, and J. Zupan, "Non-standard neutrino interactions and low energy experiments," *JHEP* **09** (2019) 083, arXiv:1812.02778 [hep-ph].

[212] K. Babu, D. Gonçalves, S. Jana, and P. A. Machado, "Neutrino Non-Standard Interactions: Complementarity Between LHC and Oscillation Experiments," arXiv:2003.03383 [hep-ph].

[213] D. Liu, C. Sun, and J. Gao, "Constraints on neutrino non-standard interactions from LHC data with large missing transverse momentum," arXiv:2009.06668 [hep-ph].

[214] R. E. Shrock, "Electromagnetic Properties and Decays of Dirac and Majorana Neutrinos in a General Class of Gauge Theories," *Nucl. Phys. B* **206** (1982) 359–379.

[215] J.-M. Frère, J. Heeck, and S. Mollet, "Triangle Inequalities for Majorana-Neutrino Magnetic Moments," *Phys. Rev. D* **92** (2015) no. 5, 053002, arXiv:1506.02964 [hep-ph].

[216] **NuTeV** Collaboration, G. P. Zeller *et al.*, "A Precise Determination of Electroweak Parameters in Neutrino Nucleon Scattering," *Phys. Rev. Lett.* **88** (2002) 091802, arXiv:hep-ex/0110059. [Erratum: Phys.Rev.Lett. 90, 239902 (2003)].

[217] **XENON** Collaboration, E. Aprile *et al.*, "Excess electronic recoil events in XENON1T," *Phys. Rev. D* **102** (2020) no. 7, 072004, arXiv:2006.09721 [hep-ex].

[218] **XENON** Collaboration, E. Aprile *et al.*, "Search for New Physics in Electronic Recoil Data from XENONnT," arXiv:2207.11330 [hep-ex].

[219] D. Croon, S. D. McDermott, and J. Sakstein, "Missing in axion: Where are XENON1T's big black holes?," *Phys. Dark Univ.* **32** (2021) 100801, arXiv:2007.00650 [hep-ph].

[220] J. Sakstein, D. Croon, S. D. McDermott, M. C. Straight, and E. J. Baxter, "Beyond the Standard Model Explanations of GW190521," *Phys. Rev. Lett.* **125** (2020) no. 26, 261105, arXiv:2009.01213 [gr-qc].

[221] M. B. Voloshin, "On Compatibility of Small Mass with Large Magnetic Moment of Neutrino," *Sov. J. Nucl. Phys.* **48** (1988) 512.

[222] R. Barbieri and R. N. Mohapatra, "A Neutrino With a Large Magnetic Moment and a Naturally Small Mass," *Phys. Lett. B* **218** (1989) 225–229.

[223] S. Rajpoot, "DIRAC NEUTRINO MAGNETIC MOMENTS IN THE LEFT-RIGHT SYMMETRIC MODEL," *Phys. Lett. B* **237** (1990) 77–80.

[224] A. Aboubrahim, T. Ibrahim, A. Itani, and P. Nath, "Large Neutrino Magnetic Dipole Moments in MSSM Extensions," *Phys. Rev. D* **89** (2014) no. 5, 055009, arXiv:1312.2505 [hep-ph].

[225] M. Lindner, B. Radovčić, and J. Welter, "Revisiting Large Neutrino Magnetic Moments," *JHEP* **07** (2017) 139, arXiv:1706.02555 [hep-ph].

[226] K. S. Babu, S. Jana, and M. Lindner, "Large Neutrino Magnetic Moments in the Light of Recent Experiments," *JHEP* **10** (2020) 040, arXiv:2007.04291 [hep-ph].

[227] K. S. Babu, S. Jana, M. Lindner, and V. P. K, "Muon $g-2$ Anomaly and Neutrino Magnetic Moments," arXiv:2104.03291 [hep-ph].

[228] A. G. Beda, V. B. Brudanin, V. G. Egorov, D. V. Medvedev, V. S. Pogosov, M. V. Shirchenko, and A. S. Starostin, "The results of search for the neutrino magnetic moment in GEMMA experiment," *Adv. High Energy Phys.* **2012** (2012) 350150.

[229] **TEXONO** Collaboration, H. T. Wong *et al.*, "A Search of Neutrino Magnetic Moments with a High-Purity Germanium Detector at the Kuo-Sheng Nuclear Power Station," *Phys. Rev. D* **75** (2007) 012001, arXiv:hep-ex/0605006.

[230] **LSND** Collaboration, L. B. Auerbach *et al.*, "Measurement of electron - neutrino - electron elastic scattering," *Phys. Rev. D* **63** (2001) 112001, arXiv:hep-ex/0101039.

[231] **DONUT** Collaboration, R. Schwienhorst *et al.*, "A New upper limit for the tau - neutrino magnetic moment," *Phys. Lett. B* **513** (2001) 23–29, arXiv:hep-ex/0102026.

[232] R. C. Allen *et al.*, "Study of electron-neutrino electron elastic scattering at LAMPF," *Phys. Rev. D* **47** (1993) 11–28.

[233] **Borexino** Collaboration, C. Arpesella *et al.*, "Direct Measurement of the Be-7 Solar Neutrino Flux with 192 Days of Borexino Data," *Phys. Rev. Lett.* **101** (2008) 091302, arXiv:0805.3843 [astro-ph].

[234] **Borexino** Collaboration, M. Agostini *et al.*, "Limiting neutrino magnetic moments with Borexino Phase-II solar neutrino data," *Phys. Rev. D* **96** (2017) no. 9, 091103, arXiv:1707.09355 [hep-ex].

[235] P. Coloma, M. C. Gonzalez-Garcia, M. Maltoni, J. a. P. Pinheiro, and S. Urrea, "Constraining New Physics with Borexino Phase-II spectral data," arXiv:2204.03011 [hep-ph].

[236] S. K. A., A. Majumdar, D. K. Papoulias, H. Prajapati, and R. Srivastava, "First results of LZ and XENONnT: A comparative study of neutrino properties and light mediators," arXiv:2208.06415 [hep-ph].

[237] **LZ** Collaboration, J. Aalbers *et al.*, "First Dark Matter Search Results from the LUX-ZEPLIN (LZ) Experiment," arXiv:2207.03764 [hep-ex].

[238] D. Aristizabal Sierra, O. G. Miranda, D. K. Papoulias, and G. S. Garcia, "Neutrino magnetic and electric dipole moments: From measurements to parameter space," *Phys. Rev. D* **105** (2022) no. 3, 035027, arXiv:2112.12817 [hep-ph].

[239] G. Magill, R. Plestid, M. Pospelov, and Y.-D. Tsai, "Dipole Portal to Heavy Neutral Leptons," *Phys. Rev. D* **98** (2018) no. 11, 115015, arXiv:1803.03262 [hep-ph].

[240] I. M. Shoemaker, Y.-D. Tsai, and J. Wyenberg, "Active-to-sterile neutrino dipole portal and the XENON1T excess," *Phys. Rev. D* **104** (2021) no. 11, 115026, arXiv:2007.05513 [hep-ph].

[241] A. Ismail, S. Jana, and R. M. Abraham, "Neutrino up-scattering via the dipole portal at forward LHC detectors," *Phys. Rev. D* **105** (2022) no. 5, 055008, arXiv:2109.05032 [hep-ph].

[242] K. A. Kouzakov and A. I. Studenikin, "Electromagnetic properties of massive neutrinos in low-energy elastic neutrino-electron scattering," *Phys. Rev. D* **95** (2017) no. 5, 055013, arXiv:1703.00401 [hep-ph]. [Erratum: Phys.Rev.D 96, 099904 (2017)].

[243] C. Giunti, J. Gruszko, B. Jones, L. Kaufman, D. Parno, and A. Pocar, "Report of the Topical Group on Neutrino Properties for Snowmass 2021," arXiv:2209.03340 [hep-ph].

[244] W. Grimus and T. Schwetz, "Elastic neutrino electron scattering of solar neutrinos and potential effects of magnetic and electric dipole moments," *Nucl. Phys. B* **587** (2000) 45–66, arXiv:hep-ph/0006028.

[245] J. F. Beacom and P. Vogel, "Neutrino magnetic moments, flavor mixing, and the Super-Kamiokande solar data," *Phys. Rev. Lett.* **83** (1999) 5222–5225, arXiv:hep-ph/9907383.

[246] C. Q. Geng and R. E. Marshak, "Uniqueness of Quark and Lepton Representations in the Standard Model From the Anomalies Viewpoint," *Phys. Rev. D* **39** (1989) 693.

[247] K. S. Babu and R. N. Mohapatra, "Quantization of Electric Charge From Anomaly Constraints and a Majorana Neutrino," *Phys. Rev. D* **41** (1990) 271.

[248] A. Das, D. Ghosh, C. Giunti, and A. Thalapillil, "Neutrino charge constraints from scattering to the weak gravity conjecture to neutron stars," *Phys. Rev. D* **102** (2020) no. 11, 115009, arXiv:2005.12304 [hep-ph].

[249] K. Fujikawa and R. Shrock, "The Magnetic Moment of a Massive Neutrino and Neutrino Spin Rotation," *Phys. Rev. Lett.* **45** (1980) 963.

[250] P. Vogel and J. Engel, "Neutrino Electromagnetic Form-Factors," *Phys. Rev. D* **39** (1989) 3378.

[251] P. B. Pal and L. Wolfenstein, "Radiative Decays of Massive Neutrinos," *Phys. Rev. D* **25** (1982) 766.

[252] R. N. Mohapatra, S.-P. Ng, and H.-b. Yu, "Reactor searches for neutrino magnetic moment as a probe of extra dimensions," *Phys. Rev. D* **70** (2004) 057301, arXiv:hep-ph/0404274.

[253] K. S. Babu and R. N. Mohapatra, "Model for Large Transition Magnetic Moment of the ν_e," *Phys. Rev. Lett.* **63** (1989) 228.

[254] S. M. Barr, E. M. Freire, and A. Zee, "A Mechanism for large neutrino magnetic moments," *Phys. Rev. Lett.* **65** (1990) 2626–2629.

[255] J. Bernabeu, J. Papavassiliou, and J. Vidal, "The Neutrino charge radius is a physical observable," *Nucl. Phys. B* **680** (2004) 450–478, arXiv:hep-ph/0210055.

[256] J. Bernabeu, L. G. Cabral-Rosetti, J. Papavassiliou, and J. Vidal, "On the charge radius of the neutrino," *Phys. Rev. D* **62** (2000) 113012, arXiv:hep-ph/0008114.

[257] C. Ahdida *et al.*, "SND@LHC - Scattering and Neutrino Detector at the LHC," tech. rep., CERN, Geneva, Jan, 2021. https://cds.cern.ch/record/2750060.

[258] **SHiP** Collaboration, C. Ahdida *et al.*, "SND@LHC," arXiv:2002.08722 [physics.ins-det].

[259] **DONuT** Collaboration, K. Kodama *et al.*, "Final tau-neutrino results from the DONuT experiment," *Phys. Rev. D* **78** (2008) 052002, arXiv:0711.0728 [hep-ex].

[260] **OPERA** Collaboration, N. Agafonova *et al.*, "Final Results of the OPERA Experiment on ν_τ Appearance in the CNGS Neutrino Beam," *Phys. Rev. Lett.* **120** (2018) no. 21, 211801, arXiv:1804.04912 [hep-ex]. [Erratum: Phys.Rev.Lett. 121, 139901 (2018)].

[261] **MicroBooNE, LAr1-ND, ICARUS-WA104** Collaboration, M. Antonello *et al.*, "A Proposal for a Three Detector Short-Baseline Neutrino Oscillation Program in the Fermilab Booster Neutrino Beam," arXiv:1503.01520 [physics.ins-det].

[262] **DUNE** Collaboration, B. Abi *et al.*, "Deep Underground Neutrino Experiment (DUNE), Far Detector Technical Design Report, Volume II: DUNE Physics," arXiv:2002.03005 [hep-ex].

[263] **FASER** Collaboration, "FASERν 2: A Forward Neutrino Experiment at the HL LHC." https://www.snowmass21.org/docs/files/summaries/NF/SNOWMASS21-NF10$_N F6 - EF6_E F9 - IF0_F ASERnu2 - 006.pdf$.

[264] B. Batell, J. L. Feng, A. Ismail, F. Kling, R. M. Abraham, and S. Trojanowski, "Discovering dark matter at the LHC through its nuclear scattering in far-forward emulsion and liquid argon detectors," *Phys. Rev. D* **104** (2021) no. 3, 035036, arXiv:2107.00666 [hep-ph].

[265] B. Batell, J. L. Feng, M. Fieg, A. Ismail, F. Kling, R. M. Abraham, and S. Trojanowski, "Hadrophilic dark sectors at the Forward Physics Facility," *Phys. Rev. D* **105** (2022) no. 7, 075001, arXiv:2111.10343 [hep-ph].

[266] A. Ismail, R. Mammen Abraham, and F. Kling, "Neutral current neutrino interactions at FASERν," *Phys. Rev. D* **103** (2021) no. 5, 056014, arXiv:2012.10500 [hep-ph].

[267] **FASER** Collaboration, H. Abreu *et al.*, "The FASER Detector," arXiv:2207.11427 [physics.ins-det].

[268] E.-J. Ahn, R. Engel, T. K. Gaisser, P. Lipari, and T. Stanev, "Cosmic ray interaction event generator SIBYLL 2.1," *Phys. Rev.* **D80** (2009) 094003, arXiv:0906.4113 [hep-ph].

[269] F. Riehn, R. Engel, A. Fedynitch, T. K. Gaisser, and T. Stanev, "A new version of the event generator Sibyll," *PoS* **ICRC2015** (2016) 558, arXiv:1510.00568 [hep-ph].

[270] F. Riehn, H. P. Dembinski, R. Engel, A. Fedynitch, T. K. Gaisser, and T. Stanev, "The hadronic interaction model SIBYLL 2.3c and Feynman scaling," *PoS* **ICRC2017** (2018) 301, arXiv:1709.07227 [hep-ph].

[271] F. Riehn, R. Engel, A. Fedynitch, T. K. Gaisser, and T. Stanev, "Hadronic interaction model Sibyll 2.3d and extensive air showers," *Phys. Rev. D* **102** (2020) no. 6, 063002, arXiv:1912.03300 [hep-ph].

[272] J. A. Formaggio and G. P. Zeller, "From eV to EeV: Neutrino Cross Sections Across Energy Scales," *Rev. Mod. Phys.* **84** (2012) 1307–1341, arXiv:1305.7513 [hep-ex].

[273] K. S. McFarland, "Neutrino Interactions," in *61st Scottish Universities Summer School in Physics: Neutrinos in Particle Physics, Astrophysics and Cosmology (SUSSP61)*, pp. 65–90. 4, 2008. arXiv:0804.3899 [hep-ex].

[274] A. de Gouvea and J. Jenkins, "What can we learn from neutrino electron scattering?," *Phys. Rev. D* **74** (2006) 033004, arXiv:hep-ph/0603036.

[275] W. Grimus and P. Stockinger, "Effects of neutrino oscillations and neutrino magnetic moments on elastic neutrino - electron scattering," *Phys. Rev. D* **57** (1998) 1762–1768, arXiv:hep-ph/9708279.

[276] S. Foroughi-Abari, F. Kling, and Y.-D. Tsai, "Looking forward to millicharged dark sectors at the LHC," *Phys. Rev. D* **104** (2021) no. 3, 035014, arXiv:2010.07941 [hep-ph].

[277] F. Kling, J.-L. Kuo, S. Trojanowski, and Y.-D. Tsai, "FLArE up dark sectors with EM form factors at the LHC Forward Physics Facility," arXiv:2205.09137 [hep-ph].

[278] V. Mathur, I. M. Shoemaker, and Z. Tabrizi, "Using DUNE to Shed Light on the Electromagnetic Properties of Neutrinos," arXiv:2111.14884 [hep-ph].

[279] **Particle Data Group** Collaboration, R. L. Workman and Others, "Review of Particle Physics," *PTEP* **2022** (2022) 083C01.

[280] M. Cadeddu, F. Dordei, C. Giunti, Y. F. Li, E. Picciau, and Y. Y. Zhang, "Physics results from the first COHERENT observation of coherent elastic neutrino-nucleus scattering in argon and their combination with cesium-iodide data," *Phys. Rev. D* **102** (2020) no. 1, 015030, arXiv:2005.01645 [hep-ph].

[281] J. Bernstein and T. D. Lee, "Electromagnetic Form-factor of the Neutrinos," *Phys. Rev. Lett.* **11** (1963) 512–516.

[282] A. Grau and J. A. Grifols, "Neutrino Charge Radius and Substructure," *Phys. Lett. B* **166** (1986) 233–237.

[283] W. Bai, M. Diwan, M. V. Garzelli, Y. S. Jeong, and M. H. Reno, "Far-forward neutrinos at the Large Hadron Collider," *JHEP* **06** (2020) 032, arXiv:2002.03012 [hep-ph].

[284] Y. S. Jeong, W. Bai, M. Diwan, M. V. Garzelli, F. K. Kumar, and M. H. Reno, "Neutrinos from charm: forward production at the LHC and in the atmosphere," *PoS* **ICRC2021** (2021) 1218, arXiv:2107.01178 [hep-ph].

[285] R. Maciula and A. Szczurek, "Far-forward production of charm mesons and neutrinos at Forward Physics Facilities at the LHC and the intrinsic charm in the proton," arXiv:2210.08890 [hep-ph].

[286] A. N. Khan, "New limits on neutrino electromagnetic interactions and light new physics with XENONnT," arXiv:2208.02144 [hep-ph].

[287] M. Atzori Corona, M. Cadeddu, N. Cargioli, F. Dordei, C. Giunti, Y. F. Li, C. A. Ternes, and Y. Y. Zhang, "Impact of the Dresden-II and COHERENT neutrino scattering data on neutrino electromagnetic properties and electroweak physics," *JHEP* **09** (2022) 164, arXiv:2205.09484 [hep-ph].

[288] **CONUS** Collaboration, H. Bonet *et al.*, "First upper limits on neutrino electromagnetic properties from the CONUS experiment," *Eur. Phys. J. C* **82** (2022) no. 9, 813, arXiv:2201.12257 [hep-ex].

[289] S. N. Gninenko, N. V. Krasnikov, and A. Rubbia, "Search for millicharged particles in reactor neutrino experiments: A Probe of the PVLAS anomaly," *Phys. Rev. D* **75** (2007) 075014, arXiv:hep-ph/0612203.

[290] J.-W. Chen, H.-C. Chi, H.-B. Li, C. P. Liu, L. Singh, H. T. Wong, C.-L. Wu, and C.-P. Wu, "Constraints on millicharged neutrinos via analysis of data from atomic ionizations with germanium detectors at sub-keV sensitivities," *Phys. Rev. D* **90** (2014) no. 1, 011301, arXiv:1405.7168 [hep-ph].

[291] A. Studenikin, "New bounds on neutrino electric millicharge from limits on neutrino magnetic moment," *EPL* **107** (2014) no. 2, 21001, arXiv:1302.1168 [hep-ph]. [Erratum: EPL 107, 39901 (2014), Erratum: Europhys.Lett. 107, 39901 (2014)].

[292] **XMASS** Collaboration, K. Abe *et al.*, "Search for exotic neutrino-electron interactions using solar neutrinos in XMASS-I," *Phys. Lett. B* **809** (2020) 135741, arXiv:2005.11891 [hep-ex].

[293] G. G. Raffelt, "Limits on neutrino electromagnetic properties: An update," *Phys. Rept.* **320** (1999) 319–327.

[294] A. I. Studenikin and I. Tokarev, "Millicharged neutrino with anomalous magnetic moment in rotating magnetized matter," *Nucl. Phys. B* **884** (2014) 396–407, arXiv:1209.3245 [hep-ph].

[295] G. Barbiellini and G. Cocconi, "Electric Charge of the Neutrinos from SN1987A," *Nature* **329** (1987) 21–22.

[296] K. J. Kelly and Y.-D. Tsai, "Proton fixed-target scintillation experiment to search for millicharged dark matter," *Phys. Rev. D* **100** (2019) no. 1, 015043, arXiv:1812.03998 [hep-ph].

[297] A. N. Khan, "Electric charge dequantization with Dirac neutrinos in CEνNS," arXiv:2201.10578 [hep-ph].

[298] **CHARM-II** Collaboration, P. Vilain *et al.*, "Experimental study of electromagnetic properties of the muon-neutrino in neutrino - electron scattering," *Phys. Lett. B* **345** (1995) 115–118.

[299] **CCFR, E744, E770** Collaboration, K. S. McFarland *et al.*, "A Precision measurement of electroweak parameters in neutrino - nucleon scattering," *Eur. Phys. J. C* **1** (1998) 509–513, arXiv:hep-ex/9701010.

[300] M. Hirsch, E. Nardi, and D. Restrepo, "Bounds on the tau and muon neutrino vector and axial vector charge radius," *Phys. Rev. D* **67** (2003) 033005, arXiv:hep-ph/0210137.

[301] **TEXONO** Collaboration, M. Deniz *et al.*, "Measurement of Nu(e)-bar -Electron Scattering Cross-Section with a CsI(Tl) Scintillating Crystal Array at the Kuo-Sheng Nuclear Power Reactor," *Phys. Rev. D* **81** (2010) 072001, arXiv:0911.1597 [hep-ex].

[302] J. Erler and M. J. Ramsey-Musolf, "The Weak mixing angle at low energies," *Phys. Rev. D* **72** (2005) 073003, arXiv:hep-ph/0409169.

[303] **ALEPH, CDF, D0, DELPHI, L3, OPAL, SLD, LEP Electroweak Working Group, Tevatron Electroweak Working Group, SLD Electroweak, Heavy Flavour Groups** Collaboration, "Precision Electroweak Measurements and Constraints on the Standard Model," arXiv:1012.2367 [hep-ex].

[304] K. S. Kumar, S. Mantry, W. J. Marciano, and P. A. Souder, "Low Energy Measurements of the Weak Mixing Angle," *Ann. Rev. Nucl. Part. Sci.* **63** (2013) 237–267, arXiv:1302.6263 [hep-ex].

[305] **PVDIS** Collaboration, D. Wang *et al.*, "Measurement of parity violation in electron–quark scattering," *Nature* **506** (2014) no. 7486, 67–70.

[306] C. S. Wood, S. C. Bennett, D. Cho, B. P. Masterson, J. L. Roberts, C. E. Tanner, and C. E. Wieman, "Measurement of parity nonconservation and an anapole moment in cesium," *Science* **275** (1997) 1759–1763.

[307] J. Guena, M. Lintz, and M. A. Bouchiat, "Measurement of the parity violating 6S-7S transition amplitude in cesium achieved within 2 x 10(-13) atomic-unit accuracy by stimulated-emission detection," *Phys. Rev. A* **71** (2005) 042108, arXiv:physics/0412017.

[308] V. A. Dzuba, J. C. Berengut, V. V. Flambaum, and B. Roberts, "Revisiting parity non-conservation in cesium," *Phys. Rev. Lett.* **109** (2012) 203003, arXiv:1207.5864 [hep-ph].

[309] M. S. Safronova, D. Budker, D. DeMille, D. F. J. Kimball, A. Derevianko, and C. W. Clark, "Search for New Physics with Atoms and Molecules," *Rev. Mod. Phys.* **90** (2018) no. 2, 025008, arXiv:1710.01833 [physics.atom-ph].

[310] **SLAC E158** Collaboration, P. L. Anthony *et al.*, "Precision measurement of the weak mixing angle in Moller scattering," *Phys. Rev. Lett.* **95** (2005) 081601, arXiv:hep-ex/0504049.

[311] **Qweak** Collaboration, D. Androić *et al.*, "Precision measurement of the weak charge of the proton," *Nature* **557** (2018) no. 7704, 207–211, arXiv:1905.08283 [nucl-ex].

[312] **COHERENT** Collaboration, D. Akimov *et al.*, "Measurement of the Coherent Elastic Neutrino-Nucleus Scattering Cross Section on CsI by COHERENT," *Phys. Rev. Lett.* **129** (2022) no. 8, 081801, arXiv:2110.07730 [hep-ex].

[313] A. Majumdar, D. K. Papoulias, R. Srivastava, and J. W. F. Valle, "Physics implications of recent Dresden-II reactor data," *Phys. Rev. D* **106** (2022) no. 9, 093010, arXiv:2208.13262 [hep-ph].

[314] H. Davoudiasl, H.-S. Lee, and W. J. Marciano, "Muon Anomaly and Dark Parity Violation," *Phys. Rev. Lett.* **109** (2012) 031802, arXiv:1205.2709 [hep-ph].

[315] H. Davoudiasl, H.-S. Lee, and W. J. Marciano, "Low Q^2 weak mixing angle measurements and rare Higgs decays," *Phys. Rev. D* **92** (2015) no. 5, 055005, arXiv:1507.00352 [hep-ph].

[316] J. Erler and R. Ferro-Hernández, "Weak Mixing Angle in the Thomson Limit," *JHEP* **03** (2018) 196, arXiv:1712.09146 [hep-ph].

[317] A. de Gouvea, P. A. N. Machado, Y. F. Perez-Gonzalez, and Z. Tabrizi, "Measuring the Weak Mixing Angle in the DUNE Near Detector Complex," *Phys. Rev. Lett.* **125** (2020) no. 5, 051803, arXiv:1912.06658 [hep-ph].

[318] R. Boughezal, A. Emmert, T. Kutz, S. Mantry, M. Nycz, F. Petriello, K. Şimşek, D. Wiegand, and X. Zheng, "Neutral-current electroweak physics and SMEFT studies at the EIC," *Phys. Rev. D* **106** (2022) no. 1, 016006, arXiv:2204.07557 [hep-ph].

[319] **MOLLER** Collaboration, J. Mammei, "The MOLLER Experiment," *Nuovo Cim. C* **035N04** (2012) 203–208, arXiv:1208.1260 [hep-ex].

[320] N. Berger *et al.*, "Measuring the weak mixing angle with the P2 experiment at MESA," *J. Univ. Sci. Tech. China* **46** (2016) no. 6, 481–487, arXiv:1511.03934 [physics.ins-det].

[321] **H1, ZEUS** Collaboration, P. A. Souder, "Parity-violating PVDIS with SoLID," *AIP Conf. Proc.* **1441** (2012) no. 1, 123–125.

[322] J. Alonso *et al.*, "Neutrino physics opportunities with the IsoDAR source at Yemilab," *Phys. Rev. D* **105** (2022) no. 5, 052009, arXiv:2111.09480 [hep-ex].

[323] T. S. Kosmas, O. G. Miranda, D. K. Papoulias, M. Tortola, and J. W. F. Valle, "Sensitivities to neutrino electromagnetic properties at the TEXONO experiment," *Phys. Lett. B* **750** (2015) 459–465, arXiv:1506.08377 [hep-ph].

[324] B. C. Canas, E. A. Garces, O. G. Miranda, M. Tortola, and J. W. F. Valle, "The weak mixing angle from low energy neutrino measurements: a global update," *Phys. Lett. B* **761** (2016) 450–455, arXiv:1608.02671 [hep-ph].

[325] B. C. Cañas, E. A. Garcés, O. G. Miranda, and A. Parada, "Future perspectives for a weak mixing angle measurement in coherent elastic neutrino nucleus scattering experiments," *Phys. Lett. B* **784** (2018) 159–162, arXiv:1806.01310 [hep-ph].

[326] M. Lindner, W. Rodejohann, and X.-J. Xu, "Coherent Neutrino-Nucleus Scattering and new Neutrino Interactions," *JHEP* **03** (2017) 097, arXiv:1612.04150 [hep-ph].

[327] **Particle Data Group** Collaboration, P. A. Zyla *et al.*, "Review of Particle Physics," *PTEP* **2020** (2020) no. 8, 083C01.

[328] J. Bernstein, M. Ruderman, and G. Feinberg, "Electromagnetic Properties of the neutrino," *Phys. Rev.* **132** (1963) 1227–1233.

[329] G. G. Raffelt, "Particle physics from stars," *Ann. Rev. Nucl. Part. Sci.* **49** (1999) 163–216, arXiv:hep-ph/9903472.

[330] S. N. Gninenko, "The MiniBooNE anomaly and heavy neutrino decay," *Phys. Rev. Lett.* **103** (2009) 241802, arXiv:0902.3802 [hep-ph].

[331] S. N. Gninenko, "A resolution of puzzles from the LSND, KARMEN, and MiniBooNE experiments," *Phys. Rev. D* **83** (2011) 015015, arXiv:1009.5536 [hep-ph].

[332] D. McKeen and M. Pospelov, "Muon Capture Constraints on Sterile Neutrino Properties," *Phys. Rev. D* **82** (2010) 113018, arXiv:1011.3046 [hep-ph].

[333] S. N. Gninenko, "New limits on radiative sterile neutrino decays from a search for single photons in neutrino interactions," *Phys. Lett. B* **710** (2012) 86–90, arXiv:1201.5194 [hep-ph].

[334] S. Vergani, N. W. Kamp, A. Diaz, C. A. Argüelles, J. M. Conrad, M. H. Shaevitz, and M. A. Uchida, "Explaining the MiniBooNE Excess Through a Mixed Model of Oscillation and Decay," arXiv:2105.06470 [hep-ph].

[335] **MiniBooNE** Collaboration, A. A. Aguilar-Arevalo *et al.*, "Significant Excess of ElectronLike Events in the MiniBooNE Short-Baseline Neutrino Experiment," *Phys. Rev. Lett.* **121** (2018) no. 22, 221801, arXiv:1805.12028 [hep-ex].

[336] C. Cowan, F. Reines, and F. Harrison, "Upper limit on the neutrino magnetic moment," *Phys. Rev.* **96** (1954) 1294.

[337] R. Davis, K. Lande, B. Cleveland, J. Rowley, and J. Ullman, "Report on the chlorine solar neutrino experiment,".

[338] R. Davis, K. Lande, C. Lee, B. Cleveland, and J. Ullman, "Results of the Homestake chlorine solar neutrino experiment," in *21st International Cosmic Ray Conference*, pp. 155–158. 1990.

[339] G. Vidyakin, V. Vyrodov, I. Gurevich, Y. Kozlov, V. Martemyanov, S. Sukhotin, V. Tarasenkov, E. Turbin, and S. Khakhimov, "Limitations on the magnetic moment and charge radius of the electron-anti-neutrino," *JETP Lett.* **55** (1992) 206–210.

[340] A. Derbin, A. Chernyi, L. Popeko, V. Muratova, G. Shishkina, and S. Bakhlanov, "Experiment on anti-neutrino scattering by electrons at a reactor of the Rovno nuclear power plant," *JETP Lett.* **57** (1993) 768–772.

[341] **MUNU** Collaboration, Z. Daraktchieva *et al.*, "Final results on the neutrino magnetic moment from the MUNU experiment," *Phys. Lett. B* **615** (2005) 153–159, arXiv:hep-ex/0502037.

[342] **TEXONO** Collaboration, M. Deniz *et al.*, "Measurement of Nu(e)-bar -Electron Scattering Cross-Section with a CsI(Tl) Scintillating Crystal Array at the Kuo-Sheng Nuclear Power Reactor," *Phys. Rev. D* **81** (2010) 072001, arXiv:0911.1597 [hep-ex].

[343] **Muon g-2** Collaboration, B. Abi *et al.*, "Measurement of the Positive Muon Anomalous Magnetic Moment to 0.46 ppm," *Phys. Rev. Lett.* **126** (2021) no. 14, 141801, arXiv:2104.03281 [hep-ex].

[344] N. Viaux, M. Catelan, P. B. Stetson, G. Raffelt, J. Redondo, A. A. R. Valcarce, and A. Weiss, "Neutrino and axion bounds from the globular cluster M5 (NGC 5904)," *Phys. Rev. Lett.* **111** (2013) 231301, arXiv:1311.1669 [astro-ph.SR].

[345] N. Viaux, M. Catelan, P. B. Stetson, G. Raffelt, J. Redondo, A. A. R. Valcarce, and A. Weiss, "Particle-physics constraints from the globular cluster M5: Neutrino Dipole Moments," *Astron. Astrophys.* **558** (2013) A12, arXiv:1308.4627 [astro-ph.SR].

[346] F. Capozzi and G. Raffelt, "Axion and neutrino bounds improved with new calibrations of the tip of the red-giant branch using geometric distance determinations," *Phys. Rev. D* **102** (2020) no. 8, 083007, arXiv:2007.03694 [astro-ph.SR].

[347] K. S. Babu, D. Chang, W.-Y. Keung, and I. Phillips, "Comment on 'Mechanism for large neutrino magnetic moments'," *Phys. Rev. D* **46** (1992) 2268–2269.

[348] "Forward Physics Facility Kickoff Meeting." https://indico.cern.ch/event/955956, November, 2020.

[349] "Second Forward Physics Facility Meeting." https://indico.cern.ch/event/1022352, May, 2021.

[350] B. Batell, J. Berger, and A. Ismail, "Probing the Higgs Portal at the Fermilab Short-Baseline Neutrino Experiments," *Phys. Rev. D* **100** (2019) no. 11, 115039, arXiv:1909.11670 [hep-ph].

[351] B. Batell, J. Berger, L. Darmé, and C. Frugiuele, "Inelastic Dark Matter at the Fermilab Short Baseline Neutrino Program," arXiv:2106.04584 [hep-ph].

[352] **MicroBooNE** Collaboration, R. Acciarri *et al.*, "Design and Construction of the MicroBooNE Detector," *JINST* **12** (2017) no. 02, P02017, arXiv:1612.05824 [physics.ins-det].

[353] M. Atkinson, P. Coloma, I. Martinez-Soler, N. Rocco, and I. M. Shoemaker, "Heavy neutrino searches through double-bang events at super-kamiokande, dune, and hyper-kamiokande," arXiv:2105.09357 [hep-ph].

[354] Y.-S. Tsai, "Pair Production and Bremsstrahlung of Charged Leptons," *Rev. Mod. Phys.* **46** (1974) 815. [Erratum: Rev.Mod.Phys. 49, 421–423 (1977)].

[355] J. E. Kim, A. Dasgupta, and S. K. Kang, "Probing Neutrino Dipole Portal at COHERENT Experiment," arXiv:2108.12998 [hep-ph].

[356] **XENON** Collaboration, E. Aprile *et al.*, "Dark Matter Search Results from a One Ton-Year Exposure of XENON1T," *Phys. Rev. Lett.* **121** (2018) no. 11, 111302, arXiv:1805.12562 [astro-ph.CO].

[357] **NOMAD** Collaboration, J. Altegoer *et al.*, "Search for a new gauge boson in pi0 decays," *Phys. Lett. B* **428** (1998) 197–205, arXiv:hep-ex/9804003.

[358] **L3** Collaboration, O. Adriani *et al.*, "Search for anomalous production of single photon events in e+ e- annihilations at the Z resonance," *Phys. Lett. B* **297** (1992) 469–476.

[359] **OPAL** Collaboration, R. Akers *et al.*, "Measurement of single photon production in e+ e- collisions near the Z0 resonance," *Z. Phys. C* **65** (1995) 47–66.

[360] **DELPHI** Collaboration, P. Abreu *et al.*, "Search for new phenomena using single photon events in the DELPHI detector at LEP," *Z. Phys. C* **74** (1997) 577–586.

[361] J. L. Lopez, D. V. Nanopoulos, and A. Zichichi, "Single photon signals at LEP in supersymmetric models with a light gravitino," *Phys. Rev. D* **55** (1997) 5813–5825, arXiv:hep-ph/9611437.

[362] N. Bar, K. Blum, and G. D'Amico, "Is there a supernova bound on axions?," *Phys. Rev. D* **101** (2020) no. 12, 123025, arXiv:1907.05020 [hep-ph].

[363] **PandaX-4T** Collaboration, Y. Meng *et al.*, "Dark Matter Search Results from the PandaX-4T Commissioning Run," *Phys. Rev. Lett.* **127** (2021) no. 26, 261802, arXiv:2107.13438 [hep-ex].

[364] S. Alekhin *et al.*, "A facility to Search for Hidden Particles at the CERN SPS: the SHiP physics case," *Rept. Prog. Phys.* **79** (2016) no. 12, 124201, arXiv:1504.04855 [hep-ph].

[365] **SuperCDMS** Collaboration, R. Agnese *et al.*, "Low-mass dark matter search with CDMSlite," *Phys. Rev. D* **97** (2018) no. 2, 022002.

[366] I. M. Shoemaker and J. Wyenberg, "Direct Detection Experiments at the Neutrino Dipole Portal Frontier," *Phys. Rev. D* **99** (2019) no. 7, 075010, arXiv:1811.12435 [hep-ph].

[367] R. Plestid, "Luminous solar neutrinos i: Dipole portals," arXiv:2010.04193 [hep-ph].

[368] **BOREXINO** Collaboration, M. Agostini *et al.*, "Comprehensive measurement of *pp*-chain solar neutrinos," *Nature* **562** (2018) no. 7728, 505–510.

[369] **Super-Kamiokande** Collaboration, K. Abe *et al.*, "Solar Neutrino Measurements in Super-Kamiokande-IV," *Phys. Rev. D* **94** (2016) no. 5, 052010, arXiv:1606.07538 [hep-ex].

[370] O. G. Miranda, D. K. Papoulias, O. Sanders, M. Tórtola, and J. W. F. Valle, "Low-energy probes of sterile neutrino transition magnetic moments," *JHEP* **12** (2021) 191.

[371] B. Holdom, "Two U(1)'s and Epsilon Charge Shifts," *Phys. Lett. B* **166** (1986) 196–198.

[372] C. Boehm and P. Fayet, "Scalar dark matter candidates," *Nucl. Phys. B* **683** (2004) 219–263, arXiv:hep-ph/0305261.

[373] M. Pospelov, A. Ritz, and M. B. Voloshin, "Secluded WIMP Dark Matter," *Phys. Lett. B* **662** (2008) 53–61, arXiv:0711.4866 [hep-ph].

[374] J. L. Feng and J. Kumar, "The WIMPless Miracle: Dark-Matter Particles without Weak-Scale Masses or Weak Interactions," *Phys. Rev. Lett.* **101** (2008) 231301, arXiv:0803.4196 [hep-ph].

[375] E. Izaguirre, G. Krnjaic, P. Schuster, and N. Toro, "Analyzing the Discovery Potential for Light Dark Matter," *Phys. Rev. Lett.* **115** (2015) no. 25, 251301, arXiv:1505.00011 [hep-ph].

[376] G. Krnjaic, "Probing Light Thermal Dark-Matter With a Higgs Portal Mediator," *Phys. Rev. D* **94** (2016) no. 7, 073009, arXiv:1512.04119 [hep-ph].

[377] B. Batell, T. Han, D. McKeen, and B. Shams Es Haghi, "Thermal Dark Matter Through the Dirac Neutrino Portal," *Phys. Rev. D* **97** (2018) no. 7, 075016, arXiv:1709.07001 [hep-ph].

[378] **FASER** Collaboration, H. Abreu *et al.*, "First neutrino interaction candidates at the LHC," arXiv:2105.06197 [hep-ex].

[379] **FASER** Collaboration, "FASER 2: Forward Search Experiment at the HL LHC." https://www.snowmass21.org/docs/files/summaries/EF/SNOWMASS21-EF9$_E$F6 − NF3$_N$F6 − RF6$_R$F0 − CF7$_C$F0 − AF5$_A$F0$_F$ASER2 − 038.*pdf*.

[380] H. Abreu *et al.*, "Neutrino / Dark Particle Detectors for the HL-LHC Forward Beam." https://www.snowmass21.org/docs/files/summaries/NF/SNOWMASS21-NF10$_N$F0 − EF0$_E$F0$_A$riga − 072.*pdf*.

[381] B. Batell, M. Pospelov, and A. Ritz, "Exploring Portals to a Hidden Sector Through Fixed Targets," *Phys. Rev. D* **80** (2009) 095024, arXiv:0906.5614 [hep-ph].

[382] P. deNiverville, M. Pospelov, and A. Ritz, "Observing a light dark matter beam with neutrino experiments," *Phys. Rev. D* **84** (2011) 075020, arXiv:1107.4580 [hep-ph].

[383] P. deNiverville, D. McKeen, and A. Ritz, "Signatures of sub-GeV dark matter beams at neutrino experiments," *Phys. Rev. D* **86** (2012) 035022, arXiv:1205.3499 [hep-ph].

[384] B. Batell, P. deNiverville, D. McKeen, M. Pospelov, and A. Ritz, "Leptophobic Dark Matter at Neutrino Factories," *Phys. Rev. D* **90** (2014) no. 11, 115014, arXiv:1405.7049 [hep-ph].

[385] B. A. Dobrescu and C. Frugiuele, "GeV-Scale Dark Matter: Production at the Main Injector," *JHEP* **02** (2015) 019, arXiv:1410.1566 [hep-ph].

[386] Y. Kahn, G. Krnjaic, J. Thaler, and M. Toups, "DAEδALUS and dark matter detection," *Phys. Rev. D* **91** (2015) no. 5, 055006, arXiv:1411.1055 [hep-ph].

[387] P. Coloma, B. A. Dobrescu, C. Frugiuele, and R. Harnik, "Dark matter beams at LBNF," *JHEP* **04** (2016) 047, arXiv:1512.03852 [hep-ph].

[388] P. deNiverville, M. Pospelov, and A. Ritz, "Light new physics in coherent neutrino-nucleus scattering experiments," *Phys. Rev. D* **92** (2015) no. 9, 095005, arXiv:1505.07805 [hep-ph].

[389] **MiniBooNE-DM** Collaboration, A. Aguilar-Arevalo *et al.*, "Dark Matter Search in a Proton Beam Dump with MiniBooNE," *Phys. Rev. Lett.* **118** (2017) no. 22, 221803, arXiv:1702.02688 [hep-ex].

[390] V. De Romeri, K. J. Kelly, and P. A. Machado, "DUNE-PRISM Sensitivity to Light Dark Matter," *Phys. Rev. D* **100** (2019) no. 9, 095010, arXiv:1903.10505 [hep-ph].

[391] B. Dutta, D. Kim, S. Liao, J.-C. Park, S. Shin, and L. E. Strigari, "Dark matter signals from timing spectra at neutrino experiments," *Phys. Rev. Lett.* **124** (2020) no. 12, 121802, arXiv:1906.10745 [hep-ph].

[392] B. Dutta, D. Kim, S. Liao, J.-C. Park, S. Shin, L. E. Strigari, and A. Thompson, "Searching for Dark Matter Signals in Timing Spectra at Neutrino Experiments," arXiv:2006.09386 [hep-ph].

[393] M. Battaglieri *et al.*, "US Cosmic Visions: New Ideas in Dark Matter 2017: Community Report," in *U.S. Cosmic Visions: New Ideas in Dark Matter*. 7, 2017. arXiv:1707.04591 [hep-ph].

[394] J. Beacham *et al.*, "Physics Beyond Colliders at CERN: Beyond the Standard Model Working Group Report," *J. Phys. G* **47** (2020) no. 1, 010501, arXiv:1901.09966 [hep-ex].

[395] **Planck** Collaboration, P. A. R. Ade *et al.*, "Planck 2015 results. XIII. Cosmological parameters," *Astron. Astrophys.* **594** (2016) A13, arXiv:1502.01589 [astro-ph.CO].

[396] T. R. Slatyer, N. Padmanabhan, and D. P. Finkbeiner, "CMB Constraints on WIMP Annihilation: Energy Absorption During the Recombination Epoch," *Phys. Rev. D* **80** (2009) 043526, arXiv:0906.1197 [astro-ph.CO].

[397] D. Tucker-Smith and N. Weiner, "Inelastic dark matter," *Phys. Rev. D* **64** (2001) 043502, arXiv:hep-ph/0101138.

[398] A. Berlin, N. Blinov, G. Krnjaic, P. Schuster, and N. Toro, "Dark Matter, Millicharges, Axion and Scalar Particles, Gauge Bosons, and Other New Physics with LDMX," *Phys. Rev. D* **99** (2019) no. 7, 075001, arXiv:1807.01730 [hep-ph].

[399] J. L. Feng and J. Smolinsky, "Impact of a resonance on thermal targets for invisible dark photon searches," *Phys. Rev. D* **96** (2017) no. 9, 095022, arXiv:1707.03835 [hep-ph].

[400] A. Berlin, P. deNiverville, A. Ritz, P. Schuster, and N. Toro, "Sub-GeV dark matter production at fixed-target experiments," *Phys. Rev. D* **102** (2020) no. 9, 095011, arXiv:2003.03379 [hep-ph].

[401] E. Bernreuther, S. Heeba, and F. Kahlhoefer, "Resonant sub-GeV Dirac dark matter," *JCAP* **03** (2021) 040, arXiv:2010.14522 [hep-ph].

[402] R. Acquafredda *et al.*, "The OPERA experiment in the CERN to Gran Sasso neutrino beam," *JINST* **4** (2009) P04018.

[403] **SHiP** Collaboration, C. Ahdida *et al.*, "SND@LHC," arXiv:2002.08722 [physics.ins-det].

[404] **DUNE** Collaboration, R. Acciarri *et al.*, "Long-Baseline Neutrino Facility (LBNF) and Deep Underground Neutrino Experiment (DUNE): Conceptual Design Report, Volume 2: The Physics Program for DUNE at LBNF," arXiv:1512.06148 [physics.ins-det].

[405] **ArgoNeuT** Collaboration, R. Acciarri *et al.*, "Detection of Back-to-Back Proton Pairs in Charged-Current Neutrino Interactions with the ArgoNeuT Detector in the NuMI Low Energy Beam Line," *Phys. Rev. D* **90** (2014) no. 1, 012008, arXiv:1405.4261 [nucl-ex].

[406] **ArgoNeuT** Collaboration, R. Acciarri *et al.*, "Demonstration of MeV-Scale Physics in Liquid Argon Time Projection Chambers Using ArgoNeuT," *Phys. Rev. D* **99** (2019) no. 1, 012002, arXiv:1810.06502 [hep-ex].

[407] **MicroBooNE** Collaboration, R. Acciarri *et al.*, "Design and Construction of the MicroBooNE Detector," *JINST* **12** (2017) no. 02, P02017, arXiv:1612.05824 [physics.ins-det].

[408] **ICARUS** Collaboration, B. Ali-Mohammadzadeh *et al.*, "Design and implementation of the new scintillation light detection system of ICARUS T600," *JINST* **15** (2020) no. 10, T10007, arXiv:2006.05261 [physics.ins-det].

[409] J. Blümlein and J. Brunner, "New Exclusion Limits on Dark Gauge Forces from Proton Bremsstrahlung in Beam-Dump Data," *Phys. Lett. B* **731** (2014) 320–326, arXiv:1311.3870 [hep-ph].

[410] T. Leitner, "Neutrino Interactions with Nucleons and Nuclei." Thesis, Giessen U., 2005. https://gibuu.hepforge.org/trac/chrome/site/files/dipl/leitner.pdf.

[411] **K2K** Collaboration, S. Nakayama *et al.*, "Measurement of single pi0 production in neutral current neutrino interactions with water by a 1.3-GeV wide band muon neutrino beam," *Phys. Lett. B* **619** (2005) 255–262, arXiv:hep-ex/0408134.

[412] **MicroBooNE** Collaboration, "Study towards an event selection for neutral current inclusive single pi0 production in microboone,". https://www.osti.gov/biblio/1573043.

[413] **MiniBooNE** Collaboration, A. A. Aguilar-Arevalo *et al.*, "Measurement of ν_μ and $\bar{\nu}_\mu$ induced neutral current single π^0 production cross sections on mineral oil at $E_\nu \sim \mathcal{O}(1\text{GeV})$," *Phys. Rev. D* **81** (2010) 013005, arXiv:0911.2063 [hep-ex].

[414] P. Machado, H. Schulz, and J. Turner, "Tau neutrinos at DUNE: New strategies, new opportunities," *Phys. Rev. D* **102** (2020) no. 5, 053010, arXiv:2007.00015 [hep-ph].

[415] **European Muon** Collaboration, M. Arneodo *et al.*, "Multiplicities of Charged Hadrons in 280-GeV/c Muon - Proton Scattering," *Nucl. Phys. B* **258** (1985) 249–266.

[416] X. Qian, C. Zhang, B. Viren, and M. Diwan, "Three-dimensional Imaging for Large LArTPCs," *JINST* **13** (2018) no. 05, P05032, arXiv:1803.04850 [physics.ins-det].

[417] **MicroBooNE** Collaboration, P. Abratenko *et al.*, "Neutrino Event Selection in the MicroBooNE Liquid Argon Time Projection Chamber using Wire-Cell 3-D Imaging, Clustering, and Charge-Light Matching," arXiv:2011.01375 [physics.ins-det].

[418] **MicroBooNE** Collaboration, P. Abratenko *et al.*, "Cosmic Ray Background Rejection with Wire-Cell LArTPC Event Reconstruction in the MicroBooNE Detector," arXiv:2101.05076 [physics.ins-det].

[419] **BaBar** Collaboration, J. P. Lees *et al.*, "Search for Invisible Decays of a Dark Photon Produced in e^+e^- Collisions at BaBar," *Phys. Rev. Lett.* **119** (2017) no. 13, 131804, arXiv:1702.03327 [hep-ex].

[420] D. Banerjee *et al.*, "Dark matter search in missing energy events with NA64," *Phys. Rev. Lett.* **123** (2019) no. 12, 121801, arXiv:1906.00176 [hep-ex].

[421] **BEBC WA66** Collaboration, H. Grassler *et al.*, "Prompt Neutrino Production in 400-{GeV} Proton Copper Interactions," *Nucl. Phys. B* **273** (1986) 253–274.

[422] **CHARM-II** Collaboration, K. De Winter *et al.*, "A Detector for the Study of Neutrino - Electron Scattering," *Nucl. Instrum. Meth. A* **278** (1989) 670.

[423] J. D. Bjorken, S. Ecklund, W. R. Nelson, A. Abashian, C. Church, B. Lu, L. W. Mo, T. A. Nunamaker, and P. Rassmann, "Search for Neutral Metastable Penetrating Particles Produced in the SLAC Beam Dump," *Phys. Rev. D* **38** (1988) 3375.

[424] B. Batell, R. Essig, and Z. Surujon, "Strong Constraints on Sub-GeV Dark Sectors from SLAC Beam Dump E137," *Phys. Rev. Lett.* **113** (2014) no. 17, 171802, arXiv:1406.2698 [hep-ph].

[425] **NOvA** Collaboration, B. Wang, J. Bian, T. E. Coan, S. Kotelnikov, H. Duyang, and A. Hatzikoutelis, "Muon Neutrino on Electron Elastic Scattering in the NOvA Near Detector and its Applications Beyond the Standard Model," *J. Phys. Conf. Ser.* **888** (2017) no. 1, 012123.

[426] L. Marsicano, M. Battaglieri, M. Bondí, C. D. R. Carvajal, A. Celentano, M. De Napoli, R. De Vita, E. Nardi, M. Raggi, and P. Valente, "Novel Way to Search for Light Dark Matter in Lepton Beam-Dump Experiments," *Phys. Rev. Lett.* **121** (2018) no. 4, 041802, arXiv:1807.05884 [hep-ex].

[427] **BDX** Collaboration, M. Battaglieri *et al.*, "Dark Matter Search in a Beam-Dump eXperiment (BDX) at Jefferson Lab," arXiv:1607.01390 [hep-ex].

[428] **SHiP** Collaboration, C. Ahdida *et al.*, "Sensitivity of the SHiP experiment to light dark matter," *JHEP* **04** (2021) 199, arXiv:2010.11057 [hep-ex].

[429] S. N. Gninenko, D. V. Kirpichnikov, M. M. Kirsanov, and N. V. Krasnikov, "Combined search for light dark matter with electron and muon beams at NA64," *Phys. Lett. B* **796** (2019) 117–122, arXiv:1903.07899 [hep-ph].

[430] **LDMX** Collaboration, T. Åkesson *et al.*, "Light Dark Matter eXperiment (LDMX)," arXiv:1808.05219 [hep-ex].

[431] **Belle-II** Collaboration, W. Altmannshofer *et al.*, "The Belle II Physics Book," *PTEP* **2019** (2019) no. 12, 123C01, arXiv:1808.10567 [hep-ex]. [Erratum: PTEP 2020, 029201 (2020)].

[432] **FASER** Collaboration, H. Abreu *et al.*, "First neutrino interaction candidates at the LHC," *Phys. Rev. D* **104** (2021) no. 9, L091101, arXiv:2105.06197 [hep-ex].

[433] **Belle-II** Collaboration, W. Altmannshofer *et al.*, "The Belle II Physics Book," *PTEP* **2019** (2019) no. 12, 123C01, arXiv:1808.10567 [hep-ex]. [Erratum: PTEP 2020, 029201 (2020)].

[434] **NA64, Physics Beyond Colliders Conventional Beams Working Group** Collaboration, D. Banerjee, "Search for Dark Sector Physics at the NA64 experiment in the context of the Physics Beyond Colliders Projects," *PoS* **LeptonPhoton2019** (2019) 061, arXiv:1909.04363 [hep-ex].

[435] **SENSEI** Collaboration, J. Tiffenberg, M. Sofo-Haro, A. Drlica-Wagner, R. Essig, Y. Guardincerri, S. Holland, T. Volansky, and T.-T. Yu, "Single-electron and single-photon sensitivity with a silicon Skipper CCD," *Phys. Rev. Lett.* **119** (2017) no. 13, 131802, arXiv:1706.00028 [physics.ins-det].

[436] B. A. Dobrescu and C. Frugiuele, "Hidden GeV-scale interactions of quarks," *Phys. Rev. Lett.* **113** (2014) 061801, arXiv:1404.3947 [hep-ph].

[437] S. Tulin, "New weakly-coupled forces hidden in low-energy QCD," *Phys. Rev. D* **89** (2014) no. 11, 114008, arXiv:1404.4370 [hep-ph].

[438] D. E. Soper, M. Spannowsky, C. J. Wallace, and T. M. P. Tait, "Scattering of Dark Particles with Light Mediators," *Phys. Rev. D* **90** (2014) no. 11, 115005, arXiv:1407.2623 [hep-ph].

[439] J. A. Dror, R. Lasenby, and M. Pospelov, "New constraints on light vectors coupled to anomalous currents," *Phys. Rev. Lett.* **119** (2017) no. 14, 141803, arXiv:1705.06726 [hep-ph].

[440] J. A. Dror, R. Lasenby, and M. Pospelov, "Dark forces coupled to nonconserved currents," *Phys. Rev. D* **96** (2017) no. 7, 075036, arXiv:1707.01503 [hep-ph].

[441] P. Fileviez Perez and M. B. Wise, "Baryon and lepton number as local gauge symmetries," *Phys. Rev. D* **82** (2010) 011901, arXiv:1002.1754 [hep-ph]. [Erratum: Phys.Rev.D 82, 079901 (2010)].

[442] M. Duerr, P. Fileviez Perez, and M. B. Wise, "Gauge Theory for Baryon and Lepton Numbers with Leptoquarks," *Phys. Rev. Lett.* **110** (2013) 231801, arXiv:1304.0576 [hep-ph].

[443] M. Duerr and P. Fileviez Perez, "Baryonic Dark Matter," *Phys. Lett. B* **732** (2014) 101–104, arXiv:1309.3970 [hep-ph].

[444] P. Fileviez Perez, S. Ohmer, and H. H. Patel, "Minimal Theory for Lepto-Baryons," *Phys. Lett. B* **735** (2014) 283–287, arXiv:1403.8029 [hep-ph].

[445] A. Haas, C. S. Hill, E. Izaguirre, and I. Yavin, "Looking for milli-charged particles with a new experiment at the LHC," *Phys. Lett. B* **746** (2015) 117–120, arXiv:1410.6816 [hep-ph].

[446] J. L. Feng, F. Kling, *et al.*, *Forward Physics Facility: Snowmass 2021 Letter of Interest*, Aug., 2020. https://doi.org/10.5281/zenodo.4009640.

[447] T. Han and R. Hempfling, "Messenger sneutrinos as cold dark matter," *Phys. Lett. B* **415** (1997) 161–169, arXiv:hep-ph/9708264.

[448] L. J. Hall, T. Moroi, and H. Murayama, "Sneutrino cold dark matter with lepton number violation," *Phys. Lett. B* **424** (1998) 305–312, arXiv:hep-ph/9712515.

[449] M. Bauer, P. Foldenauer, and J. Jaeckel, "Hunting All the Hidden Photons," *JHEP* **07** (2018) 094, arXiv:1803.05466 [hep-ph].

[450] B. Batell, A. Freitas, A. Ismail, and D. Mckeen, "Flavor-specific scalar mediators," *Phys. Rev. D* **98** (2018) no. 5, 055026, arXiv:1712.10022 [hep-ph].

[451] B. Batell, A. Freitas, A. Ismail, and D. Mckeen, "Probing Light Dark Matter with a Hadrophilic Scalar Mediator," *Phys. Rev. D* **100** (2019) no. 9, 095020, arXiv:1812.05103 [hep-ph].

[452] B. Batell, A. Freitas, A. Ismail, D. McKeen, and M. Rai, "Renormalizable Models of Flavor-Specific Scalars," arXiv:2107.08059 [hep-ph].

[453] F. Kling and S. Trojanowski, "Forward experiment sensitivity estimator for the LHC and future hadron colliders," *Phys. Rev. D* **104** (2021) no. 3, 035012, arXiv:2105.07077 [hep-ph].

[454] S. Foroughi-Abari and A. Ritz, "Dark Sector Production via Proton Bremsstrahlung," arXiv:2108.05900 [hep-ph].

[455] P. Ilten, Y. Soreq, M. Williams, and W. Xue, "Serendipity in dark photon searches," *JHEP* **06** (2018) 004, arXiv:1801.04847 [hep-ph].

[456] T. Plehn, P. Reimitz, and P. Richardson, "Hadronic Footprint of GeV-Mass Dark Matter," *SciPost Phys.* **8** (2020) 092, arXiv:1911.11147 [hep-ph].

[457] P. Gondolo and G. Gelmini, "Cosmic abundances of stable particles: Improved analysis," *Nucl. Phys. B* **360** (1991) 145–179.

[458] G. Steigman, B. Dasgupta, and J. F. Beacom, "Precise Relic WIMP Abundance and its Impact on Searches for Dark Matter Annihilation," *Phys. Rev. D* **86** (2012) 023506, arXiv:1204.3622 [hep-ph].

[459] M. Pospelov, A. Ritz, and M. B. Voloshin, "Bosonic super-WIMPs as keV-scale dark matter," *Phys. Rev. D* **78** (2008) 115012, arXiv:0807.3279 [hep-ph].

[460] S. D. McDermott, H. H. Patel, and H. Ramani, "Dark Photon Decay Beyond The Euler-Heisenberg Limit," *Phys. Rev. D* **97** (2018) no. 7, 073005, arXiv:1705.00619 [hep-ph].

[461] F. Kling, "Probing Light Gauge Bosons in Tau Neutrino Experiments," arXiv:2005.03594 [hep-ph].

[462] **NA62** Collaboration, E. Cortina Gil *et al.*, "Search for production of an invisible dark photon in π^0 decays," *JHEP* **05** (2019) 182, arXiv:1903.08767 [hep-ex].

[463] M. Atiya *et al.*, "Search for the decay $\pi^0 \to \gamma X$," *Phys. Rev. Lett.* **69** (1992) 733–736.

[464] **Crystal Barrel** Collaboration, C. Amsler *et al.*, "Search for a new light gauge boson in decays of pi0 and eta," *Phys. Lett. B* **333** (1994) 271–276.

[465] **BNL-E949** Collaboration, A. Artamonov *et al.*, "Study of the decay $K^+ \to \pi^+ \nu\bar{\nu}$ in the momentum region $140 < P_\pi < 199$ MeV/c," *Phys. Rev. D* **79** (2009) 092004, arXiv:0903.0030 [hep-ex].

[466] M. Pospelov, "Secluded U(1) below the weak scale," *Phys. Rev. D* **80** (2009) 095002, arXiv:0811.1030 [hep-ph].

[467] **BES** Collaboration, M. Ablikim *et al.*, "Search for the invisible decay of J / psi in psi(2S) — pi+ pi- J / psi," *Phys. Rev. Lett.* **100** (2008) 192001, arXiv:0710.0039 [hep-ex].

[468] **BaBar** Collaboration, B. Aubert *et al.*, "A Search for Invisible Decays of the Upsilon(1S)," *Phys. Rev. Lett.* **103** (2009) 251801, arXiv:0908.2840 [hep-ex].

[469] **CDF** Collaboration, T. Aaltonen *et al.*, "A Search for dark matter in events with one jet and missing transverse energy in $p\bar{p}$ collisions at $\sqrt{s} = 1.96$ TeV," *Phys. Rev. Lett.* **108** (2012) 211804, arXiv:1203.0742 [hep-ex].

[470] I. M. Shoemaker and L. Vecchi, "Unitarity and Monojet Bounds on Models for DAMA, CoGeNT, and CRESST-II," *Phys. Rev. D* **86** (2012) 015023, arXiv:1112.5457 [hep-ph].

[471] **Serpukhov-Brussels-Los Alamos-Annecy(LAPP)** Collaboration, D. Alde *et al.*, "Neutral Decays of η' (958)," *Z. Phys. C* **36** (1987) 603.

[472] **ARGUS** Collaboration, H. Albrecht *et al.*, "An Upper Limit for Two Jet Production in Direct Υ (1s) Decays," *Z. Phys. C* **31** (1986) 181.

[473] A. Aranda and C. D. Carone, "Limits on a light leptophobic gauge boson," *Phys. Lett. B* **443** (1998) 352–358, arXiv:hep-ph/9809522.

[474] J. Blumlein *et al.*, "Limits on neutral light scalar and pseudoscalar particles in a proton beam dump experiment," *Z. Phys.* **C51** (1991) 341–350.

[475] **MiniBooNE** Collaboration, A. A. Aguilar-Arevalo *et al.*, "Dark Matter Search in a Proton Beam Dump with MiniBooNE," *Phys. Rev. Lett.* **118** (2017) no. 22, 221803, arXiv:1702.02688 [hep-ex].

[476] **MiniBooNE DM** Collaboration, A. A. Aguilar-Arevalo *et al.*, "Dark Matter Search in Nucleon, Pion, and Electron Channels from a Proton Beam Dump with MiniBooNE," *Phys. Rev. D* **98** (2018) no. 11, 112004, arXiv:1807.06137 [hep-ex].

[477] A. A. Aguilar-Arevalo *et al.*, "First Leptophobic Dark Matter Search from Coherent CAPTAIN-Mills," arXiv:2109.14146 [hep-ex].

[478] R. Barbieri and T. E. O. Ericson, "Evidence Against the Existence of a Low Mass Scalar Boson from Neutron-Nucleus Scattering," *Phys. Lett. B* **57** (1975) 270–272.

[479] V. Barger, C.-W. Chiang, W.-Y. Keung, and D. Marfatia, "Proton size anomaly," *Phys. Rev. Lett.* **106** (2011) 153001, arXiv:1011.3519 [hep-ph].

[480] E. Ma and D. Roy, "Phenomenology of the B - 3L(τ) gauge boson," *Phys. Rev. D* **58** (1998) 095005, arXiv:hep-ph/9806210.

[481] T. Han, J. Liao, H. Liu, and D. Marfatia, "Nonstandard neutrino interactions at COHERENT, DUNE, T2HK and LHC," *JHEP* **11** (2019) 028, arXiv:1910.03272 [hep-ph].

[482] J. Heeck, M. Lindner, W. Rodejohann, and S. Vogl, "Non-Standard Neutrino Interactions and Neutral Gauge Bosons," *SciPost Phys.* **6** (2019) no. 3, 038, arXiv:1812.04067 [hep-ph].

[483] I. Esteban, M. Gonzalez-Garcia, M. Maltoni, I. Martinez-Soler, and J. Salvado, "Updated Constraints on Non-Standard Interactions from Global Analysis of Oscillation Data," *JHEP* **08** (2018) 180, arXiv:1805.04530 [hep-ph].

[484] **CRESST** Collaboration, A. H. Abdelhameed *et al.*, "First results from the CRESST-III low-mass dark matter program," *Phys. Rev. D* **100** (2019) no. 10, 102002, arXiv:1904.00498 [astro-ph.CO].

[485] **DarkSide** Collaboration, P. Agnes *et al.*, "Low-Mass Dark Matter Search with the DarkSide-50 Experiment," *Phys. Rev. Lett.* **121** (2018) no. 8, 081307, arXiv:1802.06994 [astro-ph.HE].

[486] **XENON** Collaboration, E. Aprile *et al.*, "Search for Coherent Elastic Scattering of Solar ^{8}B Neutrinos in the XENON1T Dark Matter Experiment," *Phys. Rev. Lett.* **126** (2021) 091301, arXiv:2012.02846 [hep-ex].

[487] **Planck** Collaboration, N. Aghanim *et al.*, "Planck 2018 results. VI. Cosmological parameters," *Astron. Astrophys.* **641** (2020) A6, arXiv:1807.06209 [astro-ph.CO]. [Erratum: Astron.Astrophys. 652, C4 (2021)].

[488] M. Escudero, D. Hooper, G. Krnjaic, and M. Pierre, "Cosmology with A Very Light $L_\mu - L_\tau$ Gauge Boson," *JHEP* **03** (2019) 071, arXiv:1901.02010 [hep-ph].

[489] M. Bauer, P. Foldenauer, and M. Mosny, "Flavor structure of anomaly-free hidden photon models," *Phys. Rev. D* **103** (2021) no. 7, 075024, arXiv:2011.12973 [hep-ph].

[490] J. B. Dent, F. Ferrer, and L. M. Krauss, "Constraints on Light Hidden Sector Gauge Bosons from Supernova Cooling," arXiv:1201.2683 [astro-ph.CO].

[491] H. K. Dreiner, J.-F. Fortin, C. Hanhart, and L. Ubaldi, "Supernova constraints on MeV dark sectors from e^+e^- annihilations," *Phys. Rev. D* **89** (2014) no. 10, 105015, arXiv:1310.3826 [hep-ph].

[492] D. Kazanas, R. N. Mohapatra, S. Nussinov, V. L. Teplitz, and Y. Zhang, "Supernova Bounds on the Dark Photon Using its Electromagnetic Decay," *Nucl. Phys. B* **890** (2014) 17–29, arXiv:1410.0221 [hep-ph].

[493] E. Rrapaj and S. Reddy, "Nucleon-nucleon bremsstrahlung of dark gauge bosons and revised supernova constraints," *Phys. Rev. C* **94** (2016) no. 4, 045805, arXiv:1511.09136 [nucl-th].

[494] J. H. Chang, R. Essig, and S. D. McDermott, "Revisiting Supernova 1987A Constraints on Dark Photons," *JHEP* **01** (2017) 107, arXiv:1611.03864 [hep-ph].

[495] J. H. Chang, R. Essig, and S. D. McDermott, "Supernova 1987A Constraints on Sub-GeV Dark Sectors, Millicharged Particles, the QCD Axion, and an Axion-like Particle," *JHEP* **09** (2018) 051, arXiv:1803.00993 [hep-ph].

[496] A. Sung, H. Tu, and M.-R. Wu, "New constraint from supernova explosions on light particles beyond the Standard Model," *Phys. Rev. D* **99** (2019) no. 12, 121305, arXiv:1903.07923 [hep-ph].

[497] N. Bar, K. Blum, and G. D'Amico, "Is there a supernova bound on axions?," *Phys. Rev. D* **101** (2020) no. 12, 123025, arXiv:1907.05020 [hep-ph].

[498] P. S. B. Dev, D. Kim, K. Sinha, and Y. Zhang, "New interference effects from light gauge bosons in neutrino-electron scattering," *Phys. Rev. D* **104** (2021) no. 7, 075001, arXiv:2105.09309 [hep-ph].

[499] R. Mammen Abraham, D. Gonçalves, T. Han, S. C. I. Leung, and H. Qin, "Directly probing the Higgs-top coupling at high scales," *Phys. Lett. B* **825** (2022) 136839, arXiv:2106.00018 [hep-ph].

[500] R. Mammen Abraham and D. Gonçalves, "Boosting New Physics Searches in $t\bar{t}Z$ and tZj Production with Angular Moments," arXiv:2208.05986 [hep-ph].

[501] R. Mammen Abraham, S. Foroughi-Abari, F. Kling, and Y.-D. Tsai, "Neutrino Electromagnetic Properties and the Weak Mixing Angle at the LHC Forward Physics Facility," arXiv:2301.10254 [hep-ph].

VITA

Roshan Mammen Abraham

Candidate for the Degree of

Doctor of Philosophy

Dissertation: PHYSICS AT HIGH AND LOW p_T AT THE LHC

Major Field: Physics

Biographical:

Education:

Completed the requirements for the Doctor of Philosophy in Physics at Oklahoma State University, Stillwater, Oklahoma in August, 2023.

Completed the requirements for the Master of Science in Physics at Case Western Reserve University, Cleveland, Ohio in 2016.

Completed the requirements for the Bachelor of Technology in Electronics and Communication Engineering at National Institute of Technology, Calicut, Calicut, India in 2013.

Recognition:

Awarded "TASI Fellowship 2022" from University of Colorado, Boulder, USA in 2022.

Awarded the "PITT PACC Travel Award" for Phenomenology Symposium at University of Pittsburgh in 2022.

Awarded the "Robberson Summer Dissertation Fellowship 2022" in 2022, and Dr. Swamy Memorial Scholarship in 2021 from Oklahoma State University.